Breakdowns in U.S. Antarctic program disrupt research p. 1148

High-frequency combustion-based actuators pp. 1152 & 1212

Presynaptic pruning linked to neurodevelopmental disorders p. 1197

Science

$15
15 SEPTEMBER 2023
science.org
AAAS

BRAINY BIRDS

More-advanced vocal learners are better problem-solvers p. 1170

EDITORIAL

Science needed now, for action

Csaba Kőrösi
Csaba Kőrösi was president of the 77th session of the UN General Assembly (UNGA 77), New York, NY, USA and is director of the Blue Planet Foundation, Budapest, Hungary. csaba.korosi@mfa.gov.hu

Johannes Cullmann
was scientific adviser to the president of UNGA 77, New York, NY, USA and is vice chair of UN-Water, Geneva, Switzerland. He is also director for Water and Cryosphere, World Meteorological Organization, Geneva, Switzerland. jcullmann@wmo.int

At the beginning of the 77th session of the United Nations General Assembly (UNGA 77) in September 2022, UN members agreed to design and implement solutions to guarantee food, water, and education for all; improve human development; reform the global financial system; secure a healthy environment; and embark on a path toward a less unjust global society. Transformative solutions are needed to respond to the multiple related crises of the Anthropocene and to help reach the Sustainable Development Goals (SDGs). As the 78th session of the UNGA now gets underway, the importance of science in helping the UN to make progress on these issues is as clear and critical as ever. Yet participation of the scientific community is not what it could and needs to be.

Within the UN, the role of science as a unifying platform for political negotiation to address global and systemic challenges is well recognized, through entities such as the Intergovernmental Panel on Climate Change and the Intergovernmental Science-Policy Platform on Biodiversity and Ecosystem Services. Reports from such bodies provide the latest knowledge to the international community to help address systemic issues and identify transformative solutions for coordinated action at the local, national, and global levels.

> **"Leaders of the UN are committed to working with scientists..."**

Yet existing science mechanisms that support work of the UN have recognized shortcomings. For example, data and information are mostly not in real time, meaning that science support is often not up to date and relevant. Also, data are frequently provided and analyzed by institutions that only represent UN members partially. Data often reflect snapshot assessments, rather than consistent joint monitoring and analysis of trends over time and space. In addition, positive and negative externalities of development are too often not understood; therefore, many seemingly good investments backfire in other sectors.

In attempts to address such challenges, a "science summit" is being convened at UNGA 78. The goal is to develop and launch collaborations that demonstrate global science mechanisms and activities that support and validate sustainable development. Leaders of the UN are committed to working with scientists to identify transformative solutions and to put them before member states. Other efforts include the Multi-stakeholder Forum on Science, Technology and Innovation for the Sustainable Development Goals, the UN secretary general's recently announced scientific advisory board, and the Group of Friends on Science for Action launched during UNGA 77.

To support transformation within the UN and at the country level, research needs to be cross-sectoral, encouraging collaboration across domains, sectors, and ministries, focused on missions to promote an equitable and sustainable future. Central to discussions in the UNGA in the years ahead are how nations can secure food and water for all, increase carbon uptake in natural ecosystems, and decouple resource consumption from development. Other questions include how countries can guarantee affordable, sustainable health and education for all and how they can restore and protect the water cycle to improve human and ecosystem health, mitigate and adapt to climate change, and make our economy more resilient to shocks. It will also be important to ask how nations can design and implement a future, affordable, inclusive climate- and natural-resource–smart energy provision system, and how they can manage urbanization; build and retrofit safe, resilient, and sustainable cities and communities to end poverty; and prioritize equity, human well-being, and ecological health. How countries steer away from dangerous extractive business models, amend the concept of gross domestic product to include social and environmental sustainability, and adjust the international financial system accordingly will also be key questions.

One step toward a real-time system for describing trends that are relevant for policy-making in the UNGA just occurred during the 3rd International Forum on Big Data for Sustainable Development Goals in Beijing. The World Meteorological Organization and the Group on Earth Observations convened a panel of world-leading institutions to discuss how to best support policy development through key descriptors of sustainability. These descriptors integrate indicators across the 17 SDGs; provide real-time information products on economy, environment, and social development; and highlight trends that can be used to correct policy and financing for sustainable development.

Mistrust, conflict, and insecurity are undermining global cooperation and slowing our progress toward a common, sustainable future. But 2024 presents a new opportunity, and with strong scientific underpinnings and broad participation, we may yet build pathways to a unified, sustainable future*.

–Csaba Kőrösi and Johannes Cullmann

*The authors thank J. Espey for important contributions to this text.

10.1126/science.adk6920

Future generations are watching

Sudip Parikh
is the chief executive officer of the American Association for the Advancement of Science and executive publisher of the *Science* journals.
ceo@aaas.org

In many ways, the current US scientific enterprise is the intellectual descendant of 87 scientists who gathered in Philadelphia 175 years ago to establish the American Association for the Advancement of Science (AAAS, the publisher of *Science*). They joined disparate, scattered scientific disciplines to identify and address key challenges of the day. Today's research community and AAAS itself are reflections of their backgrounds and actions—for better or worse. Fairly or not, society judges the AAAS founders by the consequences of their choices for today. When future generations reflect upon the state of the world and science's role in shaping it, will they celebrate what AAAS and the research community have done?

Scientists have made extraordinary advances to improve lives around the world. AAAS has much to celebrate within this, such as supporting the robust scientific forum in the *Science* family of journals, fostering generations of experts who live at the intersection of science and policy through AAAS Science & Technology Policy Fellowships, and working with the United Kingdom's Royal Society to create a global framework for science diplomacy. For all its achievements, AAAS has also contributed to damaging ideas such as the promotion of eugenics. Ultimately, the organization must learn from its past to better understand how to ignite progress for the future.

"Does the world still need an organization incorporating the whole scientific ecosystem?"

The world is at a critical juncture. One path leads to ethical and transparent scientific collaboration with the potential to heal the sick, feed the hungry, and protect the planet. Another path leads to barriers that slow progress, distort scientific evidence, and even use science in harmful ways. Both futures are possible, but neither is inevitable. AAAS and the research community must make an active decision to engage in the former, or the latter vision may become the reality by default. AAAS must take a leadership role to cultivate an inclusive and mobilized global scientific community that enables and celebrates scientific excellence and science-informed decisions that lead to the first vision.

AAAS is committed to advancing scientific achievement. An open and inclusive scientific enterprise is essential to confronting the world's complex problems. Since the 1970s, AAAS has worked to expand access to the science, technology, engineering, mathematics, and medicine (STEMM) ecosystem, but there is much more to do. In the United States, this work has become controversial. AAAS must not be deterred, even as policies and legal challenges complicate the path to progress. One day, any child anywhere will consider it their birthright, have the support structures, and feel the sense of belonging needed to pursue opportunities in STEMM—and the enterprise will be more successful for it. Specifically, leadership here means working with hundreds of cross-sector partners to construct and implement a national strategy to achieve STEMM equity and inclusive excellence by 2050.

Scientists need the tools to participate and build trust in the communities where they live. The COVID-19 pandemic exposed cracks in the foundation of that trust and perpetuated polarization and misinformation in many countries. AAAS is focusing on building deep relationships among scientists, members of government, the judiciary, faith leaders, and journalists before those relationships are needed in times of crisis throughout the world. In the United States, efforts include placing scientists and engineers in media and policy settings to inform decision-making; matching scientific experts with members of the press on deadline to ensure more accurate news coverage; advising judges on the effective use of scientific evidence in courts; and facilitating constructive dialogues on the connection between science and faith.

AAAS must also continue to ensure that the voice of science is heard in policy-making, so that relevant, solutions-oriented, and actionable evidence is clear and available to federal, state, and local decision-makers. As an example, in the United States, AAAS partners with government membership organizations to provide state and local policy-makers with evidence on timely societal issues to inform their policies and programs.

Does the world still need an organization incorporating the whole scientific ecosystem? Now more than ever, science is essential to the decisions that will determine the prospects for future health, prosperity, and peace. The scientific enterprise and AAAS must help shape the next 175 years and not be bystanders as history unfolds before us. Future generations are watching.

–Sudip Parikh

PHOTO: AAAS

10.1126/science.adk7572

NEWS

> “What next, a trip for *Homo naledi* down to the *Titanic*?”
>
> **Radiocarbon expert Tom Higham**, on X (formerly Twitter), after paleoanthropologist Lee Berger provided rare hominin fossils to be sent briefly into space on a commercial flight to promote “exploration.” Higham and others called it an unethical publicity stunt that put irreplaceable fossils at risk.

IN BRIEF

Edited by **Jeffrey Brainard**

Cobalt mining raises trade-offs between promoting clean energy and protecting workers, two Sustainable Development Goals.

POLICY

Scientists call for revamped Sustainable Development Goals

New analyses confirm the world is failing to meet the Sustainable Development Goals, a set of ambitious objectives agreed to in 2015 by the United Nations, and scientists are among those calling for a reboot. The 17 goals include ending poverty and hunger and ensuring sustainable consumption by 2030. To meet them, the agreement includes 169 specific targets, but skeptics have long contended that many are not well defined, measurable, and scientifically rigorous. In an independent analysis the U.N. will publish next week ahead of a meeting it is holding to kick-start action, a panel of scientists found only two of 36 targets examined are on course to be met by 2030; 14 may be reached if current efforts are increased. In this week’s issue of *Nature*, a group of these authors urge the scientific community to help policymakers identify new practical and economical approaches to make progress on all the goals. In a Policy Forum in this week’s issue of *Science* (p. 1159), a separate group of scientists calls for four reforms to global policy to accelerate the work, such as making some of the targets binding in international treaties.

U.S. funds ocean CO_2 removal

CLIMATE | The U.S. government last week announced its first research grants for soaking up carbon dioxide in the ocean, a geoengineering approach that would lock away atmospheric carbon and blunt global warming. The 17 projects, financed by $24 million mostly from the National Oceanic and Atmospheric Administration, include lab experiments, modeling, and field trials. Topics of study include farming seaweed, fertilizing algae growth with iron, and adding antacid to increase the ocean’s ability to absorb carbon dioxide. The grants come as interest in marine carbon sequestration has soared in the past year, with field trials and startups already underway.

NIH nominee to get hearing

LEADERSHIP | President Joe Biden’s nominee to lead the U.S. National Institutes of Health (NIH) will get a confirmation hearing next month after a lawmaker who had blocked it on policy grounds since May relented. Senator Bernie Sanders (I–VT), who chairs the Senate health committee

that will consider the nomination of surgical oncologist Monica Bertagnolli, had refused to hold the hearing as a way to press the White House for more progress on reducing drug prices. Sanders gave in last week after the White House announced it will work with manufacturer Regeneron to hold down the cost of a possible new antibody drug to prevent COVID-19. Last month another holdout, health committee member Senator Elizabeth Warren (D–MA), had dropped her opposition to the hearing after Bertagnolli agreed not to take a drug industry job for 4 years after leaving federal service. NIH has lacked a permanent director since Francis Collins stepped down in December 2021.

CIA COVID-19 bribe alleged

PUBLIC HEALTH | A CIA whistleblower has alleged the agency bribed six analysts there to withdraw their support for the theory that a lab leak was the trigger of the COVID-19 pandemic, a congressman says. Representative Brad Wenstrup (R–OH), who chairs a House of Representatives subcommittee on the pandemic, said in a press release that the anonymous whistleblower "presents as a highly credible senior-level CIA officer." Wenstrup said the whistleblower testified to his committee that only the most senior analyst of a seven-member CIA team believed SARS-CoV-2 made a direct zoonotic jump from animals to humans. But the whistleblower alleged that the six supporting the lab origin were then "given a significant monetary incentive to change their position." Wenstrup said the agency concluded it was "unable to determine" whether the pandemic's origin was zoonotic or a lab leak. A CIA spokesperson told *Science*, "We do not pay analysts to reach specific conclusions," and a scientist who supports the zoonotic origin and has discussed the issue with the agency called the allegation "ludicrous."

Germany makes up with Elsevier

PUBLISHING | German science organizations and the publishing giant Elsevier last week resolved a long-running dispute by inking a deal that will allow academics to publish papers immediately free to read in its journals at discounted fees. The open-access "transformative agreement" also allows scholars at institutions in Germany's Project DEAL consortium to read all Elsevier titles at no extra cost. DEAL negotiators have signed similar pacts with other publishers. But talks with Elsevier stalled, and consortium members let Elsevier subscriptions lapse. Under the new deal, Elsevier will charge €2550 to publish an open-access article in most of its journals that require subscriptions and €6450 for Cell Press and *The Lancet* journals. A DEAL negotiator says the agreement will save money compared with the previous, subscription-based arrangements.

Retraction Watch data go public

RESEARCH INTEGRITY | The Retraction Watch and Crossref online platforms announced this week they will make all of Retraction Watch's data about more than 42,000 retracted research articles freely available on Crossref, which will fund Retraction Watch to continue to collect the data for the next 5 years. The move is meant to support tools that flag research articles that have been retracted and help scholars avoid citing them by accident. Crossref manages digital object identifiers, a system of links widely used to find and cite research articles and their metadata. Retraction Watch's data set is believed to be the largest of its kind.

EU research chief confirmed

LEADERSHIP | The European Commission has a new research chief after the European Parliament overwhelmingly approved the appointment of Iliana Ivanova on 12 September. Her portfolio covers innovation, research, culture, education, and youth. Ivanova, a Bulgarian, has worked as a member of the parliament and in the European Court of Auditors.

Scientists to help protect rhinos

CONSERVATION | Biologists will help develop plans to protect and monitor 2000 southern white rhinos (*Ceratotherium simum*) that a conservation group acquired from what was the species' largest captive breeding program. African Parks announced last week its purchase of the privately owned animals, which represent 15% of the species' population. White rhinos are classified as near threatened, largely because of poaching.

INVASIVE SPECIES

Feared ant invader lands in Europe

The red fire ant (*Solenopsis invicta*), a dreaded pest that packs a painful sting and infests houses and crops, has been confirmed for the first time in Europe. Native to South America, the insect can drive out native ants and other wildlife and damage electrical equipment. Acting on a tip, Italian researchers found 88 nests in 5 hectares by a river in Sicily in late 2022, they report this week in *Current Biology*. Based on maps of suitable habitat, they estimate the ants could invade 7% of Europe, including farms and half of Europe's urban areas. The species can spread via shipping containers and nursery plants. The researchers and government agencies are beginning an eradication campaign in Sicily and hope to recruit residents across Europe to keep an eye out for more fire ants.

PHOTO: MICHAEL DURHAM/MINDEN PICTURES

U.K. Prime Minister Rishi Sunak (left) and European Commission President Ursula von der Leyen have renewed research ties.

EUROPE

U.K. finally rejoins Horizon Europe

After years of excruciating delays, elated scientists welcome research funding agreement

By **Cathleen O'Grady**

Following years of Brexit-induced uncertainty and despair, U.K. scientists breathed a collective sigh of relief last week after the government announced it will rejoin the European Union's €95 billion research funding program known as Horizon Europe. The "agreement in principle" between the United Kingdom and the European Commission, announced early on 7 September, gives U.K. scientists access to a major source of grants they had benefited from before their country pulled out of the EU in early 2020. It also opens the way to new collaborations with colleagues in Europe.

"It couldn't be better news," says Daniel Rathbone, deputy executive director of the Campaign for Science and Engineering. But some lamented the lost years where the U.K. was shut out of the program. The delays have "caused a lot of damage and created a lot of distrust," says Kieron Flanagan, a science policy researcher at the University of Manchester. "It will take a few years to recover from that."

Horizon Europe funds individual researchers and cross-border scientific consortia in the EU and "associated" non-EU countries, which pay into the scheme. All that was put in jeopardy in 2016 when U.K. voters decided in a referendum to leave the EU. Although the 2020 Brexit withdrawal agreement included a mechanism for the U.K. to remain part of Horizon Europe, disputes over trade in Northern Ireland soured relations with the EU, and the Commission refused to sign off on the deal. The impasse over Northern Ireland broke in February, but funding remained a sticking point because the U.K. no longer felt its original deal was good value for money.

Now, negotiations have concluded and U.K. researchers will once again be able to fully participate in the program. From the beginning of next year, the U.K. will rejoin Horizon Europe as an associated country, paying €2.6 billion per year for access to the scheme, according to the Commission's announcement. The U.K. will also rejoin Copernicus, the EU's Earth observation program. But it will not rejoin the fusion program Euratom, instead pursuing a £650 million "domestic alternative," according to an announcement from the U.K. prime minister's office.

Under the newly negotiated deal, the U.K.'s contribution is reduced to account for its 3 years of absence. And it will be able to recoup funding if U.K. scientists receive "significantly less money" than the U.K.'s annual contribution, according to the government's announcement. It's a "shrewd agreement," according to a public statement by Conservative lawmaker Greg Clark, who leads the cross-party Science, Innovation and Technology Committee and has been outspoken about the damage done by the delays.

The deal still needs approval by EU member states, but James Wilsdon, a science policy researcher at University College London, sees no reason to doubt that will happen. And with the new clarity and certainty, "levels of U.K. participation will kick back in—hopefully, with some speed," he says. Researchers in the U.K. will be able to apply to Horizon funding calls this year, and under a transitional arrangement, the U.K. will provide the funding for any grants that they win until EU money begins to flow. (This is essentially a continuation of the government's guarantee during the U.K.'s years of limbo to fund scientists who successfully bid for Horizon grants but were unable to take them up.)

Researchers will particularly welcome the chance to lead Horizon collaborations again, says Martin Smith, a policy manager at the Wellcome Trust, a U.K. charity that supports research. Since 2020, U.K. scientists have not been allowed to serve as the "intellectual driving force" leading Horizon projects, which has limited the options of local scientists and made the U.K. an unattractive destination for talented hires, he says. The U.K. once had "recognized expertise and capability" in leading scientific consortia, says Jamie Arrowsmith, director of Universities UK International—and researchers will be excited to exercise those skills again.

The scope for collaborations is large, because Horizon extends beyond Europe to associated countries including New Zealand and Israel, with Canada and South Korea seeking to join. "Horizon is really the place where it's happening when it comes to international collaboration," Smith says. "For the U.K. to be part of this is very exciting." But as Horizon's successor program approaches in 2028, the U.K. may find itself back at the negotiating table, with the outcome dependent on ongoing good relations with the EU, Flanagan says.

The drop in EU-U.K. collaborations should now "snap back" quickly, says Thomas Jørgensen, director of policy coordination and foresight at the European University Association: "It's about calling your British colleagues who you were afraid to call before because you didn't know of the status of Horizon, and say[ing], 'OK, now we know. Let's get working.'" ■

PLANETARY SCIENCE

Mars Sample Return risks consuming NASA science

Forthcoming cost estimate for budget-busting mission could lead to strict caps from Congress

By **Paul Voosen**

The motto at NASA's Jet Propulsion Laboratory (JPL) is "dare mighty things," and in building Mars Sample Return (MSR), it is certainly doing that. The multispacecraft mission, planetary scientists' top priority, will collect rocks gathered by the Perseverance rover that is now exploring Mars. It will rocket them off Mars, catch them in orbit, and, as early as 2033, ferry them to Earth—where they will be scrutinized for signs of life and clues to martian history (*Science*, 22 November 2019, p. 932).

The cost of the mission may become altogether too mighty, however. The most recent official figure now puts it at some $6 billion, up from some $4 billion, and a leaked report suggests that, in one scenario, it could exceed $8 billion. Cost overruns for MSR and a few other large missions have already forced NASA to squeeze or delay other science missions, and calls to rethink—or even kill—MSR have grown. When an independent review of the project delivers a fresh cost estimate later this month, advocates are praying it stays well below $10 billion, which has emerged as a sort of red line for the mission. "It's fair to say that the future of Mars Sample Return lives and dies with the recommendations of that panel," says Casey Dreier, chief of space policy at the Planetary Society.

The increases stem in part from underestimates of how big the lander needs to be, along with the extensive steps needed to prevent earthly contamination of the samples, and vice versa. Inflation and supply chain shortages also played a role. But NASA hasn't clarified the issues further, Dreier says. "We don't really know what the problem is here."

Fears for the mission escalated in July, when the Senate committee that oversees NASA spending warned it would be canceled if the agency couldn't keep costs to $5.3 billion. The corresponding House of Representatives committee is likely to be more supportive, however. In the end Congress might work with the agency to set a new but stricter cost cap, much as it did a decade ago for the $10 billion JWST space telescope, a budget-busting mission that became too big to fail, says Allen Cutler, CEO of the Coalition for Deep Space Exploration and a former appropriations staffer focused on NASA. "Nerves have been touched. The Senate is letting NASA know that they've got some work to do."

But some planetary scientists would be glad to see the Senate follow through with its threat. One is Darby Dyar of Mount Holyoke College, who serves as deputy principal investigator for Veritas, a mission selected in 2021 to map Venus with radar. Late last year, NASA delayed Veritas until 2031 or later because of staffing shortages at JPL and cost overruns with MSR and other large missions. NASA has kept the science team on a "life support" fund of $1.5 million, Dyar says, but "the team is losing people like crazy." Meanwhile, MSR's potential scientific return does not excite her. "Do I actually believe we'll find signs of life in the returned samples? No."

NASA has also postponed its next billion-dollar mission in the New Frontiers series by 3 years, and it is delaying work on a flagship Uranus probe. The damage is not confined to NASA's planetary science division. Most prominently, the agency postponed work on the $1.4 billion Geospace Dynamics Constellation, six satellites that will study the upper atmosphere, causing universities to lay off staff hired to work on GDC instruments. "You're cutting the artery, the lifeblood, of our science," says space physicist Allison Jaynes of the University of Iowa. "All of NASA science is taking a hit because of the MSR burden."

NASA has been using its smaller missions as "piggy banks" for problems with larger projects, says Sean Solomon, retired director of Columbia University's Lamont–Doherty Earth Observatory. But MSR is not the only culprit, says Philip Christensen, a Mars scientist at Arizona State University and co-chair of last year's decadal report, which set MSR as the field's top priority. The price tag for Europa Clipper, launching next year to explore Jupiter's icy moon, grew from $2 billion to $5 billion. Psyche, an asteroid explorer, gained several hundred million dollars in unexpected costs after its launch was postponed from last year to October. Dragonfly, a mission to Saturn's moon Titan and the most recent New Frontiers selection, could cost $2.5 billion or more. And the price for NEO Surveyor, a congressionally ordered infrared telescope to chart hazardous asteroids, has risen to $1.2 billion—partly because of NASA-imposed delays to fund other shortfalls. "These missions haven't gotten the same blame," says Christensen, who points out that Congress has provided more money for MSR as its costs have grown.

JPL Director Laurie Leshin adds that MSR designers are looking for savings. "People think it's getting more complex, but it's actually getting simpler." After the European Space Agency (ESA) scrapped its plan to build a small "fetch" rover, NASA will now rely on Perseverance itself to transfer samples to the rocket-carrying lander, with small helicopters as backups. Other simplifica-

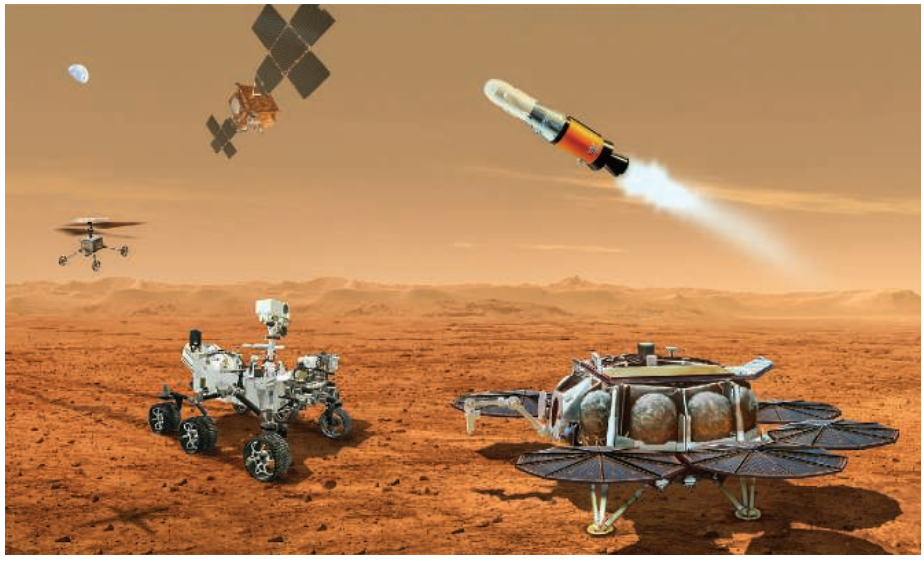

The multistage Mars Sample Return is an ambitious mission—with a budget to match.

ILLUSTRATION: NASA/ESA/JPL-CALTECH

tions include braking the lander with single-propellent thrusters like those that lowered Perseverance to Mars, rather than new ones that use two fuels; using the sample capsule itself as the nose cone on the return rocket; simplifying the containment vessel of the ESA-built spacecraft that will catch the capsule; and easing that rendezvous by launching the capsule to an orbit above the spacecraft, where it will stand out against the black of space.

Perseverance would be 10 years old by 2030, the earliest the MSR lander could arrive. But if NASA does have to cancel MSR or delay it past the end of the rover's life, Perseverance could lay down its cache of samples for future pickup by helicopters or some other mission, Dyar says. "Once we cache the samples, nothing is going to happen to them," she says. In the years to come, she suggests, "we can do it better, faster, and cheaper."

No matter what, MSR shouldn't be canceled, Christensen says. Such a move, Dreier adds, would undermine the influence of decadal surveys, pushing the field back to the time when the missions that were most politically savvy got selected. "If you allow the Senate to pick and choose what the priorities of the science community are, eventually that comes back to bite you."

But if the new MSR cost review predicts the mission will cost something like $10 billion, Cutler thinks it may not be salvageable. That would be bad not just for Mars exploration, but also for planetary science in general, Dreier says. After all, the Senate has already said that if MSR is canceled, its money mostly wouldn't go to science, but instead to human spaceflight and the Artemis program to return astronauts to the Moon. Artemis would be "the lion feeding on the carcass" of MSR, Dreier says. "The planetary science community is tied to MSR, whether they like it or not." ■

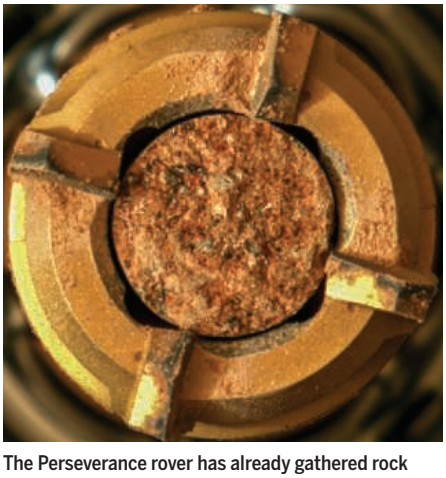

The Perseverance rover has already gathered rock cores to be returned to Earth as soon as 2033.

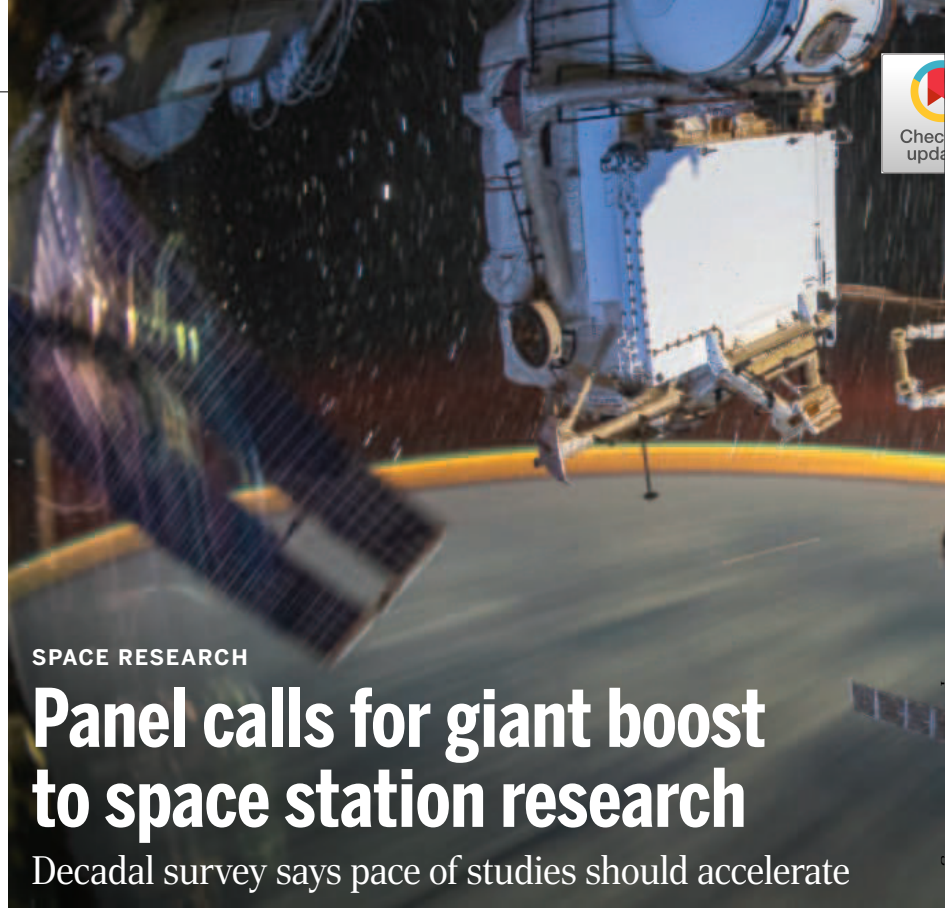

SPACE RESEARCH

Panel calls for giant boost to space station research

Decadal survey says pace of studies should accelerate

By **Michael Greshko**

What is the point of the International Space Station (ISS)? For some, the station—by some accounts the most expensive structure ever built—represents a triumph of engineering. It has also hosted astronauts for more than 2 decades straight, showcasing the endurance of international partnerships, and it has provided a destination for space agencies that cannot yet afford to return humans to the Moon. For University of Florida biologist Rob Ferl, however, the ISS is a one-of-a-kind laboratory—one that is just beginning to be utilized well.

Since the first ISS components were launched in 1998, researchers have done more than 3000 experiments there to understand how the topsy-turvy space environment affects everything from protein crystallization to combustion. But with access to space getting cheaper, and with commercial replacements to the ISS on the horizon, Ferl hopes the number of studies will rise dramatically. He was among 75 scientists who this week called for NASA's funding of biological and physical science on the ISS and elsewhere to expand by a factor of 10, to deliver both basic research and science that could advance the agency's human space exploration goals.

"There is an absolutely huge movement into space, for which we need a huge amount of science," says Ferl, who co-chaired the panel, which was overseen by the National Academies of Sciences, Engineering, and Medicine. The resulting "decadal survey," the first on research in space since 2011, offers research priorities to NASA and Congress.

The report finds that NASA's Division of Biological & Physical Sciences (BPS), which oversees much of this work, is "severely underfunded" relative to the prominent role it is expected to play in the agency's exploration efforts. BPS receives $85 million per year, less than 3% of the $3.2 billion allocated to NASA's planetary science division. To support the required base of scientific researchers, the panel estimates that BPS will need roughly $1 billion a year before the decade's end.

The report coincides with a sea change in human spaceflight. NASA's Artemis program is promising to return humans to the Moon. Rocket companies have lowered the cost of getting people and hardware into low-Earth orbit. And NASA is encouraging private interests to use its portion of the ISS for research and tourism until it is retired in 2030—and manage the station's successors. In 2021, NASA awarded more than $415 million to three companies to develop concepts for commercial space stations that NASA astronauts would visit along with private researchers and space tourists.

"We were actively waiting for this decadal survey because [its priorities] will drive a lot of the hardware that's put onboard these commercial space stations," says David

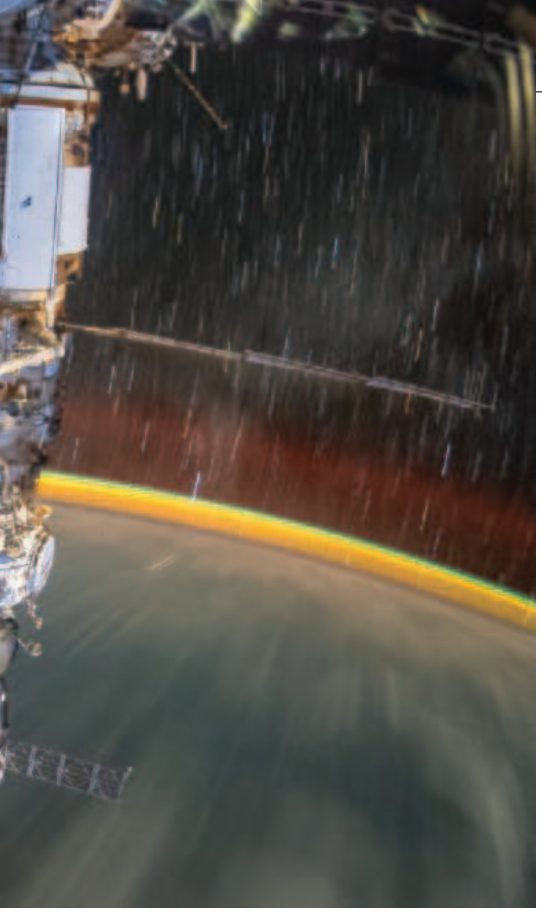

The International Space Station has hosted more than 3000 experiments. Scientists want more.

Marsh, director of space station strategy for Voyager Space, one of the three companies developing station concepts.

Space stations provide long-duration conditions for testing the effect of microgravity—the apparent weightlessness that comes with free falling in orbit. Some researchers have worked to tease out precisely how plants respond to mechanical strain when they cannot sense gravity, for example, whereas others have investigated the behavior of fluids when surface tension dominates. "There are a lot of things that are obscured by gravity," says decadal member Debjyoti Banerjee, a mechanical engineer at Texas A&M University.

And gravity itself is worth investigating. The panel sketches out a major multiagency initiative that would send atomic and optical clocks on future space missions, possibly including a future Uranus orbiter. When synchronized, this network could test theories of gravity by measuring spacetime's curvature across the Solar System, with up to 100,000 times the sensitivity of Earth-based experiments.

NASA's BPS division doesn't just focus on fundamental science, however: Its mission is also to enable human space exploration. To address this second prong, the survey calls for focusing much of the increased spending on two ambitious ground- and space-based research campaigns, each costing between $100 million and $400 million per year—on the scale of NASA spacecraft missions.

One would gather the fundamental science needed to build life-based systems that could keep crews alive in deep space for years at a time. For example, the report proposes studying how spacecraft bioreactors could harness algae, bacteria, and fungi to produce precursor compounds for medicines and bioplastics.

The other would supercharge research into zero-waste recycling methods and the techniques needed to "live off the land" on the Moon and elsewhere. Among other things, the report suggests studying how 3D-printed objects could be made from raw planetary materials such as lunar soil and how the products could be recycled back into feedstocks again and again.

The panel also recommends that NASA examine refitting a retired ISS crew capsule, such as one of SpaceX's Crew Dragon vehicles, with habitats for dozens of rats. These "rat-stronauts" would be launched on a 90-day mission to orbit over Earth's poles, where Earth's magnetic field is weak and provides little shielding from radiation. Researchers could study how a large, genetically diverse population of mammals contends with microgravity and high radiation at the same time: conditions resembling what future crews would face on the way to Mars.

The survey calls not just for more research in space, but also for it to be conducted at a faster pace. Until recently, launching experiments to the ISS often took years of planning, and almost as long to get samples back to Earth. Many ISS experiments ended up being "one and done," with few opportunities for replication and follow-up work. "It's really been set up for failure, in my opinion, the way science has been done on the space station," says Olivia Gamez Holzhaus, founder and CEO of the firm Rhodium Scientific, which helps researchers design and execute biotechnology experiments on the ISS.

But the growing capacity of rockets and their increasing launch pace is making it easier to do science quickly. NASA's BPS division is also seeking enough funding to send scientists into space to conduct research themselves. "We need to do experiments faster in space," NASA BPS Director Lisa Carnell wrote in an email to *Science*.

Decadal Co-Chair Krystyn Van Vliet, vice president for research and innovation at Cornell University, wants this acceleration to carry beyond the ISS to its commercial successors. "The next decade is going to be full of discovery and transformation," she says. "But now we have to seize it." ■

Michael Greshko is a science journalist in Washington, D.C.

SCIENTIFIC COMMUNITY

Iran prepares to erect a digital wall

Researchers feel increasingly isolated as government moves to restrict internet access

By **Richard Stone**

Last year, a machine learning expert in Silicon Valley embarked on a long-distance partnership with two neuroscientists in Tehran, Iran. They planned to gather data on how neurons respond to visual cues, hoping to develop a marker for early detection of Parkinson's disease. "I'd handle the modeling and analysis, and we'd co-author papers," says the U.S.-based computer scientist, who asked to remain anonymous because he has family in Iran.

Then, on 16 September 2022, 22-year-old Mahsa Jina Amini died after Iran's morality police detained her for allegedly wearing her hijab improperly. Her death ignited protests across Iran. The government's response included mass detentions and internet blackouts that disrupted international communication. The neuroscience collaboration sputtered and then "fell apart," the U.S. scientist says. Many projects met a similar fate, he and others say.

As the anniversary of Amini's death approaches, Iran's government is again clamping down on internet access, but this time it appears ready to go a step further, by launching a National Information Network (NIN) intended to keep most Iranians off the web. The NIN, which has been under development for 2 decades, "is meant to suppress and control the information space in Iran," says Fereidoon Bashar, executive director of ASL19, a tech outfit in Canada that helps Iranians securely connect to the web using circumvention tools and virtual private networks (VPNs). "With the current situation in Iran, and the potential for unrest, we're all expecting [the NIN] to come fully online any day," says an Iranian physicist living in Canada who requested anonymity because he's obligated to return to Iran.

The new cyberwalls threaten to worsen the increasingly dark conditions facing Iranian scientists. Universities were flash points for

An Iranian woman uses her cellphone to check social media. A new government-sponsored intranet could enable officials to track and censor users.

the protests after Amini's death; hundreds of students and some faculty members were among the more than 19,000 people detained and 537 killed, according to human rights activists. To subdue restive campuses, the government stepped up a decadelong effort to purge faculty perceived as opponents. "Many people I know there feel very uncomfortable on campus now," says Mercedeh Khajavikhan, an Iranian-born specialist in photoelectronics at the University of Southern California.

The purges had largely targeted the humanities and social sciences until late last month, when Iran's prestigious Sharif University of Technology sacked Ali Sharifi-Zarchi, a prominent specialist in bioinformatics and artificial intelligence. He had criticized the government in social media posts with a substantial following. Now, even some of Iran's most senior scientists are expressing concerns about the toll on academia. "The most essential and profound ingredient of a university is its qualified faculty and academicians," says Ali Akbar Salehi, a nuclear scientist at Sharif and former head of the Atomic Energy Organization of Iran. "If this fact under any excuse is disturbed," he told *Science*, "we should witness the waning of science, knowledge, and eventually society."

Iranian science was already under siege. Two decades of international sanctions and a currency in free fall have squelched imports of instruments and research materials, halting experiments. The sanctions have prompted many scientific journals in Europe and the United States to bar access to servers in Iran—forcing "Iranian scientists to rely on pirated ebooks and papers," says the Canada-based physicist. On many campuses, isolation has bred a culture of deceit. The Majlis Research Center, the research arm of Iran's parliament, announced in May that it had detected rampant plagiarism—"textual similarity" exceeding 30%—in nearly half of 750,000 master's and Ph.D. theses and dissertations it examined over 4 years.

The gloom is compelling more Iranian scientists to seek opportunities abroad. "Friends from my undergraduate days have been getting in touch, asking if there is any way for them to get out," says Khajavikhan, who studied electrical engineering at Amirkabir University of Technology in the early 2000s. "They don't see a future in Iran."

The NIN could hasten that brain drain. Iran promoted the multibillion-dollar project as a pan-Islamic network that would be free of immoral Western thoughts and ideals. But other Islamic nations showed little interest in a so-called "halal internet." Instead, the NIN—an intranet not linked to the outside world—is emerging as a bespoke, shadow network for Iran. North Korea has a similar intranet, called Kwangmyong, that enables officials to control access, censor content, and surveil users.

"If you know your connection is going through the government, you're going to behave quite differently. You'll censor yourself."

Arturo Filastò,
Open Observatory of Network Interference

Iranian authorities have vowed to complete the NIN by spring 2024. So far, it offers a messaging app, called Bale, and domestic versions of YouTube and Amazon, for example. The NIN's landing page links to a variety of institutions, including universities and research groups. But the material on offer is mostly generic profiles, biographies, and historical accounts of scientific developments.

The U.S. government has sought to throw up impediments to the NIN, arguing it will undermine freedom of expression and suppress dissent. In June, the Department of the Treasury sanctioned Arvan Cloud, an Iran-based company that has helped build the NIN. But Iran has a powerful ally—China—that is adept at both skirting U.S. sanctions and creating digital firewalls. Chinese experts are believed to have helped build the NIN's infrastructure and surveillance algorithms, Bashar says. The NIN's full deployment now likely awaits only a nod from Iranian Supreme Leader Ali Khamenei, he adds.

Authorities envision a system of tiered access, according to Iranian news reports. Only the NIN would be available to most Iranians. But some, including academic scientists, could gain broader access through government-issued VPNs. Iran's science minister, Mohammad Ali Zolfigol, has reportedly asked universities to provide lists of academics who would be among the privileged few.

VPN users could bypass the NIN, but the government could easily monitor them, says Arturo Filastò of the Open Observatory of Network Interference, a nonprofit that documents internet censorship. That's bound to influence which sites people visit, he says. "If you know your connection is going through the government, you're going to behave quite differently. You'll censor yourself."

Even as Iran completes a digital iron curtain certain to further stymie research collaborations with the West, it's encouraging its scientists to forge closer ties with China and Russia. For many, that's little consolation. "We feel that our world is getting smaller," the Iranian physicist says, "and our prospects bleaker." ■

VIROLOGY

U.S. kills effort to hunt dangerous viruses

Critics feared DEEP VZN project could help pathogens jump from animals to humans

By **Jon Cohen**

Amid concerns that researchers studying viruses collected from wild bats might have triggered the COVID-19 pandemic, the U.S. Agency for International Development (USAID) has prematurely ended a $125 million program aimed at identifying viruses in animals that might harm humans.

USAID launched the program, known as the Discovery & Exploration of Emerging Pathogens – Viral Zoonoses (DEEP VZN), in 2021. It tapped the Paul G. Allen School for Global Health at Washington State University (WSU) to lead a consortium that planned to work in up to 12 foreign countries over 5 years. Goals included training people in those countries to safely collect and characterize animal viruses, and to develop strategies to thwart pathogens that might jump to humans and cause a pandemic.

In late July, however, USAID told WSU investigators that it had canceled DEEP VZN (pronounced "deep vision"). The news was first reported on 7 September by *The BMJ*. "This decision is in no way a reflection on the performance or capability of … [WSU] or its consortium," a USAID spokesperson said.

USAID did not reply to questions about whether DEEP VZN's demise was linked to intense concerns voiced by congressional lawmakers—mostly Republicans—and some scientists that SARS-CoV-2 originated from a laboratory in Wuhan, China, that studied bat coronaviruses. No compelling evidence supports this theory, but it has gained traction. USAID said the decision flowed from an effort to assess its "priorities and approach to pandemic preparedness" as well as "how to optimally allocate USAID's global health security resources."

WSU veterinarian Guy Palmer, who founded its global health school in 2007, says he's disappointed by the move. "Stepping away from global surveillance is not wise," Palmer says. "It creates a vacuum, and there are certainly other nations that are less committed to data transparency that are more than happy to fill that gap."

Palmer is convinced political pressure helped kill DEEP VZN. "It's hard to think of a way to sugarcoat that. There's a lot of concern about lab leaks and creating a human-animal interface that wouldn't naturally exist," he says.

Researchers critical of what they see as risky virus research applauded the decision. "Wow! … This is a major win in the global fight against lab-generated pandemics," quantitative biologist Justin Kinney of Cold Spring Harbor Laboratory posted on X (formerly Twitter). Kinney is a co-founder of Biosafety Now, a nonprofit that advocates for improving laboratory safety and prohibiting research that modifies pathogens in ways that could make them more dangerous to humans.

Epidemiologist Jennifer Nuzzo, who heads the Brown University Pandemic Center, saw value in DEEP VZN but said it likely faced a "land mine of hearings" in Congress. She also questioned why it was housed at USAID. "It seems like the wrong vehicle for this kind of work," Nuzzo says. "If anything, you'd want to do it through a science agency that goes through an external peer-review process to make sure that the projects are … most likely to net scientific benefit."

Veterinarian Alessandra Nava (right) of Fiocruz Amazônia samples bats in Brazil in 2022. She previously led a PREDICT virus hunting program.

PHOTO: J. COHEN/*SCIENCE*

DEEP VZN was a follow-on to a $200 million USAID program called PREDICT that ran from 2009 to 2020. PREDICT emerged from USAID's interest in helping countries combat avian influenza, which devastated poultry farmers and threatened to spark pandemics. PREDICT funds were used to strengthen labs in more than 60 countries, train some 6000 people, and detect more than 1100 unique viruses.

Critics, however, assailed PREDICT, questioning its emphasis on hunting viruses in animals. Researchers have little chance of predicting which viruses detected by animal surveillance might harm humans, argued biologists Edward Holmes, Kristian Andersen, and Andrew Rambaut in a comment published in June 2018 in *Nature*. "[G]iven the rarity of outbreaks and the complexity of host–pathogen interactions, it is arrogant to imagine that we could use such surveys to predict and mitigate the emergence of disease," they wrote.

In the wake of COVID-19, PREDICT also drew sharp scrutiny because its consortium included the EcoHealth Alliance, a nonprofit that collaborated with the Wuhan lab at the center of the lab-leak theory.

USAID billed DEEP VZN as a virus hunting program, but Palmer says his main aim was to train scientists in how to safely monitor animal pathogens. Team members planned to inactivate samples as soon as possible after collection, which would reduce risks but allow scientists to collect viral sequences. If researchers spotted an interesting virus and wanted to study intact samples, they would revisit a site wearing higher level protective gear.

Palmer says DEEP VZN researchers knew USAID had developed cold feet about the program, and he says they also met with lawmakers to discuss their concerns. "They had legitimate questions that we thought we could address," Palmer says.

Prior to its cancellation, DEEP VZN had received about 10% of the promised funding. But researchers had not yet conducted sampling, Palmer says, because USAID never approved any fieldwork. ■

FEATURES

ANTARCTIC MELTDOWN

The U.S. Antarctic research program is in trouble, as canceled field seasons imperil data sets and demoralize researchers

By **Jeffrey Mervis**

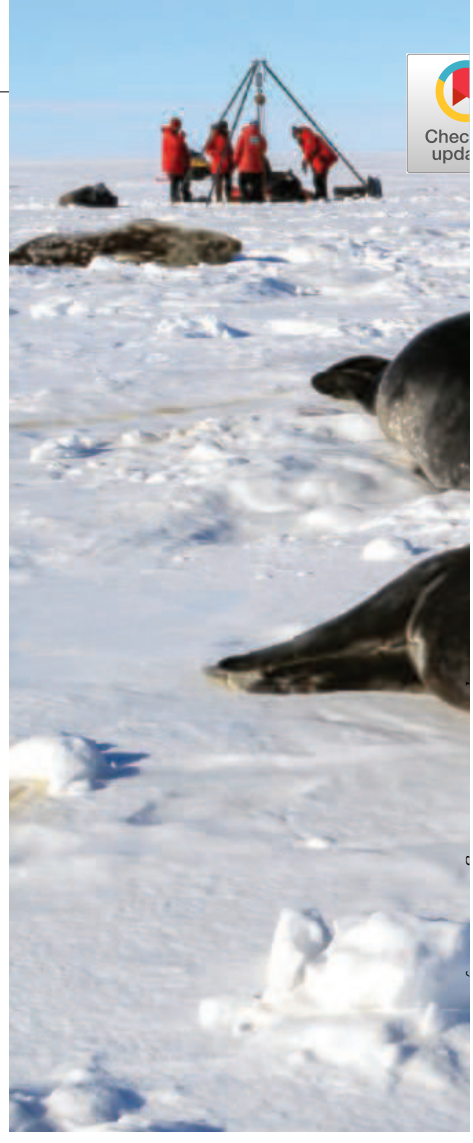

Marine biologist Michelle Shero had every reason to expect this to be a better year on the Antarctic ice.

Since receiving a 5-year, $1.1 million grant from the National Science Foundation (NSF) in 2019 to study the reproductive success of Weddell seals in McMurdo Sound, Shero has been sent down for just one, truncated field season. But in January NSF had assured Shero that her team would be deployed in October for a full 4 months, and by June she had packed up and shipped out some $200,000 in equipment and supplies.

So Shero, a tenure-track assistant scientist at the Woods Hole Oceanographic Institution, was stunned when her program manager told her in July that this season, too, was over before it started. There weren't enough beds at NSF's McMurdo Station to accommodate her team of five, the minimal crew needed to safely handle animals that can weigh up to 500 kilograms.

Shero isn't the only NSF-funded Antarctic scientist saying goodbye to another planned field season. This summer NSF decided to cancel or curtail 67—more than half—of the 131 projects and activities funded for the 2023–24 austral summer after concluding it couldn't provide them with the necessary logistical support.

The housing shortage is part of a triad of factors generating a perfect storm that is battering the United States Antarctic Program (USAP), long regarded as the best in the world. One element, the COVID-19 pandemic, shut down most research for 2 years and then, when cases spiked, severely disrupted the 2022–23 season. The pandemic, in turn, has stretched out a $500 million renovation project at McMurdo, reducing the number of available beds for both scientists and those who provide them with essential logistical support. Simultaneously, the rising cost of providing that support has forced NSF, which operates the research program for the U.S. government, to curtail the scope and duration of projects its program managers have already approved.

The resulting dysfunction poses a significant risk to the endeavors of hundreds of Antarctic scientists.

"It used to be that getting an NSF grant to work in Antarctica was the hard part, and that once you got the award you knew you could get some really cool science done," says marine biologist Jennifer Burns of Texas Tech University, a co-leader on Shero's grant and a former NSF Antarctic program officer with extensive experience in the field. "But something has changed. And unless and until we can get a good handle on why it's gone so wrong, I'd be very cautious about telling anybody that they should build a career around research in the Antarctic."

The reduced level of activity coincides with dramatic changes taking place in the Antarctic ecosystem and the Southern Ocean because of climate change. While other nations are beefing up their presence in Antarctica to better understand those changes, the U.S. government seems to be headed in the opposite direction, says Oscar Schofield, principal investigator (PI) for a project that has monitored ecosystems on the western Antarctic Peninsula for 33 years as part of NSF's global Long-Term Ecological Research (LTER) program.

"We're the canary in the coal mine, and there's lots of coal dust in the air," says Schofield, a biological oceanographer at Rutgers University who first came to Antarctica as a graduate student in the early 1990s. "And just when we need to know even more about what's happening to the canary, it feels like the United States is in a period of retreat."

THE U.S. HAS BY FAR the biggest footprint of any nation supporting science in Antarctica. McMurdo, the largest of the three U.S. stations and the hub of USAP operations, is a bustling 1200-person village at its summer peak and seven times the size of the next largest facility on the continent, the United Kingdom's Rothera Station. And NSF's Amundsen-Scott South Pole Station, although serving a much

Weddell seals sprawl on the sea ice at Erebus Bay last year as Michelle Shero and her team (background) prepare to weigh an animal.

smaller population, hosts an unrivaled array of major scientific instruments.

NSF supports a host of research and education activities in Antarctica, on topics ranging from climate change to the origins of the universe. "The work that I'm doing in Antarctica can't really be done anywhere else," says sedimentary microbiologist Tyler Mackey of the University of New Mexico, who studies primitive organisms at the bottom of an ice-covered lake. "And I think that's the rationale for every project NSF funds down here."

But making all this happen in a remote, demanding environment requires some "very challenging logistics," says James Ulvestad, acting head of NSF's Office of Polar Programs (OPP), which manages USAP. "And there's never less demand" from scientists, he adds.

Shero, who has traveled to Antarctica 10 times since her first visit as a graduate student in 2011, is intimately familiar with how things are supposed to work. Once NSF greenlights a research proposal, a private contractor provides the logistics to make it happen. Currently, that is Leidos; the company has received almost $2.7 billion since 2016 under a logistics support contract that expires in March 2025.

Shero's team, for example, requires a helicopter or snowmobiles for a daily commute from McMurdo over the frozen Ross Sea to the foot of snow-covered Mount Erebus, an active volcano. Once on the ice, the five-member team captures, examines, and collects tissue and blood samples from pairs of adult and pup seals. They also need helicopters to track down radar-tagged seals that stray from the main colony. And they hope to keep at it from October to mid-January, the height of the austral summer, for 3 years running.

But Shero and dozens of investigators can no longer count on that level of support—or even a place to sleep. Among the many improvements covered by the renovation project at McMurdo is a new dorm. To minimize its environmental impact, the new 285-bed dormitory—one of several housing units at the station—will be located on the same site as an aging building containing 150 beds that was razed in 2019.

NSF's timing couldn't have been worse. Within months of the demolition, the pandemic had halted nearly all USAP activities, including work on the new dorm. The new housing is now scheduled to be ready for the 2025–26 season, 3 years later than originally hoped.

The resulting bed shortage impinges on every aspect of Antarctic logistics, limiting not just the number of researchers, but also the pilots, cooks, mechanics, IT technicians, construction workers, and other personnel who support the research effort. The shortage is exacerbated by NSF's decision to set aside 50 beds at McMurdo this season for people testing positive for COVID-19, a response to last year's muddled handling of a midseason surge in cases. The much smaller Palmer Station will only have one of its 44 beds reserved for COVID-19 patients, but an overdue heating repair project will claim eight beds that otherwise would have been filled by researchers.

At the same time, rising costs have crimped NSF's ability to fly people and cargo to and from Antarctica. For example, the hourly rate for the LC-130 planes that can land on the ice has more than tripled since 2017, Ulvestad says. And the fleet's advanced age means more downtime for repairs. That's

also true for the C-17 transport planes that were tardy in delivering Shero's equipment last year, shortening her time in the field.

Costs have also curtailed helicopter support for scientists like Shero who work on sea ice, or in remote locations. The craft will stop flying in early December, 3 months earlier than usual. And researchers whose projects rely on an annual 6-week cruise from Palmer Station have been told to plan on it becoming a biennial event after this season.

Ulvestad says a flat OPP budget has robbed NSF of the option of simply paying more to provide the same level of support. "We understand their disappointment, and we can't pretend there won't be negative impacts," he says about the researchers impacted by the most recent cuts. "But we're still absolutely committed to funding the best science."

Natasja van Gestel's team installed open-top warming chambers on experimental plots last year to measure the impact of climate change on soils near Palmer Station.

THE CUTS AND POSTPONEMENTS will inevitably take their toll on research, however, especially on projects that require continuous data sets or precisely timed observations. Among the victims are the two Antarctic LTER projects, which have been running for more than 3 decades. Their data sets are crucial for monitoring a vulnerable and rapidly changing ecosystem. Nonetheless, the size of the teams contributing to the two projects is being reduced by up to two-thirds, and their field seasons drastically shortened.

Scientists affiliated with the McMurdo Dry Valleys LTER project, which NSF began funding in 1992, will only receive 10 beds this fall rather than their usual complement of 31. And because of the reduced helicopter availability, scientists will be deployed for a much shorter field season, as little as 3 weeks in November rather than the 4 months that is typical. That means fewer data will be collected, and some components of the research will be omitted.

"We appreciate the support that NSF has given us for all these years," says project director Michael Gooseff, an environmental engineer at the University of Colorado Boulder, "and the fact that we'll still be able to have a team in the field this season when other science groups have been canceled. But given all the cuts, it doesn't feel like we've been prioritized."

Dawn Sumner, a paleogeobiologist at the University of California, Davis, has fared worse; her field season has been canceled. "I'm by nature a half-full glass kind of person and I've always told my students to have backup plans," says Sumner, who is studying seasonal changes in microbial communities at the bottom of ice-covered Lake Fryxell in the Dry Valleys. But the disruption has put her resiliency to the test.

Sumner's team is measuring oxidation and other biochemical changes in microbial mats caused by light and photosynthesis. During the 2022–23 austral summer field season, the first for this project, the researchers found a surprising amount of variability in oxygen concentrations that couldn't be explained. Before her team left in February, divers installed shades over some of the mats. The plan was to return in October to remove them and observe the resulting metabolic changes over the following months as the Antarctic winter gives way to spring.

The timing is critical. Losing this field season, Sumner explains, "means we're going to basically have to start over. We can't leave the shades in for 2 years and get the data that we want." Instead, the team will have 6 days to simply retrieve instruments installed last year.

Natasja van Gestel, a biologist at Texas Tech, faced a different hurdle: a last-minute request from NSF to lengthen the amount of time she would spend tracking the impact of global warming on organisms living on the western Antarctic Peninsula.

Last season, her team installed open-top chambers over vegetation to capture more solar radiation. Its goal was to simulate future climate warming and see how it affected carbon flux. The field season ran from late November to mid-March, dates dictated by when the snow melts and then returns. To maintain her normal university teaching load, van Gestel doubled up on courses in the fall semester so she could be away in the spring.

This year, however, NSF asked her to fly to Antarctica 6 weeks earlier and stay until April to avoid peak demand for the ship that takes her to and from Palmer Station, the base for her operations. She had to decline the offer—and forgo her deployment. "It would have meant leaving in the middle of the semester," she says. "And we would have been down there way before I'd have anything to do."

NSF has asked contractors to put out the warming chambers at the end of the season so they will be in place the following year, and van Gestel says she's grateful for that support. "But we won't be able to collect any data," she says, because taking the carbon flux measurements requires special training. "And if something goes wrong, we may have to restart the experiment," she adds—assuming her team can be deployed for the 2024–25 season.

THE SUSTAINED DISRUPTIONS in recent years have left many Antarctic scientists wondering whether USAP will ever regain its former glory—and remain an attractive career option.

"From the early 1990s into the 2010s, the logistical support was really good," Burns says. "There were always surprises, but [NSF and the contractor] used to plan to need, plus something for dealing with the unexpected."

The program has lost that resilience, some researchers say. Many experienced and well-trained personnel working for Leidos or one of its subcontractors haven't returned to the ice after their positions disappeared during the first 2 years of the pandemic, and their absence exposed long-standing concerns about safety and the viability of aging equipment.

Shero and 30 other sea-ice scientists laid out the problem in a February letter to NSF after an uneven field season. "We are deeply

Last year, Dawn Sumner (far left) and her team made repeated dives into Lake Fryxell in Antarctica's Dry Valleys to study microbial mats on the lake bottom (right).

concerned about the ability of [field safety and training personnel] to adequately support our research efforts," they wrote. "It is clear that [USAP] cannot continue with 'business as usual' and expect sea-ice science to be safe and productive."

Animal ecologist Jay Rotella of Montana State University has built his career on NSF's ability to deliver on its promise of adequate logistics support. He's spent nearly 3 decades studying the population dynamics of a colony of Weddell seals in the Ross Sea that has been monitored since the 1960s and has compiled detailed reproductive histories on more than 10,000 female seals. His team was one of the few allowed to work during the depths of the pandemic, an opportunity he attributes to the importance NSF places on long-term data sets.

Even so, Rotella will also feel the effects of this year's squeeze. His six-member team will have to commute daily by snowmobile from McMurdo rather than living in portable huts on the sea ice because setting up that ice camp would require crews that NSF doesn't have room to house. The commute eats up 2 hours on each end of a 12-hour day, meaning less science will be done. The reduced logistics support will also limit his plans to study an influx of seals from a colony farther north—a migration he thinks could offer valuable clues about how climate change is affecting this iconic species.

Many Antarctic scientists believe NSF and Leidos should have been able to better anticipate how COVID-19, construction, and rising costs would affect the Antarctic program. "They knew last year how many beds would be available," Burns says. "And the projects that have been canceled have been on the books for years. So why these decisions [to cancel the 2023–24 field seasons of so many projects] were made so late is beyond me."

Ulvestad says a major factor for the last-minute notifications is the recurring failure of Congress to approve annual budgets for every federal agency until well into the next fiscal year. "We have a very detailed planning process, but we can't get very far along until we have a known budget," he says.

Stephanie Short, who manages NSF's Antarctic logistics office, cautions scientists not to look for a simple explanation for why their season was canceled. "The pandemic, budget, and space constraints all play a role," she explains.

Her words are cold comfort to Mackey, a member of Sumner's team. Mackey expected to have a slew of papers about sediment transport in Lake Fryxell when he came up for tenure review next year. But the recurring delays have put a serious dent in those plans.

The delay is also affecting his other research, outside Antarctica. For example, Mackey had hoped to use data from the lake for an ongoing NASA-funded project looking at environments that could have once supported life on Mars. And in a recently submitted NSF grant proposal for work on the Greenland Ice Sheet, Mackey agonized over a routine question asking him to provide "evidence of results from previous NSF support."

"I don't know if reviewers will care," he says. "But I had to be honest and say we haven't been able to do the work because of these extenuating circumstances."

Mackey hopes to become a co-PI on the McMurdo LTER project if, as expected, it wins another 6 years of NSF funding. But the logistics snafus have forced him to rethink the best path to achieve his career goals.

"There's just a lot of unanswered questions about how long we can keep doing long-term work like the McMurdo LTER if we have these episodic interruptions," he says. "What I'm seeing definitely gives me pause."

For Shero, the discrepancy between the project NSF has funded and what research can actually be supported is a particular source of frustration. Her grant proposal for her current project was rejected twice because it wasn't sufficiently ambitious, she says, and was ultimately funded only after she increased the intended sample size and time frame. "Of course, the logistical problems last year meant we ended up studying many fewer seals, and now we're shut down for another year," she says. "If we are also unable to go down next year, my only option may be to submit a new proposal—with no guarantee of funding."

Ulvestad says NSF is doing everything it can to minimize the impact on scientists until the agency can ride out the perfect storm. "But shifting gears takes us years," he cautions.

Shero worries the Antarctic research community could pay a heavy price as the disruptions continue. "My fear is that NSF will continue to fund fieldwork proposals based on resources that have historically been available," she says, "and then, because those resources aren't available and there's such a huge backlog, force everyone to significantly [shrink] their projects for years to come." ■

PHOTOS: (TOP TO BOTTOM) DAWN SUMNER; ABBEY DIAS

An insect-sized robot powered by methane jumps distances up to 20 times its body length.

ROBOTICS

Chemically fueling new microrobot abilities

A combustion-powered soft actuator takes microrobots to new heights and speeds

By **Ryan L. Truby**[1,2,3]

Mobile robots have the potential to be useful, intelligent partners, assisting in needs as diverse as exploration in high-risk environments, domestic service, infrastructural maintenance, and health care. However, building robots to match the nimbleness and efficiency of living organisms, as these applications demand, is difficult owing to the challenges of meeting the energy costs of autonomy. The essential elements of robotics—actuation, perception, and control—pose energy inefficiencies and system-integration constraints that can hamper robot capabilities. Shortcomings in portable energy supplies also hinder the development of deployable mobile robots. At small scales, these challenges are compounded by performance losses from component miniaturization and the limitations of microfabrication and manufacturing (*1*). On page 1212 of this issue, Aubin *et al.* (*2*) describe a chemically powered microactuator that generates rapid, high-force actuation for centimeter-scale robots. It uses the energy released from combustion reactions to bring impressive maneuverability and jumping abilities to insect-scale machines.

Compared with living organisms, mobile robots possess exceedingly short operating times. Increasing the energy density of batteries and other portable energy-storage technologies will help improve both the lifetime and endurance of robots. However, the high energy costs of robotic actuators, sensors, and computing elements will remain problematic for battery-powered robots. Powering untethered microrobots poses even more challenges, given the hurdles of installing an energy supply onboard of an agent whose power output and load-bearing capacity diminish with size (*1*, *3*). By contrast, organisms of all sizes are chemically powered. Biological organisms metabolize chemical fuels to power chemomechanical actuators such as muscles (*4*). Thus, the energy inefficiencies and scale-dependent challenges of modern robotics have motivated the search for alternative power strategies (*1*, *3*).

One growing area of interest is the use of high–energy density chemical fuels to power mobile robots. Hydrocarbon fuels can provide high energy densities that amount to ~2 to 50 times those of lithium-ion batteries. The key barrier to using chemical power in robotics is developing actuators that are capable of converting chemical energy to mechanical work (*3*–*5*). A decade ago, a study exploring the combustion of energy-dense methane to power soft robotic actuators was published. With an energy density of ~55 MJ/kg, methane combustion was shown to quickly inflate a pneumatically actuated soft robot without bulky electronic pumps (*6*). The combustion of butane (which stores ~50 MJ/kg) later powered directional jumping in an early demonstration of an untethered, partially soft robot (*7*). In 2016, the Octobot was introduced as an untethered, completely soft, hardware-free robot. It operated entirely on the catalytic decomposition of a hydrogen peroxide fuel with an energy density of ~1.4 MJ/kg (*8*). Four years later, the 88-mg microrobot RoBeetle achieved untethered locomotion by using a methanol fuel that stored ~20 MJ/kg. It used an artificial muscle composed of a

[1]Department of Materials Science and Engineering, Northwestern University, Evanston, IL 60208, USA. [2]Department of Mechanical Engineering, Northwestern University, Evanston, IL 60208, USA. [3]Center for Robotics and Biosystems, Northwestern University, Evanston, IL 60208, USA. Email: rtruby@northwestern.edu

catalytically active shape-memory alloy fiber that contracted as it combusted the fuel (*9*). Despite the novelties of each approach and the use of high–energy density fuels, chemically powered robots have typically displayed slow, low-force actuation. Furthermore, for small-scale untethered machines like the Octobot and RoBeetle, chemically powered actuation cannot be controlled for sophisticated behaviors.

To improve the force output, speed, and controllability of chemically powered robots, Aubin *et al.* built a miniaturized, 325-mg internal combustion engine. The chemically powered microactuator builds off from an operating principle similar to that used to create dense arrays of soft actuators for tactile displays (*10*). The microactuator of Aubin *et al.* comprises a 3-dimensional (3D)–printed combustion chamber, an inflatable elastomeric membrane, a pair of electrodes, and tubing for fuel injection. During a single actuation cycle, methane and oxygen gas flow into the chamber. Combustion is then triggered by a spark produced by applying a high voltage (~1 kV) across the electrodes. Heat generated from methane combustion drives the volumetric expansion of gas within the chamber, inflating the actuator's elastomeric membrane. Finally, exhaust vents passively reverse the cycle. The carbon dioxide and water vapor that are produced exit the chamber, and the pneumatically actuated membrane deflates. The result is a high–energy density, miniature actuator with ranges of motion (up to 140% actuation strain), speed (up to 100-Hz actuation frequency), and strength (up to 9 N of force) that are unprecedentedly high for devices at this length scale. By comparison, the actuators in Octobot and RoBeetle are far slower, providing actuation frequencies of ~0.01 to 0.03 Hz and ~1 to 2 Hz, respectively (*8*, *9*). The high frequencies, speeds and strengths allow Aubin *et al.*'s actuators to provide microrobots with locomotion capabilities that were previously available only to much larger robots.

Aubin *et al.* used an insect-scale quadrupedal robot outfitted with a pair of their microactuators to showcase their performance (see the photo). Each actuator, located above a forefoot-hindfoot pair, independently inflates two of the quadruped's footpads, enabling limited control over directional locomotion. For example, tuning the sparking sequences for combustion enabled directional turning as well as crawling and hopping gaits at speeds of ~5 and ~17 cm/s, respectively. Simultaneously activating both microactuators led to leaping, with maximum vertical and horizontal jumping distances of 59 and 16 cm, respectively, which correspond to 20 and 5.5 times the robot's body length.

Although promising, Aubin *et al.*'s microactuators present new considerations and challenges. In addition to producing flames that must be quenched, their actuators are presently tethered to heavy, off-board auxiliary components. Their actuators require combustible gases that are delivered from cylinders, and the high-voltage sparking electrodes have their own offboard power and control hardware. Aubin *et al.* see potential in using combustible gases that evaporate from liquid fuels, such as methanol and heptane, as a possible avenue for untethered operation. The combustible vapors could migrate into the actuator combustion chambers from embedded liquid-fuel reservoirs. However, a careful, systems-level balance of fuel supply rate, reactant stoichiometry, sparking rate, and venting rate would be necessary, which requires bespoke tuning for each specific robot design. The envisioned untethered systems would also likely be sensitive to ambient temperatures and other environmental conditions. In addition, using liquid fuels does not entirely address the challenge of going tether-free. The high-voltage sparking needed for actuation still requires a battery or another onboard electric energy supply.

As progress in chemically powered mobile robots grows, materials innovations are critical to achieving untethered, autonomous performance at long operating times. These include the design and fabrication of multifunctional robotic materials (*11*) and strategies for embedding energy supplies throughout robot bodies (*3*, *4*). A key advantage of the microactuators of Aubin *et al.* is their ability to be electronically controlled. This maintains their compatibility with microelectronic controllers and sensing hardware for the development of intelligent mobile-robot behaviors (*12*). Continued work in this research area may even require incorporating the source of the inspiration itself—living biological systems for biohybrid designs that allow robots to directly harness nature's efficiency (*1*, *3*, *13*). ■

REFERENCES AND NOTES

1. G.-Z. Yang *et al.*, *Sci. Robot.* **3**, eaar7650 (2018).
2. C. A. Aubin *et al.*, *Science* **381**, 1212 (2023).
3. C. A. Aubin *et al.*, *Nature* **602**, 393 (2022).
4. C. A. Aubin *et al.*, *Nature* **571**, 51 (2019).
5. R. L. Truby, S. Li, *Sci. Robot.* **5**, eabd7338 (2020).
6. R. F. Shepherd *et al.*, *Angew. Chem. Int. Ed.* **52**, 2892 (2013).
7. N. W. Bartlett *et al.*, *Science* **349**, 161 (2015).
8. M. Wehner *et al.*, *Nature* **536**, 451 (2016).
9. X. Yang, L. Chang, N. O. Pérez-Arancibia, *Sci. Robot.* **5**, eaba0015 (2020).
10. R. H. Heisser *et al.*, *Proc. Natl. Acad. Sci. U.S.A.* **118**, e2106553118 (2021).
11. R. L. Truby, *Acc. Mater. Res.* **2**, 854 (2021).
12. A. L. Evenchik, A. Q. Kane, E. Oh, R. L. Truby, *Annu. Rev. Mater. Res.* **53**, 225 (2023).
13. S. Kriegman, D. Blackiston, M. Levin, J. Bongard, *Proc. Natl. Acad. Sci. U.S.A.* **117**, 1853 (2020).

10.1126/science.adk0522

IMMUNOLOGY

Protection from inflammatory bowel disease

Immunomodulation of lymphocytes by intestinal epithelial cells could lead to new therapies

By **Heather J. Galipeau** *and* **Elena F. Verdu**

Intraepithelial lymphocytes (IELs) are a heterogenous population of immune cells that are abundant at mucosal sites such as the skin and intestine. In the gastrointestinal tract, T cell receptor (TCR)–expressing IELs patrol the epithelium and participate in host defense against pathogens, wound repair, and barrier function. The different subtypes of IELs have overlapping and distinct roles that include physiological and pathological functions, and therefore different subsets have been implicated in chronic intestinal conditions that clinically overlap but that have distinct pathophysiology, such as celiac disease (*1*) and inflammatory bowel disease (IBD) (*2*). On page 1169 of this issue, Dart *et al.* (*3*) show that a distinct population of γδ T cells, an unconventional IEL subset, are maintained in the human colonic epithelium through TCR-mediated interactions with butyrophilin-like (BTNL) proteins expressed on intestinal epithelial cells. This interaction seems to confer protection against IBD progression in humans and could be a target for immunotherapy.

The TCR of conventional T cells consists of variable (V) α and β chains that recognize antigens presented by major histocompatibility complex (MHC) molecules. Conversely, γδ T cells express combinations of Vγ and Vδ chains, which are not restricted to recognizing antigens presented by MHC molecules. Although they seem to play crucial roles in maintaining gut homeostasis, the precise function of γδ T cells, and how they are maintained in the epithelium, particularly in humans, is not fully understood.

Unraveling γδ T cell development, differentiation, homing, and activation in the gut has been hampered by the absence of a known selective or activating TCR ligand.

catalytically active shape-memory alloy fiber that contracted as it combusted the fuel (*9*). Despite the novelties of each approach and the use of high–energy density fuels, chemically powered robots have typically displayed slow, low-force actuation. Furthermore, for small-scale untethered machines like the Octobot and RoBeetle, chemically powered actuation cannot be controlled for sophisticated behaviors.

To improve the force output, speed, and controllability of chemically powered robots, Aubin *et al.* built a miniaturized, 325-mg internal combustion engine. The chemically powered microactuator builds off from an operating principle similar to that used to create dense arrays of soft actuators for tactile displays (*10*). The microactuator of Aubin *et al.* comprises a 3-dimensional (3D)–printed combustion chamber, an inflatable elastomeric membrane, a pair of electrodes, and tubing for fuel injection. During a single actuation cycle, methane and oxygen gas flow into the chamber. Combustion is then triggered by a spark produced by applying a high voltage (~1 kV) across the electrodes. Heat generated from methane combustion drives the volumetric expansion of gas within the chamber, inflating the actuator's elastomeric membrane. Finally, exhaust vents passively reverse the cycle. The carbon dioxide and water vapor that are produced exit the chamber, and the pneumatically actuated membrane deflates. The result is a high–energy density, miniature actuator with ranges of motion (up to 140% actuation strain), speed (up to 100-Hz actuation frequency), and strength (up to 9 N of force) that are unprecedentedly high for devices at this length scale. By comparison, the actuators in Octobot and RoBeetle are far slower, providing actuation frequencies of ~0.01 to 0.03 Hz and ~1 to 2 Hz, respectively (*8*, *9*). The high frequencies, speeds and strengths allow Aubin *et al.*'s actuators to provide microrobots with locomotion capabilities that were previously available only to much larger robots.

Aubin *et al.* used an insect-scale quadrupedal robot outfitted with a pair of their microactuators to showcase their performance (see the photo). Each actuator, located above a forefoot-hindfoot pair, independently inflates two of the quadruped's footpads, enabling limited control over directional locomotion. For example, tuning the sparking sequences for combustion enabled directional turning as well as crawling and hopping gaits at speeds of ~5 and ~17 cm/s, respectively. Simultaneously activating both microactuators led to leaping, with maximum vertical and horizontal jumping distances of 59 and 16 cm, respectively, which correspond to 20 and 5.5 times the robot's body length.

Although promising, Aubin *et al.*'s microactuators present new considerations and challenges. In addition to producing flames that must be quenched, their actuators are presently tethered to heavy, off-board auxiliary components. Their actuators require combustible gases that are delivered from cylinders, and the high-voltage sparking electrodes have their own offboard power and control hardware. Aubin *et al.* see potential in using combustible gases that evaporate from liquid fuels, such as methanol and heptane, as a possible avenue for untethered operation. The combustible vapors could migrate into the actuator combustion chambers from embedded liquid-fuel reservoirs. However, a careful, systems-level balance of fuel supply rate, reactant stoichiometry, sparking rate, and venting rate would be necessary, which requires bespoke tuning for each specific robot design. The envisioned untethered systems would also likely be sensitive to ambient temperatures and other environmental conditions. In addition, using liquid fuels does not entirely address the challenge of going tether-free. The high-voltage sparking needed for actuation still requires a battery or another onboard electric energy supply.

As progress in chemically powered mobile robots grows, materials innovations are critical to achieving untethered, autonomous performance at long operating times. These include the design and fabrication of multifunctional robotic materials (*11*) and strategies for embedding energy supplies throughout robot bodies (*3*, *4*). A key advantage of the microactuators of Aubin *et al.* is their ability to be electronically controlled. This maintains their compatibility with microelectronic controllers and sensing hardware for the development of intelligent mobile-robot behaviors (*12*). Continued work in this research area may even require incorporating the source of the inspiration itself—living biological systems for biohybrid designs that allow robots to directly harness nature's efficiency (*1*, *3*, *13*). ■

REFERENCES AND NOTES

1. G.-Z. Yang *et al.*, *Sci. Robot.* **3**, eaar7650 (2018).
2. C. A. Aubin *et al.*, *Science* **381**, 1212 (2023).
3. C. A. Aubin *et al.*, *Nature* **602**, 393 (2022).
4. C. A. Aubin *et al.*, *Nature* **571**, 51 (2019).
5. R. L. Truby, S. Li, *Sci. Robot.* **5**, eabd7338 (2020).
6. R. F. Shepherd *et al.*, *Angew. Chem. Int. Ed.* **52**, 2892 (2013).
7. N. W. Bartlett *et al.*, *Science* **349**, 161 (2015).
8. M. Wehner *et al.*, *Nature* **536**, 451 (2016).
9. X. Yang, L. Chang, N. O. Pérez-Arancibia, *Sci. Robot.* **5**, eaba0015 (2020).
10. R. H. Heisser *et al.*, *Proc. Natl. Acad. Sci. U.S.A.* **118**, e2106553118 (2021).
11. R. L. Truby, *Acc. Mater. Res.* **2**, 854 (2021).
12. A. L. Evenchik, A. Q. Kane, E. Oh, R. L. Truby, *Annu. Rev. Mater. Res.* **53**, 225 (2023).
13. S. Kriegman, D. Blackiston, M. Levin, J. Bongard, *Proc. Natl. Acad. Sci. U.S.A.* **117**, 1853 (2020).

10.1126/science.adk0522

IMMUNOLOGY

Protection from inflammatory bowel disease

Immunomodulation of lymphocytes by intestinal epithelial cells could lead to new therapies

By **Heather J. Galipeau** *and* **Elena F. Verdu**

Intraepithelial lymphocytes (IELs) are a heterogenous population of immune cells that are abundant at mucosal sites such as the skin and intestine. In the gastrointestinal tract, T cell receptor (TCR)–expressing IELs patrol the epithelium and participate in host defense against pathogens, wound repair, and barrier function. The different subtypes of IELs have overlapping and distinct roles that include physiological and pathological functions, and therefore different subsets have been implicated in chronic intestinal conditions that clinically overlap but that have distinct pathophysiology, such as celiac disease (*1*) and inflammatory bowel disease (IBD) (*2*). On page 1169 of this issue, Dart *et al.* (*3*) show that a distinct population of γδ T cells, an unconventional IEL subset, are maintained in the human colonic epithelium through TCR-mediated interactions with butyrophilin-like (BTNL) proteins expressed on intestinal epithelial cells. This interaction seems to confer protection against IBD progression in humans and could be a target for immunotherapy.

The TCR of conventional T cells consists of variable (V) α and β chains that recognize antigens presented by major histocompatibility complex (MHC) molecules. Conversely, γδ T cells express combinations of Vγ and Vδ chains, which are not restricted to recognizing antigens presented by MHC molecules. Although they seem to play crucial roles in maintaining gut homeostasis, the precise function of γδ T cells, and how they are maintained in the epithelium, particularly in humans, is not fully understood.

Unraveling γδ T cell development, differentiation, homing, and activation in the gut has been hampered by the absence of a known selective or activating TCR ligand.

Context matters in gut inflammation

In healthy human intestinal epithelium, γδ T cells expressing cytotoxicity receptors (NKp44 and NKp46), CD103 (a marker of tissue residency), and TCRs containing Vγ4 are maintained by interactions with the BTNL3-BTNL8 heterodimer that is expressed on epithelial cells. In the small intestine, celiac disease results in reduced BTNL8 expression on intestinal epithelial cells and loss of Vγ4⁺ T cells, which are replaced by IFN-γ–producing Vδ1⁺ T cells that no longer respond to BTNL3-BTNL8. In the large intestine, active IBD results in loss of BTNL3-BTNL8–reactive Vγ4⁺ T cells, and those that remain have an altered phenotype (increased expression of CD18), which correlates with IBD severity.

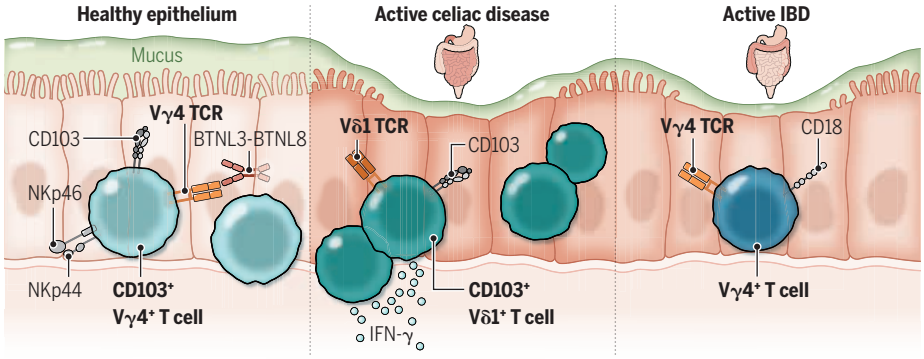

BTNL, butyrophilin-like protein; IBD, inflammatory bowel disease; IFN-γ, interferon-γ; NKp, natural killer cell–related protein; TCR, T cell receptor; Vγ4, variable γ 4 chain.

Recent work, however, has implicated BTNL molecules as γδ TCR ligands. These molecules are expressed within intestinal epithelial cells, and they are members of the immunoglobin superfamily that are structurally similar to B7 costimulatory receptors that regulate activation of αβ T cells (*4*). Dart *et al.* confirm that BTNL3 and BTNL8 expressed on human intestinal epithelial cells interact with CD103⁺Vγ4⁺ cells, a specific γδ T cell subtype that resides in the human colon (*5*–*7*). Ligands similar to BTNL for other γδ T cell subsets are found in the skin and thymus, suggesting that epithelial cells can provide the local signals that are needed for the development and maintenance of "tissue-sensing" γδ T cells (*8*).

Dart *et al.* find that CD103⁺Vγ4⁺ cells are reduced in number and have an altered phenotype in biopsies from inflamed areas in patients with IBD (see the figure). Notably, a "normal" γδ T cell compartment in the colonic epithelium was observed in macroscopically healed mucosal sections of patients with ulcerative colitis (a form of IBD) and was associated with long-term remission in Crohn's disease patients (another form of IBD), suggesting a tissue-protective and wound-healing role in the colon. This normalization contrasts with what has been observed in celiac disease, an autoimmune enteropathy triggered by dietary gluten that is more frequently diagnosed in people with IBD than in the general population (*9, 10*). In patients with celiac disease, chronic inflammation permanently reshapes the small intestinal γδ T cell compartment such that the normally tissue-protective Vγ4⁺ T cells are replaced with inflammatory interferon-γ (IFN-γ)–producing γδ T cells from the periphery. This population remains elevated in the small intestine, even in treated celiac patients on a gluten-free diet (*11*).

Why there are stark differences in the role of γδ T cells between IBD and celiac disease is unclear but could reflect tissue-specific differences and heterogeneity of the IEL compartment. For instance, Vγ4⁺ T cells were absent from the duodenum but were present at normal frequencies in the colon of treated celiac patients (*11*), suggesting that local cues may differentially affect the γδ T cell compartment. Additionally, in celiac disease, chronic low levels of gluten exposure, despite maintaining a gluten-free diet (*12*), may provide long-lasting inflammatory cues that alter the IEL population. Dart *et al.* focused on colonic IBD, but whether ileal Vγ4⁺ T cells are similarly dysfunctional, are replaced by circulating inflammatory γδ T cells, or normalize upon remission is unknown.

A polymorphism in the *BTNL8* gene, resulting in its reduced surface expression on intestinal epithelial cells, is associated with a low frequency of Vγ4⁺ T cells in the colon and severe Crohn's disease, although a similar correlation with ulcerative colitis severity was not observed. Therefore, Dart *et al.* suggest that these cells are not simply a biomarker of disease, but that their loss is involved in disease progression. A frequent Neanderthal-derived allele variant of *TRGV4* (which encodes Vγ4) mediates reduced responsiveness to BTNL8 and BTNL3 (*13*). Whether this variant is associated with chronic inflammatory diseases was not investigated but should be clarified in future studies, given the findings of Dart *et al.* Moreover, findings from potential celiac disease patients, who demonstrate a CD4⁺ T cell response to dietary gluten but without histological evidence of small intestinal villous atrophy, suggest that γδ T cell dysfunction starts before any tissue destruction, and their loss plays an important role in disease progression (*11*).

Conversely, the finding that IBD-associated cytokines can alter both the function and numbers of Vγ4⁺ T cells and that reduced expression of BTNL8 has been reported in patients with IBD and colon cancer (*14*) suggests that the inflamed milieu of the IBD colon itself can modulate these cells, and their dysfunction could be a result of disease-associated inflammation rather than the cause. Nevertheless, whether the loss of specific γδ T cell subsets are a cause or consequence of IBD is still up for debate. Although logistically difficult, future studies should longitudinally follow individuals at risk of developing IBD with precise sampling of the gastrointestinal anatomy to help elucidate these questions. Moreover, studies in patients with disease associations such as those diagnosed with both celiac disease and IBD could provide a distinct perspective on the role and biogeography of IEL subpopulations and their regulators.

The exact mechanism explaining how Vγ4⁺ T cells and the signals provided by BTNL8 and BTNL3 elicit protection or dampen inflammation in the context of IBD remains to be determined. This is an important pathway to understand because it could reveal new avenues for therapies targeting the early programming of the IEL compartment to prevent IBD progression. ■

Farncombe Family Digestive Health Research Institute, Department of Medicine, McMaster University, Hamilton, Canada. Email: verdue@mcmaster.ca

REFERENCES AND NOTES

1. B. Jabri, L. M. Sollid, *J. Immunol.* **198**, 3005 (2017).
2. M. Kadivar, J. Petersson, L. Svensson, J. Marsal, *J. Immunol.* **197**, 4584 (2016).
3. R. J. Dart *et al.*, *Science* **381**, eadh0301 (2023).
4. B. D. McDonald, B. Jabri, A. Bendelac, *Nat. Rev. Immunol.* **18**, 514 (2018).
5. D. Melandri *et al.*, *Nat. Immunol.* **19**, 1352 (2018).
6. R. Di Marco Barros *et al.*, *Cell* **167**, 203 (2016).
7. C. R. Willcox *et al.*, *Immunity* **51**, 813 (2019).
8. J. C. Ribot, N. Lopes, B. Silva-Santos, *Nat. Rev. Immunol.* **21**, 221 (2021).
9. M. I. Pinto-Sanchez *et al.*, *Gastroenterology* **159**, 884 (2020).
10. K. Mårild *et al.*, *Am. J. Gastroenterol.* **117**, 1471 (2022).
11. T. Mayassi *et al.*, *Cell* **176**, 967 (2019).
12. J. A. Silvester *et al.*, *Aliment. Pharmacol. Ther.* **52**, 1469 (2020).
13. M. Corcoran *et al.*, *Immunity* **56**, 635 (2023).
14. C. Lebrero-Fernández *et al.*, *Immun. Inflamm. Dis.* **4**, 191 (2016).

ACKNOWLEDGMENTS

E.F.V. and H.J.G. are supported by a Canadian Institutes of Health Research (CIHR) Project Grant (PJT 183881), and a CIHR Project Grant (PFT-168840) to E.F.V. E.F.V. holds a Tier 1 Canada Research Chair in Microbial Therapeutics and Nutrition and Gastroenterology. H.J.G. received the J. A. Campbell Research Award from Celiac Canada.

10.1126/science.adj9724

HYPOTHESIS

Defining microglial-synapse interactions

The brain's resident macrophages have many roles beyond synaptic pruning

By **Ukpong Eyo**[1] *and* **Anna Victoria Molofsky**[2]

Innate immune pathways play important roles in brain health and disease, and microglia, the dominant immune cells of the brain, are essential partners in this process. The discovery that synaptic proteins are found in microglia was an important step in reaching this conclusion because it suggested that microglia affect synaptic connectivity and thereby brain function (*1*, *2*). Notably, some of the same molecular mechanisms that promote microglial engulfment during development also restrict excitatory synapse numbers. This inverse correlation could be conservatively interpreted to mean that microglia contribute to the elimination of synapses, either directly or indirectly. Instead, it is frequently assumed that microglia eliminate synapses by active engulfment—a process often called "microglial synapse pruning." We propose that this model of microglial function is only one of many that are consistent with current data.

Imaging fixed tissues from genetically modified mice led to the identification of molecular mechanisms that both promote microglial engulfment activity and restrict synapse numbers. However, these studies have limitations. Observing proteins within microglia in fixed tissues cannot reveal the sequence of events that came before. In addition, the identified molecular mechanisms could regulate more than one mode of microglial phagocytosis. For example, canonical phagocytic signals implicated in pruning include complement and phosphatidylserine (*2*, *3*). Yet, both pathways also play important roles in cell death—by cell lysis or as a driver of efferocytosis (uptake of apoptotic cells), respectively. Thus, in some settings, activation of these pathways could promote neuronal death, and microglia might scavenge this debris rather than engulfing live synapses.

Other signaling molecules implicated in pruning include fractalkine and interleukin-33 (IL-33) (*1*, *4*). Neither of these are part of classical phagocytic pathways, which should prompt investigation of alternate mechanisms. Fractalkine is a chemokine that is important in microglial recruitment and activation and has multiple cellular effects. IL-33 is a member of the IL-1 family of cytokines and has pleiotropic effects, some of which may play distinctive roles in excitatory synapse remodeling. For example, IL-33 promotes microglial clearance of extracellular matrix (*5*), which, in the developing brain, could reduce synapse stability and contribute to synapse elimination. Thus, deeper investigation of the downstream effects of known signaling molecules may suggest new models of how microglia and neurons interact.

One line of evidence that has not provided support for the model of direct synapse engulfment is live imaging. In the 10 or more years since the discovery of synaptic proteins in microglia, no real-time imaging evidence of a microglial cell eliminating a synapse by engulfment has been documented. A study that analyzed 171 microglial-synaptic contacts in mouse hippocampal slices did not observe such events (*6*), although this study was ex vivo and examined only one brain region. Because negative data often go unpublished, it is difficult to estimate how extensively the matter has been pursued. However, many live-imaging studies have observed fascinating interactions between microglia and synapses that were not synaptic engulfment events. For example, microglial contact with dendritic shafts or spines was followed by the formation of filopodia—evidence of newborn or plastic spines—in both the mouse cortex at postnatal day 10 and brain slices cultured from postnatal mice (*6*, *7*). This suggests that unknown molecular events occurring during these microglial-dendritic contacts contribute to new synapse formation. In mouse brain slices and in intact *Xenopus laevis* (clawed frog) larvae, microglia were observed to trogocytose presynaptic axon terminals (*6*, *8*), meaning that they took up neuronal material, but the synapse was still present

Potential mechanisms of microglial-synaptic interactions

Several mechanisms are consistent with the evidence that synaptic proteins are found within microglia. Microglia might destabilize synapses by removing extracellular matrix or modulating synaptic excitability, leading to as-yet poorly defined mechanisms of neuron-autonomous synapse elimination in extracellular vesicles, such as exophers or apoptotic bodies, which are cleared by microglia (blue) (**1**). Microglia also clear debris produced by the death of neurons or portions of neurons (such as the axon) (**2**). Microglia modify synapses by partial phagocytosis (trogocytosis) and synaptic stripping (interposing between pre- and postsynaptic membranes, nonphagocytic). Both mechanisms might affect synaptic excitability or stability (**3**). Another hypothesis is that microglia actively engulf and remove entire pre- or postsynaptic elements (**4**).

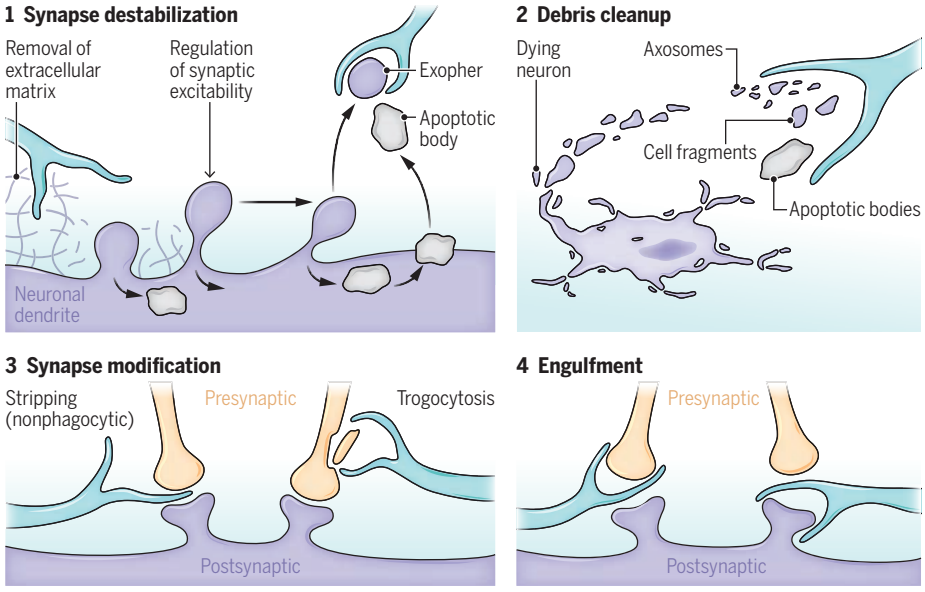

GRAPHIC: A. MASTIN/*SCIENCE*

[1]Center for Brain Immunology and Glia, Neuroscience Department, University of Virginia School of Medicine, Charlottesville, VA, USA. [2]Department of Psychiatry and Behavioral Sciences and Weill Institute for Neurosciences, Kavli Institute for Fundamental Neurosciences, University of California San Francisco, San Francisco, CA, USA. Email: ube9q@virginia.edu; anna.molofsky@ucsf.edu"

at the end of the interaction. This process could modulate synaptic function or stability without leading to the elimination of entire synapses. Studies that included live imaging in intact mouse and zebrafish brains showed that microglial contact reduced neuronal activity, which is a nonphagocytic role that has important effects on circuit function (*9, 10*).

Most biological models are based on inference, and a lack of live-imaging evidence does not mean that direct synapse engulfment does not occur. It is challenging to visualize the intact developing mammalian brain, but the adult brain undergoes much less synaptic turnover, which would make these events harder to detect. Microglia in sliced brains might lose the capacity to engulf. Pre- and postsynaptic materials have different stabilities in the lysosome, such that presynaptic engulfment may be more difficult to detect. Cytoplasmic dyes and fluorophores might not be captured or might not be bright enough to visualize an engulfed bouton or spine. These caveats could mean that the "pinching off" of synapses by microglia exists but that efforts to directly observe this need to be optimized.

There are also technical limitations to the studies in fixed tissues that suggest microglial synaptic pruning by direct engulfment. For example, the resolution limits of light microscopy and difficulties colocalizing synaptic proteins with microglial lysosomes could lead to false colocalization and the misclassification of microglial-synaptic contacts as engulfment events. In addition, most studies have quantified only synaptic proteins without considering that they could be only one of many proteins or molecules taken up by microglia. If, for example, an entire cell was eliminated, both synaptic and cytoskeletal proteins would be phagocytosed by microglia.

In lieu of direct engulfment, what could explain the finding that microglia both restrict synapse numbers and take up synaptic proteins? We hypothesize that in many cases, neuron-autonomous pruning mechanisms may precede phagocytic uptake by microglia (see the figure). An extensive literature that predates microglial inclusion in the pruning process has shown that neurons undergo synapse elimination in a cell-autonomous and activity-dependent manner (*11*). Microglia might enhance these neuron-autonomous processes of synapse elimination. For example, microglia inhibit neuronal excitability (*8*, *9*) and clear the extracellular matrix (*5*). Both functions would destabilize synapses, which might then be eliminated by neurons through the release of extracellular vesicles, such as exophers (*12*), and subsequently be taken up by microglia as debris. This might be more efficient than transporting proteins long distances to be broken down within neurons, which can digest proteins but are not professional phagocytes like macrophages.

Microglia could also engulf debris from dying neurons or portions of neurons, such as debris from shedding axons (axosomes) (*13*). These bits of debris would include synaptic proteins. In these scenarios, microglia are taking up synaptic material after it has been eliminated by the neuron. Microglia can also trogocytose portions of synapses (*6*, *8*) or interpose between pre- and postsynaptic membranes in a nonphagocytic manner (stripping), both of which could affect synaptic transmission without eliminating synapses.

If any or all of these hypotheses are correct, microglia would be critical to the health of the brain, but they would not initiate synapse elimination. However, the well-established ability of microglia to sense and respond to neuronal activity would still be essential to their function by enabling them to distinguish between a living neuron and neuronal debris and to tailor phagocytosis as needed.

How should these findings affect future studies? Implicit assumptions must be considered. The word "pruning" long predates microglia and stems from the observation that synapse numbers in humans peak in infancy and decrease in adolescence (*14*). Yet, in the context of phagocytic microglia, the image evoked by the word pruning (defined as "to cut away what is superfluous") could lead to misunderstanding. We propose that less catchy terms, such as microglia-dependent synapse elimination, are more consistent with the currently available data.

A deeper investigation into the molecular mechanisms that regulate microglial function will also be essential. These experiments should include cell type–specific disruption of the proposed phagocytic pathways in microglia to determine whether the effects are cell autonomous. Additionally, new approaches may be needed to obtain an unbiased view of which proteins could end up inside these cells along with or independent of synaptic proteins. Investigating the complexity of microglial-synapse interactions may ultimately yield precise therapeutic targets for the many neurodevelopmental and neurodegenerative brain disorders involving microglia. ■

REFERENCES AND NOTES

1. R. C. Paolicelli *et al.*, *Science* **333**, 1456 (2011).
2. D. P. Schafer *et al.*, *Neuron* **74**, 691 (2012).
3. N. Scott-Hewitt *et al.*, *EMBO J.* **39**, e105380 (2020).
4. I. D. Vainchtein *et al.*, *Science* **359**, 1269 (2018).
5. P. T. Nguyen *et al.*, *Cell* **182**, 388 (2020).
6. L. Weinhard *et al.*, *Nat. Commun.* **9**, 1228 (2018).
7. A. Miyamoto *et al.*, *Nat. Commun.* **7**, 12540 (2016).
8. T. K. Y. Lim, E. S. Ruthazer, *eLife* **10**, e62167 (2021).
9. M. Merlini *et al.*, *Nat. Neurosci.* **24**, 19 (2021).
10. Y. Li *et al.*, *Dev. Cell* **23**, 1189 (2012).
11. T. E. Faust *et al.*, *Nat. Rev. Neurosci.* **22**, 657 (2021).
12. I. Melentijevic *et al.*, *Nature* **542**, 367 (2017).
13. D. L. Bishop *et al.*, *Neuron* **44**, 651 (2004).
14. P. R. Huttenlocher, *Brain Res.* **163**, 195 (1979).

10.1126/science.adh7906

NEURODEGENERATION

Role for cell death pathway in Alzheimer's disease

Human neurons transplanted into mice with amyloid plaques die by necroptosis

By **Daniel W. Sirkis**[1] *and* **Jennifer S. Yokoyama**[1,2]

Central, longstanding problem in the study of Alzheimer's disease (AD) has been an inability to fully recapitulate the biochemical and neuropathological hallmarks of the disease in mouse models, which are important tools of biomedical research. These hallmarks include extracellular plaques of aggregated amyloid-β (Aβ), intraneuronal neurofibrillary tangles composed of hyperphosphorylated tau protein, and the loss of neurons. Although some progress has been made in this area (*1*, *2*), much work remains to be done. On page 1176 of this issue, Balusu *et al.* (*3*) report a mouse model that results in the generation of AD-like tau pathology and neuronal death in a manner that depends on both the presence of amyloid pathology and transplanted human neurons. The findings suggest an explanation for why it has been challenging to produce Aβ-dependent tau pathology and neurodegeneration in mouse models. The work also provides evidence for the importance of a cell death pathway in AD that may be therapeutically tractable.

The new mouse model makes use of a previously designed line of mice that express a humanized version of the amyloid precursor protein (*App*) gene, which encodes the precursor to Aβ. This version harbors three pathogenic mutations ($App^{NL\text{-}G\text{-}F}$ mice; named to indicate the relevant single-letter amino acid substitutions) (*4*); each mutation causes familial forms of AD in humans, and collectively, they increase extracellular Aβ levels and promote Aβ aggregation in mice. Balusu *et al.* bred the $App^{NL\text{-}G\text{-}F}$ mice with mice lacking an adaptive immune system [recombination-activating protein 2 $(Rag2)^{-/-}$ mice] to allow human neuronal transplantation experiments. Although previous work in another xenograft model had suggested that

at the end of the interaction. This process could modulate synaptic function or stability without leading to the elimination of entire synapses. Studies that included live imaging in intact mouse and zebrafish brains showed that microglial contact reduced neuronal activity, which is a nonphagocytic role that has important effects on circuit function (*9, 10*).

Most biological models are based on inference, and a lack of live-imaging evidence does not mean that direct synapse engulfment does not occur. It is challenging to visualize the intact developing mammalian brain, but the adult brain undergoes much less synaptic turnover, which would make these events harder to detect. Microglia in sliced brains might lose the capacity to engulf. Pre- and postsynaptic materials have different stabilities in the lysosome, such that presynaptic engulfment may be more difficult to detect. Cytoplasmic dyes and fluorophores might not be captured or might not be bright enough to visualize an engulfed bouton or spine. These caveats could mean that the "pinching off" of synapses by microglia exists but that efforts to directly observe this need to be optimized.

There are also technical limitations to the studies in fixed tissues that suggest microglial synaptic pruning by direct engulfment. For example, the resolution limits of light microscopy and difficulties colocalizing synaptic proteins with microglial lysosomes could lead to false colocalization and the misclassification of microglial-synaptic contacts as engulfment events. In addition, most studies have quantified only synaptic proteins without considering that they could be only one of many proteins or molecules taken up by microglia. If, for example, an entire cell was eliminated, both synaptic and cytoskeletal proteins would be phagocytosed by microglia.

In lieu of direct engulfment, what could explain the finding that microglia both restrict synapse numbers and take up synaptic proteins? We hypothesize that in many cases, neuron-autonomous pruning mechanisms may precede phagocytic uptake by microglia (see the figure). An extensive literature that predates microglial inclusion in the pruning process has shown that neurons undergo synapse elimination in a cell-autonomous and activity-dependent manner (*11*). Microglia might enhance these neuron-autonomous processes of synapse elimination. For example, microglia inhibit neuronal excitability (*8*, *9*) and clear the extracellular matrix (*5*). Both functions would destabilize synapses, which might then be eliminated by neurons through the release of extracellular vesicles, such as exophers (*12*), and subsequently be taken up by microglia as debris. This might be more efficient than transporting proteins long distances to be broken down within neurons, which can digest proteins but are not professional phagocytes like macrophages.

Microglia could also engulf debris from dying neurons or portions of neurons, such as debris from shedding axons (axosomes) (*13*). These bits of debris would include synaptic proteins. In these scenarios, microglia are taking up synaptic material after it has been eliminated by the neuron. Microglia can also trogocytose portions of synapses (*6*, *8*) or interpose between pre- and postsynaptic membranes in a nonphagocytic manner (stripping), both of which could affect synaptic transmission without eliminating synapses.

If any or all of these hypotheses are correct, microglia would be critical to the health of the brain, but they would not initiate synapse elimination. However, the well-established ability of microglia to sense and respond to neuronal activity would still be essential to their function by enabling them to distinguish between a living neuron and neuronal debris and to tailor phagocytosis as needed.

How should these findings affect future studies? Implicit assumptions must be considered. The word "pruning" long predates microglia and stems from the observation that synapse numbers in humans peak in infancy and decrease in adolescence (*14*). Yet, in the context of phagocytic microglia, the image evoked by the word pruning (defined as "to cut away what is superfluous") could lead to misunderstanding. We propose that less catchy terms, such as microglia-dependent synapse elimination, are more consistent with the currently available data.

A deeper investigation into the molecular mechanisms that regulate microglial function will also be essential. These experiments should include cell type–specific disruption of the proposed phagocytic pathways in microglia to determine whether the effects are cell autonomous. Additionally, new approaches may be needed to obtain an unbiased view of which proteins could end up inside these cells along with or independent of synaptic proteins. Investigating the complexity of microglial-synapse interactions may ultimately yield precise therapeutic targets for the many neurodevelopmental and neurodegenerative brain disorders involving microglia. ■

REFERENCES AND NOTES

1. R. C. Paolicelli *et al.*, *Science* **333**, 1456 (2011).
2. D. P. Schafer *et al.*, *Neuron* **74**, 691 (2012).
3. N. Scott-Hewitt *et al.*, *EMBO J.* **39**, e105380 (2020).
4. I. D. Vainchtein *et al.*, *Science* **359**, 1269 (2018).
5. P. T. Nguyen *et al.*, *Cell* **182**, 388 (2020).
6. L. Weinhard *et al.*, *Nat. Commun.* **9**, 1228 (2018).
7. A. Miyamoto *et al.*, *Nat. Commun.* **7**, 12540 (2016).
8. T. K. Y. Lim, E. S. Ruthazer, *eLife* **10**, e62167 (2021).
9. M. Merlini *et al.*, *Nat. Neurosci.* **24**, 19 (2021).
10. Y. Li *et al.*, *Dev. Cell* **23**, 1189 (2012).
11. T. E. Faust *et al.*, *Nat. Rev. Neurosci.* **22**, 657 (2021).
12. I. Melentijevic *et al.*, *Nature* **542**, 367 (2017).
13. D. L. Bishop *et al.*, *Neuron* **44**, 651 (2004).
14. P. R. Huttenlocher, *Brain Res.* **163**, 195 (1979).

10.1126/science.adh7906

NEURODEGENERATION

Role for cell death pathway in Alzheimer's disease

Human neurons transplanted into mice with amyloid plaques die by necroptosis

By **Daniel W. Sirkis**[1] *and* **Jennifer S. Yokoyama**[1,2]

Central, longstanding problem in the study of Alzheimer's disease (AD) has been an inability to fully recapitulate the biochemical and neuropathological hallmarks of the disease in mouse models, which are important tools of biomedical research. These hallmarks include extracellular plaques of aggregated amyloid-β (Aβ), intraneuronal neurofibrillary tangles composed of hyperphosphorylated tau protein, and the loss of neurons. Although some progress has been made in this area (*1*, *2*), much work remains to be done. On page 1176 of this issue, Balusu *et al.* (*3*) report a mouse model that results in the generation of AD-like tau pathology and neuronal death in a manner that depends on both the presence of amyloid pathology and transplanted human neurons. The findings suggest an explanation for why it has been challenging to produce Aβ-dependent tau pathology and neurodegeneration in mouse models. The work also provides evidence for the importance of a cell death pathway in AD that may be therapeutically tractable.

The new mouse model makes use of a previously designed line of mice that express a humanized version of the amyloid precursor protein (*App*) gene, which encodes the precursor to Aβ. This version harbors three pathogenic mutations ($App^{NL\text{-}G\text{-}F}$ mice; named to indicate the relevant single-letter amino acid substitutions) (*4*); each mutation causes familial forms of AD in humans, and collectively, they increase extracellular Aβ levels and promote Aβ aggregation in mice. Balusu *et al.* bred the $App^{NL\text{-}G\text{-}F}$ mice with mice lacking an adaptive immune system [recombination-activating protein 2 $(Rag2)^{-/-}$ mice] to allow human neuronal transplantation experiments. Although previous work in another xenograft model had suggested that

human neurons may be particularly susceptible to Aβ-induced injury, the analysis was limited by the short life span of the mouse model used (*2*). By contrast, the new mouse model lived more than twice as long.

Balusu *et al.* found that transplantation of human neuronal progenitor cells (which differentiate into mature neurons after engraftment) into the *App*$^{NL\text{-}G\text{-}F}$*Rag2*$^{-/-}$ mice resulted in development of tau pathology and death of the transplanted neurons. They observed increased levels of phosphorylated tau in the brain and blood as well as neurofibrillary tangles within the transplanted human neurons that occurred as early as 6 months after transplantation. By contrast, neither mouse neurons—whether endogenous or transplanted—nor human neurons transplanted into control mouse brains developed such pathological changes, even at 18 months after engraftment. These findings suggest that human neurons respond to Aβ within the brain in a way that mouse neurons do not.

Analysis of gene expression changes by means of bulk RNA-sequencing identified increased expression of a long noncoding RNA, maternally expressed gene 3 (*MEG3*), in the human neurons transplanted into the *App*$^{NL\text{-}G\text{-}F}$*Rag2*$^{-/-}$ mice compared with those transplanted into control mice. Long noncoding RNAs do not encode polypeptides; they instead regulate the expression of other genes (*5*). The authors found that expression of the mouse version of this gene (*Meg3*) was not increased in mouse neurons in the *App*$^{NL\text{-}G\text{-}F}$*Rag2*$^{-/-}$ mice that underwent transplantation with human neurons, suggesting a human-specific function for *MEG3* in the context of AD. They also found evidence for increased expression of *MEG3* in post mortem brain samples from humans with AD, confirming that Aβ-associated *MEG3* dysregulation extends beyond the animal model.

But how is human-specific *MEG3* dysregulation connected to neuronal death? Balusu *et al.* demonstrated that the loss of transplanted neurons in this model involves a form of programmed cell death called necroptosis. Necroptosis involves the phosphorylation of proteins such as receptor-interacting serine/threonine-protein kinase 1 (RIPK1), RIPK3, and mixed-lineage kinase domain-like protein (MLKL), which culminates in cellular necrosis (*6*). These proteins and the necroptotic pathway have been associated with another hallmark of AD—granulovacuolar degeneration (granule-containing vacuoles within the cytoplasm of neurons, typically associated with tau pathology) (*7*)—in neuropathological studies (*8*). Balusu *et al.* demonstrated that *MEG3* overexpression in human neurons is sufficient to induce necroptotic death in vitro, whereas reduction of *MEG3* expression in human neurons before transplantation leads to improved neuronal survival 6 months after engraftment in *App*$^{NL\text{-}G\text{-}F}$*Rag2*$^{-/-}$ mice. Moreover, cell culture and transplantation experiments that used genetic and pharmacologic approaches showed that necroptosis was the prominent mode of neurodegeneration downstream of *MEG3* in this model (see the figure).

A key limitation of the xenograft model developed by Balusu *et al.* is that it lacks an adaptive immune system. Given the potential importance of adaptive immune cells in AD (*9*, *10*), this limitation is not trivial. Although reconstituting an adaptive immune system into an immunodeficient mouse model would be technically challenging, future work might instead focus on augmenting the model through additional transplantation of human microglia (*11*). This would enable the investigation of human-specific aspects of the innate immune response. Given findings from human genetics that suggest the importance of microglia in mediating risk for AD (*12*), this modification would be likely to produce notable insights. Another open question is whether the improved neuronal survival that results from reduction of *MEG3* expression occurs by modulating the emergence of tau pathology or despite such pathology. Future work should be able to address this question relatively easily.

By leveraging the powerful combination of mouse genetics and human stem cell–derived neurons, Balusu *et al.* have generated a model of AD that recapitulates key aspects of disease pathobiology. The effects of additional genetic modifiers can now be studied in a model in which tau pathology and neuronal death occur in an Aβ-dependent manner. In addition, it may eventually be possible to genetically modify endogenous mouse neurons to become susceptible to Aβ-induced tau pathology and cell death. Such an advance could lead to mouse models that would require neither transplantation experiments nor immunodeficiency. The model developed by Balusu *et al.* should also prove highly useful for preclinical testing of experimental AD therapeutics, as exemplified by the authors, who found that a necroptosis inhibitor improved neuronal survival in the face of prolonged exposure to Aβ. ■

A human-specific response to amyloid plaques

Human neuronal progenitor cells are transplanted into amyloid-β–producing mutant mice at postnatal day 1. Amyloid neuropathology results in production of phosphorylated tau protein and neurofibrillary tangles (NFTs) in transplanted human neurons. In these neurons, expression of long noncoding RNA maternally expressed gene 3 (*MEG3*) is strongly induced, followed by activation of the necroptotic cell death pathway. Neither tau pathology nor necroptosis is observed in mouse neurons.

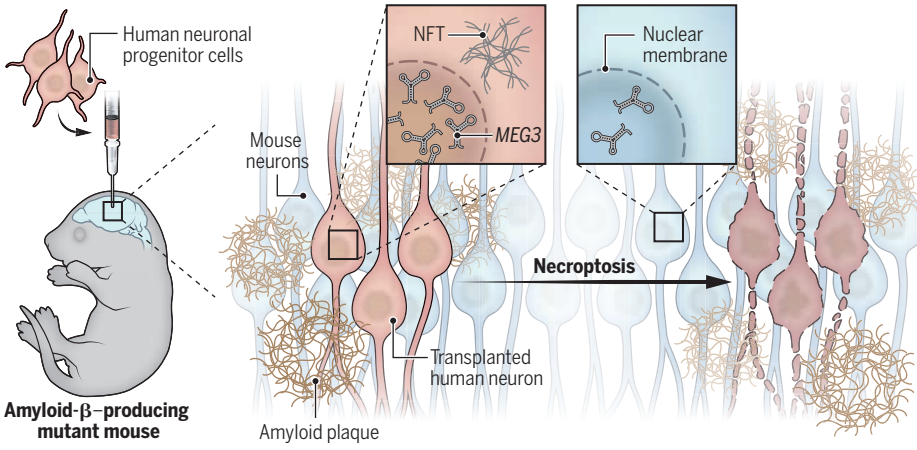

GRAPHIC: N. BURGESS/*SCIENCE*

[1]Memory and Aging Center, Department of Neurology, Weill Institute for Neurosciences, University of California, San Francisco, CA, USA. [2]Department of Radiology and Biomedical Imaging, University of California, San Francisco, CA, USA. Email: daniel.sirkis@ucsf.edu

REFERENCES AND NOTES

1. S. H. Choi *et al.*, *Nature* **515**, 274 (2014).
2. I. Espuny-Camacho *et al.*, *Neuron* **93**, 1066 (2017).
3. S. Balusu *et al.*, *Science* **381**, 1176 (2023).
4. T. Saito *et al.*, *Nat. Neurosci.* **17**, 661 (2014).
5. R.-W. Yao *et al.*, *Nat. Cell Biol.* **21**, 542 (2019).
6. M. Pasparakis, P. Vandenabeele, *Nature* **517**, 311 (2015).
7. C. Köhler, *Acta Neuropathol.* **132**, 339 (2016).
8. M. J. Koper *et al.*, *Acta Neuropathol.* **139**, 463 (2020).
9. D. Gate *et al.*, *Nature* **577**, 399 (2020).
10. Y. Chen, M. Colonna, *Curr. Opin. Immunol.* **77**, 102233 (2022).
11. J. Hasselmann *et al.*, *Neuron* **103**, 1016 (2019).
12. C. Romero-Molina *et al.*, *Neuron* **110**, 3513 (2022).

ACKNOWLEDGMENTS

J.S.Y. receives funding from NIH-NIA R01AG062588, R01AG057234, P30AG062422, P01AG019724, and U19AG079774; NIH-NINDS U54NS123985; NIH-NIDA 75N95022C00031; the Rainwater Charitable Foundation; the Bluefield Project to Cure Frontotemporal Dementia; the Alzheimer's Association; the Global Brain Health Institute; the French Foundation; and the Mary Oakley Foundation. J.S.Y. serves on the scientific advisory board for the Epstein Family Alzheimer's Research Collaboration.

10.1126/science.adk2009

RETROSPECTIVE

Albert Eschenmoser (1925–2023)

Organic chemist who demystified the logic of natural product structures

By **Scott E. Denmark**[1] *and* **Erik J. Sorensen**[2]

Albert Eschenmoser, pioneer in the synthesis of complex organic compounds, died on 14 July at the age of 97. Eschenmoser profoundly influenced the theory and practice of organic and bioorganic chemistry. His scientific contributions included new methods of chemical synthesis, the total synthesis of complex natural products, and the study of the chemical etiology of biomolecular structures. A penetrating thinker, he identified profound questions in organic chemistry and executed experimental plans to answer them.

Born in Erstfeld, Switzerland, on 5 August 1925, Eschenmoser received his scientific training and spent his career at Eidgenössische Technische Hochschule (ETH) Zürich. In 1949, he received a diploma in the natural sciences. In 1951, he obtained his doctorate of natural sciences in organic chemistry under Nobel Prize winner Leopold Ružička. As a member of Hans Schinz's working group, Eschenmoser studied acid-catalyzed cyclizations in mono- and sesquiterpenes. He rose through the ranks, reaching full professor in 1965. He retired in 1992 but continued his research for another 17 years at ETH Zürich as well as Goethe University in Frankfurt, Germany, and the Scripps Research Institute in La Jolla, California.

Eschenmoser's early studies served as guidelines for critical reexamination of structural assignments of many terpenes. These plant-derived compounds have complex structures with multiple fused carbon rings. After detailed analysis, Eschenmoser proposed a plausible mechanism whereby acid could initiate a cascade of bond-forming reactions that folded simple linear carbon chains with alternating double bonds into these polycyclic architectures. These studies provided a rigorous mechanistic foundation to what was previously an empirical rule for how isoprene precursors gave rise to particular terpenes. Eschenmoser's insights allowed the deduction of both the structure and configuration of the 13 known basic representatives of the cyclic triterpenes and also rectified a number of flawed structural proposals. The ideas led to the publication of a landmark paper in 1955 that articulated the final formulation of the biogenetic isoprene rule.

In the area of organic synthesis, Eschenmoser's achievements were characterized by originality, intellectual rigor, and experimental ingenuity. His investigation into the synthesis of corrin compounds culminated in the total synthesis of the biochemically crucial cofactor vitamin B_{12} (the result of a 12-year "competitive collaboration" with R. B. Woodward and his group at Harvard), which redefined the frontier of organic natural product synthesis. At the outset, the unique connection between the

A and D rings (which differentiates corrins from porphyrins) posed a daunting synthetic challenge, and early approaches created this union in an indirect and classical fashion. Eschenmoser chose to conquer the molecule at its seemingly most impenetrable flank. Among the many successful methods he developed for the construction of this crucial union, the most brilliant is the light-initiated migration of a hydrogen atom to a site that is 16 carbons away in the molecular framework.

Later, Eschenmoser focused on the search for a chemical etiology of the structure of natural nucleic acids. He wondered why the sugars in nucleic acids have five- rather than six-membered rings (pentose as opposed to hexose). In addressing this fundamental question, Eschenmoser and his co-workers created structural alternatives to the natural nucleic acids and compared their chemical and structural properties with those of the natural nucleic acids to establish the criteria by which ribonucleic and deoxyribonucleic acids are selected in the genetic system.

Eschenmoser's research clarified the nature of nucleic acids. He found that maximization of base-pairing strengths is not the decisive selection criterion in the domain of pentose-derived oligonucleotide systems, and that the helical shape of double-stranded DNA is a direct consequence of the sugar ring's five-membered structure. He observed that DNA's helical shape allows it to achieve optimal base-pair stacking distances and selects purine-pyrimidine pairings over purine-purine pairings, and that Watson-Crick pairing rules arise not only from the constitutions of the nucleic acid bases but also from the structure of the sugar backbone. By showing that potential nucleic acid alternatives are inferior to the natural nucleic acids with respect to those chemical properties that are fundamental to biological function, Eschenmoser provided support for the hypothesis that the evolutionary choice of RNA and DNA was made from a diversity of constitutionally related alternatives on the basis of functional criteria.

One of us (S.E.D.) was a PhD student of Eschenmoser's, and the other (E.J.S.) was his colleague at Scripps. We both marveled at his uncanny ability to formulate, ad hoc, compelling and lucid explanations for impenetrable problems. The lessons he shared in group seminars and during coveted teatime discussions in his laboratories were but a glimpse into the workings of an extraordinary intellect. Eschenmoser set a difficult-to-emulate example of scientific standards and an ability to address the most important questions in chemistry. He was also known for his incisive wit and his compassion and abiding respect for each individual co-worker. Students, postdocs, and visiting professors were treated as if they were his personal guests, making his laboratory a friendly and supportive environment for the many international scholars who worked with him.

Eschenmoser's research, insights, and lecturing style brought him worldwide speaking invitations, and his foundational discoveries are now enshrined in chemistry textbooks. He received many awards, including the Wolf Prize (1986), the Roger Adams Award (2003), and the Benjamin Franklin Medal (2008). He was a member of numerous national academies and a recipient of the Austrian Decoration for Science and Art.

Eschenmoser will be remembered for his piercing intellect, his warmheartedness, and his sense of humor. His work profoundly changed organic chemistry, and his generosity and mentorship inspired all those who came into his orbit. ■

10.1126/science.adk2553

[1]Department of Chemistry, University of Illinois Urbana-Champaign, Urbana, IL, USA. [2]Department of Chemistry, Princeton University, Princeton, NJ, USA. Email: sdenmark@illinois.edu

POLICY FORUM

SUSTAINABLE DEVELOPMENT

Four governance reforms to strengthen the SDGs

A demanding policy vision can accelerate global sustainable development efforts

By **Frank Biermann[1], Yixian Sun[2], Dan Banik[3], Marianne Beisheim[4], Michael J. Bloomfield[2], Aurelie Charles[2], Pamela Chasek[5], Thomas Hickmann[6], Prajal Pradhan[7,8], Carole-Anne Sénit[1]**

In 2015, the United Nations (UN) General Assembly agreed on 17 Sustainable Development Goals (SDGs) with 169 targets as part of the 2030 Agenda for Sustainable Development. Although the SDGs, which are to be achieved by 2030, are not the first attempt to guide policy actors through global goals, they go far beyond earlier agreements in their detail, comprehensiveness, and ambition. Yet the 2022 SDG Impact Assessment, conducted by a global consortium of researchers, has shown that the first phase of SDG implementation did not lead to a transformative reorientation of political systems and societies (*1, 2*). As the UN SDG Summit gets underway this month to review the halfway point in SDG implementation, and a further UN "Summit of the Future" is planned for 2024 to debate global governance reforms, we present here a demanding yet realistic policy vision to adjust the course of SDG implementation.

CORE ELEMENTS

The SDGs have had some discursive impacts through influencing how government, civil society, and business actors frame sustainable development policies in their external and internal communications. In terms of more concrete political impacts, however, the goals have, in most cases, not yet succeeded in transforming government policies, institutional arrangements, public and private funding allocations, or international cooperation. We suggest a set of governance reforms to breathe new life into efforts to achieve the global goals, based on four core elements: differentiation, dynamization, legalization, and stronger institutionalization.

Differentiation

First, the current SDG framework needs to be strengthened in a way that commits high-income countries to stronger and more concrete action. In principle, the SDGs lay down normative aspirations for all countries, and here they differ from earlier goal-setting efforts such as the Millennium Development Goals that focused on low-income countries. The SDGs are presented as universal, indivisible, and interlinked, even though many targets remain qualitative and all governments are allowed to set their own national implementation targets, which may consider their special circumstances while still being guided by the global level of ambition.

This approach was progressive in bringing high-income countries under the UN normative framework (*3*). Yet in practice, it also resulted in widespread cherry-picking, allowing leaders in affluent countries to focus on those global goals and targets they could easily reach. Goals that are more challenging for high-income countries, however, are still insufficiently addressed, such as reducing unsustainable consumption (SDG 12), phasing out fossil fuels (linked to SDG 7 and 13), protecting terrestrial and marine biodiversity (SDG 14 and 15), and increasing financial support for poorer countries and strengthening global partnerships for sustainable development (SDG 17). The universal framing of the SDGs may have also supported a persistent Western perspective in global media, academia, and civil society, suggesting a unified "humankind" while obscuring unequal consumption and emissions patterns among and within countries, including their spillover effects that impede the fiscal and policy space in low-income countries (*4*). In short, the global sustainability transition requires that high-income countries define, and deliver on, more ambitious national commitments within the overall SDG framework.

Dynamization

In addition, the original 17 goals and their 169 targets should not be seen as static. The current goals and targets reflect many political compromises during their negotiation (*5*), and they are often inadequate today given the escalating crises of ecological breakdown, global pandemics, persistent extreme poverty, and rising inequalities. Similar to the 2015 Paris Agreement on climate change and its ratcheting-up process, the SDGs should undergo regular rounds of revisions by which countries can raise their ambition.

For this purpose, the UN High-level Political Forum on Sustainable Development, which reviews progress on the existing goals and targets, must evolve into a mechanism that over time also adjusts these targets to the exigencies of multiple global crises. Governments should view this process as an opportunity for more effective peer learning, leveraging synergies, tackling trade-offs, and overall increasing ambition (*6*). During this regular adjustment process, the role of global scientific assessments in reviewing the adequacy of SDG targets needs to be strong. Equally important is a greater involvement of civil society in the reporting and review process to strengthen the ratcheting-up of ambition that we propose.

Legalization

The SDGs have been crafted as non–legally binding and often qualitative commitments that cover broad areas of human activity. Although this nonbinding approach has historically allowed for universal support by governments, it can also reduce incentives for governments to enact the institutional and normative transformations that are needed. Stronger commitments are now crucial. Although the entire set of 17 SDGs is unlikely to become binding under international law, like-minded countries should work toward a series of legally binding, plurilateral agreements and governance arrangements in support of specific goals and targets. Examples are the international treaty to end plastic pollution (*7*), which is linked to SDG 12; the agreement on the conservation and sustainable use of marine biological diversity of areas beyond national jurisdiction (*8*), linked to SDG 14; the existing UN convention against corruption, linked to SDG 16; or the civil society initiative for a fossil fuel nonproliferation treaty (*9*), linked, among others, to SDG 13.

[1]Copernicus Institute of Sustainable Development, Utrecht University, Netherlands. [2]Centre for Development Studies and Department of Social and Policy Sciences, University of Bath, UK. [3]Centre for Development and the Environment, University of Oslo, Norway. [4]German Institute for International and Security Affairs, Stiftung Wissenschaft und Politik, Berlin, Germany. [5]Department of Political Science, Manhattan College, USA. [6]Department of Political Science, Lund University, Sweden. [7]Energy and Sustainability Research Institute Groningen, University of Groningen, Netherlands. [8]Potsdam Institute for Climate Impact Research, Germany. Email: f.biermann@uu.nl

Smaller, focused, plurilateral agreements and "coalitions of the willing" that expand over time would bring some progress in times of geopolitical tensions, which often block new universal agreements. This progressive legalization of some SDGs will also improve governance in sectors that lack effective global mechanisms, such as the international regulation of mining activities by multinational corporations in low-income countries or pollution of outer space. In addition, the SDGs need to be better aligned with other legal frameworks, such as global trade and investment agreements and the UN human rights system.

Institutionalization

Lastly, global policy progress in some areas is impeded by governance fragmentation and insufficient institutional support. Whereas some SDGs, such as health (SDG 3), can build on strong international organizations and national agencies, other areas are barely institutionalized, notably the goals on reducing inequality (SDG 10), responsible consumption and production (SDG 12), and strengthening of institutions and governance (SDG 16). Moreover, various UN agencies act as custodians for individual SDGs, with responsibilities being widely spread among ministries and local institutions (*10*, *11*).

United Nations bodies and governments should thus support further institutionalization around the SDGs and enhance steering capacities in global governance and national policymaking. For example, some researchers have proposed strengthening implementation of SDG 12 by setting up a new "UN forum on sustainable lifestyles" that would "enable international peer learning and elevate action on SDG12" (*12*). Similar new institutions are conceivable to enable and build capacities for the integrated transformative shifts that are envisaged in the Global Sustainable Development Reports (*13*).

POST-2030: THE ROAD AHEAD

The future of the SDGs beyond 2030 is uncertain. Despite all shortcomings and criticisms, it would be ill-advised to terminate or to fundamentally redesign the 17 SDGs after 2030. The necessary negotiations within the UN system would cost valuable time and divert political attention, and the eventual outcome would most likely not be very different given current global power constellations. Instead, we propose four reforms to strengthen governance for achieving the SDGs. Our proposals of differentiation, dynamization, legalization, and institutionalization holds the potential to drive policy processes that continue beyond 2030 and generate a global policy framework that would not only be more ambitious but also more effective.

Three complementary reforms would further support the changes that we propose. First, governments should agree on stronger global governance arrangements to initiate, oversee, and refine these processes of differentiation, dynamization, legalization, and institutionalization. In 1992, governments created the UN Commission on Sustainable Development, which was widely judged as unsuccessful. After 2012, the High-level Political Forum on Sustainable Development was set up to replace this commission; yet most observers agree that this forum has also not lived up to expectations (*14*). Governments should thus establish a stronger mechanism at the heart of the UN with a clear mandate to not only support but also oversee the proposed differentiation, dynamization, legalization, and institutionalization of the SDGs. One option would be a new UN Sustainable Development Council (*15*) that could serve among others as a compulsory, systematic, and more consequential review mechanism for the SDGs, which would go beyond the more voluntary nature of the High-level Political Forum and its predecessor. The 2024 UN Summit of the Future will be an important venue to discuss such innovations.

"...subnational success stories are not...sufficiently supported by transnational institutions and networks..."

Second, assessments of the influence of the SDGs have shown that they had sizeable impact beyond national governments, notably in cities and with regional authorities (*2*). Such subnational success stories are not, however, sufficiently supported by transnational institutions and networks, and the UN is currently unable to provide such coordination. A new post-2030 governance system must therefore recognize the valuable role of local and provincial governments and provide stronger institutions, within the UN and beyond, to support subnational action.

Third, assessments of the role of the SDGs in supporting sustainability transformations in low-income countries have shown that lack of finance is a severe limitation for SDG implementation. The 2023 SDG Summit should thus include stronger commitments by high-income countries to support sustainability transformations in the Global South. In addition, the 2024 Summit of the Future is expected to discuss reforms of the international financial architecture, and bold steps are also needed here. Important to consider are innovative financial mechanisms that increase the costs of harmful consumption and production and channel new funding into sustainability projects in low-income nations. A Global Energy Transition Fund, new mechanisms to fund global public goods, or regional levies on air transportation and other high-emitting sectors are examples of financial mechanisms that must be explored.

In sum, research has shown that the 17 SDGs have not led to the global sustainability transformation that is urgently needed. The claim by the UN General Assembly in the 2030 Agenda for Sustainable Development that the SDGs would enable governments to take "bold and transformative steps that are urgently needed to shift the world on to a sustainable and resilient path" has not materialized.

The SDG Summit in September 2023 must pave the way toward a major reform of the SDGs that further differentiates the goals to enable greater ambitions for high-income countries; dynamizes goals and targets by regular pledge-and-review rounds; legalizes certain goals and targets in a network of plurilateral agreements among like-minded countries; and institutionalizes global and national governance in areas where the SDGs lack political and institutional anchoring and support. These four governance measures could be game changers. They are not only central for the acceleration of SDG implementation leading up to 2030 but would also be important cornerstones for a revised SDG framework beyond 2030. Governance for the SDGs must be substantially strengthened to allow these goals to "transform our world," as the original 2015 UN declaration promised. ■

REFERENCES AND NOTES

1. F. Biermann *et al.*, *Nat. Sustain.* **5**, 795 (2022).
2. F. Biermann, T. Hickmann, C.-A. Sénit, Eds., *The Political Impact of the Sustainable Development Goals. Transforming Governance through Global Goals?* (Cambridge Univ. Press, 2022).
3. S. Fukuda-Parr, "Sustainable Development Goals (SDGs) and the promise of a transformative agenda" in *International Organization and Global Governance* (Routledge, 2023), pp. 708–723.
4. D. Banik, *Anthropocene Sci.* **1**, 233 (2022).
5. M. Kamau, P. Chasek, D. O'Connor, *Transforming Multilateral Diplomacy: The Inside Story of the Sustainable Development Goals* (Routledge, 2018).
6. M. Beisheim, F. Fritzsche, *Glob. Policy* **13**, 683 (2022).
7. N. Simon *et al.*, *Science* **373**, 43 (2021).
8. E. M. De Santo *et al.*, *Earth Syst. Gov.* **2**, 100029 (2019).
9. Fossil Fuel Non-Proliferation Treaty Initiative, https://fossilfueltreaty.org/.
10. M. van Driel *et al.*, *Glob. Policy* **13**, 669 (2022).
11. M. Bexell, K. Jönsson, *The Politics of the Sustainable Development Goals: Legitimacy, Responsibility, and Accountability* (Taylor & Francis, 2021).
12. Stockholm Environment Institute, Council on Energy, Environment and Water, Stockholm+50: Unlocking a Better Future (SEI and CEEW, 2022).
13. Independent Group of Scientists, Global Sustainable Development Report, Advance Unedited Version, (United Nations, 2023).
14. M. Beisheim, S. Bernstein, "The High-Level Political Forum Review 2020" in *Implementing the 2030 Agenda for Sustainable Development and Addressing Key Climate and Environmental Issues* (New World Frontiers, 2022).
15. F. Biermann *et al.*, *Science* **335**, 1306 (2012).

10.1126/science.adj5434

PHOTO: AP PHOTO/MONTEREY HERALD, ORVILLE MYERS

Significant sliding rendered this section of Highw
in Big Sur, California, temporarily impassable in 2011.

ENVIRONMENTAL SCIENCE

Managed retreat or unmanaged disaster

A journalist offers insight into California's coastal climate change dilemma

By **Clare Fieseler**

Imagine California without its iconic beaches. This is an exercise in seeing the future. In the coming decades, two-thirds of the sandy shores of Santa Monica, Los Angeles, Orange County, and San Diego may be lost to the Pacific Ocean's rising levels and increasing wave strength as more fossil fuel burns and more land is swallowed up and scraped away. Traditional defenses are futile; one sea wall, built to last 20 years, lasted just 6 weeks, writes journalist Rosanna Xia in *California Against the Sea*. The book invites readers to envision the future of California's coasts, consider more-transformative solutions, and conjure the bravery to let (some things) go.

California Against the Sea: Visions for Our Vanishing Coastline
Rosanna Xia
Heyday, 2023. 336 pp.

For Xia, an environment reporter for the *Los Angeles Times*, adapting to sea level rise is like an eye exam that tests one's field of vision. By 2100, California's waters will rise at least 6 feet. A narrow vision of the state's response focuses on deploying more of the same strategies used in the past: holding back the ocean with more armament and better engineering. An expansive view, however, allows one to see opportunities for change and avenues to put public safety and the public good over property rights and private profit.

Few people are more qualified to explain and analyze this landscape. Xia's reporting on this topic earned her a spot as a finalist for a Pulitzer Prize for Explanatory Reporting in 2020. In this, her first nonfiction book, she breathes exquisite detail and dialogue into a rich narrative held up by years of beat reporting.

California Against the Sea starts with the state's oldest story about coastal adaptation. At the end of the last ice age, the Chumash people settled and then retreated from the Channel Islands, marking their own hard decision in the face of 400 feet of sea level change. The book then moves to the mainland and the glamorous homes of Laguna Beach, where uberwealthy owners are at war with state regulators. Private seawalls, clandestinely constructed, are protecting beachfront mansions—for a time—while dangerously accelerating the erosion of public beaches. (Concrete infrastructure is deeply fascinating in Xia's capable hands.)

Xia goes on to profile 12 more sites up and down the coast, building out stories that embody a different vision of the vanishing coast—some cautionary failures, some spots of hope. Her journey features all of the hallmarks of a good California road trip: the movie stars turned advocates, an eroded beach that birthed the pseudo-sport "skimboarding," and, most of all, residents grappling with the decision of whether to stay put or prepare to leave.

Managing a coastline involves managing emotions too. California has explored "managed retreat" more than any other state, pioneering at large scales a term that proved, over time, to be counterproductive. Advocates say "retreat" is inevitable; the choice is between two kinds, managed versus unmanaged—or, as one California resident put it, "unmanaged disaster." But this language has sparked confusion in Imperial Beach and emotional backlash in Pacifica. Other states would do well to adopt alternative terms, such as "community-led relocation," that suit their own communities.

This book is about California but holds relevance for other states, such as Florida, Louisiana, and South Carolina, which are also losing battles with rising water. Xia shows how visionary legislation, such as the California Coastal Act of 1976, provides structure and oversight for addressing emerging coastal problems, even if the outcomes are not all conservation wins. Few states have similar laws, but many should.

Xia keeps an eye on the future while chronicling the heated debates playing out at 13 coastal California locales. She continuously uplifts Indigenous wisdom and voices, highlighting Native people's growing role in coastal stewardship. Readers learn, for example, about a first-of-its-kind returning of undeveloped coastal land to the Kashia Band of Pomo Indians—an act that saves the region from risky development and will help preserve its natural defenses.

Along the way, the dogged reporter transforms into a kind of wayfinder. Xia writes: "To resist change is to miss out on opportunities to create a better future. To remain unchanged is to buy into the long-held myth that the world today is as good as it gets." Here and in several other passages, she elevates the discussion of "managed retreat" and "climate adaptation" beyond the realms of science and politics, allowing readers to glimpse a new way to think about the urgent phenomena defining our times. ■

The reviewer is at the National Museum of Natural History, Smithsonian Institution, Washington, DC 20013, USA, and *The Post and Courier*, Charleston, SC 29403, USA. Email: clare.fieseler@gmail.com

10.1126/science.adj0809

SCIENCE AND SOCIETY

Resisting efficiency's overreach

Society's obsession with optimization has a cost, argues a mathematical modeler

By **Dov Greenbaum**[1,2] *and* **Mark Gerstein**[2,3]

Optimal Illusions: The False Promise of Optimization
Coco Krumme
Riverhead Books, 2023.
256 pp.

In her new book, *Optimal Illusions*, mathematical modeler and Silicon Valley alum Coco Krumme reflects on her gradual disillusionment with society's obsession with better living through optimization. Through a series of vignettes, Krumme explores the societal drawbacks, consequences, and nuanced complexities of this philosophical framework that are often overlooked amid the allure of the efficiency and certainty it promises.

The book is divided into three sections that examine society's preoccupation with optimization and the approach's shortcomings and presents a pessimistic outlook on the potential future ramifications of embracing this attitude toward life. Spanning eight chapters, it candidly recounts Krumme's initial fascination with the concept of optimization, which eventually evolved into a conviction that the zealous pursuit of efficiency has overreached, failing in various sectors ranging from agriculture to artificial intelligence (AI).

Krumme defines optimization as "the practice of pinning down an understanding of the world, of assigning boundaries and finding peaks within." It is, in her view, a top-down process that begins with a desired end goal from which one works backward to determine how best to achieve it. The "dominant mindset of the modern West," optimization blends quasi-religious overtones with quintessentially American ideals of self-sufficiency and individual responsibility for "making the world a better place."

The book outlines the historical trajectory of optimization, tracing it as far back as Isaac Newton's early efforts with calculus, which Krumme suggests represented the modern beginning of the idea of atomization, and to the World War II era efforts of mathematician Stanley Ulam and physicist Nick Metropolis, who developed a method for random sampling that serves as one of the best techniques for modeling complex phenomena. Modern optimization, Krumme argues, is rooted in the foundational belief that everything can be reduced to measurable components, a mindset exemplified by the Silicon Valley mantra "What gets measured gets managed."

The book next endeavors to tackle the question of why "no one questions whether we should be optimizing in the first place." Here, Krumme explores how our continued faith in optimization, despite its frequent failures to deliver, has engendered modern malaise. At the crux of her thesis is the notion that our unchecked pursuit of optimization has precipitated the erosion of three fundamental pillars within systems: "slack [the ability to adjust to setbacks], place, and scale."

Incremental failures, often dismissed or concealed, accumulate stealthily in optimized systems, she argues, until an unexpected breakdown ensues, precipitating a seemingly abrupt collapse that reverberates across systems as "entire industries seem brought to their knees." The consequences of losing slack are most visible in just-in-time supply chains with systems tailored for lean efficiency rather than resilience. (Krumme only briefly alludes to the related concepts of sensitivity, robustness, and evolvability, strategies regularly employed by biological systems, which sacrifice immediate perfection for the ability to adapt to future conditions.)

Meanwhile, our relentless pursuit of optimization has inflicted a profound loss of scale, argues Krumme, as characterized by the rigidity of systems that are hamstrung in their capacity to change course or evolve when the necessity arises. "The better we get at optimizing locally, the more uses we find for optimizations generally—and the worse we get at reconsidering the idea of optimization itself," she writes.

Optimization also erodes "place," diminishing the distinct wisdom that fosters a diverse range of practices and distancing individuals from the underlying data context that underpins the algorithms. This predicament becomes evident, Krumme maintains, when those entrusted with an optimized system "lose track both of its design and of its vulnerabilities"—a paradoxical outcome of obsessive refinement.

In the book's final section, Krumme advocates optimizing locally, toward simpler-to-describe optima as an effective strategy for deliberate deoptimization. This approach addresses the pitfalls associated with optimization "while maintaining its many virtues."

Optimal Illusions urges readers to contemplate the far-reaching consequences of modern society's perpetuation of optimization as a default approach to system management. However, the book, which includes a prescient interview with Sam Altman, CEO and cofounder of OpenAI, does not delve deeply into an optimized AI's potential existential threat to civilization. For such a discussion, readers might consider Yuval Noah Harari's 2018 book, *21 Lessons for the 21st Century*. ■

A visitor views a battery production line at a power plant in Kawasaki, Japan.

The reviewers are at the [1]Zvi Meitar Institute for Legal Implications of Emerging Technologies and Harry Radzyner Law School, Reichman University, Herzliya, Israel; [2]Department of Molecular Biophysics and Biochemistry, Yale University, New Haven, CT, USA; and [3]Program in Computational Biology and Bioinformatics and Department of Computer Science, Yale University, New Haven, CT, USA. Email: dov.greenbaum@aya.yale.edu

10.1126/science.adj6399

Conservation plans are in place to protect China's spotted seal (*Phoca largha*) population, but policy implementation and enforcement have fallen short.

PHOTO: ZONGXING WANG

Edited by **Jennifer Sills**

Enforce China's plan to protect spotted seals

The spotted seal (*Phoca largha*) is the only carnivorous aquatic mammal that exclusively breeds in China's waters (*1*–*4*). A flagship species within the Bohai Sea and Yellow Sea ecosystems (*5*), and genetically distinct from any other spotted seal population (*2*–*4*), the species influences prey populations through predation pressure. Because of its ecological importance, the spotted seal has been designated a Class I national key protected animal (*6*). In the 1940s, there were approximately 8137 spotted seals in China (*7*). However, over the past 80 years, human activities have drastically reduced their numbers. Based on data gathered from field observations, the population in China is estimated to have dropped to less than 2000 individuals by the 1980s and to less than 500 by the year 2020 (*8*, *9*). China must take urgent action to reverse this decline.

Humans have disrupted the species' reproductive and social groups by poaching young spotted seals to put in aquariums and killing adults for their skin and fur, endangering the population's sustainability (*7*, *8*, *10*). In addition, marine pollution, marine transportation, and fishing activities have led to habitat loss, decreased food sources, and fishing gear–related injuries (*8*, *10*). Because seals use large blocks of floating ice during the whelping, nursing, breeding, and molting periods (*9*), melting ice caused by global warming and marine pollution has also contributed to population decline (*8*, *10*, *11*).

Since the 1980s, China has implemented a series of measures to protect and restore the spotted seal population. In 1983, a ban on hunting spotted seals was imposed (*8*). In 1988, the spotted seal was listed as a Class II national key protected animal, and in 1992, the Dalian Spotted Seal Nature Reserve was established (*2*). In 2017, the Spotted Seal Conservation Action Plan (2017–2026) was released, and in 2021, the spotted seal was upgraded to a Class I national key protected animal (*5*, *6*). The implementation of these measures has led to temporary increases in the spotted seal population (*12*), but the downward trend in population size continues (*9*).

China's conservation action plan for spotted seals provides a roadmap to effective action, but implementation and enforcement have fallen short. By intensifying supervision and strictly enforcing relevant laws and regulations, the Chinese government can work toward eradicating illegal hunting and prohibiting illegal trading. Long-term and large-scale monitoring should be conducted to obtain more comprehensive data on the population, distribution, and breeding status of spotted seals. Scientific management and conservation policies in protected areas should be better executed and enforced. The Chinese government should help residents near protected areas to broaden their sources of income. By reducing their dependence on marine aquaculture and fishing, they will minimize threats to the spotted seal's food and habitat. Ensuring that spotted seals can continue to breed and thrive in China's waters is crucial to the local marine ecosystem.

Zongxing Wang
First Institute of Oceanography, Ministry of Natural Resources, Qingdao 266061, China and Key Laboratory of Marine Eco-Environmental Science and Technology, Ministry of Natural Resources, Qingdao 266061, China.
Email: zongxingwang@fio.org.cn

REFERENCES AND NOTES

1. D. J. Rugh *et al.*, *Mar. Fish. Rep.* **59**, 1 (1997).
2. J. B. Han *et al.*, *Ann. Zool. Fennici* **47**, 1 (2010).
3. X. Li *et al.*, *Trends Evol. Biol.* **2**, e6 (2010).
4. X. Gao *et al.*, *J. Biotech.* **136**, S529 (2008).
5. Ministry of Agriculture and Rural Affairs, "The Spotted Seal Conservation Action Plan (2017–2026)" (2017); http://www.moa.gov.cn/nybgb/2017/djq/201802/t20180202_6136361.htm [in Chinese].
6. National Forestry and Grassland Administration and Ministry of Agriculture and Rural Affairs, "Wildlife under special state protection list" (2021); http://www.forestry.gov.cn/html/main/main_5461/20210205122418860831352/file/20210205151950336764982.pdf [in Chinese].
7. J. H. Dong, F. Shen, *Mar. Sci.* **5**, 3 (1991) [in Chinese].
8. P. L. Wang, *Fish. Sci.* **12**, 1 (1993) [in Chinese].
9. China Biodiversity Conservation and Green Development Foundation, "2020 spotted seal scientific synchronous observation outcomes: The number of wild population is less than 500—CBCGDF CCAfa System" (2020); http://www.cbcgdf.org/English/NewsShow/5002/12045.html.
10. H. K. Yan *et al.*, *Mamm. Stud.* **43**, 1 (2018).
11. P. L. Wang, *Acta Oceanol. Sin.* **5**, 1 (1986).
12. N. Wang, K. Ding, *Mar. Sci. Bull.* **38**, 2 (2019) [in Chinese].

10.1126/science.adj9396

Iran's petrochemical plant affects wetlands

Iran plans to build a petrochemical plant, known as Mazandaran (or Miankaleh) Petrochemical (*1*), adjacent to the Miankaleh Wetland, a 90-ha environmental sanctuary for diverse wildlife, including numerous migratory waterbirds (*2*). The plant would have economic and strategic benefits (*3*) but could harm the environment. Before moving forward, Iran should evaluate the project and amend the plans to minimize environmental damage.

Environmental advocates and neighboring communities harbor concerns about the petrochemical complex's potential repercussions on the wetland's delicate ecosystem (*4*). The complex would likely consume substantial water and energy and emit pollutants that would be detrimental to the ecosystem and human well-being (*5*). The endeavor could also negatively affect the tourism sector by reducing the number of birders and naturalists who visit the wetland sanctuary.

Iran should conduct a comprehensive environmental assessment of the project before construction proceeds and share the results with the public. If the project moves ahead, green technologies and eco-friendly practices should be integrated into the plan to minimize environmental damage. For example, the plant's processes should be optimized to reduce carbon emissions. To contribute to the circular economy, bio-based materials should be used rather than fossil fuels, and the plant should be designed to maximize its potential for carbon capture and utilization (*6*).

Many European countries have engineered petrochemical units with marginal ecological footprints (*7*, *8*). Iran should take steps to meet this goal. The government should engage the public through transparent dissemination of information and subject the project to heightened accountability measures. The project plans should abide by the recommendations of environmental experts and incorporate real-time monitoring of potential pollutants. Construction teams and plant operators should adhere to enforceable environmental obligations. To make sure the project satisfies the requirements, an oversight framework that encompasses the plant's construction and operational phases should be designed to thwart the release of pollutants into the ecosystem and uphold environmental protection goals.

Morteza Asghari[1,2]* and Iman Salahshoori[3,4]
[1]Separation Processes Research Group, Department of Chemical Engineering, University of Science and Technology of Mazandaran, Behshahr, Mazandaran, Iran. [2]UNESCO Chair on Coastal Geo-Hazard Analysis, Tehran, Iran. [3]Department of Polymer Processing, Iran Polymer and Petrochemical Institute, Tehran, Iran. [4]Department of Chemical Engineering, Islamic Azad University, Science and Research Branch, Tehran, Iran. *Corresponding author. Email: asgharimore@gmail.com

REFERENCES AND NOTES

1. V. Riahi, M. Badenj, H. Zavareh, *J. Green Manage. Dev.* **1**, 105 (2022).
2. UNESCO, "Miankaleh Biosphere Reserve, Islamic Republic of Iran" (2022); https://www.unesco.org/en/mab/miankaleh-biosphere-reserve-islamic-republic-iran.
3. Shalini Gupta, Bhawana Pathak, in Abatement of Environmental Pollutants, P. Singh, A. Kumar, A. Borthakur, Eds. (Elsevier, 2020), pp. 127–149.
4. M.-H. Sinkakarimi *et al.*, *Biol. Trace Elem. Res.* **185**, 177 (2018).
5. J. Korbecki, I. Gutowska, D. Chlubek, I. Baranowska-Bosiacka, *Environ. Sci. Pollut. Res.* **26**, 12631 (2019).
6. M. Moheimany, in NGOs, Policy Networks and Political Opportunities in Hybrid Regimes: A Case Study of Islamic Republic of Iran, M. Moheimany, Ed. (Springer Singapore, Singapore, 2021), pp. 269–301.
7. C. Fetting, "The European Green Deal," EDSN Report (EDSN Office, 2020); https://www.esdn.eu/fileadmin/ESDN_Reports/ESDN_Report_2_2020.pdf.
8. M. van Noordwijk *et al.*, *Annu. Rev. Environ. Resour.* **37**, 389 (2012).

10.1126/science.adk2462

A step back from oil exploration in Brazil

The Brazilian Equatorial Margin, located along the country's northern coast between the states of Amapá and Rio Grande do Norte, is considered the new frontier for deep-water oil exploration (*1*). Recent oil discoveries in the waters of nearby countries, such as Guyana, French Guiana, and Suriname (*2*), highlight a potential that attracts the Brazilian industry and the international oil and gas market. However, this region, which includes the mouth of the Amazon River, harbors biodiversity that provides environmental services to a large riverine and Indigenous population (*3*, *4*). Brazil's government, which recently took the first step toward protecting these ecosystems and the people who rely on them, should continue to prioritize environmental protection over profit.

Brazilian Equatorial Margin biodiversity is distributed across estuaries, beaches, tidal plains, wetlands, dunes, and mangroves, all of which serve as critical environments for maintaining the connection between coastal and marine habitats. The region also encompasses ecologically, economically, and socially important biogenic reefs, known for their rich natural resources and fish stocks (*5*). Drilling activities could lead to habitat disruption, water pollution, noise disturbance, chemical risks, and long-term environmental consequences (*6*). An oil spill could jeopardize the entire ecosystem.

Petrobras, the company responsible for oil exploration in Brazil, submitted an environmental license request in August 2021 that could lead to the first exploration well for oil production in the Brazilian Equatorial Margin. In May, the Brazilian Institute of Environment and Renewable Natural Resources (IBAMA) denied the request (*7*, *8*). Given the high socio-environmental sensitivity, IBAMA recognized the need to conduct an environmental baseline assessment of the sedimentary area in the Amazon River mouth.

Once Petrobas completes the assessment, IBAMA should reevaluate the company's application and reject drilling in the Brazilian Equatorial Margin if the evidence suggests that it will cause irreparable harm. Despite political and societal actors pushing for the expansion of oil drilling, Brazil should instead work toward transitioning its energy matrix to renewable sources. Contributing to rapid decarbonization would ensure that Brazil's economic development focuses on the future rather than the past.

Thiago Simon Marques*, Guilherme Gutierrez, Barbara Protocevich Pina
Laboratório de Ecologia Aplicada, Universidade de Sorocaba, Sorocaba, Brazil.
*Corresponding author.
Email: thiago.marques@prof.uniso.br

REFERENCES AND NOTES

1. C. A. Da Cruz, H. J. P. Severiano Ribeiro, E. B. Silva, *J. South Am. Earth Sci.* **111**, 103475 (2021).
2. T. E. Wong, *Acad. J. Sur.* **10**, 1 (2019).
3. Y. Malhi *et al.*, *Science* **319**, 169 (2008).
4. P. B. M. Carneiro *et al.*, *Sci. Rep.* **12**, 17359 (2022).
5. R. L. Moura *et al.*, *Sci. Adv.* **2**, e1501252 (2016).
6. E. E. Cordes *et al.*, *Front. Environ. Sci.* **4**, 58 (2016).
7. Instituto Brasileiro do Meio Ambiente e Dos Recursos Naturais Renováveis Gabinete da Presidência do Ibama, "Despacho nº 15786950/2023-Gabin" (2023); https://www.gov.br/ibama/pt-br/assuntos/noticias/2023/ibama-nega-licenca-de-perfuracao-na-bacia-da-foz-do-amazonas/sei_ibama-15786950-despacho-presidente.pdf [in Portuguese].
8. Instituto Brasileiro do Meio Ambiente e Dos Recursos Naturais Renováveis Coordenação de Licenciamento Ambiental de Exploração de Petróleo e Gás Offshore, "Parecer Técnico nº 128/2023-Coexp/CGMac/Dilic" (2023); https://www.gov.br/ibama/pt-br/assuntos/noticias/2023/ibama-nega-licenca-de-perfuracao-na-bacia-da-foz-do-amazonas/parecer-coexp-fza-59.pdf [in Portuguese].

10.1126/science.adj7307

ERRATA

Erratum for the Research Article "Shared regulatory programs suggest retention of blastula-stage potential in neural crest cells" by E. Buitrago-Delgado *et al.*, *Science* 381, eadk1062 (2023).

Published online 11 August 2023.
10.1126/science.adk1062

RESEARCH

IN *SCIENCE* JOURNALS

Edited by **Michael Funk**

NEUROIMMUNOLOGY

Peptide promotes protection

Neuromedin U (NMU) is a neuropeptide that can drive the type 2 immune responses seen in allergy and antihelminth host defense by activating group 2 innate lymphoid cells that express the receptor NMUR1. Whether NMU activates other players in type 2 immunity remains controversial. Using single-cell RNA sequencing and fate-mapping reporter mice, Li *et al.* found that a subset of eosinophils present in the small intestine also express this receptor. NMU-mediated activation of small intestine eosinophils fuels goblet cell differentiation and the effective expulsion of intestinal worms. —STS

Science, ade4177, this issue p. 1189

Some eosinophils (green) in the small intestine produce a peptide hormone receptor important for antiparasitic immunity.

CELL BIOLOGY

Source of a lysosomal signaling molecule

Lysosomes play a crucial role in maintaining neuronal health in childhood and in age-related neurodegenerative diseases. Lysosomal function is potently enhanced by an enigmatic lipid known as bis(monoacylglycero) phosphate (BMP). Alterations in BMP levels are linked to neurodegeneration, and its accumulation is increasingly recognized as a firefighter response to lysosomal dysfunction. However, the enzyme responsible for BMP production has remained unknown for decades, hindering understanding and translational potential. Medoh *et al*. now show that the gene *CLN5*, the loss of which causes a severe neurodegenerative disease, encodes the long-sought BMP synthase. This discovery establishes the groundwork for future research on the fundamental aspects of BMP and its therapeutic applications in neurodegeneration and beyond. —SMH

Science, adg9288, this issue p. 1182

COMPARATIVE COGNITION

Learning predicts problem-solving

Birds are well known for their vocalizations. Although many people think of these sounds as instinctual, in fact, a great many bird species are flexible, vocal learners, a trait humans also have that is critical for our language development and is linked to complex cognition. Audet *et al*. used behavioral experiments in over 20 species of North American birds to test whether vocal learning in songbirds was related to a variety of cognitive skills. They found that the species with the most complex vocal learning abilities were also the best problem-solvers and had the largest brains relative to body size. —SNV

Science, adh3428, this issue p. 1170

NEUROSCIENCE

Presynaptic demolition

The ubiquitin ligase Ube3a has been associated with neurodevelopmental disorders. Its inactivation causes the developmental disorder Angelman syndrome, and increased Ube3a activity is associated with autism spectrum disorder. Furusawa *et al*. investigated the role of Ube3a at the presynaptic level, reasoning that synaptic abnormalities during development might be responsible for the occurrence of these disorders. Using fruit fly models, the authors showed that Ube3a is responsible for axonal presynapse elimination and function. High levels of Ube3a at the axon terminals led to precocious presynapse elimination, whereas elimination from axon terminals due to localization defects was associated with defects in normal presynapse elimination. The results potentially explain the mechanism mediating the development of disorders such as Ube3a-mediated Angelman syndrome and autism spectrum disorder. —MMa

Science, ade8978 this issue p. 1197

SIGNALING COMPLEXES

Multimodal analysis of a kinase complex

Mitogen-activated protein kinases (MAPKs) are a key player in cellular responses to various stimuli in eukaryotes. Signaling cascades occur through a series of upstream kinases, eventually resulting in double phosphorylation of MAPK that occurs in a complex that is transient and dynamic and thus difficult to

visualize by traditional structural approaches. Juyoux *et al*. combined cryo–electron microscopy, biophysical techniques, and molecular dynamics simulations to construct a model of the active complex between the MAPK p38α and its upstream kinase, MKK6. Based on this model, the authors discuss specific interactions, selectivity, and the overall mechanism of p38α activation. These findings will be important for researchers seeking to target MAPKs for drug development. —MAF

Science, add7859, this issue p. 1217

IMMUNOLOGY

Fighting allergies with fluoxetine

Mast cells drive allergic inflammation and chronic airway inflammatory responses. Haque *et al*. found that fluoxetine, a selective serotonin reuptake inhibitor that is clinically approved to treat depression, could be repurposed as a therapy for allergic inflammation. Fluoxetine inhibited the activation of mast cells and consequently suppressed degranulation and cytokine secretion. In a mouse model of house dust mite–induced allergic inflammation, fluoxetine improved lung function and reduced inflammation. —AEB

Sci. Signal. (2021) 10.1126/scisignal.abc9089

NEUROMORPHIC CHIPS

Implementing fully on-chip learning

Memristor-based computing technology has recently received considerable attention because of its potential to overcome the so-called "von Neumann bottleneck" of conventional computing architecture. In particular, memristor technology could realize time- and energy-efficient on-chip learning for various edge intelligence applications, although fully on-chip learning implementation remains challenging. To address this problem, Zhang *et al*. proposed a memristor-featured sign- and threshold-based learning (STELLAR) architecture. They fabricated a full-system-integrated chip consisting of multiple memristor arrays and all of the necessary complementary metal-oxide semiconductor peripheral circuits to support complete on-chip learning. The authors further demonstrated end-to-end on-chip improvement learning across various tasks, including motion control, image classification, and speech recognition, achieving software-comparable accuracy and low hardware cost. The present work is an important step in the field of computation-in-memory. —YS

Science, ade3483, this issue p. 1205

MALARIA

A window into cerebral malaria

In cerebral malaria, adhesion of infected erythrocytes to brain vascular endothelium is associated with brain swelling that can be fatal. It is unclear whether this brain swelling is caused by cerebral edema or venous congestion. Using near infrared spectroscopy to measure brain hemoglobin concentrations in Malawian children with cerebral malaria compared with uncomplicated malaria, Smith *et al.* report that hemoglobin concentrations were elevated in children with cerebral malaria and correlated with brain-swelling score determined by magnetic resonance imaging. This finding suggested that excess blood volume, potentially due to vascular congestion, may contribute to brain swelling in cerebral malaria. —OMS

Sci. Transl. Med. (2023) 10.1126/scitranslmed.adh4293

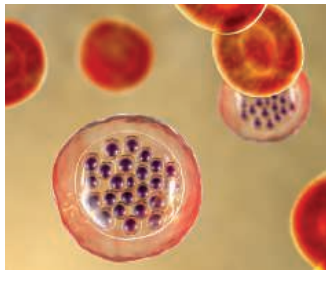

Illustration of malaria-infected red blood cells

CREDITS: (ILLUSTRATION) DR_MICROBE/ISTOCK.COM; (PHOTO) THE NATURAL HISTORY MUSEUM, LONDON/SCIENCE SOURCE

IN OTHER JOURNALS

Edited by **Caroline Ash** *and* **Jesse Smith**

Genetic material from bees, such as this honey bee preserved in copal, illuminate the evolution of this taxon.

PHYLOGENETICS

Phylogenetic trees reveal bee history

Bees serve critical functions in ecosystems by pollinating flowering plants. This means that their origin and movements through time are also intrinsically linked to the plants that rely on them for pollination. Almeida *et al.* coupled genetic sampling of 216 extant bee species with 185 bee fossils to reconstruct their evolutionary history. These data indicated that bees arose during the Early Cretaceous period in Western Gondwana (the continent that would become South America and Africa), and that they may have arrived quite recently into certain regions, including continental India. These results not only affect our understanding of bee evolution, but they also have repercussions for their angiosperm coevolutionary partners. —CNS

Curr. Biol. (2023) 10.1016/j.cub.2023.07.005

MATERIALS SCIENCE

Hydrogel fabrication in seconds

Hydrophilic polymers with a high water content, also known as hydrogels, have attracted attention because of their applicability as biocompatible materials. Bao *et al.* report a fast hydrogel fabrication method using simultaneous photo-cross-linking and interfacial bonding, which results in nanocomposite hydrogels with exceptional toughness and tensile strength that also maintain good structural stability. This speedy method is potentially suitable for hydrogel preparation using three-dimensional printing technologies and could be used for biomimetic applications. —ECF

Nat. Mater. (2023) 10.1038/s41563-023-01648-4

ALSO IN *SCIENCE* JOURNALS

Edited by **Michael Funk**

HYPOTHESIS

Do microglia engulf synapses?

Microglia, the brain's resident immune cells, can contain synaptic proteins, and some of the molecular mechanisms that promote their phagocytic activity also promote synapse loss. These are the key observations that have led to the widespread view that microglial cells engulf and remove synapses, a process referred to as "pruning." In a Perspective, Eyo and Molofsky describe several different scenarios, each of which could explain the observations made so far. They propose new terminology and call for a deeper investigation of the complex interactions between microglia and synapses. —SAL

Science, adh7906, this issue p. 1155

INFLAMMATORY DISEASE

Immune cells maintain human colon health

Inflammatory bowel disease (IBD) refers to two conditions, Crohn's disease and ulcerative colitis. Individuals with IBD have chronic intestinal inflammation in which the intestinal epithelial barrier is disrupted. Dart *et al*. examined human colon biopsy samples and identified intestinal immune cells called Vγ4 γδ T lymphocytes (see the Perspective by Galipeau and Verdu). In healthy individuals, this γδ T cell subset is kept in check by intestinal epithelial cells displaying the butyrophilin-like (BTNL) proteins BTNL3 and BTNL8. By contrast, analysis of biopsies from Crohn's disease patients revealed a polymorphism encoding a defective BTNL3:BTNL8 fusion protein, and this genetic mutation was correlated with IBD severity. These findings increase our understanding of barrier immunology and may provide new perspectives for IBD management. —PNK

Science, adh0301, this issue p. 1169; see also adj9724, p. 1153

NEURODEGENERATION

How do neurons die in Alzheimer's disease?

Neurons are one of the longest-living and enduring cell types of the human body. Balusu *et al*. xenografted human neurons into mouse brains containing amyloid plaques (see the Perspective by Sirkis and Yokoyama). The human neurons, but not the mouse neurons, displayed severe Alzheimer's pathology, including tangles and necroptosis. Human neurons up-regulated the neuron-specific maternally expressed gene 3 (MEG3) in response to amyloid plaques. Down-regulation of MEG3 protected the neurons from dying in the xenograft model of Alzheimer's disease. Downstream of MEG3, genetic or pharmacological manipulation of signaling kinases in the necroptosis pathway also protected neurons, suggesting a potential lead toward therapeutic approaches for Alzheimer's disease. —SMH

Science, abp9556, this issue p. 1176; see also adk2009, p. 1156

MICROROBOTICS

A frequent burst of power

A key challenge for microrobotic systems is the efficient delivery of power and the conversion of that power into mechanical forces and displacements. Aubin *et al*. developed a lightweight actuator that can be driven at high frequencies by the combustion of chemical fuels (see the Perspective by Truby). Key to achieving this fast performance is the passive quenching of the combustion, which eliminates the need for valves. Using this actuator, the authors fabricated an insect-scale quadruped robot that is capable of walking, turning (directional control), and jumping, a combination of locomotion capabilities that is unusual in a microrobot. —MSL

Science, adg5067, this issue p. 1212; see also adk0522, p. 1152

CANCER IMMUNOLOGY

Antitumor T cells in head and neck cancer

Immune checkpoint blockade (ICB), for example, targeting anti–programmed cell death protein 1 (anti–PD-1), reinvigorates tumor-specific T cell responses, but the mechanisms underlying specific clinical responses remain unclear. Using single-cell transcriptomics and T cell receptor sequencing, Oliveira *et al*. analyzed tumor specimens from patients with head and neck cancer enrolled in a phase 2 clinical trial testing two doses of neoadjuvant anti–PD-1 before surgical resection. Tumors responding to anti–PD-1 contained a baseline population of T cells expressing the transcription factor *ZNF683*, as well as genes associated with T cell exhaustion, tissue resident memory, and cytotoxicity. In paired pre- and posttreatment biopsies, *ZNF683*$^+$CD8$^+$ T cells were clonally expanded and exhibited the strongest change in patients responding to ICB. Reinvigoration of cytotoxicity among *ZNF683*$^+$CD8$^+$ T cells is a likely mechanism underlying response to neoadjuvant anti–PD-1 in head and neck cancers. —CO

Sci. Immunol. (2023) 10.1126/scimmunol.adf4968

AUDITORY PROCESSING

Who's a cute puppy?

Humans often talk to their dogs in a voice similar to the one they use with infants: high pitched and rich with prosody. Many studies have shown that infants respond better to these types of voices, in particular, those of women. Gergely *et al.* trained dogs to sit still within a functional MRI machine and played them various voices to determine whether they too prefer prosodic female voices. Upon hearing speech that was dog and infant directed (and thus prosodic), the dogs displayed increased brain activity in a region involved in auditory processing, especially when the speaker was female. Such preferences could not be due to intrauterine exposure to females, as has been suggested for infants, and points to alternative hypotheses for its cause, such as domestication or ontogenetic learning. —SNV

Commun. Biol. (2023) 10.1038/s42003-023-05217-y

TROPHIC CASCADES

Eating herbivores, protecting plants

Predators can benefit plants by reducing the abundance of herbivores. Sam *et al.* conducted exclusion experiments across an elevation gradient in a Papua New Guinea rainforest to determine how well ants and flying vertebrates (birds and bats) control herbivory and how these effects vary with environmental conditions. Ants reduced herbivorous arthropod density only slightly, but not at high elevations, where fewer trees hosted ants. Vertebrates consistently decreased arthropod density and herbivory damage, partly by removing the largest arthropods. These findings indicate that the loss of bats or birds from this system could have significant impacts on vegetation. —BEL

J. Biogeogr. (2023) 10.1111/jbi.14686

MEMORY

A theory of memory consolidation

Some memories go through a consolidation process (i.e., are transferred from the hippocampus to the neocortex), whereas others remain strictly hippocampus dependent. To begin to find out how the brain discriminates between different types of memories, Sun *et al.* postulated that consolidation occurs only when it can be used to make predictions based on previous experience. Therefore, memories not useful for making predictions, for example, the color of your friend's shoes, will not be stored in the neocortex and will be stashed in the hippocampus for retrieval. What remains is to test this computational theory in vivo. —MMa

Nat. Neurosci. (2023) 10.1038/s41593-023-01382-9

STEM WORKFORCE

Being a scientist in a second language

As we work to diversify the STEM workforce, it is important to consider that most of the world's population are not native English speakers. Amano *et al.* quantified the barriers that non-native English-speaking scientists face by surveying 908 non-US researchers. Their results showed that non-native English speakers spent more time reading and writing manuscripts and preparing presentations in English. Additionally, language barriers led these scientists to avoid attending and presenting at conferences conducted in English, which had downstream effects of missed networking opportunities. The stress associated with additional time and costs, in addition to lost opportunities, was not directly measured but is implied in the results. Overcoming these barriers has mostly been left to non-native English speakers improving their English. –MMc

PLOS Biol. (2023) 10.1371/journal.pbio.3002184

ARTIFICIAL MEMBRANES

Mechanoresponsive polymer membranes

A polymer membrane that mimics mechanosensory channels transmits chloride ions (Cl^-) in response to pressure-induced deformation. Li *et al.* found that a poly(1,4-isoprene)-*b*-poly(4-vinylpyridine) (PI-*b*-P4VP) film formed cylindrical channels of P4VP that could transmit Cl^-. These channels were surrounded by a PI matrix that was stiffened by cross-linking with sulfur atoms and could transfer mechanical force. The membrane did not conduct Cl^- until it was deformed by applied pressure. A bias pressure of 200 millibar applied to the solution on one side of the membrane resulted in a 5-microampere Cl^- conductance current. —PDS

J. Am. Chem. Soc. (2023) 10.1021/jacs.3c07675

RESEARCH ARTICLE SUMMARY

INFLAMMATORY DISEASE

Conserved γδ T cell selection by BTNL proteins limits progression of human inflammatory bowel disease

Robin J. Dart*†, Iva Zlatareva†, Pierre Vantourout, Efstathios Theodoridis, Ariella Amar, Shichina Kannambath, Philip East, Timothy Recaldin, John C. Mansfield, Christopher A. Lamb, Miles Parkes, Peter M. Irving, Natalie J. Prescott, Adrian C. Hayday*

INTRODUCTION: Together with B cells and αβ T cells, γδ T lymphocytes comprise a third component of adaptive immunity conserved across vertebrates. In the mouse, a signature γδ phenotype is the cells' enrichment within barrier tissues such as the epidermis and the intestinal epithelium. Therein, the local γδ T cells expressing tissue-specific Vγ chains are selected by engaging organ-specific butyrophilin-like (BTNL) molecules present on the surface of healthy epithelial cells. Such γδ lymphocytes can contribute to the maintenance of tissue homeostasis and to its restoration after injury. Thus, any conservation of this biology in humans could have profound implications for basic tissue biology and for inflammatory pathologies at barrier sites, such as inflammatory bowel disease (IBD), which comprises the relapsing and remitting conditions Crohn's disease (CD) and ulcerative colitis (UC). In humans, $V\gamma4^+$ cells that engage heteromers of BTNL3 and BTNL8 have been identified. However, the degree to which the human intestinal γδ T cell compartment mirrors that of the mouse and the potential implications for IBD are unresolved. IBD is of increasing global prevalence, and despite treatment advances, there remain many unmet needs. Although anti-inflammatory agents may ameliorate symptoms and inflammation in some cases, they have little capacity for curative epithelial repair, added to which the field lacks reliable prognostic biomarkers of disease progression.

RATIONALE: Using mucosal samples obtained at colonoscopy from more than 150 individuals, we characterized the healthy human gut γδ T cell population. We then investigated how this compartment changes in patients with IBD and in people who carry a germline [illegible]tation in BTNL3 and BTNL8. Finally, we [illegible]plored whether the status of the colonic γδ T cell compartment might be associated with remission in IBD patients on treatment.

RESULTS: We established that the human colon harbors a complex γδ T cell repertoire, within which a subcompartment comprises $V\gamma4^+$ cells coexpressing the integrin CD103, which can engage E-cadherin on epithelial cells. The $CD103^+V\gamma4^+$ cells have a distinct phenotype, combining T cell and natural killer cell ligand recognition systems, but they are also noticeably recalcitrant to conventional effector activation. By contrast, these cells respond strongly to BTNL3 and BTNL8 heteromers, and although they do not dominate the γδ T cell compartment to the degree observed for counterpart murine BTNL-reactive cells, they are BTNL selected. This was illustrated by our demonstration of the cells' loss and dysregulation in persons homozygous for a BTNL3 and BTNL8 copy number variant (CNV) allele that we showed to be severely hypomorphic. Using a case-control genetic screen, we also showed that the CNV allele is a risk modifier, predisposing CD patients to a severe, penetrating pathology. Consistent with this, the distinct $CD103^+V\gamma4^+$ T cell subset is vulnerable to the impacts of IBD-associated cytokines, and $V\gamma4^+$ T cells are disproportionately depleted and dysregulated in inflamed CD and UC. Conversely, restoration of the compartment in areas of healing was associated with on-treatment remission over a sustained period.

CONCLUSION: BTNL-mediated selection is an evolutionarily conserved biology driving the emergence of intestinal γδ T cells with a distinct phenotype. The frequent depletion and dysregulation of those BTNL-selected cells in UC and CD, and the association of BTNL hypomorphism with the CD disease phenotype, points to the cells' evolutionarily conserved roles in regulating and/or restoring tissue integrity. Thus, for a disease of increasing global incidence that is primarily treated with anti-inflammatories but remains uncurable through medical therapy, IBD may benefit from clinical modalities that restore local γδ T cell activity, thereby promoting tissue surveillance and repair. Moreover, monitoring local γδ T cell status may add a much-needed prognostic biomarker of a patient's likelihood of disease remission versus relapse. ■

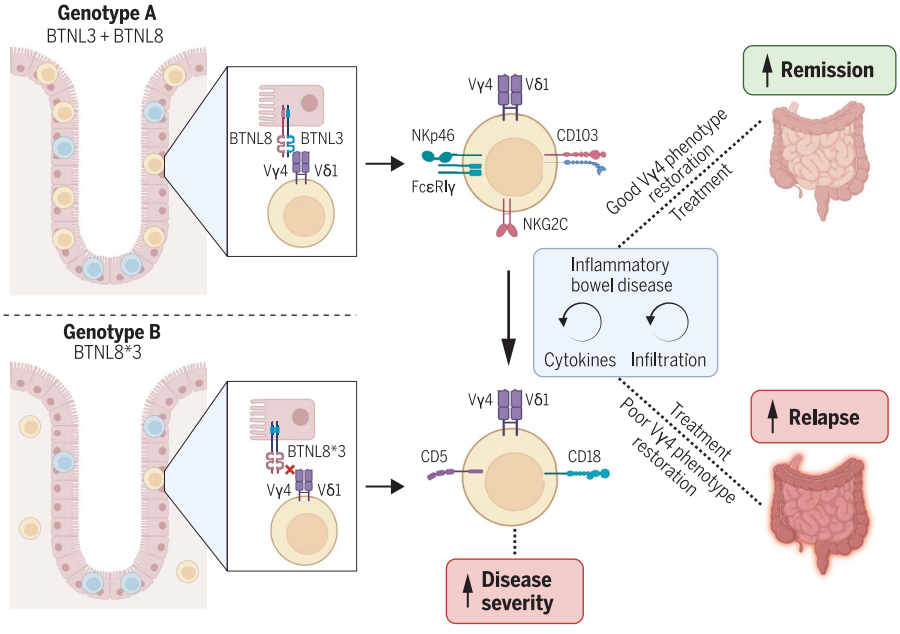

Systematic analysis of human colonic γδ T cells. Persons with genotype A (the more common genotype) harbor T cell receptor Vγ4-expressing colonic T cells that engage epithelial BTNL3+BTNL8 heteromers and display a distinct phenotype, coexpressing CD103, FcεRIγ, and natural killer (NK) receptors. That phenotype is disrupted in IBD, but its restoration on treatment is associated with sustained remission. Persons with genotype B are hypomorphic for BTNL3+8, harbor few $V\gamma4^+$ cells with the typical phenotype, and if they develop Crohn's disease they are predisposed to a severe disease phenotype. [Figure was created with BioRender.]

The list of author affiliations is available in the full article online.
*Corresponding author. Email: robin.dart@kcl.ac.uk (R.J.D.); adrian.hayday@crick.ac.uk (A.C.H.)
†These authors contributed equally to this work.
Cite this article as R. J. Dart *et al.*, *Science* **381**, eadh0301 (2023). DOI: 10.1126/science.adh0301

READ THE FULL ARTICLE AT
https://doi.org/10.1126/science.adh0301

RESEARCH ARTICLE

INFLAMMATORY DISEASE

Conserved γδ T cell selection by BTNL proteins limits progression of human inflammatory bowel disease

Robin J. Dart[1,2,3]*†, Iva Zlatareva[1,2]†, Pierre Vantourout[1,2], Efstathios Theodoridis[1,2], Ariella Amar[4], Shichina Kannambath[5], Philip East[6], Timothy Recaldin[7], John C. Mansfield[8,9], Christopher A. Lamb[8,9], Miles Parkes[10], Peter M. Irving[3], Natalie J. Prescott[4], Adrian C. Hayday[1,2]*

Murine intraepithelial γδ T cells include distinct tissue-protective cells selected by epithelial butyrophilin-like (BTNL) heteromers. To determine whether this biology is conserved in humans, we characterized the colonic γδ T cell compartment, identifying a diverse repertoire that includes a phenotypically distinct subset coexpressing T cell receptor Vγ4 and the epithelium-binding integrin CD103. This subset was disproportionately diminished and dysregulated in inflammatory bowel disease, whereas on-treatment CD103$^+$γδ T cell restoration was associated with sustained inflammatory bowel disease remission. Moreover, CD103$^+$Vγ4$^+$ cell dysregulation and loss were also displayed by humans with germline BTNL3/BTNL8 hypomorphism, which we identified as a risk factor for penetrating Crohn's disease (CD). Thus, BTNL-dependent selection and/or maintenance of distinct tissue-intrinsic γδ T cells appears to be an evolutionarily conserved axis limiting the progression of a complex, multifactorial, tissue-damaging disease of increasing global incidence.

Central and peripheral repertoire selection shapes adaptive T cell immunity, purging repertoires of autoreactive T cells while enriching for those suited to recognizing diverse pathogens. Thus, polymorphisms in major histocompatibility complex proteins that present antigen to T cells can perturb repertoire selection and show causal associations with autoimmune and auto-inflammatory diseases (*1*). However, many T cells, particularly γδ T cells, are not major histocompatibility complex restricted (*2*). In mice, for example, intraepithelial γδ T cell compartments of limited T cell receptor (TCR) diversity are selected for and/or maintained by TCR-dependent interactions with organ-specific butyrophilin-like (BTNL) proteins expressed by epithelial cells (*3*–*5*). The consequent γδ T cell repertoires appear to play major roles in maintaining and restoring tissue homeostasis, with γδ T cell–deficient mice showing increased susceptibility to hapten-elicited atopic dermatitis and to chemically induced colitis (*6*–*10*). Moreover, a recently reported anti-inflammatory role for mouse intestinal γδ T cells was manifest in their protection of Paneth cells dysregulated by an inflammatory bowel disease (IBD)–associated polymorphism in *ATG16L1* (*11*). Therefore, there are potentially profound implications of the identification in humans of colonic, TCRγδ$^+$ intraepithelial lymphocytes (IELs), a subset of which expresses Vγ4 chains that can directly bind heteromers of BTNL3+BTNL8 displayed by colonic epithelium (*12*, *13*). Nonetheless, to our knowledge, there is to date no evidence that BTNL3+BTNL8 acts as a selection or maintenance factor for human intestinal IELs in a manner akin to murine IEL selection, no clarity as to how BTNL-selected cells might differ from other gut T cells, and no resolution of whether they are even the major gut γδ T cell subset. Likewise, despite reports that BTNL3 and BTNL8 expression can be substantially reduced in IBD tissue samples as well as in celiac disease (*14*, *15*), no evidence exists linking the BTNL3+BTNL8–Vγ4 T cell axis to the regulation of IBD and/or its treatment.

[1]Peter Gorer Department of Immunobiology, King's College London at Guy's Hospital Campus, London, UK. [2]Immunosurveillance Laboratory, The Francis Crick Institute, London, UK. [3]Department of Gastroenterology, Guy's and St Thomas' Foundation Trust, London, UK. [4]Department of Medical and Molecular Genetics, King's College London, London, UK. [5]National Institute for Health and Care Research (NIHR) Biomedical Research Centre (BRC) Genomics Centre, King's College London, London, UK. [6]Bioinformatics and Biostatistics, The Francis Crick Institute, London, UK. [7]GammaDelta Therapeutics Ltd., London, UK. [8]Translational & Clinical Research Institute, Newcastle University, Newcastle upon Tyne, UK. [9]Department of Gastroenterology, Newcastle upon Tyne Hospitals National Health Service (NHS) Foundation Trust, Royal Victoria Infirmary, Newcastle upon Tyne, UK. [10]Department of Medicine, Addenbrooke's Hospital, University of Cambridge, Cambridge, UK.
*Corresponding author. Email: robin.dart@kcl.ac.uk (R.J.D.); adrian.hayday@crick.ac.uk (A.C.H.)
†These authors contributed equally to this work.

Results

Human gut γδ T cells are diverse and have distinct phenotypes

We first sought to elucidate the composition of the human colonic γδ T cell compartment so that we could more fully understand the nature of dysregulation in IBD. We established a clinical workflow permitting the analysis of intraepithelial γδ T cells from colonic endoscopic biopsies from 173 adults. Most of the immunological data were obtained from a core cohort of non-IBD controls ("Ctrl") (n = 34), uninflamed gut from patients with confirmed IBD ("IBD") (n = 42), inflamed lesions from patients with IBD ("IBDI") (n = 27), and seven individuals from whom paired inflamed and uninflamed tissue was obtained at the time of endoscopy. Additional donors provided data for a smaller number of experiments, as identified by table S1 that provides comprehensive donor information and links individual donors to each data-set presented.

First, our samples confirmed that the colon is enriched in Vδ1$^+$ cells relative to the Vδ2$^+$ cells that dominate the peripheral blood (*2*), as depicted by an illustrative flow cytometry analysis (fig. S1A). This was confirmed by deep sequencing of productively rearranged TCR VDJ gene segment transcripts, among which *TRDV1* (encoding Vδ1) accounted for 60 to 80% of reads (fig. S1B). On flow cytometry, most gut Vδ2^{neg} cells reacted to an antibody detecting Vγ2, Vγ3, or Vγ4 chains, and most were usually Vδ1$^+$ (fig. S1C). Therefore, colonic Vδ2^{neg} γδ T cells that are examined in several experiments below de facto comprise primarily Vγ2/3/4$^+$Vδ1$^+$ T cells.

Given that BTNL-selected Vγ7 cells dominate the murine gut γδ IEL compartment (*3*), the reactivity of gut T cells to anti-Vγ2/3/4 might have reflected a dominance of cells expressing TCRVγ4 that mediates responsiveness to BTNL3+BTNL8 (*13*). However, deep sequencing revealed that *TRGV4* reads often accounted for only ~20 to 35% of reads, with comparable representation of productively rearranged *TRGV2* and *TRGV5* gene segments (Fig. 1A). Moreover, high donor-to-donor variation existed for the frequencies of *TRGV4* and *TRGV2* gene rearrangements, which were inversely correlated, as reflected by paired samples (fig. S1D). There was also somewhat variable representation of *TRGV9*, the product of which (Vγ9) often, albeit not exclusively, pairs with Vδ2. However, unlike *TRGV2*, the expression levels of this and other *TRGV* genes did not correlate inversely with *TRGV4*. In sum, whereas the dominant gut γδ T cell type expressed Vδ1, transcripts encoding BTNL-reactive Vγ4 were usually not the most highly expressed of the Vγ chain mRNAs.

We next found that Vγ2$^+$, Vγ3$^+$, and Vγ4$^+$ cells that collectively accounted for >75% of the gut Vδ2^{neg} γδ T cell compartment [median 85.10%; 95% confidence interval (CI) 62.5 to 90.9; n = 14] (fig. S1C) could be segregated according to whether they expressed integrin αEβ7 (CD103), which was true for most cells (median 89.5%; 95% CI 83.5 to 93.8; n = 43) (Fig. 1B), or did not express it. CD103 is typically associated with IEL and tissue-resident memory (T_{RM}) CD8$^+$ αβ T cells (*16*), with its ligand, E-cadherin, expressed by differentiated epithelial cells (*17*). To assess the potential significance of CD103 expression by Vγ2/3/4 lymphocytes, we compared transcriptomes of paired CD103$^+$ and CD103^{neg}Vγ2/3/4$^+$ T cell preparations from four control donors (Fig. 1C and

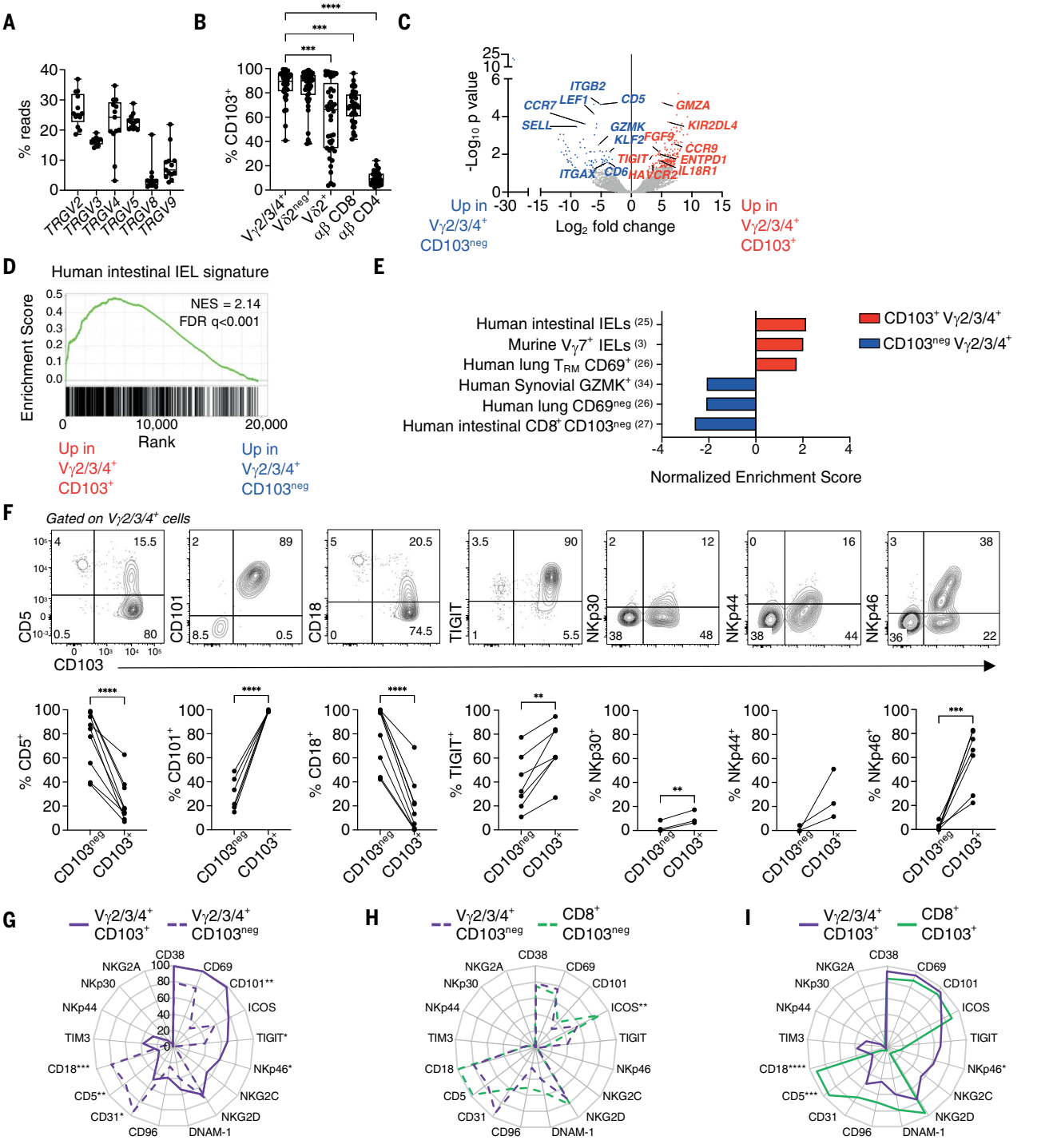

Fig. 1. Human gut γδ T cells are diverse and predominantly intraepithelial cells with distinct phenotypes. (**A**) *TRGV* gene usage in control colonic biopsies measured by mRNA TCR deep sequencing (n = 13). (**B**) Flow cytometric analysis of CD103 expression on the indicated colonic γδ and αβ T cell subsets from control donors (n = 38 to 43). Median, interquartile ratio (IQR), and min-max range shown. Symbols represent individual participants. ***P < 0.001 and ****P < 0.0001, Kruskal-Wallis test with Dunn's correction against Vγ2/3/4$^+$ cells. (**C**) Volcano plot of differentially expressed genes between CD103$^+$ and CD103^{neg} colonic Vγ2/3/4$^+$ bulk-sorted cells from control donors (n = 4 for C36, C37, C39, and C88). Red indicates significantly up-regulated in CD103$^+$; blue indicates significantly up-regulated in CD103^{neg}; gray indicates nonsignificant. Data were corrected for multiple comparisons (FDR < 0.05). (**D**) GSEA of the human colonic CD103$^+$Vγ2/3/4$^+$ signature from (C) in a published human natural IEL signature dataset (25). NES, normalized enrichment score. (**E**). Summary graph of GSEA for CD103$^+$Vγ2/3/4$^+$ (red) and CD103^{neg}Vγ2/3/4$^+$ (blue) gene signatures in published datasets (FDR q < 0.001). (**F**) Flow cytometric analysis of the expression of the indicated markers (y axis) on CD103$^+$ and CD103^{neg} colonic Vγ2/3/4$^+$ cells from control donors. Representative flow plots (top) and summary data (bottom) are shown (n = 3 to 9). Connected symbols represent individual participants. **P < 0.01, ***P < 0.001, and ****P < 0.0001, paired t tests. (**G** to **I**) Radar plot of the cell surface phenotype of Vγ2/3/4$^+$CD103$^+$ versus Vγ2/3/4$^+$CD103^{neg} T cells (G); Vγ2/3/4$^+$CD103^{neg} versus CD8$^+$CD103^{neg} αβ T cells (H); and Vγ2/3/4$^+$CD103$^+$ versus CD8$^+$CD103$^+$ αβ T cells (I) (n = 3 to 9 individuals per group). Plotted values represent the mean of included participants. *P < 0.05, **P < 0.01, ***P < 0.001, and ****P < 0.0001, multiple paired t tests with Bonferroni-Dunn's correction.

table S2). Among the most differentially and statistically significantly overexpressed genes in CD103$^+$Vγ2/3/4$^+$ cells across all donors included those encoding *TIGIT*, a negative regulator that is up-regulated by BTNL-mediated selection of mouse TCR$\gamma\delta^+$ IELs (*3*); *KIR2DL4*, an activating natural killer (NK) cell receptor (*18*); *CCR9*, which is associated with homing to gut epithelium (*19*); *GZMA*, which is associated with cytolytic potential (*20*); *IL18R*, which encodes a receptor for which the ligand [interleukin 18 (IL18)] promotes interferon γ (IFNγ) production (*21*); *ENTPD1* (CD39), which suppresses inflammation by hydrolyzing ATP (*22*); and *HAVCR2* (TIM3), which is associated with chronic TCR cell stimulation (*23*) (Fig. 1C). Additionally, at low expression levels, CD103$^+$ γδ cells differentially expressed *FGF9*, a wound-healing factor produced by murine dermal γδ T cells (*24*). These specific genes combined with others to establish significant overall similarities of CD103$^+$Vγ2/3/4$^+$ cells to human intestinal intraepithelial T cells (*25*) (Fig. 1, D and E), to mouse V$\gamma7^+$ IEL (*3*), and to human CD69$^+$CD8$^+$ lung T_{RM} cells (*26*) (which are primarily intraepithelial) (Fig. 1E), as assessed from publicly available datasets. Conversely, overlap was less with total intestinal TCR$\alpha\beta^+$CD8$^+$CD103$^+$ T_{RM} cells (*27*) (fig. S1E), a finding considered further below.

By contrast, CD103^{neg}Vγ2/3/4$^+$ T cells overexpressed genes commonly associated with circulating T cells (Fig. 1C and table S2), specifically *SELL* (CD62L) and *CCR7 (28)*; integrins *ITGB2* (CD18) and *ITGAX1* (CD11c), which mediate heterotypic cell-cell interactions (*29*); *CD5* and *CD6*, which encode proteins associated with cell signaling thresholds (*30*, *31*); *KLF2* and *LEF1*, which are commonly coexpressed in naïve, memory, and/or quiescent CD8$^+$ T cells (*32*), with *LEF1* implicated in suppressing IL17 production by mouse γδ T cells (*33*); and *GZMK*, which is associated with tissue-infiltrating human CD8$^+$αβ T cells of reduced cytolytic but high cytokine-producing potential (*34*) (Fig. 1C). Indeed, there was an overall significant similarity to tissue-infiltrating human synovial CD8$^+$αβ T cells (*34*), to human lung T cells lacking CD69 (*26*), and to human intestinal CD103^{neg}CD8$^+$ T cells (*27*) (Fig. 1E).

In validating transcriptomic differences by flow cytometry, we noted, as expected, that neither CD103$^+$ nor CD103^{neg} cells were homogeneous, as illustrated by the expression of TIGIT and TIM3, but these were nonetheless consistently expressed to a higher degree by CD103$^+$ cells than by CD103^{neg} cells (Fig. 1F and fig. S1F). Indeed, there was a consensus CD103$^+$ cell phenotype, CD101$^+$CD18^{low} CD69$^+$ ICOS$^+$, whereas most CD103^{neg} cells were CD101^{neg}CD18$^+$CD5$^+$CD31$^+$TIM3^{neg} (Fig. 1, F and G, and fig. S1F). In sum, CD103 segregated Vγ2/3/4$^+$ T cells into qualitatively distinct subsets (Fig. 1G). Moreover, whereas CD103^{neg}Vγ2/3/4$^+$ cells closely resembled human intestinal CD103^{neg}TCRαβ$^+$CD8$^+$ cells (Fig. 1, E and H), CD103$^+$Vγ2/3/4$^+$ cells appeared distinct, being clearly distinguishable from human tissue-resident CD103$^+$TCRαβ$^+$CD8$^+$ cells, e.g., by low expression of CD5 and CD18 (Fig. 1I). In addition, CD103$^+$Vγ2/3/4$^+$ cells often expressed several NK receptors, including NKp44, NKG2C, and NKp46, which were most often not expressed by either CD103^{neg}Vγ2/3/4$^+$ cells or CD103$^+$TCRαβ$^+$CD8$^+$ cells (Fig. 1, F and I, and fig. S1F). By contrast, all subsets expressed comparably high levels of NKG2D (fig. S1F), which can mediate innate responsiveness and costimulate TCR-mediated adaptive responses (*35*).

Human gut γδ T cells show selective responsiveness

We next investigated how gut CD103$^+$cells might respond to selecting and activating stimuli. As previously described (*3*), cells stained by an anti-Vγ2/3/4 antibody showed partial yet significant TCR down-regulation (reduced geometric mean fluorescent intensity of CD3) when cocultured with human embryonic kidney 293T (HEK293T) cells transduced to express BTNL3+BTNL8 (293T.L3L8) versus empty vector–transduced HEK293T cells (293T.EV) (fig. S2A). There was considerable interindividual variation (fig. S2, A and B), but as expected, BTNL3+BTNL8 responsiveness (as assessed by TCR down-regulation) correlated with the representation of productive *TRGV4* rearrangements and correlated inversely with *TRGV2* rearrangements (fig. S2C). As evidenced by flow cytometry, TCR levels on CD103$^+$ cells were higher relative to those on CD103^{neg} cells and were disproportionately down-regulated by BTNL exposure (Fig. 2A).

CD103 staining was unaffected by BTNL3+BTNL8 engagement (Fig. 2B), whereas many cells showing TCR down-regulation up-regulated the costimulatory receptor TNFRSF9 (4-1BB) (Fig. 2C). Predictably, no response to BTNL3+BTNL8 was shown by Vδ2$^+$ or TCRαβ$^+$ T cells in the same cultures (Fig. 2C). *TNFRSF9* transcript up-regulation was also noted in an RNA-sequencing study that was conducted to better understand the impact of BTNL-mediated selection on human Vγ2/3/4$^+$Vδ2^{neg} T cells (Fig. 2D). Specifically, RNA was compared from four independent donors' colonic T cells cocultured with either 293T.L3L8 cells or 293T.EV cells (fig. S2D), revealing that in addition to *TNFRSF9*, there was up-regulation of several genes, including *XCL1*, *XCL2*, and *GZMB*, whereas *CCR6* was down-regulated (Fig. 2D). Collectively, these gene expression changes strongly phenocopy the response of murine intraepidermal V$\gamma5^+$ IELs responding to Skint1, their counterpart BTNL-selecting element (*36*). Thus, CD103$^+$V$\gamma4^+$ gut γδ T cells respond strongly and in an evolutionarily conserved fashion to BTNL3+BTNL8 engagement of their TCR, with conspicuous changes in expression of coregulatory receptors, chemokines, and other effector potentials. This notwithstanding, BTNL engagement of Vδ2^{neg} cells induced neither CD107a, a surrogate marker for induced cytolytic activity (fig. S2E), nor appreciable amounts of cytokines, e.g., tumor necrosis factor α (TNFα), IFNγ, and IL2 (fig. S2, F and G). Furthermore, gut Vδ2^{neg} cells were markedly hyporesponsive to phorbol 12-myristate 13-acetate (PMA) + ionomycin (P+I), a potent activator of signal transduction downstream of the TCR, in contrast to the overt TNFα, IFNγ, and IL2 production induced in gut TCRαβ$^+$ cells in the same cultures (fig. S2, F and G). Indeed, Vγ2/3/4$^+$ cells were the least responsive of the gut T cells upon stimulation (Fig. 2, E and F). When examined by paired analysis, CD103$^+$Vγ2/3/4$^+$ cells were less responsive than CD103^{neg}Vγ2/3/4$^+$ cells (Fig. 2, G and H). By contrast, CD103 did not functionally segregate intestinal TCRαβ$^+$ cells. Finally, whereas IL17A production was observed for ~10% of gut TCRαβ$^+$CD4$^+$ cells, it was only rarely displayed by Vγ2/3/4$^+$ cells (Fig. 2I). In short, the γδ compartment of healthy human gut includes CD103$^+$ V$\gamma4^+$Vδ1$^+$ cells that respond strongly to TCR-mediated selection signals provided by BTNL3+BTNL8 but are recalcitrant to potent activating stimuli, specifically P+I.

Gut V$\gamma4^+$ cells are distinct

Focusing now on CD103$^+$V$\gamma4^+$ T cells, we sought to elucidate the potential impact of BTNL3+BTNL8 on the signature phenotypes of human gut TCR$\gamma\delta^+$ T cells. To facilitate this, we used phage display to obtain Vγ4-specific antibodies (see the materials and methods), initially screening for reactivity to recombinant Vγ4 but not to recombinant Vγ2 (the V region most similar to Vγ4). To identify Vγ4-specific antibodies unaffected by Vδ chain usage and to epitope map them, we screened for reactivity against human JRT3 cells transduced with various wild-type, mutated, and chimeric TCRs and on the basis of this, chose to use two antibodies, G4_18 and G4_9 (fig. S3A).

In control samples of colonic Vδ2^{neg} T cells, the mean frequency staining for V$\gamma4^+$ cells was 47.7% (Fig. 3A), although as was observed for *TRGV4* transcript reads (Fig. 1A), there was high interindividual variation, with V$\gamma4^+$ lymphocytes often failing to compose the majority of γδ cells. The fact that the median value for V$\gamma4^+$ cells of 48.3% [95% CI 29.8 to 60.1; n = 23] exceeds the median *TRGV4* reads (24.26%; 95% CI 18.8 to 30; n = 13) most likely reflects the respective denominators, i.e., Vδ2^{neg} T cells versus whole-gut biopsies used for the transcript reads and greater purity of the flow cytometry samples. Investigating further, it was found that the CD103$^+$Vδ2^{neg} cell subset was relatively enriched in V$\gamma4^+$ cells (Fig. 3A); consistent with this, a greater majority of V$\gamma4^+$ cells were CD103$^+$ compared with V$\gamma2/3^+$, V$\gamma5/8/9^+$, and Vδ2$^+$ cells (Fig. 3B), strongly suggesting a

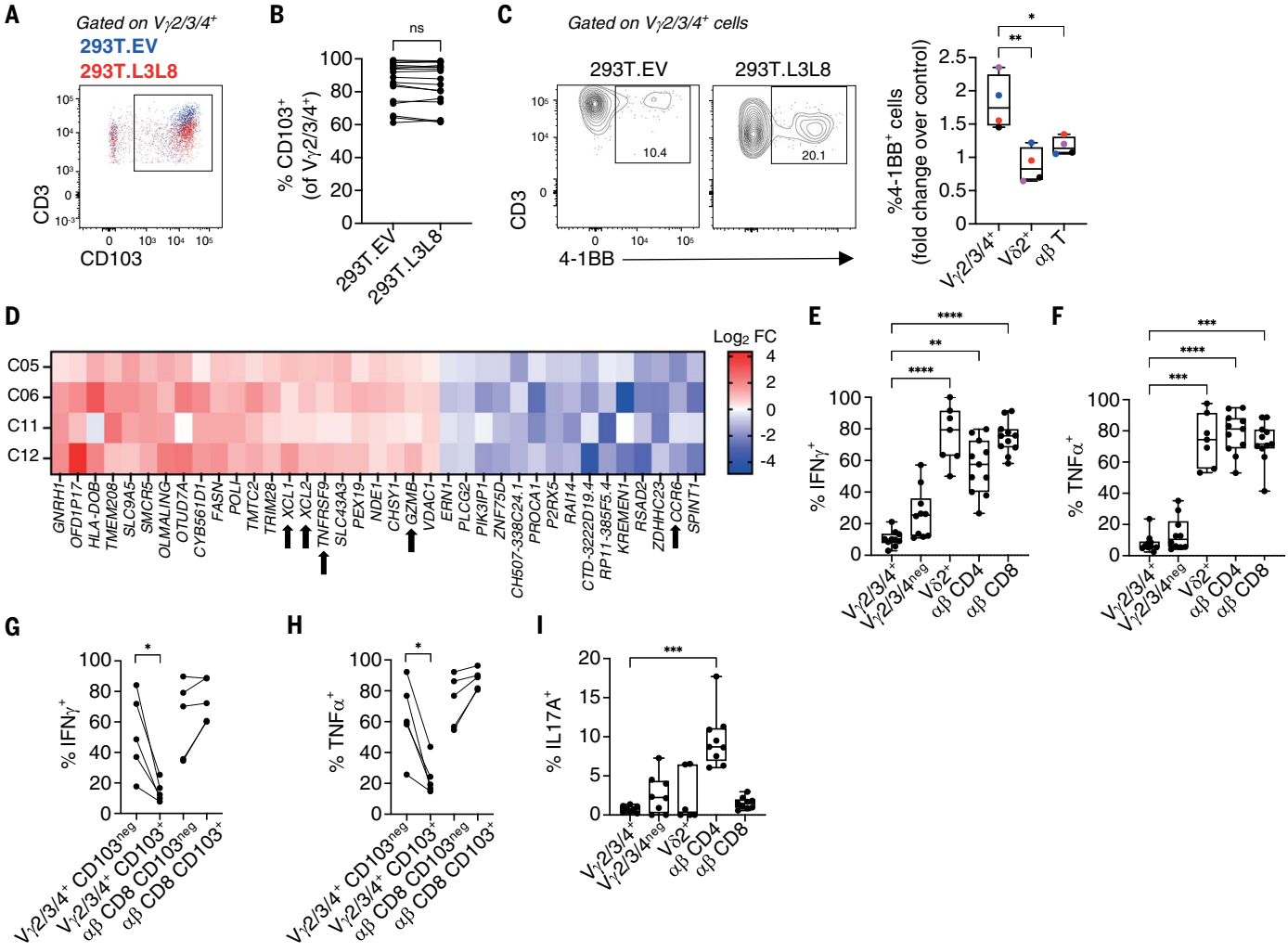

Fig. 2. Vγ2/3/4$^+$ cells make functional responses to BTNL3+BTNL8 stimulation but do not make classical effector cytokine responses. (**A**) Example flow plot of CD3 expression on colonic CD103^{neg} and CD103$^+$ Vγ2/3/4$^+$ cells after overnight coculture with 293T.EV cells (blue) or 293T.L3L8 cells (red). (**B**) Flow cytometric analysis of CD103 expression on intestinal Vγ2/3/4$^+$ cells from control donors after coculture as in (A) (n = 18). Connected symbols represent individual participants. ns, not significant by paired t test. (**C**) Flow cytometric analysis of 4-1BB expression on indicated colonic cell subsets (x axis) after coculture as in (A). Example flow plots (left) and summary graph (right) are shown (n = 4), Median, IQR, and min-max range are shown. Colored symbols represent matched frequencies from individual participants. *P < 0.05 and **P < 0.01, repeated-measures one-way ANOVA with Dunnett's correction against Vγ2/3/4$^+$ cells. (**D**) Significantly differentially expressed genes (x axis) in colonic Vγ2/3/4$^+$ cells from control donors cocultured as in (A). Data are expressed as the $\log_2$ fold change (FC) for each donor (y axis). (**E** and **F**) Flow cytometric analysis of IFNγ (E) and TNFα (F) expression by the indicated colonic cell types (x axis) from control donors (n = 7 to 11) after 4 hours of P+I stimulation. Median, IQR, and min-max range are shown. Symbols represent individual participants. **P < 0.01, ***P < 0.001, and ****P < 0.0001, Kruskal-Wallis test with Dunn's correction against Vγ2/3/4$^+$ cells. (**G** and **H**) Flow cytometric analysis of TNFα (G) and IFNγ (H) production by Vγ2/3/4$^+$ γδ and CD8$^+$ αβ T cells (x axis) (n = 5) and split by their CD103 expression (legend) after 4 hours of P+I stimulation. Connected symbols represent individual participants. *P < 0.05, multiple paired t tests with Bonferroni-Dunn's correction. (**I**) Flow cytometric analysis of IL17A expression as in (E) and (F) (n = 6 to 9). Median, IQR, and min-max range are shown. Symbols represent individual participants. ***P < 0.001, Kruskal-Wallis with Dunn's correction against Vγ2/3/4$^+$ cells.

greater propensity of Vγ4$^+$ cells to occupy intraepithelial niches.

Next, to assess whether intestinal Vγ4$^+$ T cells displayed distinct traits that might be attributable to BTNL-mediated interactions, we used an anti-Vγ4 antibody (G4_18) together with existing antibodies to purify cells for RNA sequencing from four donors. To maximize potential differences, we first compared Vγ4$^+$ with Vγ5/8/9$^+$ cells and then examined differentially expressed genes across the broader range of γδ T cells. There were very few significant differences, but attesting to the dataset's validity, *TRGV4* was the most prominently enriched RNA in Vγ4$^+$ cells, whereas *TRGV5* was significantly underrepresented (table S3). Beyond *TRGV4*, the most differentially expressed RNA was *FCER1G*, encoding FcεRIγ, a protein that can pair with and/or substitute for CD3ζ in TCR-induced signal transduction (*37*, *38*), particularly in mouse intestinal IELs (*39*), and that can transduce signals from NK receptors (see below). We noted that RNA encoding API5, which was recently implicated in protecting Paneth cells (*11*), was not significantly overexpressed in Vγ4$^+$ cells relative to other γδ T cells.

Whereas the transcriptomic analysis was undertaken on four donors, validation was sought using flow cytometry on many more independent donors. Illustrative plots presented

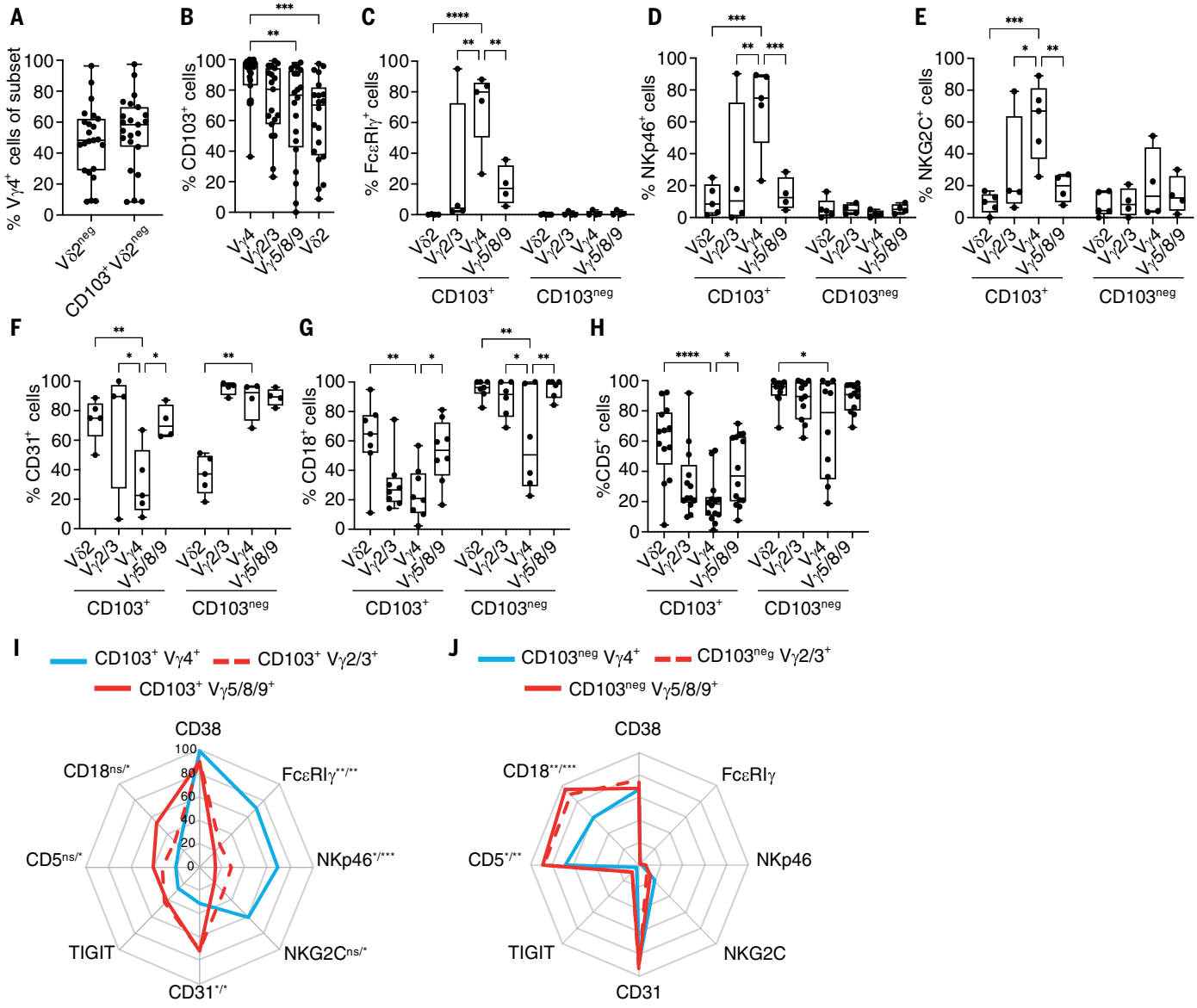

Fig. 3. Vγ4 cells are phenotypically distinct from other γδ cells. (**A**) Flow cytometric analysis of the percentage of Vγ4$^+$ cells (*y* axis) in the indicated γδ subsets (*x* axis) from control biopsies (n = 23). (**B**) Flow cytometric analysis of CD103 expression on the indicated γδ subsets (*x* axis) from control biopsies (n = 19 to 23). $^{**}P < 0.01$ and $^{****}P < 0.0001$, Kruskal-Wallis test with Dunn's correction against Vγ4$^+$ cells. (**C** to **H**) Flow cytometric analysis of the percentage of FcεRIγ$^+$ cells (n = 4 to 5) (C); the percentage of Nkp46$^+$ cells (n = 4 to 5) (D); the percentage of NKG2C$^+$ cells (n = 4 to 5) (E); the percentage of CD31$^+$ cells (n = 4 to 5) (F); the percentage of CD18$^+$ cells (n = 6 to 8) (G); and the percentage of CD5$^+$ cells (n = 10 to 14) (H) on the indicated γδ subsets (*x* axis, CD103$^+$ and CD103^{neg}) from control gut tissue. $^*P < 0.05$, $^{**}P < 0.01$, $^{***}P < 0.001$, and $^{****}P < 0.0001$, two-way ANOVA with Dunnett's correction against Vγ4$^+$ cells. For (A) to (H), median, IQR, and min-max range are shown and symbols represent individual participants. (**I** and **J**) Radar plot of the surface phenotype of CD103$^+$Vγ4$^+$ versus CD103$^+$Vγ2/3$^+$ versus CD103$^+$Vγ5/8/9$^+$ γδ T cells (I) and CD103^{neg}Vγ4$^+$ versus CD103^{neg}Vγ2/3$^+$ versus CD103^{neg}Vγ5/8/9$^+$ γδ T cells from control donors (J) (n = 4 to 14). Plotted values represent the means of included participants. $^*P < 0.05$, $^{**}P < 0.01$, $^{***}P < 0.001$, and not significant (ns), two-way ANOVA with Dunnett's correction against Vγ4$^+$ cells. Significance is displayed as versus Vγ2/3$^+$ or versus Vγ5/8/9$^+$ cells.

with graphs of multiple donor data validated that FcεRIγ was highly enriched in gut CD103$^+$ Vγ4$^+$ cells versus cells expressing any other Vγ regions, except for a single donor in which it was highly expressed by CD103$^+$Vγ2/3$^+$ Vγ4^{neg} cells (Fig. 3C and fig. S3B). There was no expression of FcεRIγ in any subset of CD103^{neg}γδ T cells (Fig. 3C), nor in any TCRVγ-subtype in peripheral blood mononuclear cells (PBMCs), including Vγ4$^+$ cells (fig. S3C). Therefore, FcεRIγ is in essence a signature phenotype of cells defined by CD103 expression, implying epithelial association by intestinal or more general extralymphoid localization and by specific usage of TCRVγ4 that distinctly facilitates BTNL3+BTNL8 responsiveness. This same pattern proved applicable to some NK receptors, e.g., NKp46 and NKG2C (Fig. 3, D and E, and fig. S3, D and E). Conversely, intestinal CD103$^+$ Vγ4$^+$ cells showed significantly lower expression of an adhesion molecule, CD31 (*PCAM1*) (Fig. 3F and fig. S3F), in contrast to the significantly higher expression of its ligand, CD38 (fig. S3G).

Likewise, whereas CD18 and CD5 were less frequently expressed by CD103$^+$ versus CD103^{neg} γδ cells (Fig. 1G), they were expressed at disproportionately low levels by CD103$^+$Vγ4$^+$ cells

(Fig. 3, G and H). Thus, by several criteria, Vγ4$^+$ CD103$^+$ gut T cells displayed a distinct phenotype compared with CD103$^+$ gut T cells expressing other Vγ chains (Fig. 3I), thereby attesting to a profound impact of interactions with BTNL3+BTNL8. At the same time, gut CD103^{neg}Vγ4$^+$cells were more similar to CD103^{neg} cells expressing other Vγ chains (Fig. 3J), which suggests that either there are modifiers of the impact of BTNL-mediated selection on Vγ4$^+$ cells or that selection of CD103^{neg}Vγ4$^+$cells was incomplete, possibly because the cells were in transit to the epithelium.

CD103$^+$Vγ4 cell loss is disproportionate in IBD

We next investigated how the gut γδ T cell compartment, and within it the distinct CD103$^+$ Vγ4$^+$ subset, might be affected in patients with IBD, by sampling inflamed (IBDI) and macroscopically uninflamed (IBD) regions. Whether sampling inflamed CD (CDI) or inflamed ulcerative colitis (UCI), γδ cell frequencies in IBDI were significantly less than in outwardly healthy gut (Fig. 4A), and this was also observed for uninflamed regions of UC (Fig. 4A). Although the representation of Vδ2$^+$ cells among colonic T cells (ordinarily the minor subset; fig S1A) was also reduced in CDI, UC, and UCI (fig. S4A), there were more overt reductions of Vδ2^{neg} cell frequencies, again being significant in UC, UCI, and CDI (Fig. 4B). Furthermore, whereas Vδ2^{neg} cells remained mostly Vδ1$^+$ (Fig. 4C), the frequencies of Vγ4$^+$ cells in IBDI were reduced in both CDI and UCI (Fig. 4D; note that red circles denote eight donors with distinct BTNL genotypes, which are discussed below). Moreover, significant disease-associated reductions in the frequency of Vγ4$^+$ cells in the CD103$^+$Vδ2^{neg} compartment were evident when paired inflamed sites were compared with uninflamed sites from the same donors (Fig. 4E). This was further corroborated by deep sequencing, which showed significant, selective reductions in *TRGV4* relative to increased *TRGV2* within the Vγ2/3/4$^+$ compartment (Fig. 4F).

In going from controls through IBD to IBDI, the overall Vγ repertoire and the Vγ2, Vγ3, and Vγ4 subrepertoires all showed increasing TCR sequence diversity as measured by Shannon entropy, reaching significance in the control versus IBDI groups even when there was no aggregate change in representation, i.e., *TRGV3* (Fig. 4G). This lack of TCR focusing strongly implied that the Vγ repertoire shifts that included the relative loss of Vγ4$^+$ cells were not driven by clonotypic antigens, unlike the clonal dynamics reported for Vδ1$^+$ cells in other settings, e.g., in the response to cytomegalovirus (*40*, *41*). This nonclonal, innate-like response of total γδ and the Vγ2, Vγ3, and Vγ4 subrepertoires was validated for IBDI by D50, an independent measure of diversity (fig. S4B).

We therefore considered that the repertoire changes might reflect cells being recruited to the gut de novo. Consistent with this, there was an increase in the proportion of Vδ2^{neg} cells that were CD103^{neg} and that coexpressed CD45RA and CD27, which jointly demarcate poorly differentiated cells. (fig. S4, C and D) (*42*). Indeed, there was more generally a significant reduction from ~90 to ~55% of Vγ2/3/4$^+$Vδ2^{neg} cells expressing CD103 in CDI and from ~90 to ~30% in UCI (Fig. 4H), albeit with interindividual variation. This was well illustrated for Vγ4$^+$Vδ2^{neg} cells by comparing paired inflamed and uninflamed regions from the same individuals sampled at the same endoscopy (fig. S4, E and F). Additionally, in a subset of donors for whom the data were available, the residual CD103$^+$Vγ2/3/4$^+$ T cells in UCI and CDI showed atypically high frequencies of CD5$^+$ cells (Fig. 4I), which in the healthy colon, is a phenotype more often associated with CD103^{neg}Vγ2/3/4$^+$ cells, as discussed above (Fig. 1F). Therefore, the main dysregulation in IBD was a shift away from the signature frequency and phenotype of CD103$^+$Vγ4$^+$ cells.

Because we had observed that among T cells in the healthy colon, the CD103$^+$Vγ2/3/4$^+$ Vδ2^{neg} subset was the most refractory to strong activation (Fig. 2, E and F), we considered that the relative increases in CD103^{neg} cells in IBDI donors might translate into precocious cytokine production. Indeed, donors with CDI, UC, and UCI showed significantly higher frequencies of Vγ2/3/4$^+$ cells producing TNFα and, for UCI, IFNγ in response to P+I (Fig. 4J). There were no significant increases in IL17A-producing Vγ2/3/4$^+$ cells (fig. S4G). Moreover, of several gut T cell subsets sampled, only Vγ2/3/4$^+$ cells showed significantly increased frequencies of cytokine-producing cells in IBDI, although it is important to note that in each case, those frequencies were substantially less than the baseline frequencies of cytokine-producing Vδ2$^+$ and αβ T cells in both healthy and diseased colon (Fig. 4J and fig. S4, G to I). Therefore, increased inflammatory cytokine production by Vγ2/3/4$^+$ cells may be more profound in its reflection of the cells' altered phenotype rather than its having any substantial contribution to local cytokine levels. Indeed, paralleling their increased effector responses, Vγ2/3/4$^+$ cells showed significantly decreased responses to 293T.L3L8 (Fig. 4K), consistent with the reductions in Vγ4$^+$ cells. We concluded that in many individuals with IBD, particularly in inflamed lesions, there was a disproportionate diminution and alteration of the distinct colonic CD103$^+$Vγ4$^+$ cell compartment, which is in turn associated with increased responses of the residual cell pool to an activating stimulus and reduced responses to a selecting stimulus. Therefore, we focused next on the prospect that a major deleterious factor in IBD was the reduction in signature CD103$^+$Vγ4$^+$ cells. This would echo the severe exacerbation of murine colitis in the absence of γδ T cells that ordinarily promote tissue repair and homeostasis (*8*).

IBD-associated cytokines dysregulate CD103$^+$Vγ4$^+$ T cells

Initially, we asked what factors might induce the depletion and/or altered phenotypes of intestinal Vγ4$^+$CD103$^+$ cells observed in IBDI. Although those altered phenotypes were suggestive of newly infiltrating CD103^{neg}CD45RA$^+$ CD27$^+$ γδ cells (fig. S4, C and D), we also hypothesized that the IBD milieu might contribute. It is challenging to quantitate gene expression in diseased versus control whole-gut preparations because cell compositions and phenotypes can change substantially. Nonetheless, the data revealed significantly increased transcripts encoding the cytokines IL12, IL18, IL23, and TNFα in IBDI (fig. S5A; note that although CD and UC samples were pooled as IBD or IBDI, their data points completely overlapped). These cytokines are germane to IBD because of their proinflammatory nature and because antibodies neutralizing TNFα, IL12/IL23, and IL23 are all efficacious in IBD (*43*–*45*). Additionally, Vγ4 cells express RNAs encoding receptors for IL12 and TNFα, and at lower levels, RNAs encoding IL18R and IL23R (fig. S5B). Thus, we cultured primary gut T cells in IL2+IL15 for 7 days, additionally supplementing with IL12+IL18, TNFα, or IL1β+IL23 (which might induce changes in Vγ4 cells indirectly through cells expressing the cognate receptors).

IL12+IL18 selectively shifted Vγ4$^+$ cells away from the signature healthy gut phenotype, showing instead significant reductions in the frequencies of cells expressing CD103 and TIGIT (Fig. 5, A and B) and significantly reduced expression levels of NKp46 (Fig. 5C). Complementing these changes, there was an increased frequency of cells expressing CD18 (Fig. 5D), which is ordinarily associated with CD103^{neg} cells (Fig. 1F). Consistent with this overall phenotypic change, Vγ2/3/4$^+$ cells showed less TCR down-regulation in response to BTNL3+BTNL8, although it was also the case that their TCR expression was lower at the outset (Fig. 5E). Conversely, no changes were observed in response to IL1β+IL23 (Fig. 5, A to E). TNFα exposure did not reduce the frequencies of cells expressing CD103 or NKp46 but did significantly reduce CD103 and NKp46 cell surface expression levels and increase both the frequencies of cells expressing CD18 and its surface expression levels (Fig. 5, F to H) while having no clear impact on TIGIT (Fig. 5I). Therefore, one can conclude that the signature CD103$^+$Vγ4$^+$ gut T cell phenotype might not only be displaced by infiltrating cells (fig. S4, C and D), but may also be vulnerable to the selective actions of cytokines characteristic

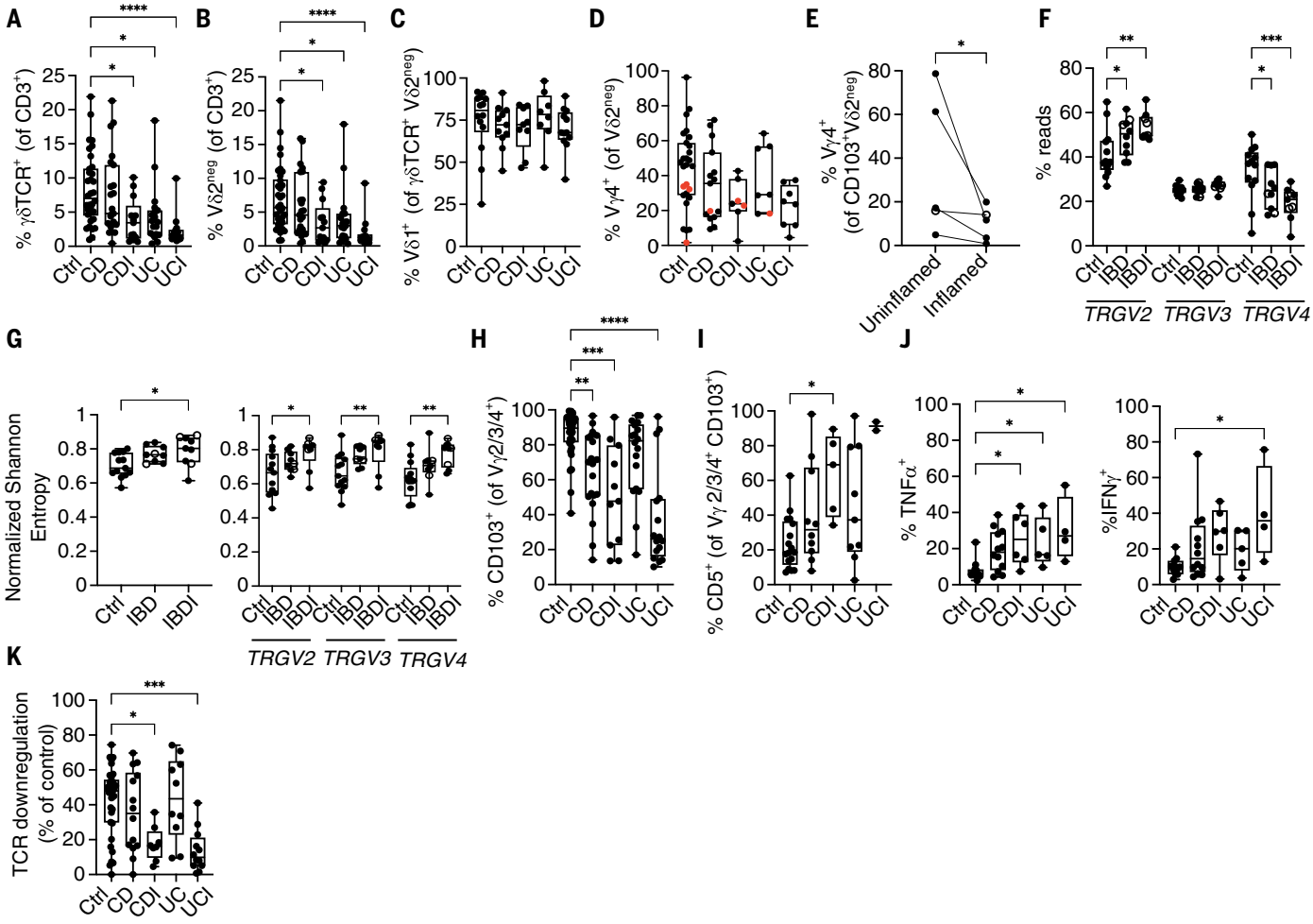

Fig. 4. Phenotypic and clonotypic changes of the intestinal γδ T cell compartment in IBD. (**A** to **C**) Flow cytometric analysis of the percentage of colonic γδTCR$^+$ cells (A) and Vδ2^{neg} cells (B) of total T lymphocytes isolated from control (n = 34), CD (n = 23), CDI (n = 13), UC (n = 19), and UCI (n = 14) donors and the percentage of Vδ1$^+$ cells of Vδ2^{neg} γδ T cells (C) isolated from control (n = 14), CD (n = 11), CDI (n = 9), UC (n = 8), and UCI (n = 12) donors. *P < 0.05 and ****P < 0.0001, Kruskal-Wallis test with Dunn's correction against control donors. (**D**) Flow cytometric analysis of the percentage of Vγ4$^+$ cells of Vδ2^{neg} colonic γδ T cells from control (n = 27), CD (n = 15), CDI (n = 7), UC (n = 7), and UCI (n = 8) biopsies. Red dots indicate the BTNL genotype discussed subsequently. (**E**) Flow cytometric analysis of the percentage of Vγ4 cells of CD103$^+$Vδ2^{neg} colonic γδ T cells from paired uninflamed and inflamed tissue from IBD donors sampled at the same endoscopy (n = 5). Connected symbols represent individual participants. Open circles are CD donors and filled circles are UC donors. *P < 0.05, ratio paired t test. (**F**) *TRGV2*, *TRGV3*, and *TRGV4* gene usage as a proportion of the total *TRGV2/3/4* reads from TCR deep sequencing of mRNA from whole colon biopsies (Ctrl, n = 13; IBD, n = 9; and IBDI, n = 9). Open circles are CD donors and filled circles are UC donors. *P < 0.05 and **P < 0.01, two-way ANOVA with Dunnett's correction against control donors. (**G**) Total γδTCR (left) and *TRGV2/3/4* (right) diversity measured by normalized Shannon entropy derived from TCR deep sequencing of mRNA from whole biopsies from control (n = 13), IBD (n = 9), and IBDI (n = 9) donors. Open circles are CD donors and filled circles are UC donors. *P < 0.05, **P < 0.01, and ***P < 0.001, two-way ANOVA with Dunnett's correction against control donors. (**H**) Flow cytometric analysis of CD103 expression on Vγ2/3/4$^+$ colonic γδ T cells derived from control (n = 43), CD (n = 22), CDI (n = 11), UC (n = 18), and UCI (n = 17) donors. **P < 0.01, ***P < 0.001, and ****P < 0.0001, Kruskal-Wallis test with Dunn's correction against control donors. (**I**) Flow cytometric analysis of CD5 expression on CD103$^+$Vγ2/3/4$^+$ colonic γδ T cells derived from control (n = 17), CD (n = 10), CDI (n = 5), UC (n = 9), and UCI (n = 2) donors. *P < 0.05, Kruskal-Wallis test with Dunn's correction against control donors. (**J**) Flow cytometric analysis of TNFα (left) and IFNγ (right) expression by Vγ2/3/4$^+$ colonic lymphocytes obtained from control (n = 11), CD (n = 12), CDI (n = 6), UC (n = 5), and UCI (n = 4) donors after 4 hours of P+I stimulation. *P < 0.05, Kruskal-Wallis test with Dunn's correction against control donors. (**K**) Flow cytometric analysis of the percentage of TCR downregulation by human colonic Vγ2/3/4$^+$ lymphocytes derived from control (n = 34), CD (n = 14), CDI (n = 8), UC (n = 10), and UCI (n = 12) donors after overnight coculture with 293T.EV or 293T.L3L8 cells. *P < 0.05 and ***P < 0.001, Kruskal-Wallis test with Dunn's correction against control donors. All box-and-whisker plots show median, IQR, and min-max range. Symbols represent individual participants.

of the IBD milieu. The prospect thus exists that the signature CD103$^+$Vγ4$^+$ gut T cell phenotype might also be disrupted by other factors of the IBD milieu that we have not tested, including reported reductions in BTNL3+BTNL8 expression (*15*, *46*).

BTNL3+BTNL8 are selection and/or maintenance factors for intestinal Vγ4$^+$ T cells

There are several challenges in investigating the potential impacts on CD103$^+$Vγ4$^+$ gut T cells of reported reductions in BTNL3+BTNL8 expression in whole IBD gut. Specifically, as was considered above in the context of cytokine expression, there are changes in cell composition and activation states, and there has been no measure of whether surface BTNL3+BTNL8 expression by colonocytes adjacent to Vγ4$^+$ T cells is de facto reduced. Therefore, to unequivocally

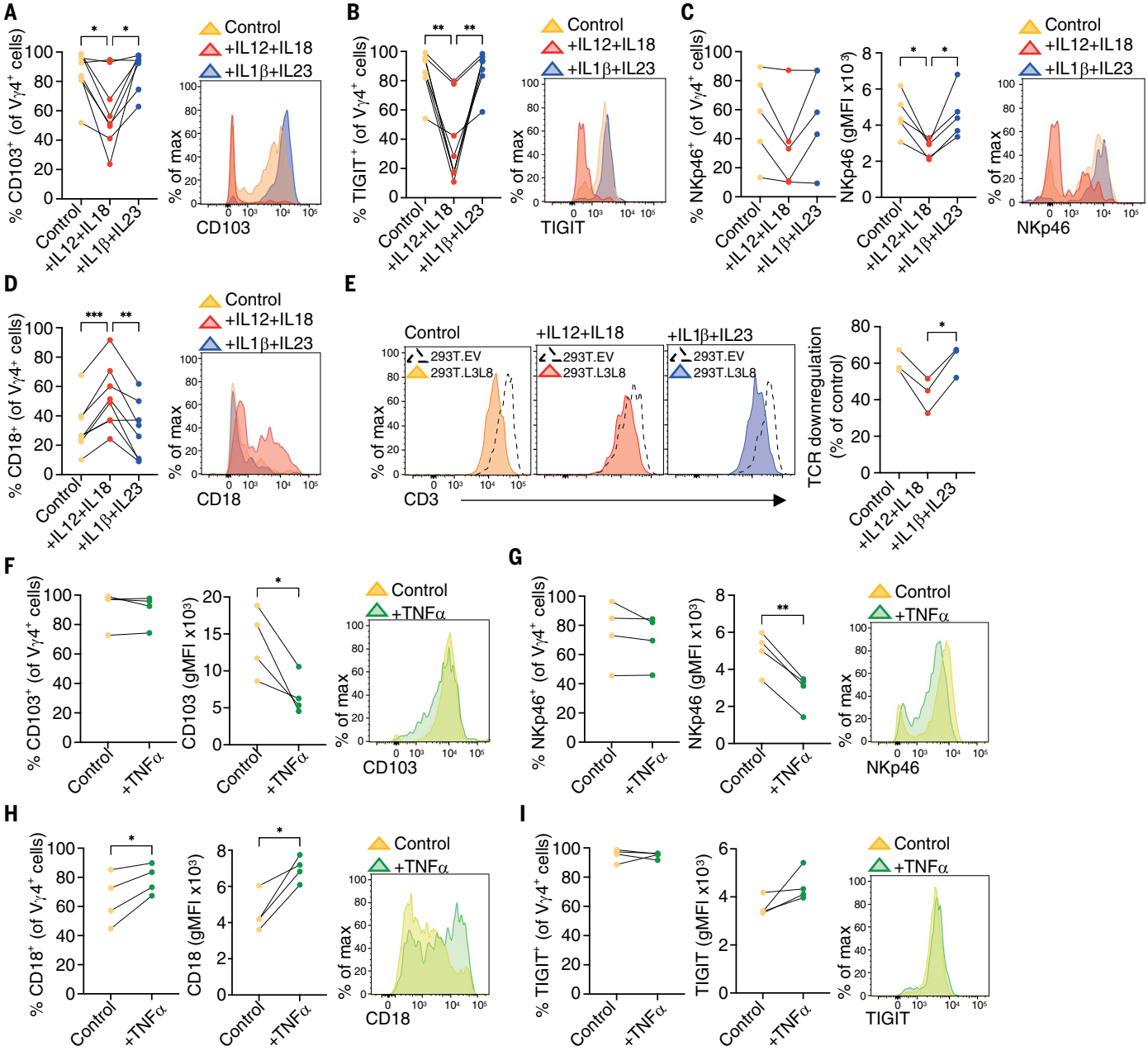

Fig. 5. The cytokine milieu can affect the phenotype of intestinal Vγ4⁺ cells. (**A** to **D**) Flow cytometric analysis of CD103 (n = 8) (A), TIGIT (n = 8) (B), NKp46 (n = 5) (C), and CD18 (n = 8) (D) expression on Vγ4⁺ colonic lymphocytes cultured for 7 days in IL2+IL15 (control), IL2+IL15+IL12+IL18, or IL2+IL15+IL1β+IL23. Summary data (left) and representative histograms (right) are shown. Connected symbols represent individual participants. *P < 0.05, **P < 0.01, and ***P < 0.001, repeated-measures one-way ANOVA with Dunnett's correction against IL12+IL18 treatment. (**E**) Flow cytometric analysis of Vγ2/3/4⁺ colonic lymphocytes cultured for 7 days as in (A) to (D) and subsequently cocultured overnight with 293T.EV and 293T.L3L8 cells (n = 3). Representative flow plots of CD3 expression and summary graph (far right) of the percentage of TCR downregulation relative to 293T.EV control are shown. *P < 0.05, repeated-measures one-way ANOVA with Dunnett's correction against IL12+IL18 treatment. (**F** to **I**) Flow cytometric analysis of CD103 (F), NKp46 (G), CD18 (H), and TIGIT (I) expression on Vγ4⁺ colonic lymphocytes cultured for 7 days in IL2+IL15 (control) and IL2+IL15+TNFα (n = 4). Summary data (left center) and representative histograms (right) are shown. gMFI, geometric mean fluorescent intensity. Connected symbols represent individual participants. *P < 0.05 and **P < 0.01, paired t test.

assess such a situation, we turned to a well-established copy number variation (CNV) polymorphism in which deletion causes an in-frame fusion of the BTNL8 N terminus to the BTNL3 C terminus (Fig. 6A) (47). Homozygosity for this allele occurs at a rate of ~9% in Europeans. The allele could be identified by a standard polymerase chain reaction (PCR) assay (fig. S6A), but given that CNVs can be challenging to detect by routine genetic analyses, we also identified a surrogate single-nucleotide polymorphism (SNP), rs72494581, to facilitate reliable identification of the CNV in DNA microarrays (fig. S6, B and C, and materials and methods). From this analysis, CNV homozygotes derived their annotation "CC"; "TT" denotes homozygosity for the high-frequency allele (full-length *BTNL8* and *BTNL3*) and "CT" denotes heterozygosity (fig. S6C).

When the C allele was cloned, FLAG-tagged, and expressed in HEK293T cells, its protein

product, BTNL8*3, showed poor cell surface expression (fig. S6D, bottom left). We previously reported BTNL8 coexpression can rescue poor surface BTNL3 expression (*3*, *48*), but by contrast, BTNL8*3 was ineffective at this (fig. S6D, second row). Moreover, whereas BTNL3 can enhance surface BTNL8 expression (fig. S6D, third row, left and center), it was less effective at rescuing BTNL8*3 expression (fig. S6D, fourth row, left and center). Added to this inefficient cell surface expression, BTNL8*3 lacks the BTNL3 N-terminal V region that directly engages human Vγ4 (*13*) and, reflecting this, BTNL8*3+BTNL8 could not drive surface Vγ4Vδ1 TCR down-regulation (Fig. 6B). Thus, in relation to γδ T cell regulation, BTNL8*3 is encoded by a severely hypomorphic allele.

Because BTNL1+BTNL6 drive selection of the mouse intestinal Vγ7$^+$ γδ cell compartment (*3*), BTNL1-deficient mice display severe, albeit incomplete, losses of Vγ7$^+$ IEL, whereas in BTNL6-deficient mice, Vγ7$^+$ IELs are reduced by ~50% (*4*). Moreover, once the compartment forms, neither BTNL1 nor BTNL6 is necessary in the short term to maintain Vγ7$^+$ IELs, but they do maintain several parameters of the cells' phenotype (*4*). Persons homozygous for BTNL8*3 offered an opportunity to investigate whether analogous mechanisms regulate the human gut γδ T cell compartment. Indeed, frequencies of Vγ4$^+$ gut T cells were significantly, albeit incompletely, reduced in healthy individuals with a CC genotype (Fig. 6, C and D, and denoted by red circles among the control cohort depicted in Fig. 4D; note, however, that even when removing a posteriori those individuals homozygous for CC from the overall comparison, there was still clear reductions in Vγ4$^+$ cell frequencies in CDI and UCI; fig. S6E). In addition to constituting a smaller fraction of the Vδ2^{neg} compartment in persons homozygous for the CC genotype, the residual Vγ4$^+$ T cells were also phenotypically altered. Thus, whereas for donors with CT and TT genotypes, most Vγ4$^+$ T cells were CD103$^+$, this association of Vγ4 and CD103 was lost in homozygotes for BTNL8*3, who displayed comparable frequencies of CD103$^+$ and CD103^{neg} Vγ4 cells (Fig. 6E).

The severed association of Vγ4 and CD103 phenocopied the shift from CD103$^+$ to CD103^{neg} cells among Vγ4$^+$Vδ2^{neg} cells in IBDI (fig. S4E). Indeed, we identified four IBD patients with the CC genotype who also showed reduced frequencies of Vγ4$^+$ T cells (also denoted in red in Fig. 4D) and a shift from CD103$^+$ to CD103^{neg} Vγ4 cells (Fig. 6E). Moreover, CD103$^+$Vγ4$^+$ lymphocytes from CC donors further phenocopied IBDI in that they showed significantly higher CD5 expression (Fig. 6F). However, because most IBD patients we studied carried either the TT or CT phenotype, we could conclude that there were two distinct settings showing comparable diminution and phenotypic alteration of colonic CD103$^+$Vγ4$^+$ T cells: IBDI, irrespective of BTNL genotype, and BTNL loss of function, irrespective of disease status. The reduction in frequency and altered phenotypes of CD103$^+$Vγ4$^+$ cells in persons homozygous for BTNL8*3 jointly establish that humans, like mice, deploy BTNL proteins to select and/or maintain cognate gut γδ T cells with a distinct phenotype. That neither BTNL-deficient mice nor humans homozygous for BTNL8*3 showed complete loss of Vγ7$^+$ and Vγ4$^+$ gut T cells is discussed below.

BTNL3+BTNL8 hypomorphism is a disease modifier

A genetic basis for Vγ4 cell dysregulation in outwardly healthy individuals offered the opportunity to investigate whether this might predispose to disease. In a pilot snapshot assessment in our clinical practice, we noted that among 64 patients with CD, the frequency of CC exceeded that among 115 control donors, and that the CC frequency was significantly greater among 52 patients with UC (Fig. 6G). We therefore investigated the frequency of CC homozygotes in 12,767 individuals with IBD comprising a locally curated test cohort (n = 4517) and a replication cohort (n = 8250) provided by the National Institute for Health and Care Research (NIHR) UK BioResource against population-based controls from the 1958 British Birth Cohort (n = 6767) (*49*). Notwithstanding a trend in UC, the CC genotype showed no significant association with disease incidence (Fig. 6H). By contrast, when disease phenotype was assessed in 6308 patients with CD (test, n = 1817; replication, n = 4491), there was a significant association of CC frequency with severe B3 disease, which penetrates through the bowel wall, forming intra-abdominal abscesses or fistulae (11.9%, 146/1225), compared with inflammatory (B1) or stricturing (B2) disease, which remains confined within the intestinal lumen (8.7%, 455/5083) (Fig. 6I) (*50*). We conclude that for those with CD, BTNL3 loss of function with consequent dysregulation of gut Vγ4$^+$CD103$^+$ cells predisposes toward penetrating disease and is therefore a disease-modifying factor. The lack of a similar severity classification based on objective disease behavioral parameters precluded a similar analysis of UC.

In identifying the association with penetrating CD, we considered several potentially confounding issues. First, the test set was an older cohort from tertiary referral centers in London and Newcastle collected between 1999 and 2017, in which B3 disease is represented at 24%, whereas the replication set is the NIHR UK IBD bioresource cohort started in 2016, in which only 16% are classified as B3, possibly reflecting improving therapeutic approaches, including anticytokine antibodies, more aggressive top-down strategies, early surgery, and standardization of care through guideline development. Moreover, to mitigate the potential effect of disease duration on findings, we increased the stringency of our study by only including patients with 5-year follow up in the B1 cohort, although clearly this could exclude some patients who might later have transitioned to B3 disease (*51*). These considerations notwithstanding, our genetic analysis was still able to identify a significant association of BTNL3+BTNL8 and consequent Vγ4$^+$ T cell deficiency with penetrating CD.

IBD treatment response is associated with γδ T cell reversion

For the final part of our study, we investigated potential associations of gut γδ cells with responses to treatment. Unlike the characteristic skip lesions of CD, UC is characterized by confluent inflammation extending proximally from the rectum. Therefore, in persons with extensive colitis, one can be confident that samples of uninflamed colonic mucosa that lie toward the rectal side of the maximal extent of disease will have previously been inflamed. Thus, we examined such areas of macroscopically healed mucosa from regions known to be previously affected and found that some displayed recovery of the healthy gut phenotype by the criteria of the frequency of Vγ2/3/4$^+$ cells among Vδ2^{neg} cells, the proportion of those Vγ2/3/4$^+$ cells expressing CD103, and the TCR down-regulation response to BTNL3+BTNL8 (Fig. 6J). Thus, in seeming contrast to reports of gut γδ T cell dysregulation in celiac disease (*14*), the nonclonal switch in the signature γδ T cell compartment observed in inflamed IBD lesions seemed to be reversible, evoking the wound-healing process to which γδ T cells can contribute, as reported in murine colitis (*8*–*10*, *52*).

The capacity of histological assessments of healing to define IBD remission, particularly in CD, has remained unclear (*53*). We therefore investigated whether the phenotypic renormalization of the colonic γδ T cell compartment might be associated with sustained remission. To this end, we assessed the status of 19 patients who at time of sampling were in complete mucosal and clinical remission on treatment (table S4). The patients were classified as Vγ2/3/4$^+$CD103^{hifreq} if the percentage of their Vγ2/3/4$^+$ cells expressing CD103 scored within the 95% CIs of the median value of control CD103 expression by Vγ2/3/4$^+$ cells (i.e., >83.5%; Fig. 1B), and contrasted them with Vγ2/3/4$^+$CD103^{lofreq} individuals who fell below that range. Of 19 patients, seven (three CD and four 4 UC) scored as Vγ2/3/4$^+$CD103^{hifreq} whereas 12 patients (eight CD and four UC) were Vγ2/3/4$^+$CD103^{lofreq}. When their disease progression was compared over the next 5 years, either until relapse or the end of the study, only one relapse was observed in the Vγ2/3/4$^+$CD103^{hifreq} group, whereas eight of 12 Vγ2/3/4$^+$CD103^{lofreq} patients relapsed [hazard ratio = 6.25 (range 1.68 to 23.32), P =0.035] (Fig. 6K).

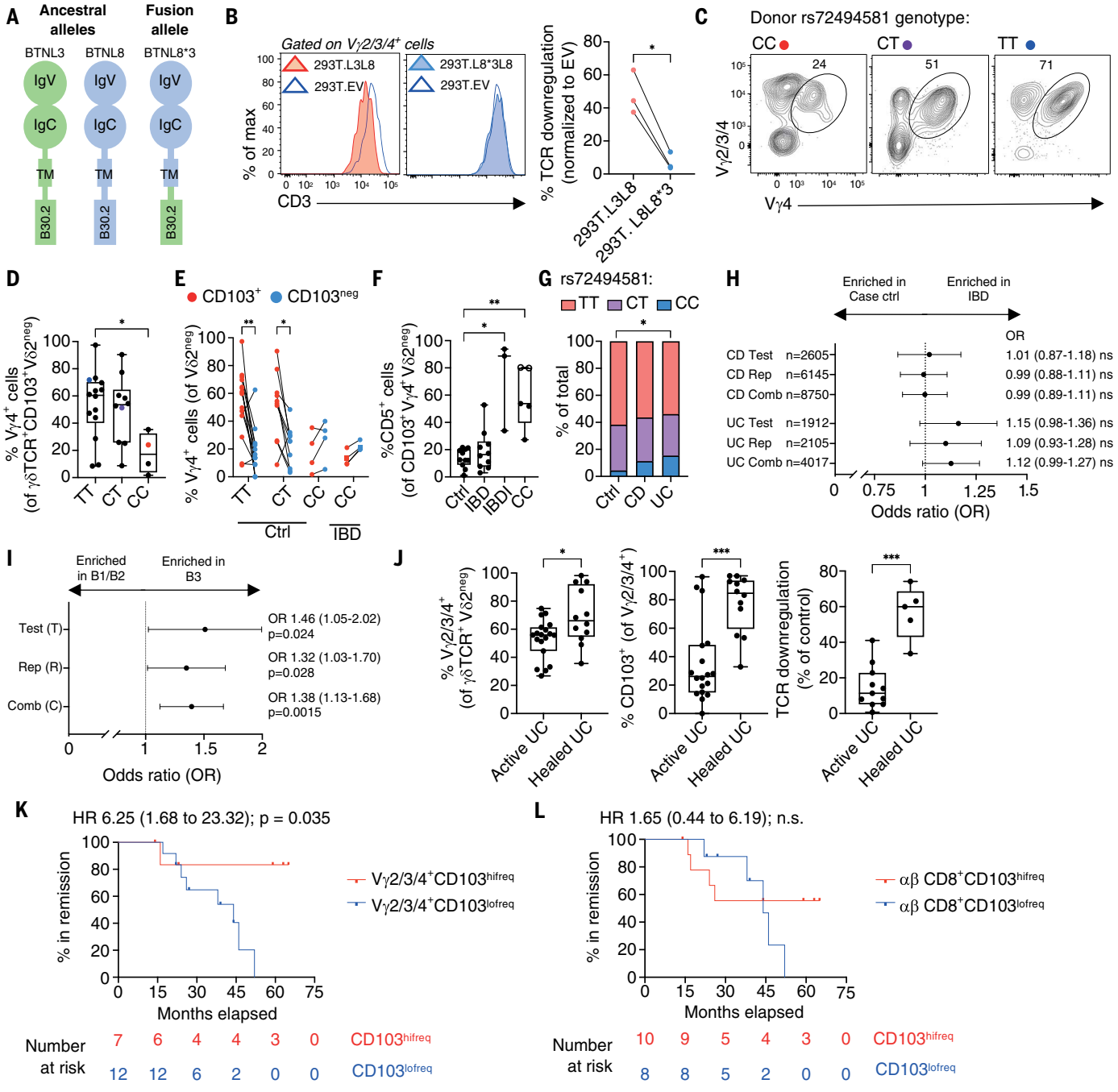

Fig. 6. A genetic influence on the Vγ4-BTNL axis. (**A**) Graphical representation of the full-length BTNL3, BTNL8, and BTNL8*3 fusion protein structure. TM, transmembrane. (**B**) Flow cytometric analysis of human colonic Vγ2/3/4$^+$ cells cocultured overnight with 293T.EV, 293T.L3L8, and 293T.L8L8*3 (n = 3). Example flow plots of CD3 expression and summary graph (far right) of the percentage of TCR down-regulation relative to 293T.EV control are shown. Connected symbols represent individual participants. *P < 0.05, paired t-test. (**C**) Example flow cytometry plots of the percentage of colonic Vγ4$^+$ cells of CD103$^+$Vδ2^{neg} γδ T cells obtained from control biopsies. rs72494581 status is indicated above plots. Colored dots correspond to data points displayed in (D). (**D**) Flow cytometric analysis of the percentage of colonic Vγ4$^+$ cells of CD103$^+$Vδ2^{neg} γδ T cells according to their rs72494581 SNP genotype in control donors (CC, n = 4; CT, n = 10; and TT, n = 14). Median, IQR, and min-max range are shown. Symbols represent individual participants. *P < 0.05, Kruskal-Wallis test with Dunn's correction against control donors. (**E**) Flow cytometric analysis of the percentage of colonic Vγ4$^+$ cells (y axis) of CD103$^+$Vδ2^{neg} (red) or CD103^{neg}Vδ2^{neg} (blue) populations in control donors with different rs72494581 genotypes (x axis) and IBD donors with the CC genotype. Square indicates the UC donor (CC Ctrl, n = 4; CC IBD, n = 4; CT Ctrl, n = 10; and TT Ctrl, n = 14). Connected symbols represent individual participants. *P < 0.05 and **P < 0.01, Wilcoxon matched-pair test. (**F**) Flow cytometric analysis of the percentage of CD5$^+$ cells of colonic Vγ4$^+$CD103$^+$Vδ2^{neg} lymphocytes from control (n = 11), IBD (n = 10), and IBDI (n = 3) TT and CT donors and control (n = 3) and uninflamed IBD (n = 2, open circles) CC donors. Median, IQR, and min-max range are shown. Symbols represent individual participants. *P < 0.05 and **P < 0.01, Kruskal-Wallis test with Dunn's correction against control donors. (**G**) Frequency of the rs72494581 genotype within the local cohort (Ctrl, n = 115; CD, n = 64; and UC, n = 52). *P < 0.05,

Fisher's exact test. (**H**) Odds ratios (OR) for the development of CD or UC compared with 1950s birth cohort data. ORs and 95% confidence intervals are presented according to the minor allele (CC) and the risk of developing disease. (**I**) OR for the development of B3 versus B1/B2 CD. ORs and 95% confidence intervals are presented according to the minor allele (CC) and the risk of developing disease complications (T, *n* = 1817; R, *n* = 4491; and C, *n* = 6308). Test indicates the test set; Rep, replication set; Comb, combined set. (**J**) Flow cytometric analysis of the percentage of $V\gamma2/3/4^+$ cells (left); the percentage of $CD103^+V\gamma2/3/4^+$ cells (middle); and the percentage of TCR down-regulation by γδ lymphocytes after overnight coculture with 293T.EV or 293T.L3L8 cells (right) in the same donors. Colonic biopsies were obtained from inflamed areas (*n* = 11 to 19) and previously inflamed (healed) areas (*n* = 5 to 12) Median, IQR (box), and min-max (whiskers) are shown. Symbols represent individual participants. *$P < 0.05$ and ***$P < 0.001$, Mann-Whitney *U* test. (**K** and **L**) Hazard ratio (HR) analysis of IBD patients in remission with intestinal $CD103^{hifreq}V\gamma2/3/4^+$ cells (CD, *n* = 3; UC, *n* = 4) and $CD103^{lofreq}V\gamma2/3/4^+$ cells (CD, *n* = 8; UC, *n* = 4) (K) and $CD103^{hifreq}CD8^+$ αβ T cells (CD, *n* = 4; UC, *n* = 6) and $CD103^{lofreq}CD8^+$ αβ T cells (CD, *n* = 6; UC *n* = 2) (L) in colonic biopsies at the time of sampling. Subjects were followed until the end of the study or relapse (marks on the curves denote censored cases; thus number at risk reduces owing to relapse and to censoring). Data were analyzed by log-rank test or HR log-rank test. ns, not significant.

Conversely, 18 of the 19 patients collectively showed no reliable association of remission or relapse with the phenotype of colonic $CD103^+$ $CD8^+$ αβ T cells (for one of the 19 patients, $CD8^+$ T cell data could not be recovered for technical reasons) (Fig. 6L).

Discussion

By investigating the human colonic T cell compartment, we have combined human genetics with tissue immunological studies to establish that the BTNL-dependent selection and phenotypic maintenance of a subset of gut-intrinsic γδ T cells is evolutionarily conserved. Although the selected $CD103^+V\gamma4^+$ cells often do not dominate the γδ compartment, which is in contrast to mice, the cells' phenotype is distinct. Moreover, persons homozygous for hypomorphic BTNL8*3 displayed significant reductions in $V\gamma4^+$ cell frequencies, and the residual cells were phenotypically altered, which are both phenotypes that closely phenocopy the situation in mice with deficiencies in BTNL1 or BTNL6 (*3*, *4*). In the setting of BTNL deficiency, the incomplete loss of $V\gamma4^+$ cells in humans and of $V\gamma7^+$ cells in mice is likely attributable to the potential of other interactions, e.g., clonotypic antigen reactivities, to promote the amplification and survival of some human $V\gamma4^+$ and mouse $V\gamma7^+$ T cells, respectively.

The combined loss and phenotypic perturbation of $CD103^+V\gamma4^+$ cells was also the single most overt γδ cell dysregulation in inflamed IBD. Whereas this dysregulation may in part be a consequence of pathology (i.e., it is a disease biomarker), causative contributions could be surmised from the association of CD severity with homozygosity for BTNL3/8 hypomorphism. Because UC currently does not benefit from the same objectively defined disease behavioral phenotypes, we could not subject it to the same analysis. Nonetheless, throughout our study, patients with UC and CD showed conspicuously similar γδ cell dysregulation, and patients with either disease who displayed a renormalized $CD103^+$γδ cell compartment showed significantly higher post-treatment remission rates than those with less obvious renormalization when assessed 5 years later. Limitations of this part of our study include the cohort size and the lack of paired longitudinal samples. Thus, we hope that a larger study will now be undertaken, because validation of our findings would pertain to two key points discussed below.

First, routine mucosal $CD103^+V\gamma4^+$ cell status assessment may offer a practical prognostic indicator. Whereas histological remission in UC is currently offering improved indicators of disease outcome, 50% of patients in the recent ERIca study who showed histological remission progressed to relapse, highlighting ongoing undetected dysregulation (*54*). Thus, a focus on local γδ T cell dynamics may offer disease stage–specific molecular signatures akin to those proving beneficial in managing bowel cancers (*55*).

The second key point is the probability that $CD103^+V\gamma4^+$ cell renormalization is likely to be of physiologic benefit. Although the nature of that benefit remains to be elucidated, the cells' wound-healing and anti-inflammatory potentials seem evident in their expression of several potentially relevant genes, including *API5* (*11*) and *FGF9* (*24*). A capacity of $CD103^+$ $V\gamma4^+$ cells to promote epithelial repair would be another conserved feature, given that the exacerbated pathology in γδ-deficient mice experiencing chemically induced colitis is ascribed to defective wound healing (*9*). From this perspective, the lack of significant benefit versus placebo observed during phase 3 UC maintenance trials of etrolizumab, which targets CD103, might in part reflect its antagonizing of homeostatic $CD103^+V\gamma4^+$cells (*56*, *57*). Irrespective of the basis of their wound-healing potential, our study has shown that BTNL-selected $CD103^+V\gamma4^+$ cells are largely distinct in terms of their sensory machinery permitting them to patrol the epithelium (*58*). That machinery is composed of the TCR; FcεRIγ, which can mediate signaling from the TCR and from NK receptors; and several NK receptors, particularly NKp46, which can recognize cells undergoing endoplasmic reticulum stress, which is a feature of the colonic epithelium in IBD (*59*).

It is formally the case that BTNL3/8 loss of function might influence IBD progression through a mechanism independent of $CD103^+$ $V\gamma4^+$ cell regulation. Nonetheless, the only clearly established biochemical function of BTNL3+8 heteromers and their mouse counterparts is to engage intestinal γδ TCR Vγ chains. Direct evidence germane to the importance of $CD103^+V\gamma4^+$ cell regulation may in the near future be provided by analyses of IBD incidence and progression in individuals carrying recently described *TRGV4* alleles encoding chains that show reduced responsiveness to BTNL3+BTNL8 (*60*).

Two additional points merit clarification. First, because $V\gamma4^+$ cells appear to be highly sensitive to BTNL3+BTNL8 engagement, the reduced levels of BTNL3+BTNL8 expression reported for IBD (*15*, *46*) are not necessarily causal to $V\gamma4^+$ cell dysregulation, in contrast to either BTNL loss of function in donors homozygous for BTNL8*3 or the IBD-associated cytokine milieu. Indeed, upstream disease-associated factors contributing to $V\gamma4^+$ cell dysregulation would seem consistent with the cells being more germane to disease progression than to disease incidence. Second, it was reported that whereas decreased BTNL3 and ablated BTNL8 expression in celiac disease could renormalize, this did not correlate with renormalization of either intestinal $V\delta1^+$ cells or *TRGV4* reads (*14*), which is also consistent with other factors contributing to the cells' dysregulation. The fact that we have observed renormalization in a cohort of patients with treated IBD may simply reflect disease-specific and treatment-specific factors distinguishing IBD from celiac disease, including but not limited to the fact that celiac disease is largely associated with increases in γδ T cell frequencies, whereas we have shown IBD to be associated with γδ T cell depletions.

Finally, we note that BTNL is not a hit in genome-wide association studies (GWASs) for disease susceptibility in either publicly available or our own datasets. BTNL variants have also not previously shown association with disease progression, but neither the imputation of our variant of interest nor clinical classifications used in previous international meta-analyses can be assumed to be sufficiently reliable to assess this. Compared with ~300 loci associated with IBD susceptibility, only a few polymorphisms disposing to IBD prognosis have been identified, *FOXO3*, *XACT*, *IGFBP1*, and *HLA*, which were identified using GWASs of patients with indolent and clinically more severe CD (*61*), rather than the stricturing

versus penetrating disease behaviors used here. Although the mechanistic impact of the few progression-associated genes has yet to be fully elucidated, such genes and pathways may offer useful prognostic indicators compared with the arguably disappointing performance of genes disposing to susceptibility (*62*, *63*). Therefore, the identification of the BTNL-γδ axis as a disease modifier may offer new insights into understanding and tracking IBD progression. Furthermore, improved tissue repair, in contrast to anti-inflammatory agents, might achieve long-term, drug-free disease remission, which is of particular importance given that IBD is common and is an increasing public health issue in more recently industrialized countries, where prevalence continues to rise (*64*, *65*).

Materials and Methods

Human samples

Colonic samples

Up to 12 endoscopic biopsies were obtained from the colons of adult donors undergoing diagnostic colonoscopy after informed consent and in compliance with local ethical approval (REC number 07/H0803/237 or 16/LO/0642). The location and macroscopic appearances of the biopsy site were carefully noted.

Non-IBD controls (Ctrl) were defined as persons undergoing colonoscopy for non-IBD indications in which no inflammatory intestinal disease was found and either no or minimal distant pathology, e.g., minor diverticulosis or sporadic adenomas, was found. In patients who underwent colonoscopy to investigate chronic diarrhea, histology was taken to exclude microscopic or collagenous colitis. Patients with celiac disease or other significant intestinal comorbidity were excluded.

Donors with IBD were identified as either patients with a known history or those with symptoms suggestive of IBD before endoscopy who prospectively consented. Sampling was performed either in macroscopically uninflamed regions (IBD, CD, or UC) or macroscopically inflamed regions (IBDI, CDI, or UCI). Demographic details are provided in table S1.

Remission was defined according to strict criteria. Endoscopic remission was defined using validated endoscopic scores: Ulcerative Colitis Endoscopic Index of Severity ≤1 and Simple Endoscopic Score for Crohn's Disease <3 (*53*) or Rutgeert's score i0 to i1 (*66*). Patients were also in clinical remission, with no evidence of ongoing biochemical or radiological inflammation. Relapse was defined as symptomatic, endoscopic, radiological, or biochemical relapse leading to treatment escalation, surgery, or hospital admission.

Samples obtained at endoscopy were placed directly into Hanks' balanced salt solution. Up to 4 hours after collection, they were placed in cell culture or frozen in 90% fetal calf serum and 10% dimethyl sulfoxide (DMSO).

Blood samples

Blood samples were obtained from cone blood from the National Health Service (NHS) Blood and Transplant service (London, UK). PBMCs were isolated using the Ficoll-Paque method and frozen in 10% DMSO with 50% fetal calf serum RPMI. This study was conducted adhering to the principles of the Declaration of Helsinki.

DNA and RNA isolation from whole tissue

A single colonic biopsy was placed in RNAlater (Thermo Fisher Scientific) at the time of acquisition. An AllPrep DNA/RNA Mini kit (Qiagen) was used to extract mRNA and genomic DNA from donor tissue following the manufacturer's instructions. Qiagen TissueLyser II was used to homogenize tissue samples.

TCR deep sequencing

Total RNA extracted from colonic biopsies was sent for γδ TCR chain (*TRDV/TRGV*) deep sequencing using the IlluminaMiSeq platform with short-read 100/150 PER primers (iRepertoire, USA). Shannon's entropy and D50 were calculated as previously described (*67*).

Quantitative PCR

cDNA was synthesized using Superscript II (Invitrogen) according to the manufacturer's instructions. Gene expression was analyzed using the PowerUp SYBR Green Master Mix (Invitrogen) following the manufacturer's instructions. Reactions were run on a ViiA7 real-time PCR machine (Applied Biosystems). Target gene expression was normalized to *RSP9* expression using the $2^{-\Delta CT}$ method. *RPS9* primer sequences were from Bamias *et al.* (*68*): RSP9 _F 5′- TCCTTTTCCACTTCGTCTGAG-3′ and RSP9_R 5′- AAGCTGATCGGCGAGTATG-3′. *TNF* primer sequences were from Rajput *et al.* (*69*): TNF_F 5′-ATGAGCACTGAAAGCATGATCC-3′ and TNF_ R 5′-GAGGGCTGATTAGAGAGAGGTC-3′.

BTNL3 exon 4_FF 5′- TGTTGTCATGGGGATGATAATTG-3′, BTNL3 econ 8_R 5′- CATACCACCCTACATTTTGTCCC-3′, BTNL8 exon 4_F 5′-GGCATTGTTGGACTGAAGATTTTC-3′, and BTNL8 exon 8_R 5′- CGCCACCTTTTATTGTGTCCTC-3′

Other primers used were Quantitect IL-12A primers (Qiagen, catalog #QT00000357), Quantitext IL-18 primers (Qiagen, catalog #QT00014560), and Quantitect IL-23A primers (Qiagen, catalog #QT00204078).

Intestinal lymphocyte isolation

Explant method

Human colonic lymphocytes were isolated as previously described (*3*) and used after a short-term crawl out (36 to 48 hours) without the addition of exogenous cytokines or after 5 to 7 days of culture in the presence of cytokines when cells were used in coculture assays or cytokine skewing experiments (see below).

Digestion

Whole colonic biopsies were digested using Miltenyi's Tumour Dissociation Kit (Miltenyi Biotec) according to the manufacturer's instructions for the isolation of lymphocytes.

Primary cell culture conditions

Samples used in coculture assays and cytokine skewing experiments were isolated using the explant method and cultured for 5 days in complete medium supplemented with IL2 (100 U/ml, Novartis Pharmaceutical UK) and IL15 (10 ng/ml, BioLegend). One milliliter of medium was aspirated every second day and replaced with complete medium containing 2× concentrated cytokines. In cytokine-skewing experiments, medium was also supplemented with IL2 (100 U/ml), IL15 (10 ng/ml), and IL12 (10 ng/ml) (all from Peprotech) and IL18 (50 ng/ml, Medical and Biological Laboratories) or with IL2 (100 U/ml), IL15 (10 ng/ml), IL1β (10 ng/ml), or IL23 (10 ng/ml) (all from BioLegend) or with IL2 (100 U/ml), IL15 (10 ng/ml), TNFα (50 ng/ml (all from BioLegend).

Flow cytometry

Flow cytometry was performed using the following antibodies coupled to the indicated fluorochromes (clones indicated in brackets). Antibodies were purchased from BioLegend unless otherwise stated in brackets. Viability dye aqua was from Invitrogen. Viability dye Zombie NIR was from BioLegend. Ultra-LEAF Purified Human IgG_1 Isotype Control antibody (QA16A12) was from BioLegend. The following antibodies were used: Vδ2-AF700 (B6); Vδ2-PerCpCy5.5 (B6); γδTCR-PE.Cy7 (IMMU510; Beckman Coulter); Vδ1-FITC (TS8.2; Thermo Fisher Scientific); Vδ1-PE (REA173; Miltenyi); Vδ1-APC (REA173; Miltenyi); CD3-BV786 (OKT3); CD3-BV510 (OKT3); CD8α-BV510 (HIT8a); CD8α-PerCpCy5.5 (HIT8a); CD8α-FITC (HIT8a); CD103-FITC (Ber-ACT8); CD103-BV605 (Ber-ACT8); CD103-PerCpCy5.5 (Ber-ACT8); CD103-BV421 (Ber-ACT8); CD5-BV421 (L17F12); CD18-PE (1B4/18); 41BB-BV605 (4B4-1); IFNγ-BV421 (4S.B3); TNFα-APC (MAb11); IL17A-BV605 (BL168); CD101-PerCpCy5.5 (BB27); TIGIT-PerCpCy5.5 (A15153D); TIGIT-PerCpCy5.5 (741182; BD Biosciences); Nkp30-BV711 (P30-15); Nkp44-BV605 (p44-8); Nkp46-PE (9E2); Nkp46-BV421 (9E2); CD49a-APC (TS2/7); CD69-BV510 (FN50); CD38-BV605 (HB-7); ICOS-BV711 (C398.4A); NKG2C-BV421 (134591; BD Biosciences); CCR9-APC (L053E8); CD31-BV421 (WM59); CD96-BV421 (NK92.39); NKG2D-BV605 (1D11); DNAM1-BV605 (DX11; BD Biosciences); CCR7-APC (G043H7); CCR7-BV421(G043H7); NKG2A-BV711 (131411; BD Biosciences); TIM3-BV421 (F38-2E2); FcεRIγ-FITC (FCABS400F; Merck); CD107a-PE (LAMP1); IL2-PE (MQ1-17H12); CD45RA-BV421 (HI100); and CD27-BV786 (O323). The biotin-conjugated antibody

against Vγ2/3/4 (23D12) (*70*) was detected by conjugation to BV650 or PE-streptavidin (BioLegend). The anti-Vγ4 antibodies (G4_9 and G4_18; Iontas) were human immunoglobulin G_1 (IgG_1) isotype, and goat antihuman IgG (H+L)-AF647 (polyclonal; Thermo Fisher Scientific) was used to detect unconjugated clones. In addition, clone G4 18 was conjugated to AF647 using the Lightning Link Fast conjugation kit (Abcam) following the manufacturer's instructions with the exception that the incubation period with modifier agent was extended to overnight at 4°C. Primary cells were fixed with BD CellFIX (BD Biosciences) for 20 min at room temperature before acquisition.

For cytokine stains, lymphocytes were stimulated with 10 ng/ml PMA (Merck) and 1 μg/ml ionomycin (Merck) in the presence of 20 μg/ml brefeldin A (Merck) for 4 hours at 37°C and 5% CO_2. After surface staining and cell fixing, lymphocytes were permeabilized with Intracellular Staining Permeabilization Wash Buffer (BioLegend) for 20 min at room temperature. The relevant conjugated monoclonal antibodies were added to the permeabilization buffer with the cells and incubated for another 20 min. The cells were washed and acquired.

When examining degranulation in the coculture assay, conjugated anti–CD107a-PE antibody was added at the start of a 6-hour coculture assay, and surface staining was performed at the end of the assay.

Experiments were acquired on BD LSRFortessa X-20 or BD FACSCanto II flow cytometer. Flow cytometry data analysis was performed on FlowJo v10.

Generation of antihuman Vγ4 antibodies

Anti-Vγ4 TCR antibodies were generated by Iontas and provided by Adaptate Biotherapeutics. They were derived using phage display following industry standard techniques (*71*). A discovery strategy was devised to exert selection pressure toward the Vγ4Vδ1 and Vγ4Vδ2 TCR complexes. To this end, phage display selections were performed with recombinant TCR antigens in solution phase. Binders were screened in soluble scFv format by subcloning the entire selection outputs in a suitable scFv expression vector. Hits were assessed by specific binding to Vγ4Vδ1 and Vγ4Vδ2 TCR antigens, and not Vγ2Vδ1, Vγ2Vδ2, and Vγ8Vδ1 TCR antigens. Distinct binder sequences were ranked according to their relative affinity to Vγ4 in a scFv capture enzyme-linked immunosorbent assay (ELISA). A final selection of 24 binders with low sequence liability, varying estimated affinities, and CDR3 diversity were chosen for IgG conversion. Of the 24 candidates, two were validated to bind $Vγ4^+$ TCR specifically, with good staining indexes and minimal background signal (fig. S3A).

Cell lines

HEK293T cells were from the ATCC and were maintained in Dulbecco's modified Eagle's medium (DMEM) supplemented with 10% fetal bovine serum (FBS) and 100 U/ml penicillin-streptomycin. The human $TCRβ^-$ cell line JRT3 was a gift from Dr. Salah Mansour, University of Southampton, and was cultured in RPMI 1640 supplemented with 10% FBS and 100 U/ml penicillin-streptomycin.

Cells transduced with empty vector (EV) or BTNL3 and BTNL8 have previously been described (*3*) and were cultured in DMEM supplemented with 10% FBS, 100 U/ml penicillin-streptomycin, 1 μg/ml puromycin (Sigma-Aldrich), and 500 μg/ml hygromycin (Thermo Fisher).

Plasmids, cloning, transfection, and lentiviral transduction

Plasmids encoding hu17 (Vγ4Vδ1), hu17.Vγ2 (Vγ2Vδ1), hu17.Vγ3 (Vγ3Vδ1), hu17.Vγ3-$Vγ4^{HV4}$ (Vγ3Vδ1), hu17.Vγ3-$Vγ4^{CDR2\text{-}HV4}$(Vγ3Vδ1), hu20 (Vγ4Vδ1) and huPB (Vγ9Vδ2) have previously been described (*12*, *13*). The plasmid encoding hu20/huPB (Vγ4Vδ2) was generated by subcloning the hu20 gamma chain using NcoI/XbaI and the huPB delta chain using XhoI/NotI into the self-inactivating lentiviral vector pCSIGPW after removal of the IRES-GFP and $CMVp\text{-}Puro^R$ cassettes (*3*, *48*).

The self-inactivating lentiviral vector pCSIGPW (SFFV promoter – Multiple Cloning Site [MCS] – IRES-GFP – CMV promoter – $Puromycin^R$), and plasmids encoding FLAG-BTNL3 and FLAG-BTNL8 were previously described (*3*). The FLAG-BTNL8*3 construct was derived from FLAG-BTNL8 and FLAG-BTNL3 plasmids by using a distinct DraIII restriction site at the beginning of the B30.2 domains of BTNL8 and BTNL3.

All plasmids were transduced and transfected following a previously established protocol (*12*, *13*).

Coculture assays

HEK293T cells (5×10^5) transduced with either EV (293T.EV), BTNL3, and BTNL8 (293T.L3L8) or BTNL8 and BTNL8*3 (293T.L8L8*3) were cocultured with 2×10^5 primary human lymphocytes harvested after 5 days of culture in the presence of IL2 and IL15, as previously described (*12*). Cells were cocultured overnight at 37°C and 5% CO_2 in 96-well round-bottom plates with complete medium without supplementary cytokines. Cells were subsequently analyzed by flow cytometry.

RNA sequencing

RNA sequencing of human intestinal CD103$^{+/neg}$ Vγ2/3/4$^+$ cells

Intestinal lymphocytes were isolated using the Miltenyi tumor dissociation kit as described above. Cells were sorted directly into TRIzol ($n = 1$) or PBS ($n = 2$) and sent to GENEWIZ (Bishop's Stortford, UK) for RNA extraction. cDNA was prepared with an ultralow input. Single-end 150 bp sequencing was undertaken on an Illumina Hiseq. The final sample (Sample A) was FACS sorted directly into lysis buffer and RNA isolated using the PicoPure kit (Thermo Fisher Scientific) as per manufacturer's instructions. cDNA was prepared with the Ovation RNA-Seq System V2 (NuGEN), and libraries were constructed with the Ultralow Library System V2 (NuGEN) and single-end sequencing undertaken on an Illumina Hiseq 2500. Seventy-five base-pair single-end reads were aligned to human genome GRCh38 from Ensembl using STAR (v2.5.2a). Gene-level quantifications using annotation release 86 from Ensembl were generated using RSEM v1.3.0. To identify differential expression raw gene-level counts were imported into DESeq2 (*72*). Genes with a mean normalized count below zero across all samples were removed before statistical analysis.

These data have been deposited in NCBI's Gene Expression Omnibus (GEO) under accession number GSE218058 (https://www.ncbi.nlm.nih.gov/geo/query/acc.cgi?acc=GSE218058) (*73*).

RNA sequencing of human intestinal Vγ2/3/4$^+$ cells cocultured with 293T.EV or 293T.L3L8 cells

Intestinal lymphocytes were isolated using the explant grid culture method for 2 weeks in IL2 and IL15. Cells were then harvested and cocultured overnight with 293T.EV or 293T.L3L8. $Vγ2/3/4^+$ cells from each condition were sorted directly into lysis buffer, and RNA was extracted using the RNEasy MicroPlus kit (Qiagen) following the manufacturer's instructions. RNA was sent for library preparation and single-end sequencing on the Illumina HiSeq 2500 at the Advanced Sequencing Facility of the Francis Crick Institute.

Seventy-five base-pair single-end reads were aligned to human genome GRCh38 from Ensembl using STAR (v2.5.2a). Gene-level quantifications using annotation release 86 from Ensembl were generated using RSEM v1.3.0. To identify differential expression, raw gene-level counts were imported into DESeq2 (*72*). Genes with a mean normalized count below zero across all samples were removed before statistical analysis. Differential expression between the $Vγ2/3/4^+$ cells cocultured with the 293T.EV and 293T.L3L8L3+L8 groups was identified by taking into account the paired structure within the replicate groups. Using a false discovery rate (FDR) of 0.01, a total of 37 culture-condition-dependent gene expression effects were identified.

These data have been deposited in GEO under accession number GSE224412 (https://www.ncbi.nlm.nih.gov/geo/query/acc.cgi?acc=GSE224412) (*73*).

RNA sequencing of human intestinal γδ T cells

Eleven biopsies from control donors were digested, and live $V\gamma4^+V\gamma2/3/4^+\gamma\delta TCR^+CD3^+V\delta2^{neg}$ and $V\gamma4^{neg}V\gamma234^{neg}\gamma\delta TCR^+CD3^+V\delta2^{neg}$ cells were sorted directly into extraction buffer using the PicoPure RNA Isolation Kit (Thermo Fisher Scientific). RNA was isolated immediately adhering to the manufacturer's instructions. Total RNA was stored at −80°C in a freezer until submission. Libraries were prepared by the Advanced Sequencing facility at the Francis Crick Institute using the NEBNext Ultra II RNA Library prep kit. Libraries were sequenced by the Biomedical Research Centre (BRC) Genomics Facility at Guy's Hospital on an Illumina NextSeq 2000.

All software for the data analysis was run with default settings unless otherwise indicated. The quality of the sequencing reads was examined using FastQC (v0.11.4). Raw sequencing reads (100 nt, paired-end) were trimmed using Trimgalore (v0.4.4). Traces of ribosomal DNA and mitochondrial DNA were removed using Bowtie2 (v2.2.5) (*74*). Reads were aligned to the human reference genome GRCh38 using STAR (v2.5.3a) with the default setting (*75*). Duplicate reads were removed using the MarkDuplicates function of Picard tools (v2.17.11). Reads were annotated using the Partek E/M (Partek software) gene count. Differentially expressed genes (DEGs) were identified using DESeq2 (v3.5) (*72*). All software for the data analysis was run with default settings unless otherwise indicated. The quality of the sequencing reads was examined using FastQC (v0.11.4). Raw sequencing reads (100 nt, paired-end) were trimmed using Trimgalore (v0.4.4). Traces of ribosomal DNA and mitochondrial DNA were removed using Bowtie2 (v2.2.5) (*74*). Reads were aligned to the human reference genome GRCh38 using STAR (v2.5.3a) with the default setting (*75*). Duplicate reads were removed using the MarkDuplicates function of Picard tools (v2.17.11). Reads were annotated using the Partek E/M (Partek software) gene count. DEGs were identified using DESeq2 (v3.5) (*72*).

These data have been deposited in GEO under accession number GSE218446 (https://www.ncbi.nlm.nih.gov/geo/query/acc.cgi?acc=GSE218446) (*73*).

Gene set enrichment analysis

Gene set enrichment analysis (GSEA) pre-ranked analysis was performed using DEGs between $V\gamma2/3/4$ $CD103^+$ (positive values) and $CD103^{neg}$ (negative values) with several published datasets (Fig. 1, D and E, and fig. S1E) (*76*).

For human datasets, the published gene signature of the cells under investigation was used. To compare the published murine $V\gamma7^+$ data, murine genes were converted to human orthologs using g:GOSt (https://biit.cs.ut.ee/gprofiler/gost) (*77*). Three published gene signatures were large (*3*, *25*, *26*), so the top 500 significant DEGs were taken as the gene signature.

DNA samples for genotyping experiments

The study included 12,767 unrelated UK patients with IBD. The ethnicity of both cases and controls was limited to white European ancestry because these alleles are underrepresented in other ethnicities (*47*). The study included a test set of 4517 IBD patients consisting of patients recruited after ethical review and obtaining of informed consent from Guy's and St Thomas' Hospitals in London UK and the Royal Victoria Infirmary in Newcastle, UK (REC 12/YH/0172). The replication set included 8250 IBD patients incorporated into the NIHR IBD bioresource. The diagnosis of IBD was made by established criteria of clinical, radiologic, and endoscopic analysis and from histology reports. Patients were classified according to the Montreal Classification into disease location (L1 to L3) and disease behavior (B1 to B3). Duration of disease was defined as onset of symptoms or date of diagnosis to date of inclusion in the database. B1 cases were included only if they had at least 5 years of documented follow-up to avoid incorporating patients who had not yet progressed to other phenotypes. B2 and B3 cases were recorded regardless of disease duration. Only patients with CD and sufficient phenotypic and disease duration data were included in the final analysis of genetic association with disease behavior (test, n = 1817; replication, n = 4491).

The study also included 6767 population controls, obtained from the 1958 British Birth Cohort, including all subjects born between 3 and 9 March 1958 in England, Scotland, and Wales as recorded in the National Child Development Study (https://cls.ucl.ac.uk/cls-studies/1958-national-child-development-study/) (*49*).

*BTNL8*3 CNV genotyping by PCR*

All locally sourced genomic DNA (gDNA) obtained from donors was used at 10 ng/reaction. PCR was performed using Q5 High Fidelity DNA polymerase (New England Biolabs) following the manufacturer's instructions and in a single tube reaction. The following primers were used: L8_F 5′-GACTTTTCACCCCCAAAACC-3′, L8_R 5′-CTCATGTCCACCTGAGATT- CTG-3′, and L3_R 5′-GTAAGCCCTCTATTTGACTT-TGTG-3′

Predicted product sizes were 1602 bp for BTNL8*3 and 1310 bp for BTNL8. PCR product was separated by 1% agarose gel.

*Identification of rs72494581 as a surrogate SNP of the BTNL8*3 CNV*

We cloned and sequenced the PCR products generated by amplification of the genomic region resulting from the CNV using primers L8_F and L3_R (sequences above), which generates a 1602-bp product (fig. S6A). After aligning the obtained sequences from six different CNV homozygous donors (GUT1 to GUT6) to the reference sequences of the genomic regions of BTNL8 (L8) and BTNL3 (L3), as well as the predicted sequence of the CNV allele (L8*3), we confirmed the location of the non-allelic homologous recombination region suggested by (*47*) (fig. S6B). This region starts with a sequence that is nearly identical to a recombination hotspot sequence reported by Myers *et al*. (*78*).

The CNV alleles from all six donors all included a T>C SNP [rs72494581, not reported by Aigner *et al*. (*47*)]. We then compared the results of the RT-PCR method using the L8_F, L8_R, and L3_R primers (sequences above and in fig. S6A) using gDNA from donors that had previously been genotyped with a custom TaqMan-based genotyping assay for rs72494581 (fig. S6C). Given the relatively limited number of samples tested, we cannot guarantee that rs72494581 is in complete linkage disequilibrium in all cases, but given its proximity to the putative break point (<200 bp) and the perfect match between the RT-PCR and TaqMan data (fig. S6, A and C), this SNP is potentially the best marker of the CNV allele.

*BTNL8*3 CNV genotyping by TaqMan assay*

Custom TaqMan SNP genotyping assay for rs72494581 was ordered from Thermo Fisher Scientific and used as per the manufacturer's instructions with TaqMan Genotyping Master Mix (Thermo Fisher Scientific) and a minimum of 4 ng of each gDNA sample per reaction. Postamplification allelic discrimination was performed using the ABI7900HT (TaqMan plate reader, end-point read). Case control association test was performed by chi-square test. Primer sequences were rs72494581_F 5′-CTCGTCCCACCTGTGCAA-3′ and rs72494581_R 5′-GAAACAGTATATTCAGTGGTG-GACACA-3′.

KASP genotyping

A KASP assay for rs72494581 was custom designed and validated against known samples. High-throughput genotyping was outsourced and undertaken by KASP genotyping (LGC Biosearch Technologies). Clinical data relating to patients tested for rs72494581 were provided by the NIHR IBD Bioresource.

Statistical analysis

With the exception of the sequencing analysis (see above), all other statistics were performed in GraphPad Prism v9. Statistical information is included in the figure legends. In all figures, horizontal bars denote the median and error bars denote the minimum and maximum data points.

REFERENCES AND NOTES

1. M. M. A. Fernando *et al*., Defining the role of the MHC in autoimmunity: A review and pooled analysis. *PLOS Genet.* **4**, e1000024 (2008). doi: 10.1371/journal.pgen.1000024; pmid: 18437207
2. A. C. Hayday, "Gamma delta T cells," in *Paul's Fundamental Immunology* (Wolters Kluwer/Lippincott Williams & Wikins, 2022), pp. 1054–1101.
3. R. Di Marco Barros *et al*., Epithelia use butyrophilin-like molecules to shape organ-specific γδ T cell compartments. *Cell* **167**, 203–218.e17 (2016). doi: 10.1016/j.cell.2016.08.030; pmid: 27641500
4. A. Jandke *et al*., Butyrophilin-like proteins display combinatorial diversity in selecting and maintaining signature intraepithelial γδ T cell compartments. *Nat. Commun.* **11**, 3769 (2020). doi: 10.1038/s41467-020-17557-y; pmid: 32724083
5. S. D. Barbee *et al*., Skint-1 is a highly specific, unique selecting component for epidermal T cells. *Proc. Natl. Acad. Sci. U.S.A.* **108**, 3330–3335 (2011). doi: 10.1073/pnas.1010890108; pmid: 21300860
6. M. Girardi *et al*., Resident skin-specific gammadelta T cells provide local, nonredundant regulation of cutaneous inflammation. *J. Exp. Med.* **195**, 855–867 (2002). doi: 10.1084/jem.20012000; pmid: 11927630
7. M. Muñoz-Ruiz *et al*., Tissue-intrinsic γδ T cells critically regulate Tissue-Resident Memory CD8 T cells. *bioRxiv*, 2022.2001.2019.476598 (2022). doi: 10.1101/2022.01.19.476598
8. A. A. Kühl *et al*., Aggravation of intestinal inflammation by depletion/deficiency of gammadelta T cells in different types of IBD animal models. *J. Leukoc. Biol.* **81**, 168–175 (2007). doi: 10.1189/jlb.1105696; pmid: 17041003
9. Y. Chen, K. Chou, E. Fuchs, W. L. Havran, R. Boismenu, Protection of the intestinal mucosa by intraepithelial gamma delta T cells. *Proc. Natl. Acad. Sci. U.S.A.* **99**, 14338–14343 (2002). doi: 10.1073/pnas.212290499; pmid: 12376619
10. K. Inagaki-Ohara *et al*., Mucosal T cells bearing TCRgammadelta play a protective role in intestinal inflammation. *J. Immunol.* **173**, 1390–1398 (2004). doi: 10.4049/jimmunol.173.2.1390; pmid: 15240735
11. Y. Matsuzawa-Ishimoto *et al*., The γδ IEL effector API5 masks genetic susceptibility to Paneth cell death. *Nature* **610**, 547–554 (2022). doi: 10.1038/s41586-022-05259-y; pmid: 36198790
12. D. Melandri *et al*., The γδ T cell receptor combines innate with adaptive immunity by utilizing spatially distinct regions for agonist-selection and antigen responsiveness. *Nat. Immunol.* (2018). doi: 10.1038/s41590-018-0253-5
13. C. R. Willcox *et al*., Butyrophilin-like 3 directly binds a human $V\gamma4^+$ T cell receptor using a modality distinct from clonally-restricted antigen. *Immunity* **51**, 813–825.e4 (2019). doi: 10.1016/j.immuni.2019.09.006; pmid: 31628053
14. T. Mayassi *et al*., Chronic inflammation permanently reshapes tissue-resident immunity in celiac disease. *Cell* **176**, 967–981.e19 (2019). doi: 10.1016/j.cell.2018.12.039; pmid: 30739797
15. C. Lebrero-Fernández *et al*., Altered expression of butyrophilin (*BTN*) and BTN-like (*BTNL*) genes in intestinal inflammation and colon cancer. *Immun. Inflamm. Dis.* **4**, 191–200 (2016). doi: 10.1002/iid3.105; pmid: 27957327
16. N. Cerf-Bensussan *et al*., A monoclonal antibody (HML-1) defining a novel membrane molecule present on human intestinal lymphocytes. *Eur. J. Immunol.* **17**, 1279–1285 (1987). doi: 10.1002/eji.1830170910; pmid: 3498635
17. K. L. Cepek *et al*., Adhesion between epithelial cells and T lymphocytes mediated by E-cadherin and the alpha E beta 7 integrin. *Nature* **372**, 190–193 (1994). doi: 10.1038/372190a0; pmid: 7969453
18. C. Cantoni *et al*., p49, a putative HLA class I-specific inhibitory NK receptor belonging to the immunoglobulin superfamily. *Eur. J. Immunol.* **28**, 1980–1990 (1998). doi: 10.1002/(SICI)1521-4141(199806)28:06<1980::AID-IMMU1980>3.0.CO;2-F; pmid: 9645380
19. J. D. Wermers, E. N. McNamee, M. A. Wurbel, P. Jedlicka, J. Rivera-Nieves, The chemokine receptor CCR9 is required for the T-cell-mediated regulation of chronic ileitis in mice. *Gastroenterology* **140**, 1526–35.e3 (2011). doi: 10.1053/j.gastro.2011.01.044; pmid: 21300065
20. I. Voskoboinik, J. C. Whisstock, J. A. Trapani, Perforin and granzymes: Function, dysfunction and human pathology. *Nat. Rev. Immunol.* **15**, 388–400 (2015). doi: 10.1038/nri3839; pmid: 25998963
21. H. Okamura, S. Kashiwamura, H. Tsutsui, T. Yoshimoto, K. Nakanishi, Regulation of interferon-gamma production by IL-12 and IL-18. *Curr. Opin. Immunol.* **10**, 259–264 (1998). doi: 10.1016/S0952-7915(98)80163-5; pmid: 9638361
22. S. Deaglio *et al*., Adenosine generation catalyzed by CD39 and CD73 expressed on regulatory T cells mediates immune suppression. *J. Exp. Med.* **204**, 1257–1265 (2007). doi: 10.1084/jem.20062512; pmid: 17502665
23. L. Monney *et al*., Th1-specific cell surface protein Tim-3 regulates macrophage activation and severity of an autoimmune disease. *Nature* **415**, 536–541 (2002). doi: 10.1038/415536a; pmid: 11823861
24. D. Gay *et al*., Fgf9 from dermal γδ T cells induces hair follicle neogenesis after wounding. *Nat. Med.* **19**, 916–923 (2013). doi: 10.1038/nm.3181; pmid: 23727932
25. N. Atlasy *et al*., Single cell transcriptomic analysis of the immune cell compartment in the human small intestine and in Celiac disease. *Nat. Commun.* **13**, 4920 (2022). doi: 10.1038/s41467-022-32691-5; pmid: 35995787
26. B. V. Kumar *et al*., Human tissue-resident memory T Cells are defined by core transcriptional and functional signatures in lymphoid and mucosal sites. *Cell Rep.* **20**, 2921–2934 (2017). doi: 10.1016/j.celrep.2017.08.078; pmid: 28930685
27. M. E. B. FitzPatrick *et al*., Human intestinal tissue-resident memory T cells comprise transcriptionally and functionally distinct subsets. *Cell Rep.* **34**, 108661 (2021). doi: 10.1016/j.celrep.2020.108661; pmid: 33472060
28. F. Sallusto, D. Lenig, R. Förster, M. Lipp, A. Lanzavecchia, Two subsets of memory T lymphocytes with distinct homing potentials and effector functions. *Nature* **401**, 708–712 (1999). doi: 10.1038/44385; pmid: 10537110
29. J. Blackford, H. W. Reid, D. J. Pappin, F. S. Bowers, J. M. Wilkinson, A monoclonal antibody, 3/22, to rabbit CD11c which induces homotypic T cell aggregation: Evidence that ICAM-1 is a ligand for CD11c/CD18. *Eur. J. Immunol.* **26**, 525–531 (1996). doi: 10.1002/eji.1830260304; pmid: 8605916
30. H. S. Azzam *et al*., CD5 expression is developmentally regulated by T cell receptor (TCR) signals and TCR avidity. *J. Exp. Med.* **188**, 2301–2311 (1998). doi: 10.1084/jem.188.12.2301; pmid: 9858516
31. M. Orta-Mascaró *et al*., CD6 modulates thymocyte selection and peripheral T cell homeostasis. *J. Exp. Med.* **213**, 1387–1397 (2016). doi: 10.1084/jem.20151785; pmid: 27377588
32. C. T. Kuo, M. L. Veselits, J. M. Leiden, LKLF: A transcriptional regulator of single-positive T cell quiescence and survival. *Science* **277**, 1986–1990 (1997). doi: 10.1126/science.277.5334.1986; pmid: 9302292
33. N. Malhotra *et al*., A network of high-mobility group box transcription factors programs innate interleukin-17 production. *Immunity* **38**, 681–693 (2013). doi: 10.1016/j.immuni.2013.01.010; pmid: 23562159
34. A. H. Jonsson *et al*., Granzyme K^+ CD8 T cells form a core population in inflamed human tissue. *Sci. Transl. Med.* **14**, eabo0686 (2022). doi: 10.1126/scitranslmed.abo0686; pmid: 35704599
35. V. Groh *et al*., Costimulation of CD8alphabeta T cells by NKG2D via engagement by MIC induced on virus-infected cells. *Nat. Immunol.* **2**, 255–260 (2001). doi: 10.1038/85321; pmid: 11224526
36. D. R. McKenzie *et al*., Normality sensing licenses local T cells for innate-like tissue surveillance. *Nat. Immunol.* **23**, 411–422 (2022). doi: 10.1038/s41590-021-01124-8; pmid: 35165446
37. H. R. Rodewald, A. R. Arulanandam, S. Koyasu, E. L. Reinherz, The high affinity Fc epsilon receptor gamma subunit (Fc epsilon RI gamma) facilitates T cell receptor expression and antigen/major histocompatibility complex-driven signaling in the absence of CD3 zeta and CD3 eta. *J. Biol. Chem.* **266**, 15974–15978 (1991). doi: 10.1016/S0021-9258(18)98503-0; pmid: 1714902
38. H. R. Rodewald *et al*., A population of early fetal thymocytes expressing Fc gamma RII/III contains precursors of T lymphocytes and natural killer cells. *Cell* **69**, 139–150 (1992). doi: 10.1016/0092-8674(92)90125-V; pmid: 1532536
39. C. P. Liu *et al*., Abnormal T cell development in CD3-zeta-/- mutant mice and identification of a novel T cell population in the intestine. *EMBO J.* **12**, 4863–4875 (1993). doi: 10.1002/j.1460-2075.1993.tb06176.x; pmid: 8223495
40. J. Déchanet *et al*., Implication of gammadelta T cells in the human immune response to cytomegalovirus. *J. Clin. Invest.* **103**, 1437–1449 (1999). doi: 10.1172/JCI5409; pmid: 10330426
41. I. Prinz *et al*., Donor Vδ1+ γδ T cells expand after allogeneic hematopoietic stem cell transplantation and show reactivity against CMV-infected cells but not against progressing B-CLL. *Exp. Hematol. Oncol.* **2**, 14 (2013). doi: 10.1186/2162-3619-2-14; pmid: 23663319
42. M. S. Davey *et al*., Clonal selection in the human Vδ1 T cell repertoire indicates γδ TCR-dependent adaptive immune surveillance. *Nat. Commun.* **8**, 14760 (2017). doi: 10.1038/ncomms14760; pmid: 28248310
43. P. Rutgeerts *et al*., Infliximab for induction and maintenance therapy for ulcerative colitis. *N. Engl. J. Med.* **353**, 2462–2476 (2005). doi: 10.1056/NEJMoa050516; pmid: 16339095
44. W. J. Sandborn *et al*., Ustekinumab induction and maintenance therapy in refractory Crohn's disease. *N. Engl. J. Med.* **367**, 1519–1528 (2012). doi: 10.1056/NEJMoa1203572; pmid: 23075178
45. G. D'Haens *et al*., Risankizumab as induction therapy for Crohn's disease: Results from the phase 3 ADVANCE and MOTIVATE induction trials. *Lancet* **399**, 2015–2030 (2022). doi: 10.1016/S0140-6736(22)00467-6; pmid: 35644154
46. K. Parikh *et al*., Colonic epithelial cell diversity in health and inflammatory bowel disease. *Nature* **567**, 49–55 (2019). doi: 10.1038/s41586-019-0992-y; pmid: 30814735
47. J. Aigner *et al*., A common 56-kilobase deletion in a primate-specific segmental duplication creates a novel butyrophilin-like protein. *BMC Genet.* **14**, 61 (2013). doi: 10.1186/1471-2156-14-61; pmid: 23829304
48. P. Vantourout *et al*., Heteromeric interactions regulate butyrophilin (BTN) and BTN-like molecules governing γδ T cell biology. *Proc. Natl. Acad. Sci. U.S.A.* **115**, 1039–1044 (2018). doi: 10.1073/pnas.1701237115; pmid: 29339503
49. C. Power, J. Elliott, Cohort profile: 1958 British birth cohort (National Child Development Study). *Int. J. Epidemiol.* **35**, 34–41 (2006). doi: 10.1093/ije/dyi183; pmid: 16155052
50. M. S. Silverberg *et al*., Toward an integrated clinical, molecular and serological classification of inflammatory bowel disease: report of a Working Party of the 2005 Montreal World Congress of Gastroenterology. *Can. J. Gastroenterol.* **19**, 5–36 (2005).
51. B. Lo *et al*., Changes in disease behaviour and location in patients with Crohn's disease after seven years of follow-up: A Danish population-based inception cohort. *J. Crohns Colitis* **12**, 265–272 (2018). doi: 10.1093/ecco-jcc/jjx138; pmid: 29506105
52. J. Jameson *et al*., A role for skin gammadelta T cells in wound repair. *Science* **296**, 747–749 (2002). doi: 10.1126/science.1069639; pmid: 11976459
53. D. Turner *et al*., STRIDE-II: An Update on the Selecting Therapeutic Targets in Inflammatory Bowel Disease (STRIDE) Initiative of the International Organization for the Study of IBD (IOIBD): Determining Therapeutic Goals for Treat-to-Target strategies in IBD. *Gastroenterology* **160**, 1570–1583 (2021). doi: 10.1053/j.gastro.2020.12.031; pmid: 33359090
54. T. Rath *et al*., Intestinal barrier healing is superior to endoscopic and histologic remission for predicting major adverse outcomes in inflammatory bowel disease: The Prospective ERIca Trial. *Gastroenterology* **164**, 241–255 (2023). doi: 10.1053/j.gastro.2022.10.014; pmid: 36279923
55. D. T. Le *et al*., PD-1 blockade in tumors with mismatch-repair deficiency. *N. Engl. J. Med.* **372**, 2509–2520 (2015). doi: 10.1056/NEJMoa1500596; pmid: 26028255
56. S. Vermeire *et al*., Etrolizumab for maintenance therapy in patients with moderately to severely active ulcerative colitis (LAUREL): A randomised, placebo-controlled, double-blind, phase 3 study. *Lancet Gastroenterol. Hepatol.* **7**, 28–37 (2022). doi: 10.1016/S2468-1253(21)00295-8; pmid: 34798037
57. L. Peyrin-Biroulet *et al*., Etrolizumab as induction and maintenance therapy for ulcerative colitis in patients previously treated with tumour necrosis factor inhibitors (HICKORY): A phase 3, randomised, controlled trial. *Lancet Gastroenterol. Hepatol.* **7**, 128–140 (2022). doi: 10.1016/S2468-1253(21)00298-3; pmid: 34798039
58. D. P. Hoytema van Konijnenburg *et al*., Intestinal epithelial and intraepithelial T cell crosstalk mediates a dynamic response to infection. *Cell* **171**, 783–794.e13 (2017). doi: 10.1016/j.cell.2017.08.046; pmid: 28942917
59. A. Kaser *et al*., XBP1 links ER stress to intestinal inflammation and confers genetic risk for human inflammatory bowel disease. *Cell* **134**, 743–756 (2008). doi: 10.1016/j.cell.2008.07.021; pmid: 18775308
60. M. Corcoran *et al*., Archaic humans have contributed to large-scale variation in modern human T cell receptor genes.

Immunity **56**, 635–652.e6 (2023). doi: 10.1016/j.immuni.2023.01.026; pmid: 36796364
61. J. C. Lee *et al*., Genome-wide association study identifies distinct genetic contributions to prognosis and susceptibility in Crohn's disease. *Nat. Genet.* **49**, 262–268 (2017). doi: 10.1038/ng.3755; pmid: 28067912
62. I. Cleynen *et al*., Inherited determinants of Crohn's disease and ulcerative colitis phenotypes: A genetic association study. *Lancet* **387**, 156–167 (2016). doi: 10.1016/S0140-6736(15)00465-1; pmid: 26490195
63. J. F. Colombel, N. Narula, L. Peyrin-Biroulet, Management strategies to improve outcomes of patients with inflammatory bowel diseases. *Gastroenterology* **152**, 351–361.e5 (2017). doi: 10.1053/j.gastro.2016.09.046; pmid: 27720840
64. G.-R. Jones *et al*., IBD prevalence in Lothian, Scotland, derived by capture-recapture methodology. *Gut* **68**, 1953–1960 (2019). doi: 10.1136/gutjnl-2019-318936; pmid: 31300515
65. S. C. Ng *et al*., Worldwide incidence and prevalence of inflammatory bowel disease in the 21st century: A systematic review of population-based studies. *Lancet* **390**, 2769–2778 (2017). doi: 10.1016/S0140-6736(17)32448-0; pmid: 29050646
66. P. Rutgeerts *et al*., Predictability of the postoperative course of Crohn's disease. *Gastroenterology* **99**, 956–963 (1990). doi: 10.1016/0016-5085(90)90613-6; pmid: 2394349
67. M. Joseph *et al*., Global patterns of antigen receptor repertoire disruption across adaptive immune compartments in COVID-19. *Proc. Natl. Acad. Sci. U.S.A.* **119**, e2201541119 (2022). doi: 10.1073/pnas.2201541119; pmid: 35943978
68. G. Bamias *et al*., Comparative study of candidate housekeeping genes for quantification of target gene messenger RNA expression by real-time PCR in patients with inflammatory bowel disease. *Inflamm. Bowel Dis.* **19**, 2840–2847 (2013). doi: 10.1097/01.MIB.0000435440.22484.e8; pmid: 24141710
69. S. Rajput, L. D. Volk-Draper, S. Ran, TLR4 is a novel determinant of the response to paclitaxel in breast cancer. *Mol. Cancer Ther.* **12**, 1676–1687 (2013). doi: 10.1158/1535-7163.MCT-12-1019; pmid: 23720768
70. D. Kabelitz *et al*., New monoclonal antibody (23D12) recognizing three different V gamma elements of the human gamma delta T cell receptor. 23D12+ cells comprise a major subpopulation of gamma delta T cells in postnatal thymus. *J. Immunol.* **152**, 3128–3136 (1994). doi: 10.4049/jimmunol.152.6.3128; pmid: 7511639
71. D. J. Schofield *et al*., Application of phage display to high throughput antibody generation and characterization. *Genome Biol.* **8**, R254 (2007). doi: 10.1186/gb-2007-8-11-r254; pmid: 18047641
72. M. I. Love, W. Huber, S. Anders, Moderated estimation of fold change and dispersion for RNA-seq data with DESeq2. *Genome Biol.* **15**, 550 (2014). doi: 10.1186/s13059-014-0550-8; pmid: 25516281
73. R. Edgar, M. Domrachev, A. E. Lash, Gene Expression Omnibus: NCBI gene expression and hybridization array data repository. *Nucleic Acids Res.* **30**, 207–210 (2002). doi: 10.1093/nar/30.1.207; pmid: 11752295
74. B. Langmead, S. L. Salzberg, Fast gapped-read alignment with Bowtie 2. *Nat. Methods* **9**, 357–359 (2012). doi: 10.1038/nmeth.1923; pmid: 22388286
75. A. Dobin *et al*., STAR: Ultrafast universal RNA-seq aligner. *Bioinformatics* **29**, 15–21 (2013). doi: 10.1093/bioinformatics/bts635; pmid: 23104886
76. A. Subramanian *et al*., Gene set enrichment analysis: A knowledge-based approach for interpreting genome-wide expression profiles. *Proc. Natl. Acad. Sci. U.S.A.* **102**, 15545–15550 (2005). doi: 10.1073/pnas.0506580102; pmid: 16199517
77. U. Raudvere *et al*., g:Profiler: a web server for functional enrichment analysis and conversions of gene lists (2019 update). *Nucleic Acids Res.* **47** (W1), W191–W198 (2019). doi: 10.1093/nar/gkz369; pmid: 31066453
78. S. Myers, C. Freeman, A. Auton, P. Donnelly, G. McVean, A common sequence motif associated with recombination hot spots and genome instability in humans. *Nat. Genet.* **40**, 1124–1129 (2008). doi: 10.1038/ng.213; pmid: 19165926

ACKNOWLEDGMENTS

We acknowledge the help of the IBD Bioresource, supported by the NIHR, Medical Research Council, Crohn's and Colitis UK, Open Targets, and the Wellcome Trust Sanger Institute. We thank O. Polyakova, A. McGinley, D. Wesch, and D. Kabelitz for provision of antibodies and J. Sanderson and the staff and patients of Guy's and St Thomas Foundation Trust for support related to clinical sampling. We also thank D. Gibbons, T. Raine, J. Spencer, and D. McKenzie for their critical review of the manuscript and their insights. The print summary figure was created with BioRender.com. **Funding:** This work was supported by the NIHR Newcastle Biomedical Research Centre; the NIHR Guy's and St Thomas Biomedical Research Centre; the NIHR Biomedical Research Centre at Cambridge University Hospital NHS Foundation Trust and the University of Cambridge; the Francis Crick Institute, which receives its core funding from Cancer Research UK (CRUK) (FC001003), the UK Medical Research Council (FC001003), and the Wellcome Trust (FC001003); a clinical research training fellowship from the Wellcome Trust (108745/Z/15/Z to R.J.D.); a studentship from the NIHR Biomedical Research Centre at Guy's and St Thomas' NHS Foundation Trust and King's College London (I.Z); and the Wellcome Trust (094491/Z/10/Z to N.J.P.) and (106292/Z/14/Z and 100156/Z/12/Z to A.C.H.). **Author contributions:** Conceptualization: R.J.D., I.Z., P.V., N.J.P., A.C.H.; Data curation: R.J.D., I.Z., S.K., P.E., J.C.M., C.A.L., M.P., N.J.P., A.C.H.; Formal analysis: R.J.D., I.Z., S.K., P.E.; Funding acquisition: R.J.D., N.J.P., A.C.H.; Investigation: R.J.D., I.Z., P.V., E.T., A.A., T.R., J.C.M., C.A.L.; Methodology: R.J.D., I.Z., P.V., S.K., P.E. N.J.P.; Project administration: R.J.D., I.Z., A.C.H.; Resources: R.J.D., I.Z., A.A., P.V., J.C.M., C.A.L., M.P., P.M.I., N.J.P. A.C.H.; Software: S.K., P.E.; Supervision: P.V., P.M.I., N.J.P., A.C.H.; Validation: R.J.D., I.Z., P.V., E.T., A.A., N.J.P., A.C.H.; Visualization: R.J.D., I.Z., P.V., P.E., N.J.P.; Writing – original draft preparation R.J.D., I.Z., P.V., A.C.H.; Writing – review and editing: all authors. **Competing interests:** R.J.D., I.Z., P.V., N.J.P., and A.C.H. are inventors on patent application WO2019053272A1 submitted by King's College London that covers the use of "compositions and methods for enhancing gamma delta T cells in the gut." R.J.D., I.Z., P.V., and A.C.H. are inventors on patent application WO2019234136A1 submitted by King's College London and Gamma Delta Therapeutics that covers the use of "BTNL3/8 targeting constructs for delivery of payloads to the gastrointestinal system." P.V. and A.C.H. are inventors on patent applications WO2021171002A1 and WO2021171003A1 submitted by Gamma Delta Therapeutics entitled "Ex vivo gamma delta T cell populations." R.J.D. has received speaking and/or consulting fees from Janssen, Takeda, and Tillotts, all of which were unrelated to this manuscript. C.A.L. declares research support and/or fees for the development and delivery of nonpromotional education from Janssen, Dr Falk, Takeda, Abbvie, AstraZeneca, Eli Lilly, Orion, Pfizer, Roche, Sanofi Aventis, Ferring, UCB, Biogen, and Genentech Inc., all of which were unrelated to this manuscript. P.M.I. declares research support and/or fees for the development and delivery of nonpromotional education from AbbVie, Arena, Boehringer-Ingelheim, BMS, Celgene, Celltrion, Falk Pharma, Ferring, Genentech Inc., Galapagos, Gilead, Hospira, MSD, Janssen, Lilly, Pfizer, Pharmacosmos, Prometheus, Roche, Sandoz, Samsung Bioepis, Takeda, Tillotts, Topivert, Sapphire Medical, Shire, VH2, Vifor Pharma, Warner Chilcott, all of which were unrelated to this manuscript. A.C.H. is a scientific consultant for Prokarium and eGenesis and Takeda and receives research funds from Takeda Pharmaceuticals. The remaining authors declare no competing interests. **Data and materials availability:** All data are available in the main manuscript or the supplementary materials or have been deposited as follows. Sequencing data generated for this study are available on the National Center for Biotechnology Information (NCBI) GeneExpression Omnibus (GEO) under accession numbers GSE218058, GSE224412, and GSE218446. All reagents derived for these studies will be shared upon request with other researchers in academia. Any material transfer agreements will be organized upon receipt of request to the corresponding authors. **License information:** Copyright © 2023 the authors, some rights reserved; exclusive licensee American Association for the Advancement of Science. No claim to original US government works. https://www.science.org/about/science-licenses-journal-article-reuse. This research was funded in whole or in part by the Wellcome Trust (grants FC001003, 108745/Z/15/Z, 094491/Z/10/Z, 106292/Z/14/Z, and 100156/Z/12/Z), a cOAlition S organization. The author will make the Author Accepted Manuscript (AAM) version available under a CC BY public copyright license.

SUPPLEMENTARY MATERIALS

science.org/doi/10.1126/science.adh0301
Figs. S1 to S6
Tables S1 to S4
Data S1
MDAR Reproducibility Checklist

Submitted 9 February 2023; accepted 19 July 2023
10.1126/science.adh0301

RESEARCH ARTICLE

COMPARATIVE COGNITION

Songbird species that display more-complex vocal learning are better problem-solvers and have larger brains

Jean-Nicolas Audet[1,2]*, Mélanie Couture[1,3], Erich D. Jarvis[1,2,3,4]*

Complex vocal learning, a critical component of human spoken language, has been assumed to be associated with more-advanced cognitive abilities. Tests of this hypothesis between individuals within a species have been inconclusive and have not been done across species. In this work, we measured an array of cognitive skills—namely, problem-solving, associative and reversal learning, and self-control—across 214 individuals of 23 bird species, including 19 wild-caught songbird species, two domesticated songbird species, and two wild-caught vocal nonlearning species. We found that the greater the vocal learning abilities of a species, the better their problem-solving skills and the relatively larger their brains. These conclusions held when controlling for noncognitive variables and phylogeny. Our results support a hypothesis of shared genetic and cognitive mechanisms between vocal learning, problem-solving, and bigger brains in songbirds.

Spoken language and problem-solving are often considered to be components of intelligence in humans. An essential and specialized component of spoken language is vocal production learning, or the ability to imitate sounds (*1*, *2*). Advanced vocal learning has been found in only a handful of taxa, including five mammalian (humans, elephants, cetaceans, pinnipeds, and bats) and three avian (songbirds, parrots, and hummingbirds) clades (*1*). Interestingly, the vocal learning taxa that display the most-complex vocal learning behavior overlap with those long thought to exhibit more-intelligent cognitive capacities [e.g., humans, cetaceans, elephants, corvid songbirds, and parrots (*3*, *4*)], although this has not been quantitatively tested across species.

The few studies that have tested for relationships between vocal learning complexity and cognitive abilities have all been within species (*5*). Some studies found positive relationships (*6*, *7*), whereas others did not (*8*–*10*), and some found negative relationships (*7*, *11*), which led Searcy and Nowicki (*5*) to conclude that there is not good evidence of such relationships. The challenge for these within-species studies is that it is difficult to tease out whether individual differences are due to genetic factors or cultural or life-experience factors, such as food deprivation (*12*) or stress (*13*).

Although vocal learning is often thought of as a dichotomous trait, considerable variation in phenotypes has been documented within lineages, with songbirds being the most speciose

[1]The Rockefeller University Field Research Center, Millbrook, NY, USA. [2]Laboratory of Neurogenetics of Language, The Rockefeller University, New York, NY, USA. [3]The Vertebrate Genome Laboratory, The Rockefeller University, New York, NY, USA. [4]Howard Hughes Medical Institute, The Rockefeller University, New York, NY, USA.
***Corresponding author. Email: jaudet@rockefeller.edu (J.-N.A.); ejarvis@rockefeller.edu (E.D.J.)**

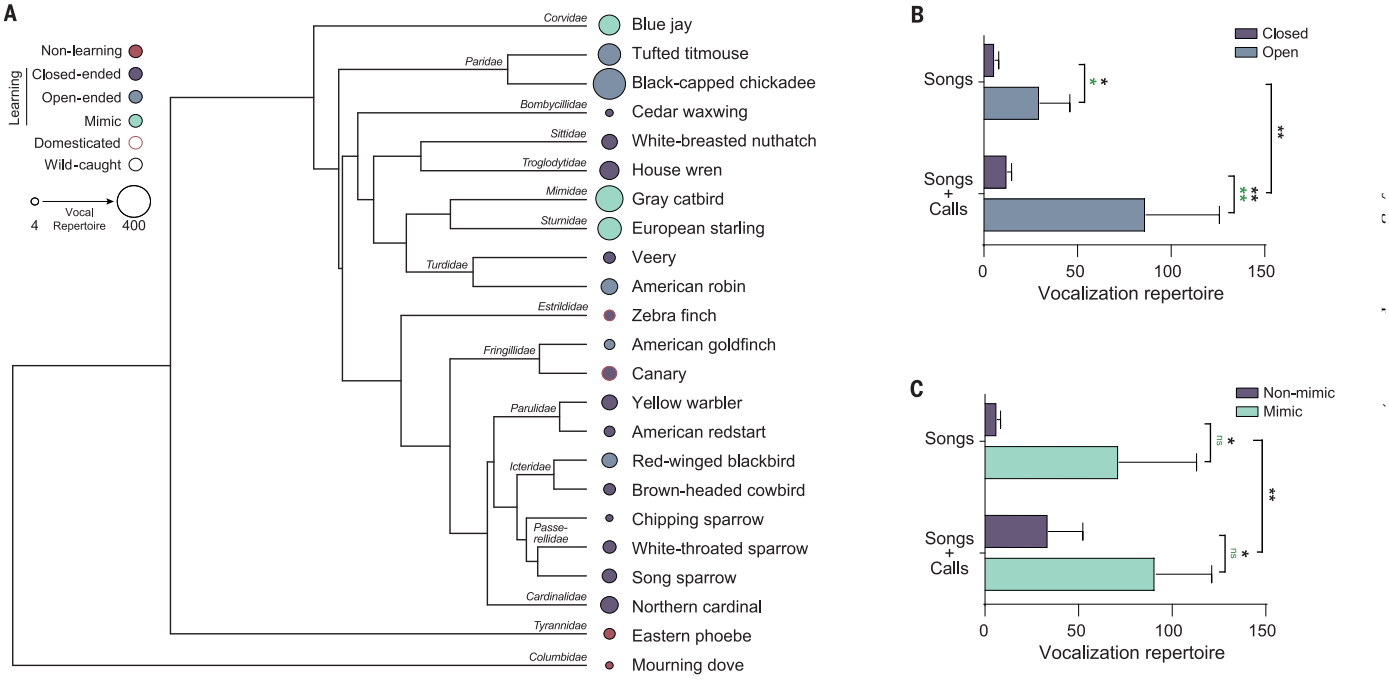

Fig. 1. The 23 study species of birds and their vocal learning characteristics. (**A**) Phylogenetic tree of the species that were studied based on (*42*). Inside circle colors indicate the type of vocal learning, perimeter circle colors indicate domesticated versus wild species, and circle size is proportional to vocalization repertoire size. (**B**) Comparisons of song and call repertoire sizes in open- versus closed-ended vocal learning songbirds (n = 21 species). (**C**) Comparison of mimic and nonmimic species. Black * and ** indicate significant P_{ANOVA} at <0.05 and <0.01, respectively. Green * and ** indicate significant $P_{AOV.PHYLO}$ (ANOVA accounting for phylogenetic relationships). ns, not significant. Full statistical values are provided in table S2. Bars are means ± SEM.

Table 1. Summary of MCMCglmm phylogenetic models. Full, separate models were implemented for vocal learning type [closed-ended (reference category), open-ended, and mimicry]; repertoire size of songs, calls, or both; and vocal learning complexity. All potential covariates were tested first (see tables S4 to S7), and the models with only the significant variables, when applicable (with species, phylogeny, and capture site as random effects), were rerun to obtain unbiased effects of vocal learning. Significant effects are highlighted in bold. All measured behaviors are expressed in logged trials; higher numbers represent lower performance (n = 23 species, 214 individuals). Post.mean, mean of the posterior distribution; CI, confidence interval; pMCMC, MCMCglmm P value.

Cognitive trait	Vocal learning feature	Post.mean	Lower 95% CI	Upper 95% CI	pMCMC
Problem-solving	**Open-endedness**	**−1.151**	**−1.806**	**−0.517**	**0.0020**
	Mimicry	**−1.036**	**−2.015**	**−0.056**	**0.0378**
	Song repertoire	**−0.174**	**−0.323**	**−0.030**	**0.0217**
	Call repertoire	**−0.187**	**−0.342**	**−0.032**	**0.0216**
	Total vocal repertoire	**−0.257**	**−0.395**	**−0.118**	**0.0018**
	Vocal learning complexity	**−0.090**	**−0.134**	**−0.046**	**0.0012**
Learning	Open-endedness	−0.391	−0.843	0.060	0.0889
	Mimicry	−0.295	−0.890	0.297	0.3065
	Song repertoire	0.024	−0.078	0.126	0.6366
	Call repertoire	−0.038	−0.141	0.068	0.4620
	Total vocal repertoire	−0.009	−0.124	0.106	0.8780
	Vocal learning complexity	−0.016	−0.054	0.021	0.3768
Reversal learning	**Open-endedness**	**−0.818**	**−1.497**	**−0.133**	**0.0269**
	Mimicry	−0.607	−1.469	0.272	0.1634
	Song repertoire	0.066	−0.092	0.227	0.4115
	Call repertoire	−0.029	−0.194	0.140	0.7206
	Total vocal repertoire	0.005	−0.173	0.185	0.9675
	Vocal learning complexity	−0.037	−0.093	0.021	0.1978
Self-control	Open-endedness	−0.111	−0.910	0.667	0.7938
	Mimicry	−0.725	−1.928	0.443	0.2026
	Song repertoire	0.003	−0.144	0.148	0.9554
	Call repertoire	−0.009	−0.162	0.147	0.8932
	Total vocal repertoire	0.002	−0.160	0.169	0.9742
	Vocal learning complexity	−0.023	−0.080	0.034	0.4057
Relative brain size	Open-endedness	0.976	−0.390	2.362	0.1571
	Mimicry	1.971	−0.248	4.242	0.0812
	Song repertoire	**1.373**	**0.114**	**2.628**	**0.0362**
	Call repertoire	**1.702**	**0.392**	**2.989**	**0.0132**
	Total vocal repertoire	**2.297**	**1.125**	**3.494**	**0.0013**
	Vocal learning complexity	**0.678**	**0.242**	**1.119**	**0.0037**

and best-characterized clade (*1*, *14*–*16*). Features that are believed to reflect more-complex vocal learning in songbirds include (i) large vocal repertoires, (ii) lifelong open-ended vocal learning ability, and (iii) mimicry of other species' vocalizations (*16*–*18*). It is unknown whether these vocal learning variations are linked with other cognitive phenotypes.

Cognition has been measured in the laboratory using a variety of behavioral tasks. Of these, problem-solving is assumed to be one of the most complex, requiring animals to figure out the best action to overcome a challenge. Problem-solving may be relevant for allowing animals to cope with ecological disturbances (*19*). Other cognitive assays that are often conceptually linked with intelligence include associative learning, reversal learning, and self-control tasks (*20*).

In this work, we quantitatively tested whether there is a linkage between vocal learning complexity and other cognitive traits. We tested 214 individuals from 23 species consisting of 21 wild-caught and two domesticated avian species; 21 species were vocal learning songbirds, and two were vocal nonlearning species (Fig. 1A). We generated a database of vocal learning characteristics of these species from an extensive literature of 80 publications (table S1), assessed species' performance on a battery of behavioral tasks (fig. S1 and supplementary methods), and found across-species relationships between vocal learning complexity, problem-solving, and relative brain size.

Vocalization repertoire size is associated with open-endedness and mimicry

Wild birds were caught at the Rockefeller University Field Research Center in New York, USA, over a 3-year period, and domesticated species were bred at the same location (zebra finches) or purchased from a local breeder (canaries). Birds were opportunistically captured in mist nets, and species were chosen if their local abundance allowed for a sufficient sample size ($n \geq 12$) of males (the vocal learning sex for most species); in addition, for eight species, we kept and tested one or two animals each to see whether they would follow a trend. All birds were habituated individually in cages for 3 days, where they could hear but not see other individuals.

For all 23 species, literature exists on their vocal behavior (table S1). We used these data to establish a consistently defined profile for each species in a database that included six vocal learning characteristics: (i) presence of vocal learning, (ii) open-ended versus closed-ended vocal learning, (iii) capacity for vocal mimicry of other species, (iv) song repertoire size per individual, (v) call repertoire size per species, and (vi) total repertoire size of both songs and calls (supplementary methods and table S1).

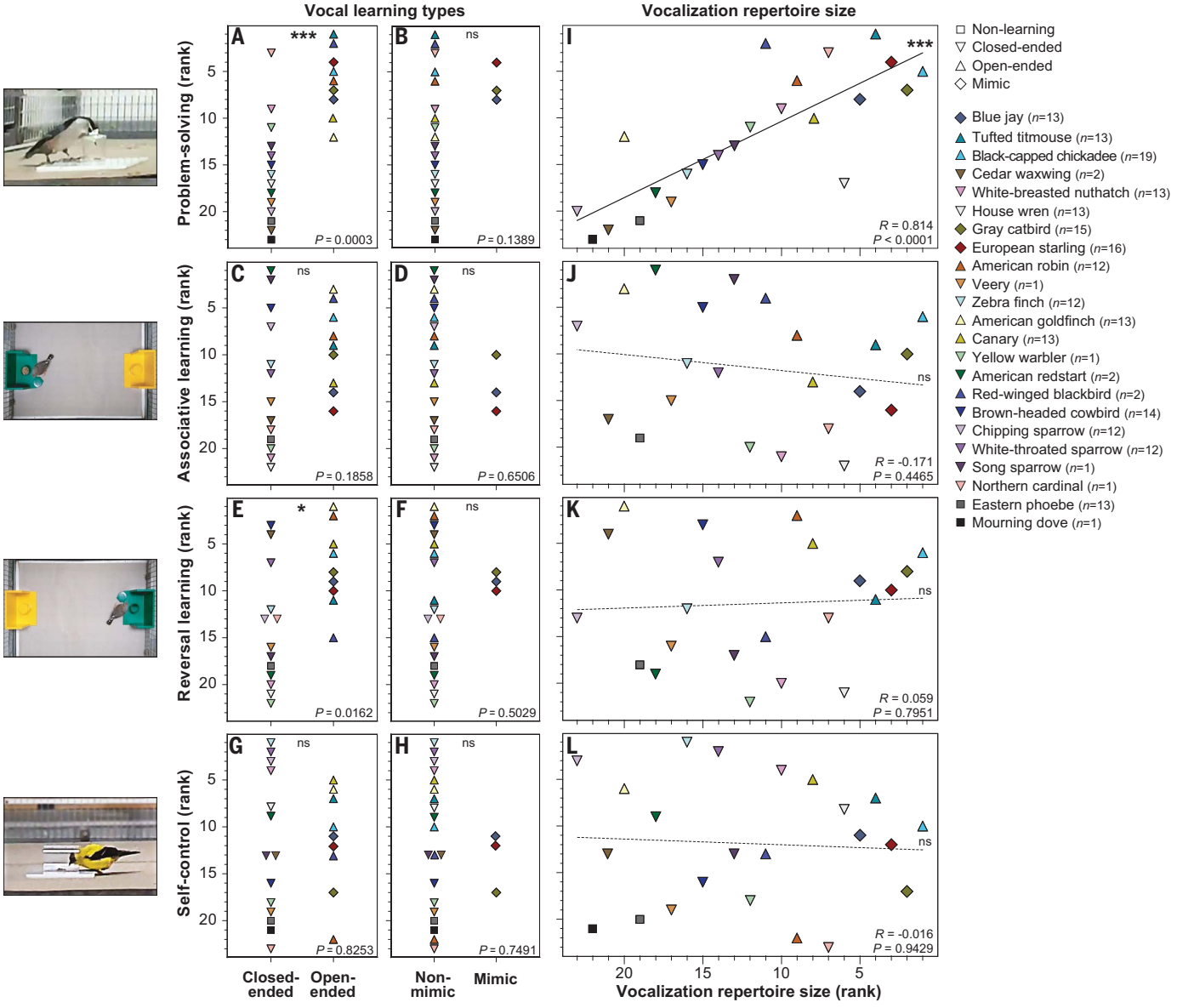

Fig. 2. Relationships between cognitive traits and vocal learning features. (**A** to **H**) Four cognitive measures (*y* axes) compared between species grouped by vocal learning features (*x* axes: closed-ended, which includes vocal nonlearning species; open-ended; and nonmimic or mimic). (**I** to **L**) Correlation analyses between the four cognitive behavioral measures (*y* axes) and vocalization repertoire size (*x* axis). Values are ranked means of species performance from all individuals (sample sizes are shown in the legend). *P* values in (A) to (H) are from Wilcoxon tests; *R* and *P* values in (I) to (L) are from Spearman correlations. Regression lines are for illustration purposes to show the significance and direction of relationships. Images to the left are examples of birds in the different tasks, which are snapshots from videos taken by the authors. ***$P < 0.001$; *$P < 0.05$; ns, not significant.

We found that, consistent with Robinson *et al.* (*18*), open-ended vocal learning songbirds had significantly larger song repertoires than closed-ended vocal learners (Fig. 1B and table S2A). Using the complete vocalization repertoires (song and calls) yielded an even greater difference between open- and closed-ended vocal learning species (Fig. 1B and table S2A). Similarly, songbird species that are capable of vocal mimicry had larger repertoires than nonmimics (Fig. 1C and table S2A). All of these differences increased in significance when including the two vocal nonlearners (the mourning dove and suboscine eastern phoebe; table S2B), which were at the lower end of the distribution for song and call repertoire sizes (table S1). Nearly all differences were still significant when accounting for phylogenetic relationships in the analysis of variance (ANOVA) model, except for repertoire size between mimic and nonmimic songbirds, which still approached significance [phylogenetic ANOVA *P* value ($P_{AOV.PHYLO}$) ~ 0.07; table S2B]. These findings demonstrate that relationships exist among different vocal learning phenotypes.

Species with more-advanced vocal learning abilities are better problem-solvers

We presented all 214 individuals of the 23 bird species with seven cognitive tasks after overnight food deprivation, the duration of which was adjusted to the night lengths and body weights of each individual. The tasks occurred over 6 days in the same sequence, with 5-min intervals between trials or tasks (supplementary

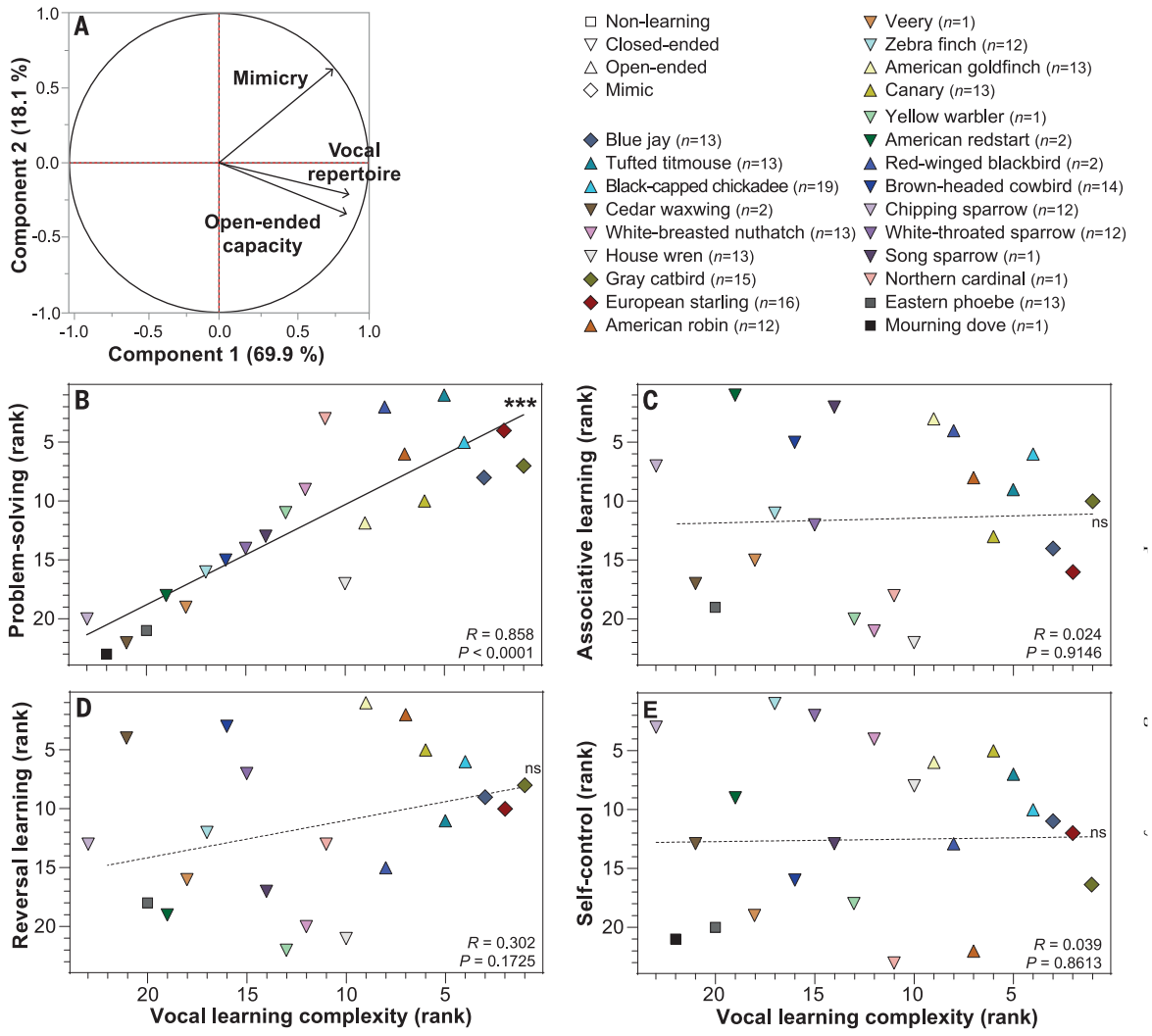

Fig. 3. Species that display higher vocal learning complexity are better problem-solvers. (**A**) PCA on open-ended capacity, mimicry capacity, and log of vocalization repertoire (songs and calls). PC1 explains 69.9% of the variance and was used as our index of vocal learning complexity. (**B**) The higher the vocal learning complexity, the better the problem-solving performance among species. (**C** to **E**) Species' associative learning (C), reversal learning (D), and self-control (E) performances are not associated with vocal learning complexity. Values are ranked means of species performance from all individuals (sample sizes are shown in the legend). *R* and *P* values are from Spearman correlations. ***$P < 0.001$; ns, not significant.

methods). The first four were different obstacle-removal tasks of increasing complexity, during which the birds had to figure out how to access a food reward (seeds or worms) by either removing, piercing, or pulling parts of the apparatuses (fig. S1, F to I, and movies S1 to S4). We used the average number of trials required to solve the four problems as our problem-solving measure. Self-control was evaluated using a typical detour-reaching task in which birds had to access a food reward without trying to obtain the food through a transparent barrier (fig. S1J and movies S5 to S6). Associative learning was measured on a standard two-color discrimination task in which birds had to associate a color with a food reward (fig. S1K and movie S7). The rewarded color was switched the next day to assess reversal learning.

Looking at the categorical vocal learning variables, we found that species classified as open-ended vocal learners were significantly better problem-solvers than the other species (Fig. 2A). Species capable of vocal mimicry were at the upper problem-solving performance range, although the difference was not significant (Fig. 2B). There were no significant differences for open-ended or mimicking vocal learning species and their associative learning abilities (Fig. 2, C and D), reversal learning (Fig. 2, E and F), or self-control (Fig. 2, G and H), except a largely overlapping, but significantly better, reversal learning performance in open-ended vocal learners (Fig. 2E). When splitting the vocal learning phenotypes into a more-sensitive multigroup ANOVA analysis, only problem-solving was significantly better for both open-ended vocal learners and mimics (fig. S2, A to D).

Looking at the continuous vocal learning variables, we found a strong and significant relationship, with species having the largest repertoires (songs and calls) being the best problem-solvers (Fig. 2I). We found no significant correlations or even qualitative signs of a correlation between vocalization repertoire size and associative learning, reversal learning, or self-control (Fig. 2, J to L). Considering only songs or calls yielded similar significant relationships with problem-solving, although the associations were weaker (table S3). Excluding vocal nonlearning and domesticated species yielded identical conclusions (fig. S2, F to I). When excluding the eight species with small sample sizes, the correlation between vocalization repertoire size and problem-solving remained (Spearman's correlation $R = 0.779$; $P = 0.0006$). Together, these results indicate a positive association between vocal learning features and problem-solving among cognitive traits.

Vocal learning complexity better predicts problem-solving performance

To obtain an estimate of general vocal learning complexity, we performed a principal components analysis (PCA) with the three vocal learning features (open-endedness, mimicry, and total vocalization repertoire size) and extracted the first principal component (PC1), which explained the majority (69.9%) of the variance in all three measures (Fig. 3A). We found a positive and significant relationship

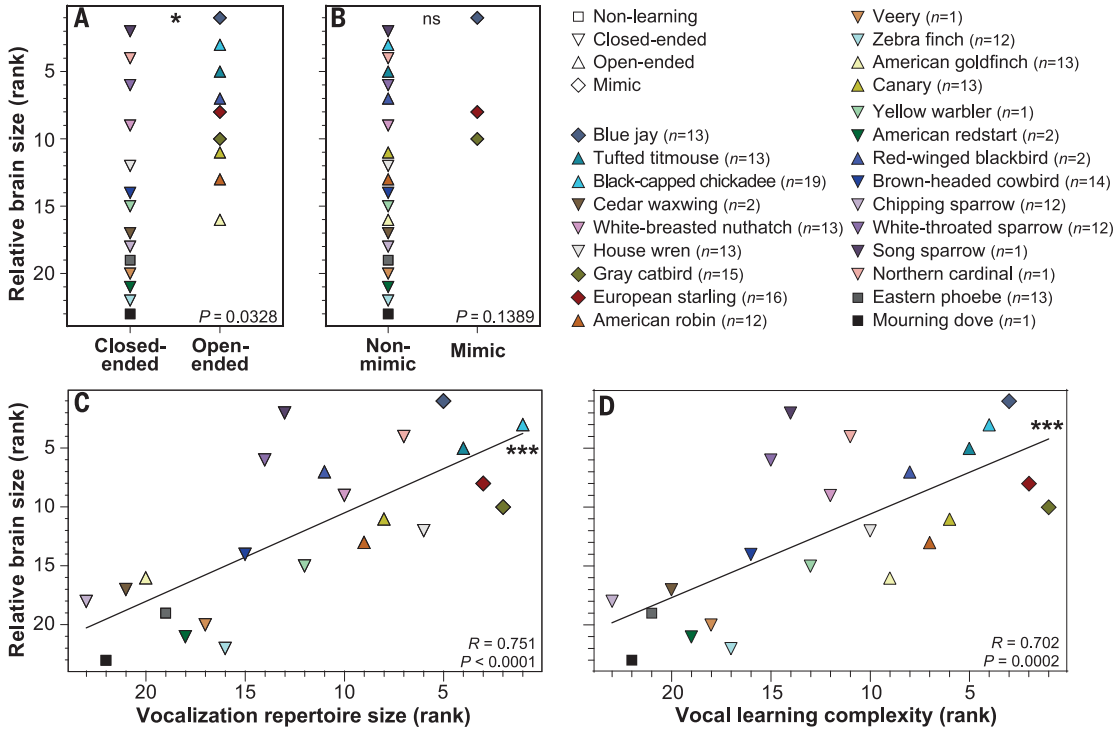

Fig. 4. Relationships between relative brain size and vocal learning features. (**A**) Open-ended vocal learning species have significantly larger relative brain sizes than the other species. (**B**) The difference in brain size between mimic and nonmimic species is not significant. (**C**) Vocalization repertoire is significantly associated with relative brain size. (**D**) Species' vocal learning complexity is also significantly associated with relative brain size. Relative brain sizes are the residuals of brain volumes with body size obtained from (*43*). *P* values in (A) and (B) are from Wilcoxon tests; *R* and *P* values in (C) and (D) are from Spearman correlations, with vocal learning complexity from PC1 of Fig. 3A. ***$P < 0.001$; *$P < 0.05$; ns, not significant.

between the vocal learning complexity PC1 and problem-solving across species, which was stronger than with any of the individual vocal learning features (Fig. 3B versus Fig. 2, A to B and I). Vocal learning complexity was unrelated to the other cognitive traits of associative learning, reversal learning, or self-control (Figs. 3, C to E). Again, excluding vocal nonlearning and domesticated species did not change the outcome of the results (fig. S3). When excluding the eight species with small sample sizes, the correlation between vocal learning complexity and problem-solving remained ($R = 0.846$; $P = 0.0001$). These findings strengthen the conclusion of an association between vocal learning abilities and problem-solving across species and provide a means to summarize overall vocal learning complexity in one measure.

More-advanced vocal learners have bigger brains

We sought a biological variable that could explain our findings and examined relative brain size (brain to body size residuals), which, although a coarse measure, was available for all the studied species (*21*). Previously, relative brain size was found to vary with counts of field innovations (*22*, *23*) and higher neuron numbers (*24*), and the size of the songbird high vocal center (HVC) vocal learning nucleus was found to vary positively with song repertoire size (*25*, *26*). We found that open-ended vocal learning species had significantly larger relative brain sizes, but there was no significant difference in mimicking species (Fig. 4, A and B). Further, there was a significant positive correlation between vocal repertoire size, as well as overall vocal learning complexity, and relative brain size (Fig. 4, C and D). These relationships again held when excluding vocal nonlearning and domesticated species (figs. S2J and S3E) or species with low sample size (vocal learning complexity $R_{VLC} = 0.714$; $P_{VLC} = 0.0028$). These findings show that vocal learning complexity, problem-solving abilities, and relatively larger brains are all related.

Vocal learning cognitive relationships are not due to noncognitive factors or phylogeny

We tested whether the relationships that we discovered could (i) also be found when including individual variation, (ii) be explained by noncognitive factors such as personality traits and captive conditions, or (iii) be explained by phylogeny relationships. To address these factors within the same analysis, we used generalized linear mixed models of Markov chain Monte Carlo techniques (MCMCglmm). The models included phylogenetic relationships between species as a random effect, personality traits (shyness, or latency to feed following human disturbance; neophobia, or latency to feed in the presence of a novel object, minus shyness), experimental conditions (capture site, food deprivation period, body weight), and captive status (wild or domesticated) on the whole dataset of the 214 individual values.

Open-endedness, mimicry, vocalization repertoire size, and vocal learning complexity all still significantly predicted problem-solving performance in the MCMCglmm modeling; they were still not associated with associative learning, reversal learning, or self-control, except for reversal learning, which was marginally associated with vocal learning open-endedness (Table 1 and tables S4 to S7). In addition, shyness was negatively associated with problem-solving and positively associated with reversal learning and self-control, neophobia was negatively associated with associative learning, and body weight was negatively associated with self-control but positively associated with reversal learning (Table 1 and tables S4 to S7). Although open-ended vocal learning or mimicry did not predict brain size, repertoire size and vocal learning complexity were significantly associated with relative brain size in the MCMCglmm modeling (Table 1 and tables S5 to S7). Excluding species with small sample sizes yielded similar relationships between vocal learning complexity and all tested cognitive traits (table S8). Thus, MCMCglmm analyses strongly support the existence of a robust relationship between vocal learning abilities, problem-solving, and brain size, even when taking into account individual variation, phylogeny, and other potential confounding covariates.

Discussion

Our findings suggest a coevolution between vocal learning complexity, problem-solving, and relative brain size. Vocal learning and innovative problem-solving have separately been linked with extinction risk, fitness, and

sexual selection (*19*, *27*). Further, both problem-solving and bird songs vary according to habitat differences, for example, urbanization (*28*, *29*). To explain our and these ecological findings, we suggest that a selective factor links these traits within a "vocal learning cognitive complex." This selective factor could be a genetic component that drives coevolution of vocal learning complexity, problem-solving, and relative brain size.

Previous studies that performed within-species comparisons on vocal learning and other cognitive traits found no or conflicting evidence of relationships [(*6*, *7*, *9*, *10*, *12*), reviewed in (*5*)]. A major factor as to why we find a clear relationship between vocal learning complexity and problem-solving is likely greater differences across than within species. In addition, some studies trained birds to first solve problems and then measured their capacity to repeat the learned solution, whereas we measured problem-solving on the first trial. We also generated a new measure of vocal learning complexity that did not ignore calls that were assumed to be innate but included calls and songs together. Calls are increasingly recognized as learned in vocal learning species (*30*, *31*).

Our finding of a link between vocal learning complexity and brain size is consistent with the prior finding that two of the three avian vocal learning lineages (songbirds and parrots) have larger relative brain sizes and a higher density of telencephalic neurons compared with vocal nonlearners (*32*). Devoogd *et al*. (*25*) found a relationship between song repertoire size and the HVC size across songbird species, but not telencephalon size [confirmed in (*26*)]. We hypothesize that the relative increase in brain size across species could be due to relative increases in the song system and the adjacent nonvocal motor circuit (*33*) that is potentially involved in problem-solving. Vocal learners can also synchronize body movements to rhythmic sounds of music (dance), which is thought to be controlled by the surrounding motor circuits (*34*, *35*) and could be another component of a vocal learning cognitive complex. Another brain region to consider is the caudal-lateral nidopallium (NCL), or avian prefrontal cortex, which is involved in complex cognitive processing (*36*). Regardless of specific brain regions, a higher density of neurons likely provides vocal learners with more brain computational power.

At the molecular level, expression levels of different *N*-methyl-D-aspartate (NMDA) glutamate receptor subunits in song nuclei and nearby brain regions have been associated with both complex vocal learning capacity (*37*, *38*) and problem-solving (*39*). Thus, this neurotransmitter receptor family is a plausible candidate to partly explain our discovered cognitive relationships.

There has been a long-standing assumption of a link between human spoken language, advanced cognition, and larger brain size relative to other species (*40*). Our study quantitatively tests such a relationship between species in a vocal learning bird lineage and serves as a model for testing other avian and mammalian lineages. Testing cognitive abilities across more-divergent species might be more challenging because it may require different apparatus designs, whereas this is not the case for comparative genomic studies across species without behavioral testing [e.g., (*41*)]. For example, some bird lineages have highly divergent beak shapes (e.g., hummingbirds, pelicans) or rely mainly on their feet to manipulate objects (e.g., parrots, birds of prey). Moreover, the vocal repertoires of many nonsongbird species are not as well characterized as those of songbirds. Nevertheless, it would be interesting to see whether the relationships we discovered here exist for other vocal learning species and innate repertoires of vocal nonlearning species. Our results support the continuum hypothesis of vocal learning within a clade (*1*). More broadly, our discoveries open the door for an unexplored sphere of research on shared neurobiological, molecular, and physiological evolutionary foundations of vocal learning and problem-solving.

REFERENCES AND NOTES

1. E. D. Jarvis, *Science* **366**, 50–54 (2019).
2. V. M. Janik, P. J. B. Slater, *Anim. Behav.* **60**, 1–11 (2000).
3. J. O. Van Horik, N. S. Clayton, N. J. Emery, in *The Oxford Handbook of Comparative Evolutionary Psychology*, T. K. Shackelford, J. Vonk, Eds. (Oxford Univ. Press, 2012).
4. S. M. Reader, K. N. Laland, Eds., *Animal Innovation* (Oxford Univ. Press, ed. 1, 2003).
5. W. A. Searcy, S. Nowicki, *Anim. Behav.* **151**, 217–227 (2019).
6. N. J. Boogert, L.-A. Giraldeau, L. Lefebvre, *Anim. Behav.* **76**, 1735–1741 (2008).
7. N. J. Boogert, R. C. Anderson, S. Peters, W. A. Searcy, S. Nowicki, *Anim. Behav.* **81**, 1209–1216 (2011).
8. C. N. Templeton, K. N. Laland, N. J. Boogert, *Anim. Behav.* **92**, 63–71 (2014).
9. R. C. Anderson *et al*., *Anim. Cogn.* **20**, 309–320 (2017).
10. A. L. DuBois, S. Nowicki, S. Peters, K. D. Rivera-Cáceres, W. A. Searcy, *Anim. Behav.* **137**, 205–213 (2018).
11. K. B. Sewall, J. A. Soha, S. Peters, S. Nowicki, *Biol. Lett.* **9**, 20130344 (2013).
12. T. M. Farrell, K. Weaver, Y.-S. An, S. A. MacDougall-Shackleton, *Behav. Ecol.* **23**, 101–111 (2012).
13. K. L. Schmidt, S. D. Moore, E. A. MacDougall-Shackleton, S. A. MacDougall-Shackleton, *Anim. Behav.* **86**, 25–35 (2013).
14. S. C. Vernes *et al*., *Philos. Trans. R. Soc. Lond. Ser. B* **376**, 20200236 (2021).
15. M. Wirthlin *et al*., *Neuron* **104**, 87–99 (2019).
16. W. A. Searcy, J. Soha, S. Peters, S. Nowicki, *Philos. Trans. R. Soc. Lond. Ser. B* **376**, 20200257 (2021).
17. P. Rundstrom, N. Creanza, *Curr. Opin. Neurobiol.* **67**, 228–239 (2021).
18. C. M. Robinson, K. T. Snyder, N. Creanza, *eLife* **8**, e44454 (2019).
19. J.-N. Audet, *Integr. Comp. Biol.* **60**, 955–966 (2020).
20. J.-N. Audet, L. Lefebvre, *Behav. Ecol.* **28**, 943–947 (2017).
21. F. Sayol, D. Sol, A. L. Pigot, *Front. Ecol. Evol.* **8**, 58 (2020).
22. L. Lefebvre, S. M. Reader, D. Sol, *Brain Behav. Evol.* **63**, 233–246 (2004).
23. S. Benson-Amram, B. Dantzer, G. Stricker, E. M. Swanson, K. E. Holekamp, *Proc. Natl. Acad. Sci. U.S.A.* **113**, 2532–2537 (2016).
24. D. Sol *et al*., *Nat. Ecol. Evol.* **6**, 1381–1389 (2022).
25. T. J. Devoogd, J. R. Krebs, S. D. Healy, A. Purvis, *Proc. Biol. Sci.* **254**, 75–82 (1993).
26. L. Z. Garamszegi, M. Eens, J. Erritzøe, A. P. Møller, *Behav. Ecol.* **16**, 335–345 (2005).
27. S. A. Macdougall-Shackleton, in *Current Ornithology*, V. Nolan, E. D. Ketterson, C. F. Thompson, Eds. (Springer, 1997), pp. 81–124.
28. J.-N. Audet, S. Ducatez, L. Lefebvre, *Behav. Ecol.* **27**, 637–644 (2016).
29. J. L. Dowling, D. A. Luther, P. P. Marra, *Behav. Ecol.* **23**, 201–209 (2012).
30. P. Marler, *Ann. N. Y. Acad. Sci.* **1016**, 31–44 (2004).
31. K. B. Sewall, A. M. Young, T. F. Wright, *Anim. Behav.* **120**, 163–172 (2016).
32. S. Olkowicz *et al*., *Proc. Natl. Acad. Sci. U.S.A.* **113**, 7255–7260 (2016).
33. G. Feenders *et al*., *PLOS ONE* **3**, e1768 (2008).
34. A. D. Patel, *Philos. Trans. R. Soc. Lond. Ser. B* **376**, 20200326 (2021).
35. M. Chakraborty, E. D. Jarvis, *Philos. Trans. R. Soc. Lond. Ser. B* **370**, 20150056 (2015).
36. O. Güntürkün, T. Bugnyar, *Trends Cogn. Sci.* **20**, 291–303 (2016).
37. F. S. Livingston, R. Mooney, *J. Neurosci.* **17**, 8997–9009 (1997).
38. M. E. Basham, E. J. Nordeen, K. W. Nordeen, *Neurobiol. Learn. Mem.* **66**, 295–304 (1996).
39. J.-N. Audet *et al*., *Sci. Adv.* **4**, eaao6369 (2018).
40. T. W. Deacon, *Symbolic Species* (Norton, 1998).
41. Y. Toda *et al*., *Science* **373**, 226–231 (2021).
42. C. R. Cooney *et al*., *Nature* **542**, 344–347 (2017).
43. F. Sayol, P. A. Downing, A. N. Iwaniuk, J. Maspons, D. Sol, *Nat. Commun.* **9**, 2820 (2018).
44. J.-N. Audet, M. Couture, E. D. Jarvis, Songbird species that display more-complex vocal learning are better problem solvers and have larger brains. Dryad (2023); https://doi.org/10.5061/dryad.tb2rbp06n.

ACKNOWLEDGMENTS

We thank G. Smith-Vidaurre for insightful discussions on vocal learning complexity; S. Ducatez for assisting with the statistical analyses; L. Lefebvre, M. Davenport, and L. Cauchard for providing helpful suggestions on the manuscript; C. Scivolette for helping with bird captures; S. Sepe for helping with the establishment of wild-bird care protocols; G. Permuy and L. Tchernichovski for helping with bird care; and W. T. Gale for assisting with the construction of the behavior laboratory at the Rockefeller University Field Research Center. **Funding:** This study was supported by a Banting postdoctoral fellowship and an NSERC postdoctoral fellowship to J.-N.A. and by the Howard Hughes Medical Institute and a Keck Foundation Award to E.D.J. **Author contributions:** Conceptualization: J.-N.A., M.C., E.D.J.; Methodology: J.-N.A., M.C.; Investigation: J.-N.A., M.C.; Visualization: J.-N.A., M.C.; Funding acquisition: J.-N.A., E.D.J.; Supervision: J.-N.A., E.D.J.; Writing – original draft: J.-N.A.; Writing – review and editing: J.-N.A., M.C., E.D.J. **Competing interests:** The authors declare that they have no competing interests. **Data and materials availability:** The raw dataset and code are available at Dryad (*44*). **License information:** Copyright © 2023 the authors, some rights reserved; exclusive licensee American Association for the Advancement of Science. No claim to original US government works. https://www.science.org/about/science-licenses-journal-article-reuse

SUPPLEMENTARY MATERIALS

science.org/doi/10.1126/science.adh3428
Materials and Methods
Figs. S1 to S3
Tables S1 to S8
References (*45–144*)
MDAR Reproducibility Checklist
Movies S1 to S7

Submitted 25 February 2023; accepted 14 August 2023
10.1126/science.adh3428

NEURODEGENERATION

MEG3 activates necroptosis in human neuron xenografts modeling Alzheimer's disease

Sriram Balusu[1,2]*, Katrien Horré[1,2], Nicola Thrupp[1,2], Katleen Craessaerts[1,2], An Snellinx[1,2], Lutgarde Serneels[1,2], Dries T'Syen[1,2], Iordana Chrysidou[1,2], Amaia M. Arranz[3,4], Annerieke Sierksma[1,2], Joel Simrén[5,6], Thomas K. Karikari[5,6,7], Henrik Zetterberg[5,6,8,9,10], Wei-Ting Chen[1,2], Dietmar Rudolf Thal[11,12], Evgenia Salta[13], Mark Fiers[1,2,9], Bart De Strooper[1,2,9]*

Neuronal cell loss is a defining feature of Alzheimer's disease (AD), but the underlying mechanisms remain unclear. We xenografted human or mouse neurons into the brain of a mouse model of AD. Only human neurons displayed tangles, Gallyas silver staining, granulovacuolar neurodegeneration (GVD), phosphorylated tau blood biomarkers, and considerable neuronal cell loss. The long noncoding RNA *MEG3* was strongly up-regulated in human neurons. This neuron-specific long noncoding RNA is also up-regulated in AD patients. *MEG3* expression alone was sufficient to induce necroptosis in human neurons in vitro. Down-regulation of *MEG3* and inhibition of necroptosis using pharmacological or genetic manipulation of receptor-interacting protein kinase 1 (RIPK1), RIPK3, or mixed lineage kinase domain-like protein (MLKL) rescued neuronal cell loss in xenografted human neurons. This model suggests potential therapeutic approaches for AD and reveals a human-specific vulnerability to AD.

Mouse models have not allowed us to address the crucial question how the defining hallmarks of Alzheimer's disease (AD)—amyloid-β (Aβ) plaques, neuronal tau tangles, granulovacuolar neurodegeneration (GVD), and neuronal cell loss—relate to each other. The major problem is that tau pathology in these models can only be induced artificially, by using frontotemporal dementia causing tau mutation or by injecting tau seeds isolated from AD patient brains (*1*–*3*). Thus, the fundamental unanswered questions remain as to whether Aβ can induce tau pathology and how neurons die in AD. Unknown human-specific features that escape modeling in rodents are likely underlying this conundrum (*4*).

Two good models are available that replicate human features of AD: a three-dimensional cell culture based on different types of human cells (*5*) and xenografted human neurons in mouse brains (*6*). In this study, we improved the previously Nod-SCID–based xenotransplantation model (*6*) using the *Rag2*$^{-/-}$ (Rag2$^{tm1.1Cgn}$) immunosuppressive genetic background and a single *App*$^{NL-G-F}$ (App$^{tm3.1Tcs}$/App$^{tm3.1Tcs}$) knock-in gene to drive Aβ pathology. Human stem cell–derived neuronal progenitor cells (NPCs) transplanted into control *Rag2*$^{-/-}$ mice integrated well and developed dendritic spines (fig. S1, A and B). Two months after transplantation, the xenografted neurons already displayed some characteristic mature neuronal (NEUN and MAP2) and cortical markers (CTIP2, SATB2, TBR1, and CUX2). Unlike rodent neurons, human neurons expressed equal amounts of 3R and 4R tau splice forms at 6 months after transplantation (figs. S1C and S5H). Compared to the previously used model (*6*), the animals showed a considerably longer life span (>18 months longer), allowing for the study of healthy human neurons during brain aging.

We xenografted 100,000 green fluorescent protein (GFP)–labeled H9-derived human cortical NPCs into *Rag2*$^{-/-}$/*App*$^{NL-G-F}$ (hereafter referred to as amyloid mice) or *Rag2*$^{-/-}$/*App*$^{mm/mm}$ (control mice). β sheet staining with dye X34 revealed robust plaque pathology in the amyloid mice (Fig. 1A and fig. S1, D and E). The number of cells (fig. S6H) and transcriptional profile of the human transplants at 2 months were very similar in control and amyloid mice (Fig. 2A). Thus, human neurons integrated and differentiated similarly in control and amyloid mice, in line with the fact that amyloid plaque pathology appeared only after 2 months in this model. Full-blown amyloid plaque pathology was seen at 18 months after transplantation. At this late point in time, human neurons in the control brain appeared generally healthy and displayed neuronal projections and dendritic spines intermingled with host microglial (IBA1) and astroglial (GFAP) cells (fig. S1D). In contrast, grafted neurons in the amyloid mice displayed severe dystrophic neurites associated with microgliosis (six to seven IBA1-positive microglia per Aβ plaque) and astrogliosis (two to three GFAP-positive astrocytes per plaque) (Fig. 1A and fig. S2, A and B). The glial cell recruitment to plaques was very similar to that seen in nongrafted control animals (fig. S3, A and B). Immunohistochemistry with anti–phosphorylated tau (p-tau) antibodies AT8 (p-tau Ser^{202} and Thr^{205}), PHF1 (p-tau Ser^{396} and Ser^{404}), and MC1 (pathological conformational tau epitope) demonstrated considerable deposition of neuritic plaque tau (NP-tau) (*1*) in the human neurons of the grafted amyloid mice (Fig. 1, C and D). About 2% (AT8), 5% (PHF1), and 3% (MC1) of the surface was stained with the indicated antibodies in a 20-μm ring around the Aβ plaques (Fig. 1, E to G). Both NP-tau– and AT8-positive neurons appeared as early as 6 months after transplantation (fig. S1E), indicating that amyloid deposition drives tau phosphorylation early on in this model. Notable tau pathology was not observed at 18 months in mouse neurons in the same animal nor in human grafted control or mouse neurons grafted in amyloid mice (Fig. 1, C and D, and figs. S1E, S3, C and H, and S4, A to C).

Pathological, β sheet X34–positive tau reactivity was seen in the xenografted human neurons (fig. S2C). Furthermore, Gallyas silver staining and tau immunogold labeling of PHF fibril-like structures extracted with sarkosyl from grafted neurons in the amyloid mice (Fig. 1, H and I) confirmed the progression of p-tau into pathological states (>20 tau fibrils per electron microscopy grid (control n = 4, amyloid n = 4) (fig. S6F). Such pathology was largely absent in grafted control or nongrafted amyloid mice (Fig. 1H and figs. S6F and S3, I and J). Finally, and of clinical relevance, we found that the increase in p-tau181 and p-tau231 (*7*, *8*) was statistically significant in the plasma of the grafted amyloid mice but not in control grafted or nongrafted mice (Fig. 1, J and K), reflecting increased secretion of soluble p-tau biomarkers into the bloodstream in response to amyloid pathology, as in human AD.

It is possible to quantify accurately up to 0.1 ng of human DNA in a mixture with 100 ng mouse genomic DNA using quantitative PCR (qPCR) (*9*) (fig. S6D). Using this assay, we estimated that up to 50% fewer human neurons were present in the amyloid animals compared with controls (Fig. 1L and fig. S6G) at 6 and 18 months after transplantation. Of note, no significant increases in human neurons in the control situation were observed (fig. S6E), and the number of mouse neurons was also not significantly affected in nongrafted control or amyloid mice (fig. S3, E to G). Thus, human, but not mouse, neurons developed AD-like tau pathology upon exposure to amyloid plaques in vivo and degenerated much like their counterparts in the human brain by an unknown death process.

[1]VIB-KU Leuven Center for Brain and Disease Research, 3000 Leuven, Belgium. [2]Leuven Brain Institute, KU Leuven, 3000 Leuven, Belgium. [3]Achucarro Basque Center for Neuroscience, 48940 Leioa, Spain. [4]Ikerbasque Basque Foundation for Science, 48009 Bilbao, Spain. [5]Clinical Neurochemistry Laboratory, Sahlgrenska University Hospital, 431 80 Mölndal, Sweden. [6]Department of Psychiatry and Neurochemistry, Sahlgrenska Academy at the University of Gothenburg, 431 80 Mölndal, Sweden. [7]Department of Psychiatry, University of Pittsburgh, Pittsburgh, PA 15213, USA. [8]Department of Neurodegenerative Disease, University College London (UCL) Institute of Neurology, London WC1N 3BG, UK. [9]UK Dementia Research Institute at UCL, London WC1E 6BT, UK. [10]Hong Kong Center for Neurodegenerative Diseases, Hong Kong, China. [11]Laboratory for Neuropathology, Department of Imaging and Pathology, Leuven Brain Institute, KU Leuven, 3000 Leuven, Belgium. [12]Department of Pathology, University Hospital Leuven, 3000 Leuven, Belgium. [13]Laboratory of Neurogenesis and Neurodegeneration, Netherlands Institute for Neuroscience, 1105BA Amsterdam, Netherlands.
*Corresponding author. Email: b.strooper@ukdri.ucl.ac.uk (B.D.S.); sriram.balusu@kuleuven.vib.be (S.B.)

Previous work has found opposite effects of *Rag2*$^{-/-}$ immunodeficiency on amyloid plaque pathology and cellular responses (*10*, *11*). Comparison of soluble Aβ (Aβ$_{40}$ and Aβ$_{42}$) and guanidine-extractable Aβ (Aβ$_{40}$ and Aβ$_{42}$) revealed no significant differences between *Rag2*$^{-/-}$/*App*$^{NL\text{-}G\text{-}F}$ and *App*$^{NL\text{-}G\text{-}F}$ mice. Bulk RNA sequencing indicated that the main aspects of the innate microglia and astroglial cellular transcriptomic responses to amyloid plaques are maintained in the *Rag2*$^{-/-}$/*App*$^{NL\text{-}G\text{-}F}$ immunodeficient mouse compared with a previously characterized nonimmunosuppressed amyloid mouse (*APP/PS1*) (*12*, *13*) (Fig. 1B) [coefficient of determination (R^2) = 0.81 for differentially expressed genes]. Thus, although we acknowledge the lack of an adaptive immune system as a weakness of the model, we note that all key features of the neuropathology of AD were reproduced.

Transcriptional changes in xenografted neurons reveal induction of necroptosis

We isolated the transplanted neuron–positive brain regions from mice at 2, 6, and 18 months after transplantation and extracted total RNA for sequencing (mean human reads: ~13.3 million) (fig. S5, A and B). Mapping to mouse and human reference databases generated species-specific datasets. As expected, up-regulation of the mouse genes *Axl*, *B2m*, *Cst7*, *Ctss*, *Itgax*, *Trem2*, *Tyrobp*, *Lyz2*, *Ccl3*, and *Ccl4* confirmed microglial activation when exposed to amyloid in *Rag2*$^{-/-}$/*App*$^{NL\text{-}G\text{-}F}$ mice (Fig. 1B; fig. S7, A to C; and table S2) (*13*). Human samples clustered according to genotype and age (fig. S5C). Differential expression (DE) analysis of the human grafts at 2 months showed only a few significantly down-regulated DE genes of unknown relevance (Fig. 2A and table S1). In contrast, DE of grafts in amyloid and control conditions at 6 and 18 months revealed 916 up-regulated and 73 down-regulated genes, and 533 up-regulated and 34 down-regulated genes, respectively (Fig. 2, B and C, and table S1). Gene alterations of interest included *CD74*, a marker for tau tangle–containing cells (*14*); *HBB*, a cortical pyramidal neuronal marker (*15*–*17*); and *A2M*, which is associated with neuritic plaques in AD human brains (*18*) (fig. S5E). In addition to the neuronal signature, in line with previous findings (*19*), we also observed astroglial and oligodendrocytic genes, including *MOBP*, *MBP*, *OPALIN*, *S100A6*, and *APOE*, among others, indicating that the grafted neural stem cells also generated glia in vivo (fig. S5F). A limitation of the current study is the lack of an accurate estimate of the cellular composition of the graft that might influence the transcriptional profile of the grafted cells. Nevertheless, the overall expression profiles of the grafts exposed to amyloid plaques at 6 and 18 months showed strong correlations (R^2 = 0.88), suggesting that the pathological

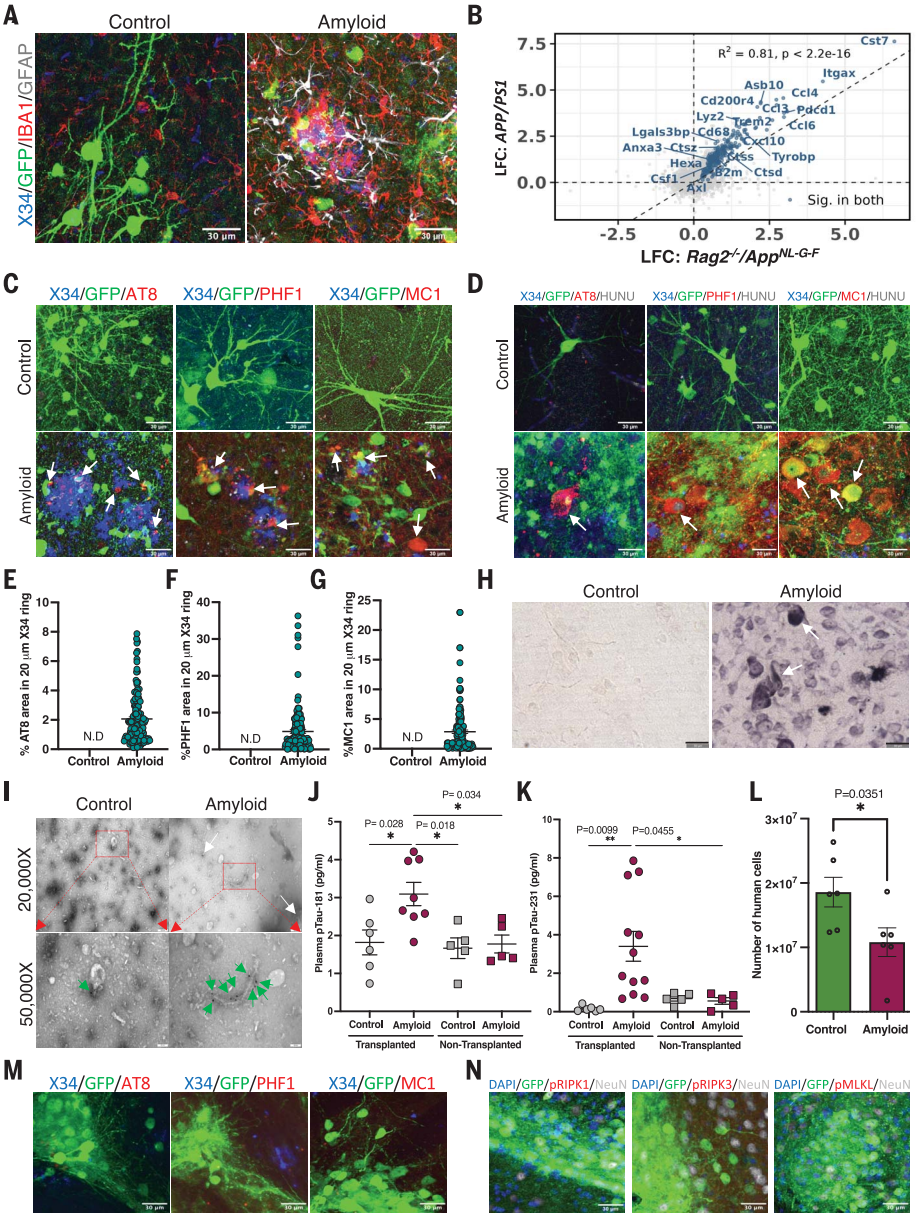

Fig. 1. Amyloid plaque deposition is sufficient to induce pathological tau in the grafts. (**A**) Representative confocal images of grafted human neurons of 18-month-old control (n = 4) and amyloid (n = 4) mice. (**B**) Scatter plot comparing log fold changes (LFC) in *APP/PS1* mice at 10 months and *Rag2*$^{-/-}$/*App*$^{NL\text{-}G\text{-}F}$ mice at 6 months old. Blue genes are significantly changed in both models (R^2 = 0.81). (**C**) Representative confocal images showing NP-tau and neuronal soma tau (**D**) in 18-month-old control (n = 4) and amyloid (n = 4) mice. White arrows indicate X34 and NP-tau–positive cells. HUNU, human nucleus. Quantification of (**E**) AT8-positive tau, (**F**) PHF1-positive tau, (**G**) MC1-positive tau around Aβ plaque within 20 µm diameter in 18-month-old animals (n = 4, >100 plaques per mice). N.D, not detected. (**H**) Representative light microscope Gallyas silver stain images from 18-month-old control (n = 4) and amyloid (n = 4) grafted animals. (**I**) Electron micrograph image of immunogold-labeled sarkosyl insoluble tau fibrils isolated from 18-month-old control (n = 4) and amyloid (n = 4) mice. Tau fibrils are indicated with white (top panel) or green (bottom panel) arrows. (**J**) Quantification of plasma p-tau181 levels (every dot represents one mouse) and (**K**) p-tau231 levels from 18-month-old grafted and nongrafted mice. (**L**) Number of human neurons at 6 months after transplantation in control (n = 6) and amyloid (n = 6) mice using qPCR. (**M**) Confocal images taken from 6-month-old amyloid animals grafted with stem cell–derived mouse neurons (n = 4) did not stain with pathological tau markers (AT8, PHF1, or MC1) or (**N**) mouse-specific necrosome antibodies [pRIPK1(Ser^{166}), pRIPK3 (Thr^{231}/Thr^{232}), or pMLKL (Ser^{345})]. The full panel, along with control mice, is shown in fig. S4, C and D. Scale bars: 30 µm [(A), (C), (D), (M), and (N)], 50 µm (H), 200 nm [(I), top row], 100 nm [(I), bottom row]. Values are presented as mean ± SEM. One-way analysis of variance (ANOVA) with Tukey's post hoc test for multiple comparisons was used in (J) to (K), and Student's t test was used in (M).

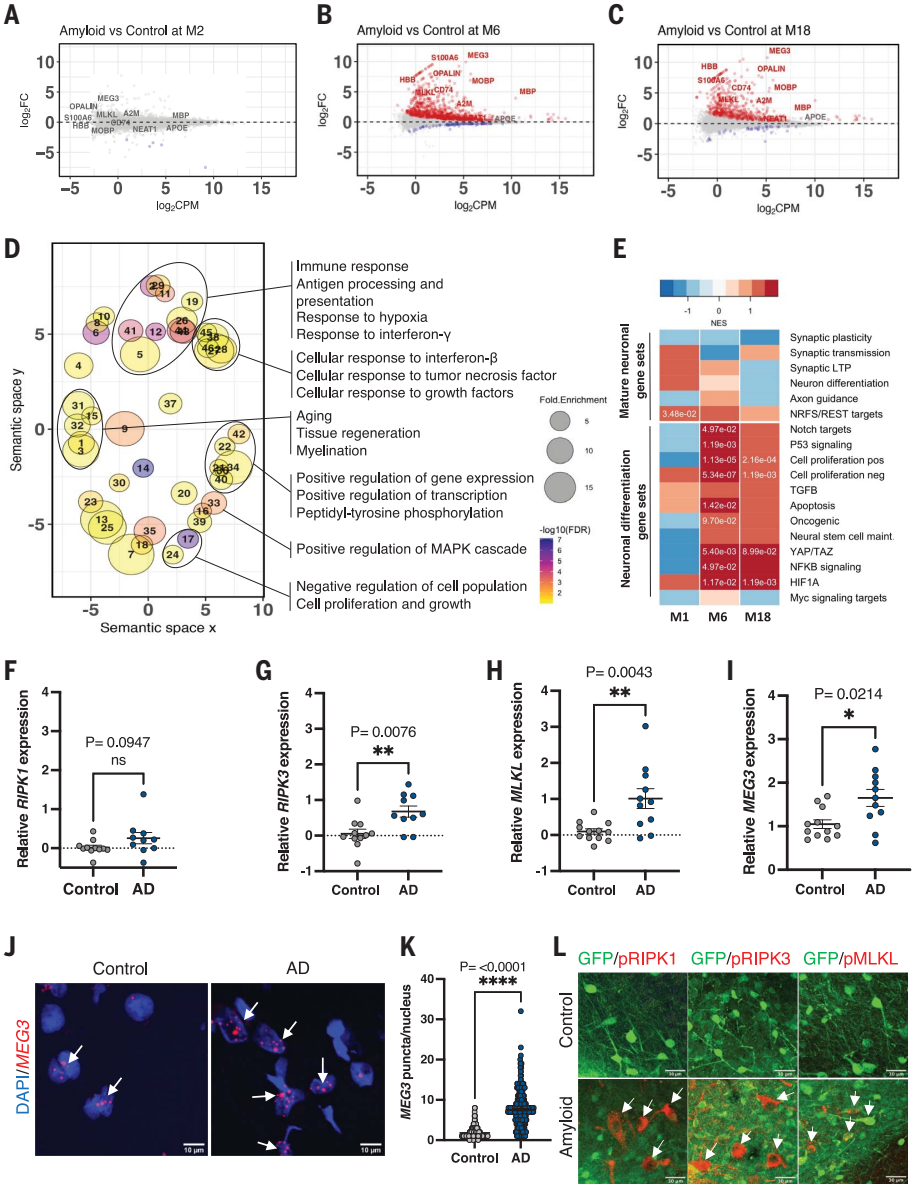

Fig. 2. Transcriptional changes in xenografted neurons. Bland-Altman MA plot showing differential expression of genes from RNA sequencing of human grafts from control and amyloid mice at (**A**) 2 months (control n = 5, amyloid n = 7), (**B**) 6 months (control n = 5, amyloid n = 5), and (**C**) 18 months (control n = 4, amyloid n = 3) after transplantation. Red indicates significantly up-regulated genes. Blue indicates significantly down-regulated genes [false discovery rate (FDR) < 0.05]. FC, fold change; CPM, counts per million. (**D**) GO analysis showing terms associated with genes up-regulated at 6 months. Point size represents the fold enrichment of up-regulated genes in the term, and color represents the $-\log_{10}$FDR. Only terms with FDR < 0.1 are shown. The x and y axes represent the "semantic space" (*54*). (**E**) Heatmap of normalized enrichment scores (NES) in neuronal dedifferentiation gene sets ranked along the differentially expressed genes in the xenografts (amyloid versus control) shown in (A) to (C). Positive enrichments in red, negative enrichments in blue. Significant FDR values (P_{adj} < 0.01) are shown as numbers. (**F** to **H**) Analysis of (F) *RIPK1*, (G) *RIPK3*, and (H) *MLKL* mRNA expression using quantitative reverse transcription polymerase chain reaction (qRT-PCR) on AD (n = 11) and control (n = 10) postmortem human brain samples. (**I**) Analysis of *MEG3* gene expression using qRT-PCR on AD (n = 11) and control (n = 10) postmortem human brain samples. (**J**) Confocal images showing *MEG3* RNAscope in the temporal gyrus of AD (n = 3) and control (n = 2) postmortem human brain samples. Scale bars: 10 μm. (**K**) Number of *MEG3* puncta per nucleus in control (>100 nuclei per sample, n = 2) and AD (>100 nuclei per sample, n = 3). (**L**) Representative confocal images showing the expression of activated necroptosis pathway markers pRIPK1, pRIPK3, or pMLKL in red (white arrows) in 18-month-old human neurons in control (n = 4) and amyloid (n = 4) mice. Scale bars: 30 μm. Values are presented as mean ± SEM. Student's t test used in (F) to (I) and (K).

cell states of neurons at 6 and 18 months are similar (fig. S5G). We found a prominent enrichment using GSEA (gene set enrichment analysis) between previously published AD datasets (table S3), including the ROSMAP (Religious Orders Study and Rush Memory and Aging Project) cohort (*20*), and our data in transplanted neurons at 6 and 18 months after transplantation [adjusted P value (P_{adj}) < 0.05] but not at 2 months (fig. S8, A and B). Furthermore, GSEA also revealed a clear enrichment in up-regulated genes from transplanted neurons and neurons directly reprogrammed from fibroblasts of AD patients (6 months: $P_{adj} = 1.64 \times 10^{-5}$; 18 months: $P_{adj} = 2.19 \times 10^{-4}$). These data confirmed that our transplanted neurons capture AD-relevant transcriptional signatures (*21*).

Functional Gene Ontology (GO) enrichment analysis of significantly up-regulated genes (P_{adj} < 0.05) at 6 months using DAVID (Database for Annotation, Visualization and Integrated Discovery) and REVIGO (Reduce and Visualize Gene Ontology) covered semantic space around positive regulation of transcription, protein phosphorylation, positive regulation of mitogen-activated protein kinase cascade, inflammatory responses, including tumor necrosis factor (TNF) and interferon signaling, cell proliferation, aging, tissue regeneration, and myelination (Fig. 2D and table S1). Some reports have suggested that neurons in AD display signatures of hypomaturity, dedifferentiation, and cell cycle reentry (*22*–*24*). Using previously published datasets (table S1) and GSEA, we found that cellular signatures of hypomaturity, dedifferentiation, P53, hypoxia-inducible factor α signaling, nuclear factor κB (NF-κB), transforming growth factor–β (TGFβ) signaling, (positive and negative) regulation of cell cycle, and cell cycle reentry were indeed enriched in the 6 and 18 month grafts but not at 2 months (Fig. 2E). Conversely, mature neuronal marker pathways, such as synaptic plasticity, synaptic transmission, long-term potentiation, and axon guidance were not significantly enriched (Fig. 2E).

How neurons die in AD remains controversial (*25*, *26*). As shown in Fig. 1L and fig. S6G, about 50% of xenografted human neurons were lost in the amyloid mice. We did not observe any significant alterations in the expression of genes associated with cell death mechanisms, such as apoptosis or ferroptosis, but found significant up-regulation of *MLKL*, the gene encoding the executor protein of necroptosis (Fig. 2, B and C, and figs. S2E and S6, A to C). This was not observed in the transcriptome of the host tissue (fig. S7, A to C). We used pRIPK1-(Ser^{166}), pRIPK3- (Ser^{227}), and pMLKL-specific (Ser^{358}) antibodies to stain brain tissue from 18-month-old grafted and nongrafted mice. We noticed intense punctuate staining with a vesicular pattern in the soma of the neurons in grafted amyloid mice. These vesicular structures

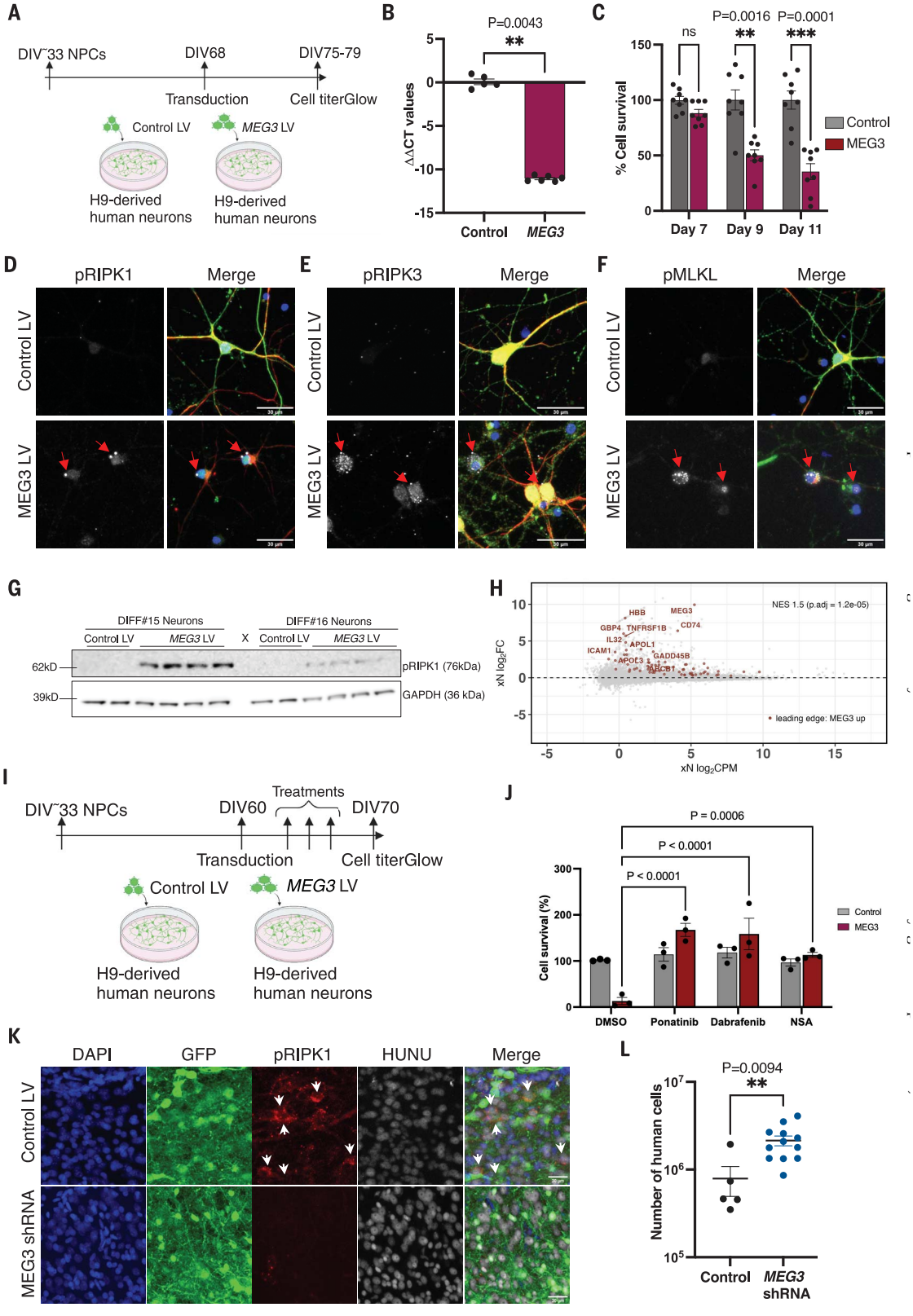

Fig. 3. Long noncoding RNA *MEG3* induces necroptosis in human neurons. (**A**) Schematic representation of the *MEG3* expression strategy using lentiviral vectors (LV) in H9-derived human neurons. (**B**) Analysis of the *MEG3* expression 7 days after transduction with control LV (n = 5) or *MEG3* LV (n = 6) in DIV75 neurons. (**C**) Analysis of neuronal cell survival using CellTiter-Glo reagent after transducing with either control LV (n = 8) or *MEG3* LV (n = 8). (**D**) Confocal images showing pRIPK1 (Ser^{166}), (**E**) pRIPK3 (Ser^{227}), (**F**) pMLKL (Ser^{358}) in neurons at DIV75 and 7 days after transduction with control LV (n = 3) or *MEG3* LV (n = 3). Scale bars: 30 μm. (**G**) Immunoblot analysis of pRIPK1 (Ser^{166}) levels 7 days after transduction (DIV75) with control LV (n = 4) or *MEG3* LV (n = 8). Glyceraldehyde phosphate dehydrogenase (GAPDH) is the loading control. Two independent differentiations were analyzed. (**H**) Same Bland-Altman MA plot showing differential expression of bulk RNA sequencing of human grafts from 6 months, as in Fig. 2B. Genes highlighted in red are the leading-edge genes identified with GSEA, taking the top 400 up-regulated genes from the bulk sequencing of the primary neurons expressing *MEG3* (fig. S10) and plotting them against the amyloid versus control fold changes of the human grafts (FDR < 0.05). (**I**) Schematic representation of the necroptosis inhibition in vitro using H9-derived human neurons (DIV60) with ponatinib (0.5 μM), dabrafenib (0.9 μM), and NSA (0.5 μM). (**J**) Analysis of neuronal cell survival using CellTiter-Glo reagent after necroptosis inhibitor treatment (n = 3). (**K**) Representative confocal images of grafted neurons showing pRIPK1 levels in samples obtained from the 6-month-old animals transplanted with control LV (n = 5) or the *MEG3* shRNA (n = 5) transduced human NPCs. White arrows indicate pRIPK1-positive cells. Scale bars: 30 μm. (**L**) The human cell number was estimated from 6-month-old xenografted mice from control (n = 5) and *MEG3* shRNA (n = 12) using qPCR. Values are presented as mean ± SEM. Student's t test used in (B) and (L), one-way ANOVA with Tukey's post hoc test for multiple comparisons used in (C), and two-way ANOVA with Dunnett's multiple comparison test used in (J) to measure the statistical significance.

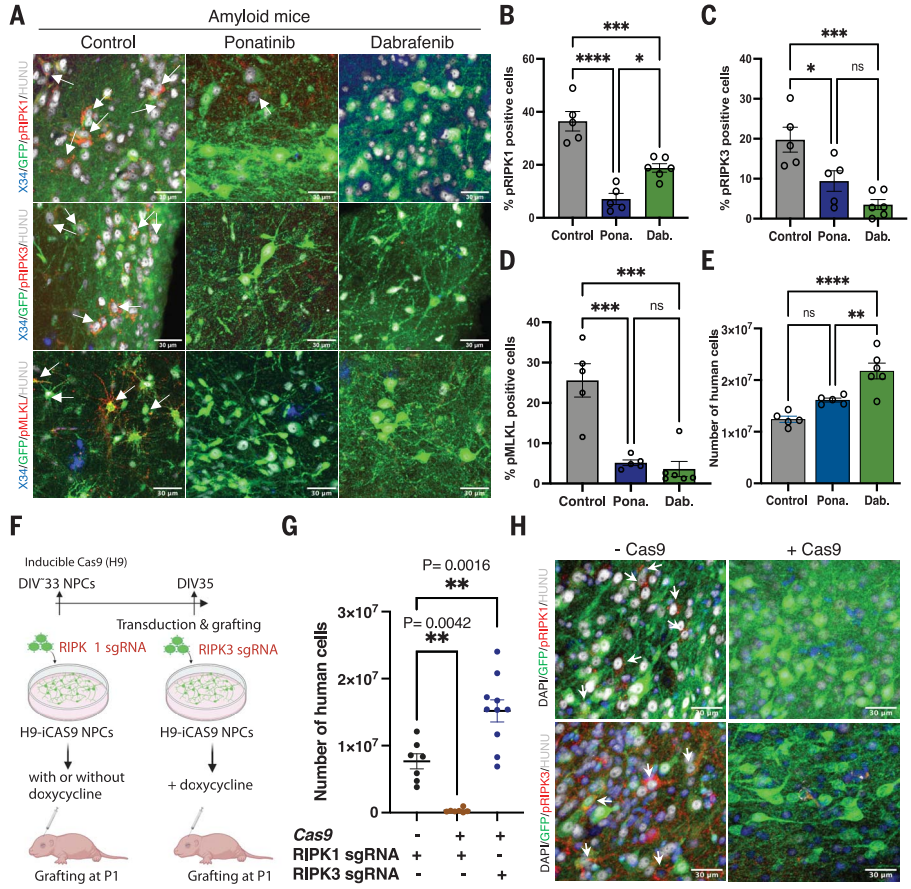

Fig. 4. Inhibition of necroptosis prevents human neuronal cell loss in vivo. (**A**) Confocal images showing activated necroptotic markers pRIPK1, pRIPK3, and pMLKL in amyloid animals (n = 5) and amyloid animals treated with ponatinib (n = 5) or dabrafenib (n = 6). White arrows indicate necroptosis marker–positive neurons. Scale bars: 30 μm. (**B**) Quantitative representation of percent of human cells immunoreactive to pRIPK1 in control (n = 5) and ponatinib-treated (Pona.; n = 5) or dabrafenib-treated (Dab.; n = 6) animals. Control versus ponatinib: $P \leq 0.0001$; control versus dabrafenib: $P = 0.0007$; ponatinib versus dabrafenib: $P = 0.015$. (**C**) Percent of human cells showing immunoreactivity to pRIPK3 in control (n = 5) and ponatinib-treated (n = 5) or dabrafenib-treated (n = 6) animals. Control versus ponatinib: $P = 0.02$; control versus dabrafenib: $P = 0.0007$; ponatinib versus dabrafenib: $P = 0.2$. (**D**) Quantitative representation of the percent of human cells showing immunoreactivity toward pMLKL in control (n = 5) and ponatinib-treated (n = 5) or dabrafenib-treated (n = 6) animals. Control versus ponatinib: $P = 0.0003$; control versus dabrafenib: $P = 0.0001$; ponatinib versus dabrafenib: $P = 0.9$. (**E**) Quantitative estimation of the number of human cells in control (n = 5) and ponatinib-treated (n = 5) or dabrafenib-treated (n = 6) grafted mice at 6 months after transplantation. Control versus ponatinib: not significant; control versus dabrafenib: $P = 0.0001$; ponatinib versus dabrafenib: $P = 0.007$. (**F**) Schematic representation of the *RIPK1* and *RIPK3* KO generation and transplantation. (**G**) Number of neurons surviving from 6-month-old mice transplanted with *RIPK1* single guide RNA (sgRNA) without doxycycline (n = 7) or *RIPK1* sgRNA with doxycycline (n = 7) or *RIPK3* sgRNA with doxycycline (n = 10) using qPCR. (**H**) Representative immunofluorescence analysis of phosphorylated necroptosis markers pRIPK1 (n = 3) pRIPK3 (n = 3) from 6-month-old mice transplanted with *RIPK1* sgRNA or *RIPK3* sgRNA without and with Cas9 induction, as indicated. White arrows indicate pRIPK1- or pRIPK3-positive cells. Scale bars: 30 μm. Values are presented as mean ± SEM. One-way ANOVA with Tukey's post hoc test for multiple comparisons was used in (B) to (E) and (G).

co-stained with casein kinase 1 delta (CK1δ), a marker for granulovacuolar degeneration (Fig. 2L and fig. S6I). Nongrafted control and amyloid animals or mouse neurons derived from NPCs and similarly transplanted into mice did not display these pathologies (figs. S3D and S4D).

We validated this observation by qPCR on RNA extracted from the temporal gyrus of AD and age-matched control brain samples, revealing significant up-regulation of *MLKL* and *RIPK3* (Fig. 2, F to H). We have, on the basis of our initial observations in the xenograft model, extensively confirmed the presence of necroptosis markers in GVD in AD patients in a previous publication (*27*). Thus, our model has predictive value for the neuropathology of AD.

MEG3 modulates the neuronal necroptosis pathway

We identified 36 up-regulated and 21 down-regulated long noncoding RNAs (lncRNAs) in the grafts of 6-month-old animals (table S1). Some of these noncoding RNAs (e.g., *NEAT1*) have been implicated in AD (*28*), but overall, it is unclear whether or how they contribute to pathogenesis. In our data, the lncRNA *MEG3* (Maternally Expressed 3) was the most strongly (~10-fold) up-regulated gene in human neurons exposed to amyloid pathology (Fig. 2, B to C, and fig. S2D) but not in the host mouse neurons (fig. S7, D to F). *MEG3* has been linked to cell death pathways (*29*) through p53 (*30*), is involved in the TGFβ pathway (*31*), and has been associated with Huntington's disease (*32*).

While *MEG3* has not been implicated in AD, we found up-regulation of *MEG3* in AD patient brains in a single-nucleus transcriptomic database (*33*). We confirmed two- to threefold up-regulation of *MEG3* in RNA extracted from the temporal gyrus of AD patients (table S5) using qPCR (Fig. 2I). *MEG3* in situ hybridization combined with cell-specific immunohistochemical markers NeuN (neurons), IBA1 (microglia), and GFAP (astrocytes) demonstrated its exclusive expression in the nucleus of neurons (fig. S9, A and B) and its strong enrichment in AD brains [2 to 3 puncta per nucleus in control and 8 to 10 puncta per nucleus in AD brain (P = <0.0001)] (Fig. 2, J and K). In AD, *MEG3*-expressing neuronal nuclei appeared blotched, with reduced 4′,6-diamidino-2-phenylindole (DAPI) intensity, and *MEG3*-positive neurons also displayed high levels of the necroptosis marker pMLKL (fig. S9C).

We performed Sanger sequencing on brain cDNA and found that from 15 known transcriptional variants (*34*), *MEG3* transcript variant 1 (accession number NR_002766.2) was most abundantly expressed in human adult brain. A lentivirus was used to express *MEG3* V1 in H9-derived mature cortical neurons (Fig. 3, A and B), resulting in strong reduction of cell viability at 9 days compared with control (Fig. 3C). Immunohistochemical analysis revealed the presence of activated necroptotic markers pRIPK1 (Ser^{166}), pRIPK3 (Ser^{227}), and pMLKL (Ser^{358}) (Fig. 3, D to F). Necroptosis-positive neurons displayed a reduced amount of cytoskeletal filament neurofilament-H (NF-H). Immunoblot analysis confirmed increased pRIPK1 (Ser^{166}) levels (Fig. 3G). Notably, *MEG3*-induced cell loss was rescued by necroptosis inhibitors ponatinib, dabrafenib, or necrosulfonamide and by CRISPR-mediated deletion of *RIPK1*, *RIPK3*, and *MLKL* in vitro (Fig. 3, I and J, and fig. S10, H to J).

We performed RNA sequencing of *MEG3*-transduced neurons 7 days after transduction and compared the transcriptomic signatures with those from the xenografted neurons using GSEA. We ranked the genes from the amyloid and control xenografts according to their log fold change differential expression (at 6 months; see Fig. 2B) and compared those to the top up-regulated genes in response to *MEG3* transduction in neurons in vitro. We found a significant enrichment of the up-regulated genes (normalized enrichment score = 1.5, $P_{adj} = 1.2 \times 10^{-5}$) (Fig. 3H and table S4), suggesting that some transcriptional changes in the xenografted neurons in vivo might be the consequence of up-regulated *MEG3*. DE analysis of *MEG3* transduced neurons revealed no changes in necroptosis genes (fig. S10, A to C). DAVID GO analysis of leading-edge genes from GSEA on up-regulated genes from 6-month transplanted human neurons and in vitro *MEG3*-expressing neurons revealed signatures of NF-κB and TNF signaling, which are related to necroptosis induction (*35*). In addition, signatures of lipid transport, interferon-γ signaling, positive regulation of peptidyl-tyrosine phosphorylation, and apolipoprotein L signaling were observed (fig. S10D and table S4).

Inhibition of necroptosis blocks human neuronal loss in the xenografted mice

Blocking *MEG3* up-regulation in NPCs using a previously characterized short hairpin RNA (shRNA) antisense construct (*36*, *37*) significantly improved neuronal survival and was associated with down-regulated expression of necrosome proteins (Fig. 3, K and L, and fig. S10, E to G). It is possible that necroptosis markers are limited to the neurons that are remaining at the stage of pathological analysis. We thus treated xenografted mice (three groups of $n = 5$) from 2 until 6 months after transplantation with the orally available necroptosis kinase inhibitors ponatinib (30 mg/kg) and dabrafenib (50 mg/kg). Ponatinib inhibits RIPK1 (*38*) and RIPK3 (*39*) and is a US Food and Drug Administration–approved drug for the treatment of acute lymphoid leukemia and chronic myeloid leukemia. Dabrafenib is a more specific inhibitor of RIPK3 (*40*). Immunostaining at 6 months revealed a large reduction in levels of pRIPK1, pRIPK3, and pMLKL in both treatment groups compared with untreated mice (Fig. 4, A to D), without alteration of the glial response to amyloid (fig. S9D). qPCR analysis of neuronal cell numbers revealed a significant increase in neurons in the dabrafenib-treated group compared with the control (Fig. 4E). Transplanting *RIPK1* knockout NPCs generated using CRISPR-Cas9, as discussed earlier, demonstrated that neurons were not viable, in agreement with the lethal phenotype of RIPK1 in mouse (*41*). In contrast, deletion of the *RIPK3* gene significantly improved neuronal survival (Fig. 4, F to H). Immunofluorescence staining confirmed the significant decrease of necrosome signals in *RIPK3*-deficient human neurons.

Conclusions

Our results demonstrate that amyloid pathology is sufficient to induce hallmark neuropathology of AD, including neuronal tangles and secretion of p-tau181 and p-tau231 biomarkers in blood, by simply exposing human neurons to amyloid plaques. We asked the crucial question of how neurons in AD die. Reports have proposed apoptotic mechanisms, but no convincing evidence has demonstrated that this drives neuronal cell loss in AD (*42*). Previous publications, one instigated by the observations in the xenograft mice, have confirmed that necroptosis occurs in the AD brain (*27*, *43*). We demonstrate here that neuronal loss can be rescued by treatment with clinically relevant necroptosis inhibitors or by ablating the *RIPK3* gene in transplanted neurons (*40*). Thus, we suggest that neuronal death in AD is largely driven by necroptosis, linking the loss of neurons to inflammatory processes that are upstream of this well-studied death pathway (*13*, *44*, *45*). Therapies that prevent neuronal cell loss, in combination with more-mainstream Aβ- and tau-targeted interventions, might be useful additions to the current efforts to develop disease-modifying strategies for AD (*46*–*48*). Necroptosis is an active area of drug development in cancer and ALS (*49*–*51*).

Our data suggest that necroptosis is downstream of the accumulation of pathological tau and is induced by the up-regulation of the noncoding RNA *MEG3*, possibly via TNF inflammatory pathway signaling. It needs to be mentioned that the imprinting status of MEG3 and its expression may differ among human embryonic stem cell lines (*52*). lncRNAs are important regulators of gene expression and influence a variety of biological processes, including brain aging and neurodegenerative disease (*53*). The large number of noncoding RNAs that are differentially expressed in our AD model warrants further investigation.

It is intriguing that human transplanted neurons display an AD phenotype, whereas mouse neurons interspersed within the graft or neurons derived from mouse NPCs and transplanted in a similar way as their human counterparts do not display such a phenotype. This suggests that unknown human-specific features define the sensitivity of the neurons to amyloid pathology. We noticed that the transplanted human neurons display signatures of down-regulation of mature neuronal properties and up-regulation of immature signaling pathways, which aligns with a recent study analyzing the transcriptional profiles in neurons directly derived from fibroblasts of AD patients (induced neurons) (*21*). Those neurons did not, however, show tangles, amyloid, or necroptosis markers, and it was therefore not clear how those observations relate to the classical hallmarks of AD. The contribution of these immature signatures to the disease process needs further investigation, but our data indicate that necroptosis is an important contributor to cell death in AD.

Transplanted human neurons, in contrast to transplanted mouse neurons, become diseased when exposed to amyloid pathology. Understanding the molecular basis of the resilience of mouse neurons to amyloid pathology will not only help to model the disease better but might also stimulate research into pathways that protect against neurodegeneration.

REFERENCES AND NOTES

1. Z. He *et al.*, *Nat. Med.* **24**, 29–38 (2018).
2. F. Grueninger *et al.*, *Neurobiol. Dis.* **37**, 294–306 (2010).
3. N. Mattsson-Carlgren *et al.*, *Sci. Adv.* **6**, eaaz2387 (2020).
4. C. Guela *et al.*, *Nat. Med.* **4**, 827–831 (1998).
5. S. H. Choi *et al.*, *Nature* **515**, 274–278 (2014).
6. I. Espuny-Camacho *et al.*, *Neuron* **93**, 1066–1081.e8 (2017).
7. S. Janelidze *et al.*, *Nat. Med.* **26**, 379–386 (2020).
8. E. H. Thijssen *et al.*, *Nat. Med.* **26**, 387–397 (2020).
9. M. Bensalah *et al.*, *PLOS ONE* **14**, e0211522 (2019).
10. S. E. Marsh *et al.*, *Proc. Natl. Acad. Sci. U.S.A.* **113**, E1316–E1325 (2016).
11. C. Späni *et al.*, *Acta Neuropathol. Commun.* **3**, 71 (2015).
12. A. Sierksma *et al.*, *EMBO Mol. Med.* **12**, e10606 (2020).
13. C. Sala Frigerio *et al.*, *Cell Rep.* **27**, 1293–1306.e6 (2019).
14. K. J. Bryan *et al.*, *Mol. Neurodegener.* **3**, 13 (2008).
15. M. Biagioli *et al.*, *Proc. Natl. Acad. Sci. U.S.A.* **106**, 15454–15459 (2009).
16. J. Y. Chuang *et al.*, *PLOS ONE* **7**, e33120 (2012).
17. N. Brown *et al.*, *J. Mol. Neurosci.* **59**, 1–17 (2016).
18. D. Van Gool, B. De Strooper, F. Van Leuven, E. Triau, R. Dom, *Neurobiol. Aging* **14**, 233–237 (1993).
19. W.-T. Chen *et al.*, *Cell* **182**, 976–991.e19 (2020).
20. S. Mostafavi *et al.*, *Nat. Neurosci.* **21**, 811–819 (2018).
21. J. Mertens *et al.*, *Cell Stem Cell* **28**, 1533–1548.e6 (2021).
22. T. Arendt, *Mol. Neurobiol.* **46**, 125–135 (2012).
23. T. Arendt *et al.*, *Ann. N.Y. Acad. Sci.* **920**, 249–255 (2000).
24. Y. Yang, D. S. Geldmacher, K. Herrup, *J. Neurosci.* **21**, 2661–2668 (2001).
25. O. Wirths, S. Zampar, *Int. J. Mol. Sci.* **21**, 8144 (2020).
26. U. Fünfschilling *et al.*, *Nature* **485**, 517–521 (2012).
27. M. J. Koper *et al.*, *Acta Neuropathol.* **139**, 463–484 (2020).
28. E. Salta, B. De Strooper, *Lancet Neurol.* **11**, 189–200 (2012).
29. N. Jiang, X. Zhang, X. Gu, X. Li, L. Shang, *Cell Death Discov.* **7**, 30 (2021).
30. Y. Zhou *et al.*, *J. Biol. Chem.* **282**, 24731–24742 (2007).
31. T. Mondal *et al.*, *Nat. Commun.* **6**, 7743 (2015).
32. K. Chanda *et al.*, *RNA Biol.* **15**, 1348–1363 (2018).
33. A. Grubman *et al.*, *Nat. Neurosci.* **22**, 2087–2097 (2019).
34. Y. Zhou, X. Zhang, A. Klibanski, *J. Mol. Endocrinol.* **48**, R45–R53 (2012).
35. A. Jayaraman, T. T. Htike, R. James, C. Picon, R. Reynolds, *Acta Neuropathol. Commun.* **9**, 159 (2021).
36. H. Zhang, *Exp. Ther. Med.* **18**, 3699–3706 (2019).
37. H. Bi *et al.*, *Med. Sci. Monit.* **26**, e920793 (2020).
38. A. Fauster *et al.*, *Cell Death Dis.* **6**, e1767 (2015).
39. J.-X. Li *et al.*, *Cell Death Dis.* **5**, e1278 (2014).
40. S. Martens, S. Hofmans, W. Declercq, K. Augustyns, P. Vandenabeele, *Trends Pharmacol. Sci.* **41**, 209–224 (2020).
41. K. Newton *et al.*, *Nature* **540**, 129–133 (2016).
42. K. A. Roth, *J. Neuropathol. Exp. Neurol.* **60**, 829–838 (2001).
43. A. Caccamo *et al.*, *Nat. Neurosci.* **20**, 1236–1246 (2017).
44. B. De Strooper, E. Karran, *Cell* **164**, 603–615 (2016).
45. A. Sierksma, V. Escott-Price, B. De Strooper, *Science* **370**, 61–66 (2020).
46. E. E. Congdon, E. M. Sigurdsson, *Nat. Rev. Neurol.* **14**, 399–415 (2018).
47. J. Sevigny *et al.*, *Nature* **537**, 50–56 (2016).
48. M. A. Mintun *et al.*, *N. Engl. J. Med.* **384**, 1691–1704 (2021).
49. Y. Ito *et al.*, *Science* **353**, 603–608 (2016).
50. J. Yuan, P. Amin, D. Ofengeim, *Nat. Rev. Neurosci.* **20**, 19–33 (2019).
51. B. Hanson, *Cancer Biol. Ther.* **17**, 899–910 (2016).

52. P. J. Rugg-Gunn, A. C. Ferguson-Smith, R. A. Pedersen, *Hum. Mol. Genet.* **16**, R243–R251 (2007).
53. E. Lauretti, K. Dabrowski, D. Praticò, *Ageing Res. Rev.* **71**, 101425 (2021).
54. F. Supek, M. Bošnjak, N. Škunca, T. Šmuc, *PLOS ONE* **6**, e21800 (2011).

ACKNOWLEDGMENTS

B.D.S. is the lead contact. We thank V. Hendrickx and J. Verwaeren for animal husbandry and S. Munck, N. Corthout, A. Kerstens, and A. Escamilla Yala for their assistance with imaging (LiMoNe, VIB). Confocal microscope equipment was acquired through a Hercules Type 1 AKUL/09/037 to W. Annaert. We thank P. Baatsen, EM-platform of the VIB Bioimaging Core at KU Leuven, for assistance with electron microscopy imaging. App^{NL-G-F} mice were kindly provided by T. Saido (RIKEN Brain Science Institute, Japan). PHF1 and MC1 antibodies were a gift from the P. Davies lab. We thank the Netherlands Brain Bank (NBB), Netherlands Institute for Neuroscience, Amsterdam, for providing the brain samples. **Funding:** S.B. is a Fonds voor Wetenschappelijk Onderzoek–Vlaanderen (FWO) senior postdoctoral scholar (12P5922N). A.M.A. receives funding from MCIN/AEI/10.13039/501100011033 (RTI2018-101850-A-I00 and PID2021-125443OB-100 grants), also by FEDER Una manera de hacer Europa and RYC2020-029494-I by FSE invierte en tu futuro, the Alzheimer's Association (grant AARG-21-850389), and the Basque Government (PIBA-2020-1-0030). E.S. receives funding from Alzheimer Nederland, the Ministry of Economic Affairs by means of the PPP allowance made available by the Top Sector Life Sciences & Health (Health Holland), and EU JPND/ZonMw. J.S. is supported by research grants from Stiftelsen för Gamla tjänarinnor, Demensfonden and Stohnes stiftelse. T.K.K. is funded by the Swedish Research Council (Vetenskåpradet, 2021-03244), the Alzheimer's Association (AARF-21-850325), the BrightFocus Foundation (A2020812F), the International Society for Neurochemistry's Career Development Grant, the Swedish Alzheimer Foundation (Alzheimerfonden, AF-930627), the Swedish Brain Foundation (Hjärnfonden, FO2020-0240), the Swedish Dementia Foundation (Demensförbundet), the Swedish Parkinson Foundation (Parkinsonfonden), Gamla Tjänarinnor Foundation, the Aina (Ann) Wallströms and Mary-Ann Sjöbloms Foundation, the Agneta Prytz-Folkes and Gösta Folkes Foundation (2020-00124), the Gun and Bertil Stohnes Foundation, and the Anna Lisa and Brother Björnsson's Foundation. H.Z. is a Wallenberg Scholar supported by grants from the Swedish Research Council (2018-02532); the European Research Council (681712); Swedish State Support for Clinical Research (ALFGBG-720931); the Alzheimer Drug Discovery Foundation (ADDF), USA (201809-2016862); the AD Strategic Fund and the Alzheimer's Association (ADSF-21-831376-C, ADSF-21-831381-C, and ADSF-21-831377-C); the Olav Thon Foundation; the Erling-Persson Family Foundation; Stiftelsen för Gamla Tjänarinnor, Hjärnfonden, Sweden (FO2019-0228); the European Union's Horizon 2020 research and innovation program under the Marie Skłodowska-Curie grant 860197 (MIRIADE); European Union Joint Program for Neurodegenerative Disorders (JPND2021-00694); and the UK Dementia Research Institute at UCL. D.R.T. receives funding from FWO (G0F8516N and G065721N) and Stichting Alzheimer Onderzoek (SAO-FRA 2020/017). The B.D.S. laboratory is supported by European Research Council (ERC) grant CELLPHASE_AD834682 (EU), FWO, KU Leuven, VIB, Stichting Alzheimer Onderzoek, Belgium (SAO), the UCB grant from the Elisabeth Foundation, a Methusalem grant from KU Leuven, and the Flemish Government and Dementia Research Institute–MRC (UK). B.D.S. is the Bax-Vanluffelen Chair for Alzheimer's Disease and is supported by the Opening the Future campaign and Mission Lucidity of KU Leuven. **Author contributions:** Conceptualization: S.B. and B.D.S. Methodology: S.B., K.H., K.C., D.T., N.T., A.Sn., L.S., I.C., A.M.A., J.S., T.K.K., H.Z., W.T.-C., D.R.T., E.S., and M.F. Investigation: S.B., K.H., K.C., D.T., A.Sn., I.C., A.A.M., A.Si., J.S., W.T.-C., E.S., L.S., J.S., T.K.K., and H.Z. Visualization: S.B., K.H., K.C., M.F., and N.T. Funding acquisition: S.B. and B.D.S. Project administration: S.B. and B.D.S. Supervision: B.D.S. Writing – original draft: S.B. and B.D.S. Writing – review & editing: S.B., K.H., K.C., A.Sn., D.T., N.T., A.Si., L.S., I.C., A.M.A., J.S., T.K.K., H.Z., W.T.-C., D.R.T., E.S., M.F., and B.D.S. **Competing interests:** H.Z. has served on scientific advisory boards and/or as a consultant for AbbVie, Alector, Annexon, Artery Therapeutics, AZTherapies, Cognition Therapeutics, Denali, Eisai, NervGen, Pinteon Therapeutics, Red Abbey Labs, Passage Bio, Roche, Samumed, Siemens Healthineers, Triplet Therapeutics, and Wave; has given lectures in symposia sponsored by Cellectricon, Fujirebio, AlzeCure, Biogen, and Roche; and is a cofounder of Brain Biomarker Solutions in Gothenburg AB (BBS), which is a part of the GU Ventures Incubator Program. D.R.T. received speaker honoraria from Novartis Pharma Basel (Switzerland) and Biogen (USA); travel reimbursement from GE Healthcare (UK) and UCB (Belgium); and collaborated with GE Healthcare (UK), Novartis Pharma Basel (Switzerland), Probiodrug (Germany), and Janssen Pharmaceutical Company (Belgium). B.D.S. is or has been a consultant for Eli Lilly, Biogen, Janssen Pharmaceutical Company, Eisai, AbbVie, and other companies. B.D.S. is also a scientific founder of Augustine Therapeutics and a scientific founder and stockholder of Muna Therapeutics. W.-T.C. is an employee and stockholder of Muna Therapeutics. **Data and materials availability:** RNA sequencing data are deposited in the Gene Expression Omnibus (accession number GSE195458). App^{NL-G-F} mice are available from T. Saido under a material transfer agreement (MTA) with RIKEN Institute. PHF1 and MC1 antibodies are available from the P. Davies lab under an MTA with Albert Einstein College. H9 cell lines are available under an MTA with WiCell. All materials used in the current work can be obtained upon request to B.D.S. and will be made available under the standard MTA of VIB. **License information:** Copyright © 2023 the authors, some rights reserved; exclusive licensee American Association for the Advancement of Science. No claim to original US government works. https://www.science.org/about/science-licenses-journal-article-reuse. This research was funded in whole or in part by the Swedish Research Council (2021-03244, 2018-02532), UK Research and Innovation (MR/Y014847/1), and the European Research Council (AD834682, 681712, JPND2021-00694), cOAlition S organizations. The author will make the Author Accepted Manuscript (AAM) version available under a CC BY public copyright license.

SUPPLEMENTARY MATERIALS

science.org/doi/10.1126/science.abp9556
Materials and Methods
Figs. S1 to S10
Tables S1 to S5
References (*55*–*69*)
MDAR Reproducibility Checklist

Submitted 8 March 2022; resubmitted 10 July 2023
Accepted 14 August 2023
10.1126/science.abp9556

CELL BIOLOGY

The Batten disease gene product CLN5 is the lysosomal bis(monoacylglycero)phosphate synthase

Uche N. Medoh[1,2,3,4], Andy Hims[1,2,3]†, Julie Y. Chen[1,2,3]†, Ali Ghoochani[1,2,3], Kwamina Nyame[1,2,3,4], Wentao Dong[1,2,3], Monther Abu-Remaileh[1,2,3]*

Lysosomes critically rely on bis(monoacylglycero)phosphate (BMP) to stimulate lipid catabolism, cholesterol homeostasis, and lysosomal function. Alterations in BMP levels in monogenic and complex neurodegeneration suggest an essential function in human health. However, the site and mechanism responsible for BMP synthesis have been subject to debate for decades. Here, we report that the Batten disease gene product CLN5 is the elusive BMP synthase (BMPS). BMPS-deficient cells exhibited a massive accumulation of the BMP synthesis precursor lysophosphatidylglycerol (LPG), depletion of BMP species, and dysfunctional lipid metabolism. Mechanistically, we found that BMPS mediated synthesis through an energy-independent base exchange reaction between two LPG molecules with increased activity on BMP-laden vesicles. Our study elucidates BMP biosynthesis and reveals an anabolic function of late endosomes/lysosomes.

Bis(monoacylglycero)phosphate (BMP), also known as lysobisphosphatidic acid, is conserved from bacteria to most eukaryotes (*1*, *2*). BMP is an anionic, late endosome/lysosome (LE/LY)-specific glycerophospholipid with unusual esterification, unsaturation, and stereochemistry. BMP potently activates lipid catabolism on intraluminal vesicles (ILVs), promotes lysosomal cholesterol egress, and regulates the formation of ILVs in LE/LYs to maintain cellular homeostasis (*3*–*5*). Notably, lysosomal dysfunction is a hallmark of neurodegeneration, and myriad studies report aberrant abundances of BMP in rare and common neurodegenerative diseases. Of these, neuronopathic lysosomal storage disorders (LSDs), Alzheimer's disease, Parkinson's disease, and frontotemporal dementia are among the most studied (*6*–*10*). Beyond neurodegeneration, BMP function is also implicated in atherosclerosis, drug-induced phospholipidosis, viral infection, and cancer (*11*–*17*). Given its stimulatory effect on lysosomal function, it is speculated that BMP accumulation in certain diseases is an ameliorative, firefighter response to lysosomal dysfunction (*18*–*20*), suggesting that inducing its synthesis may have a major therapeutic benefit in a wide spectrum of human diseases. However, the molecular mechanism responsible for BMP synthesis has been poorly understood for decades, mystifying the role of BMP in disease (*21*).

CLN5 loss substantially reduces BMP

We have been studying the function of genes whose biallelic loss of function results in a family of neurodegenerative LSDs collectively called neuronal ceroid lipofuscinosis (NCL) or Batten disease (*22*, *23*). NCLs are characterized by the accumulation of lipofuscin, infantile to juvenile onset neurodegeneration, and premature death (*24*). We were particularly interested in the soluble *CLN5* gene product given its earlier disease onset, association with Alzheimer's disease, and lack of known molecular function (*22*). Because several reports associate Batten disease with defective lipid metabolism (*9*, *25*), we used untargeted lipidomics to analyze the lipidome of *CLN5* knockout HEK293T lysosomes (fig. S1A) (*26*). We found a massive accumulation of lysophosphatidylglycerol (LPG), a detergent-like lysophospholipid (Fig. 1A and table S1). The acyl composition of LPG did not affect the accumulation phenotype, suggesting that the entire LPG class is uniformly aberrant (Fig. 1A). Notably, we also observed a marked depletion of a glycerophospholipid species consistent with BMP (Fig. 1A). BMP species were uniformly depleted in *CLN5* knockout HEK293Ts (Fig. 1B). The levels of other abundant lipid phosphatidylcholine (PC) were unchanged, and thus were used for normalization hereafter (fig. S1B). Given the alterations in LPG and BMP, we sought to quantitate their levels in *CLN5* knockout HEK293Ts at the whole-cell and lysosomal level using optimized, sensitive multiple reaction monitoring transitions for each class. This targeted analysis confirmed LPG accumulation and BMP deficiency (Fig. 1, B and C, and fig. S1B). Consistent with the exclusive localization of BMP to LE/LYs (*27*), whole cells were comparably deficient in BMP and exhibited similar LPG storage (Fig. 1, B and C, and fig. S1B).

To test whether *CLN5* loss of function affects BMP homeostasis in physiologically relevant systems, we generated CLN5-deficient human induced pluripotent stem cells (iPSCs) and differentiated them into neurons (iNeurons) (fig. S1C). Consistent with results in *CLN5* knockout HEK293Ts, targeted quantitation of BMP and LPG in CLN5-deficient iPSCs and iNeurons revealed substantial storage of LPG and depletion of BMP species at the whole-cell level (Fig. 1D). Thus, CLN5 loss of function depletes BMP levels.

CLN5 is the BMP synthase

The depletion of lysosomal BMP in *CLN5* knockout cells suggests a defect in BMP synthesis. However, despite the well-substantiated role of phosphatidylglycerol (PG) in BMP synthesis (*28*, *29*), CLN5-deficient lysosomes did not accumulate PG (fig. S1D) (*28*, *29*), but showed a minor decrease in few lysosomal PG species, which might be explained by increased catabolism and/or defective lysosomal trafficking. Conversely, LPG, which has been suggested to serve as a direct precursor for BMP, accumulated substantially (Fig. 1, A, C, and D) (*29*, *30*). Consistent with its potential role in BMP synthesis, biochemical fractionation studies support the existence of a lysosomal transacylase that mediates the formation of BMP from LPG and instead indicate that PG deacylation to LPG may be a distinct, upstream biochemical step (*31*, *32*). We were thus intrigued by the presence of two apposed, hydrophobic grooves in an experimental CLN5 crystal structure and a report of hydrolase activity against a monoacylated, anionic tool compound with LPG isosterism (fig. S2, A and B) (*33*). This led us to test whether CLN5 is the elusive BMP synthase.

We expressed and purified recombinant, His-tagged CLN5 to homogeneity as a multimeric protein (fig. S3, A to D), which possessed weak thioesterase activity (fig. S3E). Taking care to carry out experiments below the critical micellar concentration of LPG (18:1) (*34*), we then incubated recombinant CLN5 protein with LPG (18:1) at acidic pH and allowed the reaction to proceed for 15 minutes. Quantitation of LPG (18:1), BMP (18:1/18:1), and its predicted byproduct glycerophosphoglycerol (GPG) revealed the presence of BMP (18:1/18:1) and GPG only in conditions containing CLN5 and LPG (Fig. 2, A, B, and C). We validated the glycerophospholipid as BMP (18:1/18:1) against a synthetic standard (Fig. 2D); thus, we hereafter refer to CLN5 as lysosomal BMP synthase (BMPS).

A kinetic enzyme assay of BMPS activity against LPG, monitoring for BMP and GPG release, yielded moderate enzyme activity (K_{cat}/K_m = ~10^4 M^{-1} s^{-1}) for both products (Fig. 2E and fig. S4A). As a result, the kinetic quantitation of GPG product was used for all further BMPS assays. Notably, removal of the polyhistidine tag did not alter BMPS activity (fig. S4B). Consistent with its LE/LY localization, BMPS synthesized BMP at a slightly acidic optimum of 6.5 with a catalytic efficiency of

[1]Department of Chemical Engineering, Stanford University, Stanford, CA 94305, USA. [2]Department of Genetics, Stanford University, Stanford, CA 94305, USA. [3]The Institute for Chemistry, Engineering & Medicine for Human Health (Sarafan ChEM-H), Stanford University, Stanford, CA 94305, USA. [4]Department of Biochemistry, Stanford University School of Medicine, Stanford, CA 94305, USA.
*Corresponding author. Email: monther@stanford.edu
†These authors contributed equally to this work.

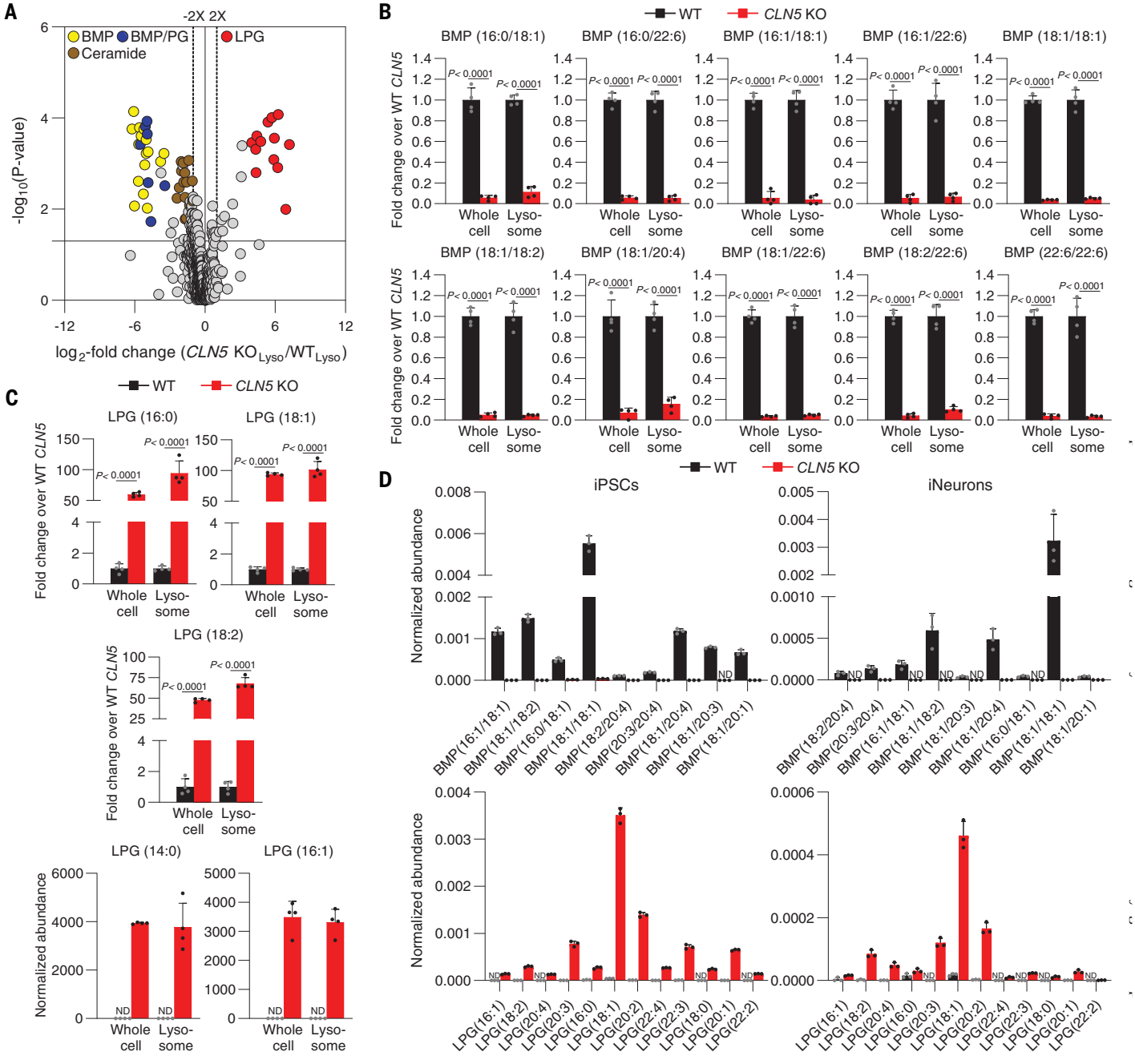

Fig. 1. CLN5 deficiency results in BMP depletion and LPG accumulation. (**A**) Untargeted lipid analysis of HEK293T lysosomes upon *CLN5* loss. Data presented as volcano plot of $\log_2$-transformed fold change in the abundance of lipids between *CLN5* knockout and wild-type HEK293T lysosomes. Significantly altered lipids include LPG (red) and BMP (yellow). BMP/PG (blue) annotation indicates compounds for which fragmentation data was not acquired. Data in table S1. The horizontal line indicates a *P*-value of 0.05 and the vertical line indicates a fold change of 2. Each genotype measurement represents $n = 4$ biologically independent samples. *P*-values were calculated by one-way analysis of variance (ANOVA) with Tukey honestly significant difference (HSD) test and corrected by the Benjamini-Hochberg method with an FDR = 5%. (**B** and **C**) Targeted analyses of BMP and LPG in whole cells and lysosomes. Fold changes in lysosomal BMPs and LPGs between *CLN5* knockout and wild-type HEK293T cells were calculated after subtracting background from control samples and normalizing to endogenous lipid. If species is not detected in wild-type cells, normalized abundance is presented. Data presented as mean ± SD of $n = 4$ biologically independent samples. (**D**) Targeted lipid analysis of LPG and BMP normalized abundances from CLN5-deficient iPSCs and iNeurons compared with the WT. Plotted values are normalized to endogenous lipids. Data presented as mean of $n = 3$ biologically independent samples. ND, not detected. WT, wild-type.

~10^5 M^{-1} s^{-1} although appreciable activity is still retained at a more acidic pH (fig. S4, C and D). To rule out exclusive activity for LPG (18:1), we tested BMPS activity with LPG species of varying lengths. BMPS displays activity against all tested LPGs (LPG 14:0, LPG 16:0, LPG 18:0, LPG 18:1) with a higher preference for longer chain lengths (fig. S4E).

BMPS N143S is a patient missense mutation known to retain protein folding and lysosome trafficking (*35*). Consistent with this literature, we did not observe alterations in recombinant BMPS N143S secondary structure, conformation, and thermal stability relative to the wild type (WT) (fig. S3F, fig. S5A, and fig. S6A). Still,

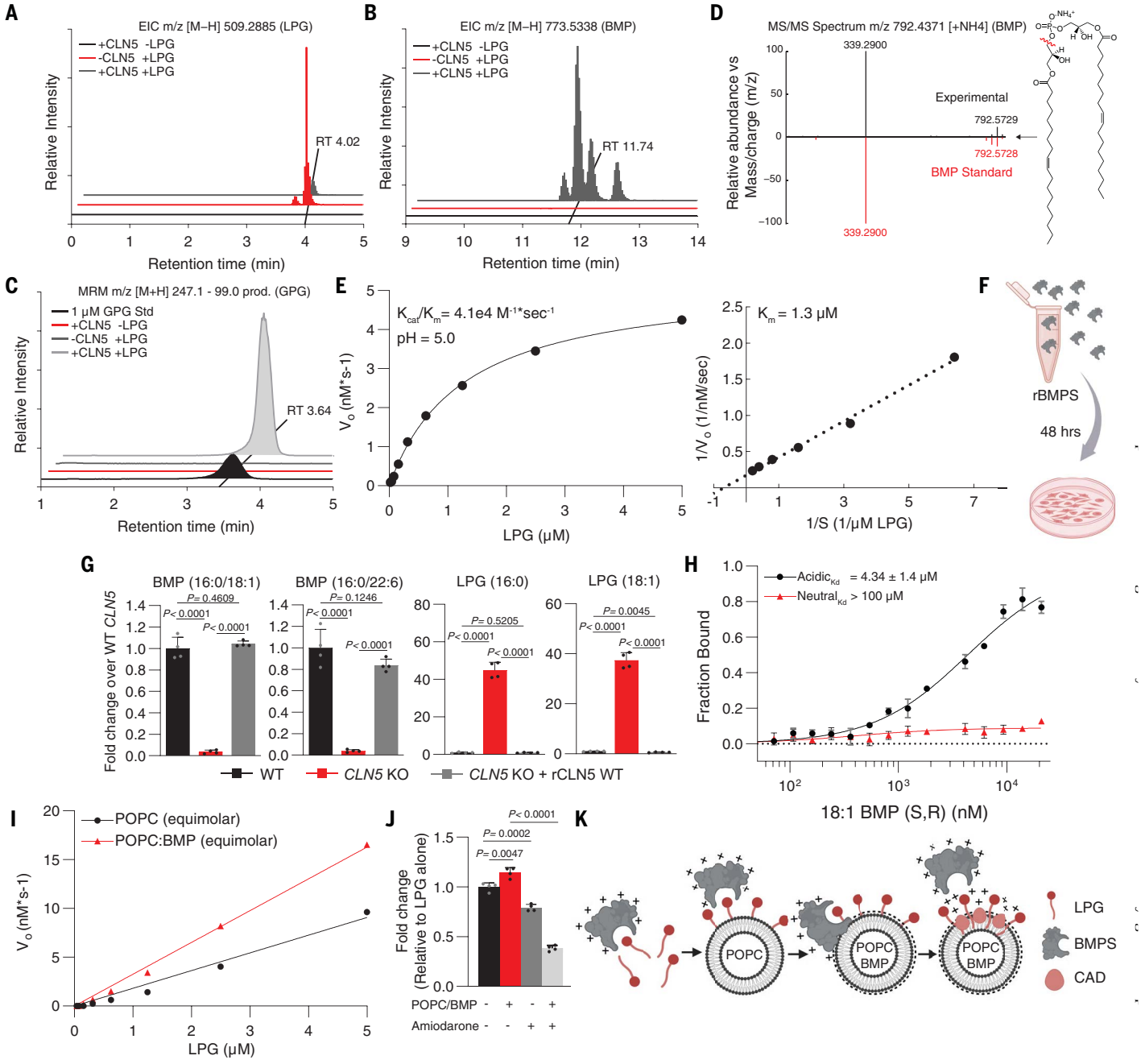

Fig. 2. *CLN5* is the bis(monoacylglycero)phosphate synthase (BMPS). (**A** and **B**) Recombinant CLN5 synthesizes BMP. Representative extracted ion chromatograms (EIC) for LPG (18:1) and BMP (18:1/18:1) from a reaction between recombinant CLN5 and LPG (18:1) under acidic conditions (pH = 5). Retention time corresponds to 3,3′ BMP isoform though acyl migration may occur in vitro. (**C**) BMPS activity results in glycerophosphoglycerol (GPG) release. Representative EIC for GPG byproduct release. (**D**) MS/MS spectral confirmation of CLN5-synthesized BMP (18:1/18:1) compared with commercial standard. (**E**) BMPS is a moderately active enzyme. (Left) Representative Michaelis-Menten curve (MM) for BMPS activity toward LPG (18:1) using GPG to monitor the reaction in acidic conditions. (Right) Lineweaver-Burk transformation of MM curve. Experiment was performed at least three times. K_{cat} (catalytic rate constant) and K_m (Michaelis constant) (**F**) Schematic for recombinant BMPS (rBMPS) supplementation experiment. HEK293T-conditioned media were supplemented with rBMPS for 48 hours prior to lipid analysis. (**G**) rBMPS rescues BMP deficiency and LPG storage. Fold changes in levels of BMP and LPG species were normalized to endogenous lipid. Data presented as mean ± SD of $n = 4$ biologically independent samples. (**H**) BMPS interacts with BMP liposomes. Recombinant BMPS was incubated with 75:25% mol POPC:BMP (18:1/18:1) liposomes under acidic and neutral conditions until reaction reached equilibrium tested by repeated temporal measurements. Data presented as mean ± SD of $n = 3$ technical replicates. Experiment was performed at least three times (**I**) BMP-laden liposomes stimulate BMP synthesis. Recombinant BMPS was incubated with either 100% mol POPC or 75:25% mol POPC/BMP (18:1/18:1) liposomes containing equimolar LPG (18:1). Representative graph shown for experiment performed at least three times. (**J**) Amiodarone inhibits BMPS activity toward monomeric and liposomal LPG. Recombinant BMPS was incubated with either monomeric LPG (18:1) or liposomal LPG (18:1) in the presence or absence of amiodarone. Data presented as mean ± SD of $n = 4$ biologically independent samples. (**K**) Diagram for BMPS activity at a lipid:water interface. BMP-laden vesicles enhance BMPS activity toward LPG. This activation is significantly inhibited by cationic amphiphilic drugs (CADs) such as amiodarone.

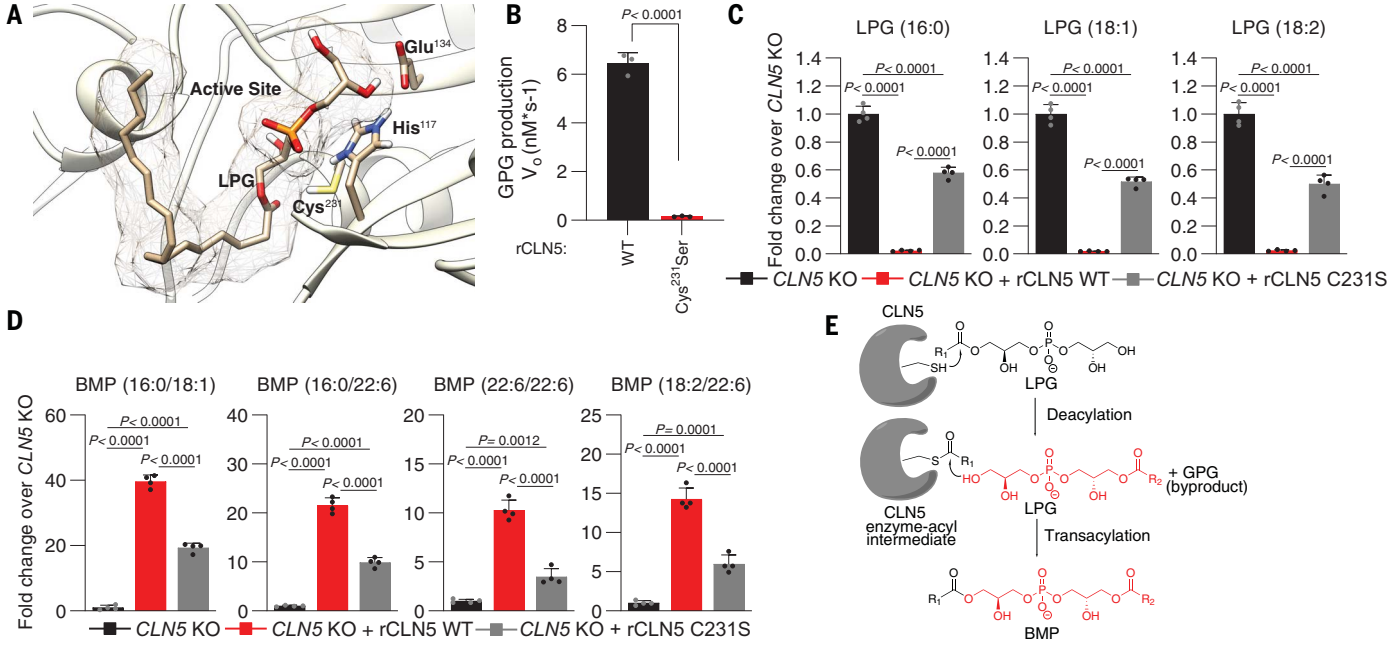

Fig. 3. An active site thiol mediates base exchange for BMP synthesis. (**A**) Schrodinger docking of LPG (18:1) onto an experimental BMPS structure (PDB 6R99). Predicted catalytic triad residues C231, H117, and E134 are annotated. (**B**) Weaker serine nucleophile attenuates BMPS activity as measured by monitoring GPG release. Recombinant BMPS WT and C231S were incubated with LPG (18:1) under acidic conditions. Data presented as mean ± SD of $n = 3$ biologically independent samples. (**C** and **D**) Recombinant BMPS C231S exhibits reduced rescue of LPG storage and BMP deficiency. Fold change in the levels of BMP and LPG species normalized to endogenous lipid. Data presented as mean ± SD of $n = 4$ biologically independent samples. (**E**) Diagram of the BMPS reaction mechanism. The BMPS active site thiol substitutes at the LPG carbonyl carbon releasing a GPG byproduct and abstracting an acyl chain to form a high-energy enzyme-acyl intermediate. Through a base-exchange reaction, the electrophilic intermediate is substituted at its carbonyl carbon by an LPG alcohol to complete the catalytic cycle and release BMP.

BMPS N143S possessed considerably weakened enzyme activity (fig. S7A), suggesting that defective BMP synthesis may drive CLN5 Batten disease.

Several studies support a role of BMPS in endosomal sorting of proteins through extralysosomal secretory compartments such as the endoplasmic reticulum (ER) and Golgi (*22*, *36*, *37*), so we sought to establish a system to evaluate the LE/LY role of BMPS activity in modulating BMP and LPG in live cells. To circumvent the secretory system, we supplemented conditioned media with fluorescently labeled BMPS for endocytic delivery to CLN5 knockout cells and confirmed its localization to LE/LYs by fluorescence microscopy (fig. S8, A to F). With this tool, we tested whether recombinant BMPS replacement in *CLN5* knockout cells can normalize their aberrant lipid profile (Fig. 2F). Recombinant BMPS protein replacement in *CLN5* knockout cells for only 48 hours rescued LPG accumulation and considerably restored BMP levels (Fig. 2G, and fig. S9, A and B). Supplementation of CLN5-deficient cells with recombinant BMPS N143S protein failed to restore LPG and BMP homeostasis (fig. S7, B and C, and fig. S8, B to G). Thus, BMPS localization to the ER or Golgi is not necessary for BMPS activity in cells and the *CLN5* gene product is the lysosomal BMP synthase.

BMP-laden vesicles enhance BMP synthesis

The activation of lipid enzymatic activity through the electrostatic attraction of cationic lysosomal enzymes onto negatively charged ILVs is a central dogma in lysosomal lipid catabolism (*3*, *38*). BMP imbues ILVs with a net negative charge. We thus asked whether BMPS can directly interact with BMP and assessed its functional consequences for BMP synthesis. Indeed, BMPS could only interact with liposomes containing both phosphatidylcholine and BMP and required an acidic pH for docking (Fig. 2H and fig. S10A).

Polyhistidine tags can mediate binding to BMP liposomes (*10*). To rule out a polyhistidine tag–mediated interaction between BMPS and BMP liposomes, we sought to identify the BMPS motif responsible for docking. Previous reports identified an evolutionarily conserved cationic amphipathic helix (CAH) postulated to mediate BMPS anchoring to the lysosome limiting membrane; however, subsequent studies demonstrated that BMPS does not display typical membrane protein characteristics and can be found in soluble fractions following membrane fractionation (*22*). Thus, we asked whether the BMPS CAH instead mediates docking onto ILVs through its well-conserved cationic residues (fig. S10, B and C). Consistent with our hypothesis, mutation of those residues to negatively charged glutamates weakened vesicular BMP binding (fig. S3, G and H, and figs. S5B, S6B, and S10D).

To test for the stimulation of BMPS activity by BMP liposomes, we integrated LPG (18:1) into liposomes at a constant lysophospholipid to liposome equimolar ratio to maintain stimulation of activity and avoid surface dilution (fig. S11A). BMP liposomes enhanced BMP synthesis as expected (Fig. 2I) (*31*). In agreement with the lipid enzyme theory, we observed a surface dilution effect with higher liposome to substrate ratios (fig. S11B) (*39*). Consistent with studies on the ability of other anionic phospholipids to stimulate lysosomal lipid enzymes (*5*, *40*, *41*), we observed increased BMPS activity on membranes containing PG, phosphatidylinositol, and phosphatidylserine, although the relatively high abundance of BMP in ILVs suggests BMP acts as the main anionic coactivator in lysosomes (fig. S11C) (*42*).

Given the stimulation of BMPS activity by BMP liposomes, we asked whether cationic amphiphilic drugs (CAD) inhibit BMP synthesis in the presence and absence of LPG-integrated BMP liposomes. Amiodarone, a CAD shown to cause drug-induced phospholipidosis (*38*), slightly inhibited BMPS activity toward nonliposomal LPG and dramatically inhibited BMPS activity toward liposomal LPG likely through

neutralization of the negative charge on the surface of BMP liposomes (Fig. 2, J and K) (*38*). Altogether, these data support a role of BMP in stimulating LE/LY lipid anabolism.

A base-exchange reaction mediates BMP synthesis

A base-exchange reaction between two LPG molecules mediates BMP synthesis in fractionated lysosomal lysates (*30*). Such a reaction mechanism should result in an initial release of glycerophosphoglycerol during LPG deacylation without any energy input. Supporting this mechanism, we detected the water-soluble GPG byproduct along with BMP (Fig. 2C). In principle, the base-exchange reaction could utilize any lysophospholipid as an acyl donor, so we asked whether other lysophospholipids—namely lysophosphatidylcholine (LPC)—lysophosphatidylserine (LPS), lysophosphatidylethanolamine (LPE), and lysophosphatidylinositol (LPI), are additional BMPS substrates. With an equimolar amount of lysophospholipid and LPG, we did not detect an appreciable release of glycerophosphocholine, glycerophosphoserine, glycerophosphoethanolamine, nor glycerophosphoinositol to support their involvement in BMP synthesis (fig. S12A). Consistent with these in vitro findings, LPC, LPE, and LPS did not accumulate in BMPS-deficient lysosomes, and LPI only modestly increased (fig. S12, B to E, and table S1). Thus, LPG represents an exclusive lysophospholipid acyl donor for base exchange.

In silico docking experiments identified a plausible active site that positioned the LPG carbonyl carbon near a cysteine 231, histidine 117, and glutamate 134 catalytic triad (Fig. 3A) (*33*). Given the predicted cysteine nucleophile, the BMPS thioester enzyme-acyl intermediate mimics an acyl-CoA coenzyme utilized by acyltransferases for extralysosomal lipid synthesis (*43*). Because thiols are more nucleophilic than alcohols, and the thioester enzyme-acyl intermediate represents a stronger electrophile than its ester counterpart for base exchange with an LPG alcohol, we asked whether a cysteine-to-serine BMPS substitution attenuates enzyme activity (figs. S3I, S5C, and S6C). Consistent with this idea, the weaker C231S BMPS retained less than 5% of the wild-type BMPS activity when monitoring GPG release (Fig. 3B and fig. S12F), and its replacement in *CLN5* knockout cells for 48 hours only partially rescued LPG accumulation and BMP deficiency relative to that of wild-type BMPS (Fig. 3, C and D, fig. S8, B to F and H, and fig. S12, G and H). These data support an energy-independent, active site thiol-mediated base exchange for BMP synthesis (Fig. 3E).

Late endosomes/lysosomes require BMPS to synthesize BMP

Given the localization of BMPS to lysosomes and the lysosomal deficiency of BMP, we sought to confirm whether LE/LYs, known for their degradative capacity, are the site of BMP synthesis (*32*). To this end, we leveraged an established method to conjugate lipid tracers to bovine serum albumin (BSA) for efficient endocytic internalization and delivery (Fig. 4A) (*44*). To *CLN5* knockout cells we fed a BSA-conjugated, deuterium-labeled (d5-)PG (16:0/18:1) tracer at various time points and assessed conversion of PG to LPG and BMP in LE/LYs by monitoring the appearance of deuterium-labeled metabolites (Fig. 4B). *CLN5* knockout cells converted d5-PG (16:0/18:1) to d5-LPG (18:1) with comparable kinetics to the WT but exhibited a complete block in d5-LPG (18:1) conversion to d5-BMP (18:1/18:1) (Fig. 4C and fig. S13A). Notably, *CLN5* knockout cells showed no decrease in uptake of the d5-PG (16:0/18:1) precursor whose levels were higher in knockout cells compared with the WT, suggesting higher endocytic uptake (fig. S13B). Thus, LE/LYs of *CLN5* knockout cells are unable to transform LPG into BMP, consistent with the molecular function of BMPS to mediate transacylation of LPG to form BMP. To further confirm LE/LYs as the site of BMP synthesis, we used the LysoIP system to monitor BMP synthesis in vitro (*26*). To this end, we immunoprecipitated BMPS-deficient LE/LYs and assessed their ability to convert deuterated PG to BMP (Fig. 4D). Indeed, BMPS-deficient lysosomal lysates were unable to convert d5-PG (16:0/18:1) to d5-BMP (18:1/18:1) and d5-BMP (16:0/18:1) (Fig. 4E). Complementation of BMPS-deficient lysosomal lysate with recombinant CLN5 restored synthesis of d5-BMP (18:1/18:1) and d5-BMP (16:0/18:1) (Fig. 4E).

Consistent with the ability of BMP to stimulate phospholipase activity (*38*), *CLN5* knockout cells fed with a BSA-conjugated d9-PC (18:0/18:0) tracer at various timepoints displayed reduced kinetic conversion of d9-PC (18:0/18:0) to d9-LPC (18:0), suggesting weakened phospholipase activity (Fig. 4, F and G). Endocytic uptake of d9-PC (18:0/18:0) was comparable between wild-type and *CLN5* knockout cells, with a slight increase in knockout cells if any (fig. S13C).

BMP is also known to stimulate glycosphingolipid catabolism within late endosomes/lysosomes (*9*). We thus tested whether CLN5 loss of function affects glucosylceramidase (GCase) activity. Indeed, CLN5-deficient HEK293Ts exhibited slower conversion of d5-Glc1Cer (d18:1/18:0) to d5-Cer (d18:1/18:0) without reduced endocytic uptake, indicating attenuated GCase activity (Fig. 4, H and I, and fig. S13D). CLN5 knockout HEK293T cells, iPSCs, and iNeurons did not exhibit an increase in the levels of hexosylceramides (fig. S14A) although CLN5 knockout HEK293T cells and iPSCs were deficient in ceramides, which were largely unaffected in iNeurons (fig. S14B). Still, CLN5 knockout iNeurons accumulated GM3 gangliosides (Fig. 4J), another lipid whose degradation is dependent on BMP. Notably, such gangliosidosis is known to drive neurodegeneration (*10*).

Given the role of BMP in stimulating ILV biogenesis (*4*), we asked whether CLN5-deficient HEK293Ts exhibit alterations to ILV abundance. Consistent with this idea, the number of ILVs in CLN5-deficient lysosomes was substantially reduced (Fig. 4K). BMP is necessary for LE/LY cholesterol homeostasis (*45*, *46*). Consistent with this idea, filipin staining revealed accessible cholesterol storage in *CLN5* knockout cells (Fig. 4L). Treatment of *CLN5* knockout cells with recombinant BMPS significantly rescued secondary cholesterol storage material below WT levels consistent with BMP's role in maintaining intracellular cholesterol homeostasis (Fig. 4L). Thus, CLN5 is the elusive BMPS whose function is essential for proper lipid catabolism and trafficking in the lysosome.

Discussion

Despite the discovery of BMP over a half a century ago, the machinery responsible for its synthesis has remained enigmatic. We identify the Batten disease gene product CLN5—whose loss leads to neurodegeneration—as the elusive BMPS (*47*). BMPS utilizes two lysophosphatidylglycerol molecules in an energy-independent fashion to synthesize BMP, the activation of which occurs on BMP-enriched ILVs. This base-exchange reaction represents the first example of anabolism within a harsh, digestive lysosomal environment and provides a reaction mechanism for other potential anabolic processes within this classically catabolic organelle.

Several questions regarding the BMP biosynthetic pathway remain. First, lysosomes are thought to contain a small amount of PG if any at all. It is thus unclear what subcellular compartment supplies the initial PG substrate for BMP synthesis. Given the nearly exclusive localization of PG in mitochondria where it serves as a precursor for cardiolipin, it is attractive to theorize that mitochondria-lysosome crosstalk is required for BMP synthesis (*48*). Second, a lysosomal phospholipase that mediates the conversion of PG to LPG in LE/LYs was recently identified (*49*), and whether other phospholipases play a role in BMP synthesis through substrate production is unknown (*32*). Furthermore, BMP exhibits an unusual (S,S) stereochemistry that may be produced by an isomeric transformation of LPG (*50*). Whether this transformation occurs spontaneously or through the action of an unidentified LPG isomerase remains to be determined. Lastly, how biallelic mutations in BMPS result in CNS-restricted pathology is unclear. Although it is possible that BMP metabolism is most relevant in the CNS where post mitotic, long-lived neurons heavily rely on lysosomes to maintain neuronal homeostasis (*51*), we speculate that other enzymes/proteins may compensate for BMPS loss of function. Indeed, BMPS acts in a complex with

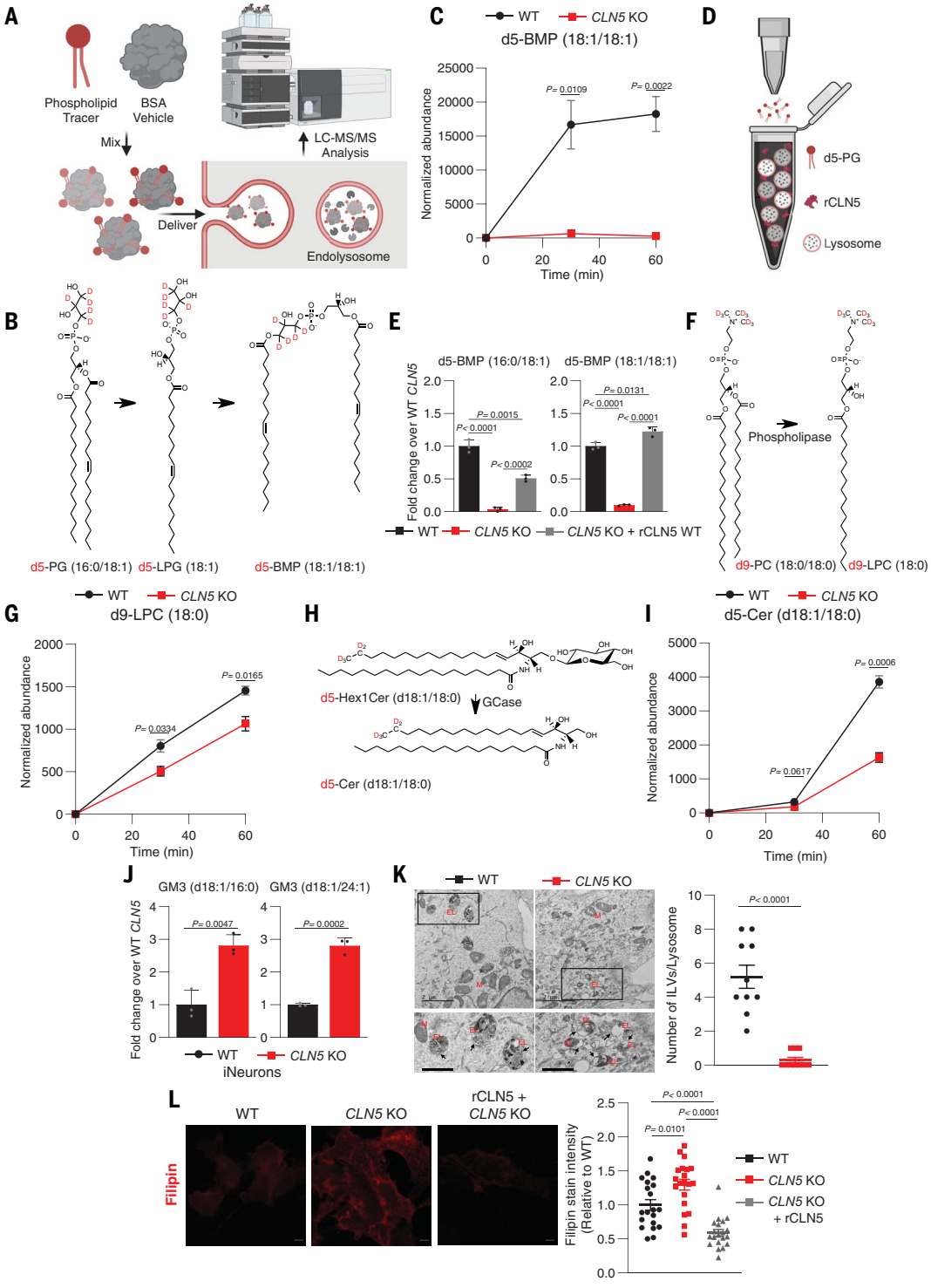

Fig. 4. Late endosomes/lysosomes synthesize BMP to maintain lipid homeostasis. (**A**) Schematic for LE/LY delivery of deuterated tracers for metabolism and LC-MS/MS analysis. Deuterated lipids are conjugated to BSA and supplemented in HEK293T-conditioned media after starvation to increase endocytic flux. After several time points, lipids were extracted for LC-MS/MS analysis. (**B**) Depiction of monitored deuterated phosphatidylglycerol metabolites bearing 5 deuterium atoms in their glycerol moiety. (**C**) *CLN5* knockout HEK293Ts are unable to synthesize deuterated BMP. Intensities for d5-BMP (18:1/18:1) in *CLN5* knockout and wild-type HEK293T cells are presented after background subtraction and normalization to endogenous lipids. Data presented as mean ± SD of $n = 3$ biologically independent samples. (**D**) Schematic for recombinant BMPS complementation experiment in BMPS deficient lysosomal protein extract. Lysosomes were immunoprecipitated and harvested for proteins. Lysosomal proteins were complemented with recombinant BMPS and supplied with d5-PG (16:0/18:1) under acidic conditions. (**E**) Lysosomal lysates require BMPS to synthesize BMP. Fold change in the levels of synthesized deuterated BMP species. Data presented as mean ± SD of $n = 3$ biologically independent samples. (**F**) Depiction of monitored deuterated phosphatidylcholine metabolites bearing 9 deuterium atoms in their methyl groups. (**G**) *CLN5* knockout HEK293T lysosomes exhibit impaired phospholipid catabolism. Intensities for d9-LPC (18:0) production in *CLN5* knockout and wild-type HEK293T cells are presented after background subtraction and normalization to endogenous lipids. Experiment was done as in (A). Data presented as mean ± SD of $n = 3$ biologically independent samples. (**H**) Depiction of monitored deuterated glucosylceramide metabolites bearing 5 deuterium atoms in their hydrocarbon chain (**I**) *CLN5* knockout HEK293T lysosomes exhibit impaired GCase activity. Intensities for d5-Hex1Cer (d18:1/18:0) production in *CLN5* knockout and wild-type HEK293T cells are presented after background subtraction and normalization to endogenous lipids. Experiment was done as in (A). Data presented as mean ± SD of $n = 3$ biologically independent samples. (**J**) CLN5-deficient iNeurons accumulate GM3 gangliosides. Fold changes in lipid species abundance between *CLN5* knockout and wild-type HEK293T cells were calculated after subtracting background from control samples and normalizing to endogenous lipids. Data presented as mean ± SD of $n = 3$ biologically independent samples. (**K**) BMPS-deficient HEK293Ts have fewer ILVs. Representative electron micrographs of *CLN5* knockout and wild-type HEK293T cells. The average number of ILVs within each identified endolysosome per cell are counted with 10 cells per condition. Arrows indicate ILVs. Scale bars, 2 μm. Inset scale bar, 1 μm. EL, endo-lysosome; M, mitochondria. (**L**) BMPS deficient HEK293T cells accumulate cholesterol. Filipin staining of cholesterol in recombinant BMPS-treated and -untreated *CLN5* knockout and wild-type HEK293T cells was determined and are presented relative to WT. Representative data shown for experiment repeated at least three times with 20 cells per condition. Scale bar = 10 μm.

CLN3 to regulate retromer function, and it is unknown whether this function is directly linked to BMP synthesis (*36*, *37*).

Several studies reveal a deficiency of BMP in other mutated Batten disease genes (CLN3, CLN11) or alterations in BMPS lysosomal trafficking and/or abundance by loss of other Batten disease gene products (CLN6, CLN7, CLN8, CLN14) (*9*, *10*, *25*, *47*, *52*–*54*). Given the identification of the Batten disease *CLN5* gene product as the BMPS, BMP dyshomeostasis may be the unified metabolic defect in Batten disease. Future studies should investigate the potential biochemical role of Batten disease gene products in maintaining BMP homeostasis.

BMP is implicated in a wide spectrum of diseases and processes, such as atherosclerosis, drug-induced phospholipidosis, viral infection, cancer, and neurodegeneration (*6*–*17*). Given the critical function of lysosomes in these contexts, we hypothesize that BMP may play a fundamental, protective role in maintaining cellular homeostasis and may promote processes that influence virulence and cancer. The identification of BMPS provides an opportunity to study the role of BMP in lysosomal biology and disease using genetic and chemical tools and positions BMPS as an attractive therapeutic target.

REFERENCES AND NOTES

1. D. R. Body, G. M. Gray, *Chem. Phys. Lipids* **1**, 254–263 (1967).
2. S. Czolkoss *et al*., *Environ. Microbiol.* **23**, 6993–7008 (2021).
3. H. D. Gallala, K. Sandhoff, *Neurochem. Res.* **36**, 1594–1600 (2011).
4. H. Matsuo *et al*., *Science* **303**, 531–534 (2004).
5. A. Abe, J. A. Shayman, *J. Lipid Res.* **50**, 2027–2035 (2009).
6. U. N. Medoh, J. Y. Chen, M. Abu-Remaileh, *Curr. Opin. Syst. Biol.* **29**, 100408 (2022).
7. A. M. Miranda *et al*., *Transl. Psychiatry* **12**, 129 (2022).
8. R. N. Alcalay *et al*., *Mov. Disord.* **35**, 134–141 (2020).
9. T. Logan *et al*., *Cell* **184**, 4651–4668.e25 (2021).
10. S. Boland *et al*., *Nat. Commun.* **13**, 5924 (2022).
11. M. Arnal-Levron, Y. Chen, I. Delton-Vandenbroucke, C. Luquain-Costaz, *Biochem. Pharmacol.* **86**, 115–121 (2013).
12. N. Liu, E. A. Tengstrand, L. Chourb, F. Y. Hsieh, *Toxicol. Appl. Pharmacol.* **279**, 467–476 (2014).
13. A. Patel, B.-P. Mohl, P. Roy, *J. Biol. Chem.* **291**, 12408–12419 (2016).
14. C. Bissig *et al*., *Dev. Cell* **25**, 364–373 (2013).
15. A. Erazo-Oliveras *et al*., *Cell Chem. Biol.* **23**, 598–607 (2016).
16. T. Kirkegaard *et al*., *Nature* **463**, 549–553 (2010).
17. A. Serrano-Puebla, P. Boya, *Biochem. Soc. Trans.* **46**, 207–215 (2018).
18. O. Ilnytska *et al*., *J. Biol. Chem.* **297**, 100813 (2021).
19. D. Moreau *et al*., *EMBO Rep.* **20**, e47055 (2019).
20. P. A. Lewis, *Sci. Transl. Med.* **14**, eabq7374 (2022).
21. M. R. Showalter *et al*., *Int. J. Mol. Sci.* **21**, 8067 (2020).
22. I. Basak *et al*., *Cell. Mol. Life Sci.* **78**, 4735–4763 (2021).
23. F. M. Platt, A. d'Azzo, B. L. Davidson, E. F. Neufeld, C. J. Tifft, *Nat. Rev. Dis. Primers* **4**, 27 (2018).
24. S. E. Mole, S. L. Cotman, *Biochim. Biophys. Acta* **1852**, 2237–2241 (2015).
25. N. N. Laqtom *et al*., *Nature* **609**, 1005–1011 (2022).
26. M. Abu-Remaileh *et al*., *Science* **358**, 807–813 (2017).
27. T. Kobayashi *et al*., *Nature* **392**, 193–197 (1998).
28. F. Hullin-Matsuda *et al*., *J. Lipid Res.* **48**, 1997–2008 (2007).
29. B. J. Poorthuis, K. Y. Hostetler, *J. Biol. Chem.* **251**, 4596–4602 (1976).
30. J. Heravi, M. Waite, *Biochim Biophys Acta Mol Cell Biol Lipids.* **1437**, 277–286 (1999).
31. S. J. Huterer, J. R. Wherrett, *Biochim Biophys Acta Mol Cell Biol Lipids.* **1001**, 68–75 (1989).
32. B. Amidon, A. Brown, M. Waite, *Biochemistry* **35**, 13995–14002 (1996).
33. A. V. Luebben *et al*., *Sci. Adv.* **8**, eabj8633 (2022).
34. R. E. Stafford, T. Fanni, E. A. Dennis, *Biochemistry* **28**, 5113–5120 (1989).
35. A. Moharir, S. H. Peck, T. Budden, S. Y. Lee, *PLOS ONE* **8**, e74299 (2013).
36. S. Yasa, E. Sauvageau, G. Modica, S. Lefrancois, *Biochem. J.* **478**, 2339–2357 (2021).
37. A. Mamo, F. Jules, K. Dumaresq-Doiron, S. Costantino, S. Lefrancois, *Mol. Cell. Biol.* **32**, 1855–1866 (2013).
38. J. A. Shayman, A. Abe, *Biochim. Biophys. Acta* **1831**, 602–611 (2013).
39. G. M. Carman, R. A. Deems, E. A. Dennis, *J. Biol. Chem.* **270**, 18711–18714 (1995).
40. G. Wilkening, T. Linke, K. Sandhoff, *J. Biol. Chem.* **273**, 30271–30278 (1998).
41. T. Linke *et al*., *Biol. Chem.* **382**, 283–290 (2001).
42. T. Kobayashi *et al*., *J. Biol. Chem.* **277**, 32157–32164 (2002).
43. T. J. Grevengoed, E. L. Klett, R. A. Coleman, *Annu. Rev. Nutr.* **34**, 1–30 (2014).
44. S. G. Scharenberg *et al*., *Sci. Adv.* **9**, eadf8966 (2023).
45. J. Chevallier *et al*., *J. Biol. Chem.* **283**, 27871–27880 (2008).
46. L. A. McCauliff *et al*., *eLife* **8**, e50832 (2019).
47. M. Savukoski *et al*., *Nat. Genet.* **19**, 286–288 (1998).
48. J. A. Mayr, *J. Inherit. Metab. Dis.* **38**, 137–144 (2015).
49. J. Chen *et al*., *Commun. Biol.* **6**, 210 (2023).
50. T. Thornburg, C. Miller, T. Thuren, L. King, M. Waite, *J. Biol. Chem.* **266**, 6834–6840 (1991).
51. V. Udayar, Y. Chen, E. Sidransky, R. Jagasia, *Trends Neurosci.* **45**, 184–199 (2022).
52. Y. Wang *et al*., *Sci. Adv.* **8**, eabm5578 (2022).
53. T. Danyukova *et al*., *Hum. Mol. Genet.* **27**, 1711–1722 (2018).
54. L. Bajaj *et al*., *J. Clin. Invest.* **130**, 4118–4132 (2020).
55. U. N. Medoh, Lipidomic analysis of WT and CLN5-deficient HEK293T cells, iPSCs, and iNeurons. Dryad (2023); https://datadryad.org/stash/dataset/doi:10.5061/dryad.gb5mkkwvq.

ACKNOWLEDGMENTS

We thank all members of the Abu-Remaileh laboratory for valuable discussions. We also thank S. Pfeffer for help and access to MST and nanoDSF instruments, L. Gan for providing the NGN2-iPSCs, and P. Kim for providing Expi293s for protein expression. Additionally, we thank the Metabolomics Knowledge Center (MKC) at Sarafan ChEM-H and the Stanford Neuroscience Microscopy Service at Wu Tsai Neurosciences Institute. **Funding:** This work was supported by the National Institute on Aging of the National Institutes of Health under award P30AG066515 supporting the Stanford Alzheimer's Disease Research Foundation (ADRC) and from Beat Batten and the NCL Foundations (NCL-Stiftung) to M.A-R. This work was further supported by the Knight Initiative for Brain Resilience and the Innovative Medicines Accelerator to M.A-R. U.N.M. and K.N. are supported by the Sarafan ChEM-H Chemistry/Biology Interface Program as O'Leary-Thiry Fellows and Kolluri Fellows, respectively. J.Y.C. was supported by the Chemical Engineering Research Experience for Undergraduates Program. A.H. is supported by the Sarafan ChEM-H/IMA Postbaccalaureate Program in Target Discovery. K.N. is additionally supported by the Bio-X Stanford Interdisciplinary Graduate Fellowship affiliated with the Wu Tsai Neurosciences Institute (Bio-X SIGF: Mark and Mary Steven's Interdisciplinary Graduate Fellow). M.A-R. is a Stanford Terman Fellow and a Pew-Stewart Scholar for Cancer Research, supported by The Pew Charitable Trusts and the Alexander and Margaret Stewart Trust. **Author contributions:** U.N.M. and M.A-R. conceptualized the study. U.N.M. designed and performed experiments with assistance from J.Y.C. and A.H. A.G. genetically modified and maintained iPSCs. U.N.M. and K.N. developed targeted mass spectrometry methods. U.N.M., K.N., and W.D. acquired mass spectrometry data. U.N.M. and W.D. analyzed mass spectrometry data. U.N.M. and M.A-R. wrote the manuscript, and all other authors reviewed its contents. **Competing interests:** U.N.M. and M.A-R. are inventors on a patent related to this work filed by Stanford University. M.A-R. is a scientific advisory board member of Lycia Therapeutics. All other authors declare no competing interests. **Data and materials availability:** All data is available in the main text or the supplementary materials. Plasmids and cell lines can be requested from, and requests will be fulfilled by, the corresponding author. Lastly, we have provided the raw data in a public repository for the lipidomic analyses in Fig. 1 (A and D) (*55*).

License information: Copyright © 2023 the authors, some rights reserved; exclusive licensee American Association for the Advancement of Science. No claim to original US government works. https://www.sciencemag.org/about/science-licenses-journal-article-reuse

SUPPLEMENTARY MATERIALS

science.org/doi/10.1126/science.adg9288
Materials and Methods
Figs. S1 to S14
Table S1
References (*56*, *57*)
MDAR Reproducibility Checklist

Submitted 31 January 2023; resubmitted 4 May 2023
Accepted 16 August 2023
10.1126/science.adg9288

NEUROIMMUNOLOGY

Neuromedin U programs eosinophils to promote mucosal immunity of the small intestine

Yu Li[1,2,3,4], Shaorui Liu[2,3,4], Kewen Zhou[2,3,4], Yinsheng Wang[2,3,4], Yan Chen[5], Wen Hu[6], Shuyan Li[7], Hui Li[2,3,4], Yan Wang[2,3,4], Qiuying Wang[2,3,4], Danyang He[2,3], Heping Xu[2,3,4]*

Eosinophils are granulocytes that play an essential role in type 2 immunity and regulate multiple homeostatic processes in the small intestine (SI). However, the signals that regulate eosinophil activity in the SI at steady state remain poorly understood. Through transcriptome profiling of eosinophils from various mouse tissues, we found that a subset of SI eosinophils expressed neuromedin U (NMU) receptor 1 (NMUR1). Fate-mapping analyses showed that NMUR1 expression in SI eosinophils was programmed by the local microenvironment and further enhanced by inflammation. Genetic perturbation and eosinophil-organoid coculture experiments revealed that NMU-mediated eosinophil activation promotes goblet cell differentiation. Thus, NMU regulates epithelial cell differentiation and barrier immunity by stimulating NMUR1-expressing eosinophils in the SI, which highlights the importance of neuroimmune-epithelial cross-talk in maintaining tissue homeostasis.

Eosinophils are granulocytes that develop from myeloid progenitors in bone marrow (BM) and can infiltrate various organs (*1*). They are commonly considered to be effector cells associated with type 2 immune responses (*2*). However, eosinophils are particularly abundant in the small intestine (SI) under homeostatic conditions (*3*, *4*), where they regulate multiple physiological processes (*5*–*7*). SI eosinophils exhibit distinctive surface proteins, transcriptional states, and signs of degranulation (*8*–*11*), which suggests that they undergo a tissue adaptation process in the SI. However, the tissue-derived cues that regulate eosinophil responses in the SI remain poorly understood.

Neuromedin U receptor 1 (NMUR1) is a receptor for neuromedin U (NMU), which potently activates group 2 innate lymphoid cells (ILC2s) to promote type 2 immune responses in mucosal tissues (*12*–*14*). A previous study has suggested that NMU-NMUR1 signaling induces eosinophil infiltration into the lung during allergic inflammation (*15*). However, two recent studies have reported that eosinophils do not express NMUR1 (*16*, *17*). Thus, whether NMU directly regulates eosinophil responses is controversial. In particular, the cell-intrinsic roles, if any, of NMUR1 in SI eosinophils are unknown.

[1]School of Medicine, Zhejiang University, Hangzhou 310058, Zhejiang, China. [2]Key Laboratory of Growth Regulation and Translational Research of Zhejiang Province, School of Life Sciences, Westlake University, Hangzhou 310024, Zhejiang, China. [3]Center for Infectious Disease Research, Westlake Laboratory of Life Sciences and Biomedicine, Hangzhou 310024, Zhejiang, China. [4]Laboratory of Systems Immunology, Institute of Basic Medical Sciences, Westlake Institute for Advanced Study, Hangzhou 310024, Zhejiang, China. [5]Center for Inflammatory Bowel Diseases, Department of Gastroenterology, The Second Affiliated Hospital, Zhejiang University School of Medicine, Hangzhou 310009, Zhejiang, China. [6]State Key Laboratory for Diagnosis and Treatment of Infectious Diseases, National Clinical Research Center for Infectious Diseases, Collaborative National Clinical Research Center for Infectious Diseases, The First Affiliated Hospital, Zhejiang University School of Medicine, Hangzhou 310003, Zhejiang, China. [7]Department of Nursing, The Second Affiliated Hospital, Zhejiang University School of Medicine, Hangzhou 310009, Zhejiang, China.
*Corresponding author. Email: xuheping@westlake.edu.cn

NMUR1 expression defines a distinctive state of eosinophils specifically in the SI

To characterize SI-specific molecular features of eosinophils, we analyzed eosinophils from different mouse tissues (fig. S1, A and B) using bulk RNA sequencing (RNA-seq) (fig. S2A). t-distributed stochastic neighbor embedding (t-SNE) reduction analysis revealed that eosinophils display divergent transcriptional states across different tissues, except for the spleen and blood, where they showed transcriptional similarities (Fig. 1A and fig. S2A). Eosinophils in the BM and SI accounted for most of the tissue-specific genes (Fig. 1B). The BM-specific transcriptional program mainly comprised mitotic genes, reflective of a progenitor stage. By contrast, eosinophils in the skin, colon, lung, and SI expressed different sets of cytokines and receptors of multiple proinflammatory signals (Fig. 1B). SI eosinophils were further characterized by high expression of many genes involved in cholesterol biosynthesis (e.g., *Hmgcs1* and *Sc5d*), which corroborates a recent study highlighting de novo cholesterol biosynthesis in SI eosinophils (*11*) and G protein–coupled receptor signaling pathways for homomers and neurotransmitters. We further ranked the tissue-specific genes (Fig. 1C and fig. S2B) and identified *Nmur1* as one of the most distinctively expressed genes in SI eosinophils (Fig. 1, C and D).

We next used single-cell RNA-seq (scRNA-seq) to further characterize the transcriptional heterogeneity of SI eosinophils (fig. S2C). Uniform manifold approximation and projection (UMAP) analysis identified three cell clusters (Fig. 1E and fig. S2D). Cluster 1 (C1) cells, exhibiting the highest expression of *Nmur1* (Fig. 1F and fig. S2D), showed enrichment of the specific transcriptional program (Fig. 1, B and C), including genes involved in cholesterol biosynthesis, degranulation, and secretory vesicle formation (e.g., *Cd63*) compared with cells in C2 and C3 (fig. S2, D and E). By contrast, genes involved in cytokine-mediated signaling pathways (e.g., *Il4*) and cell adhesion (e.g., *Sell*) were down-regulated in C1 cells (fig. S2D). Thus, the distinctive transcriptional program of eosinophils in the SI relative to other tissues (Fig. 1, B and C) is mainly attributable to *Nmur1*-expressing C1 cells.

This finding of *Nmur1*-expressing SI eosinophils differs from the observations of recent studies that have used *Nmur1*-BAC transgenic reporter mice (*16*, *17*). We reasoned that this discrepancy was a result of random transgenic insertions of exogenous reporter alleles in the BAC transgenic reporter mice (*16*, *17*), which may not accurately report the transcriptional activity of the endogenous *Nmur1* locus. To accurately track endogenous NMUR1 expression, we generated a knockin mouse strain (designated *Nmur1*$^{iCre\text{-}TdT}$) by inserting the protein coding sequence of Cre recombinase flanked by P2A coding sequences and followed by tdTomato-coding sequences (*P2A-iCre-P2A-tdTomato* cassette) after the last coding exon of the endogenous *Nmur1* gene (Fig. 1G). In these mice, NMUR1 was expressed in ILC2s (fig. S3, A to D) as well as a subset of eosinophils in the SI but not those in other organs (Fig. 1, G and H, and fig. S3, E and F). We then confirmed that tdTomato$^+$ SI eosinophils expressed significantly higher levels of *Nmur1* transcripts compared with their tdTomato$^-$ counterparts through quantitative polymerase chain reaction (qPCR) analysis (fig. S3G). We also detected NMUR1 expression in a small population of SI T cells and ILC3s (fig. S3, H and I). We observed comparable NMUR1 expression levels between SI ILC2s from postnatal day 1 (P1) mice and those from adult mice (fig. S3, H and J). However, NMUR1 expression in SI eosinophils was not observed until P3 and reached adult levels by P7 (Fig. 1G and fig. S3, K and L). In agreement with our mouse data, a subset of eosinophils in SI biopsies from multiple donors also expressed significantly higher NMUR1 protein levels compared with eosinophils in blood and colon biopsies (Fig. 1, I and J; fig. S4, A and B; and table S1).

We next leveraged our *Nmur1*$^{iCre\text{-}TdT}$ reporter strain to characterize NMUR1-expressing SI eosinophils. Both NMUR1$^+$ and NMUR1$^-$ eosinophils exhibited typical features, including high intracellular granularity (as reflected by high side scatter), high expression of CD11b and Siglec-F (fig. S5A), and eosinophilic cytoplasm (fig. S5B). Notably, NMUR1$^+$ eosinophils displayed lower eosin staining intensity compared with their NMUR1$^-$ counterparts (fig. S5B). Furthermore, the nuclei of NMUR1$^+$ eosinophils

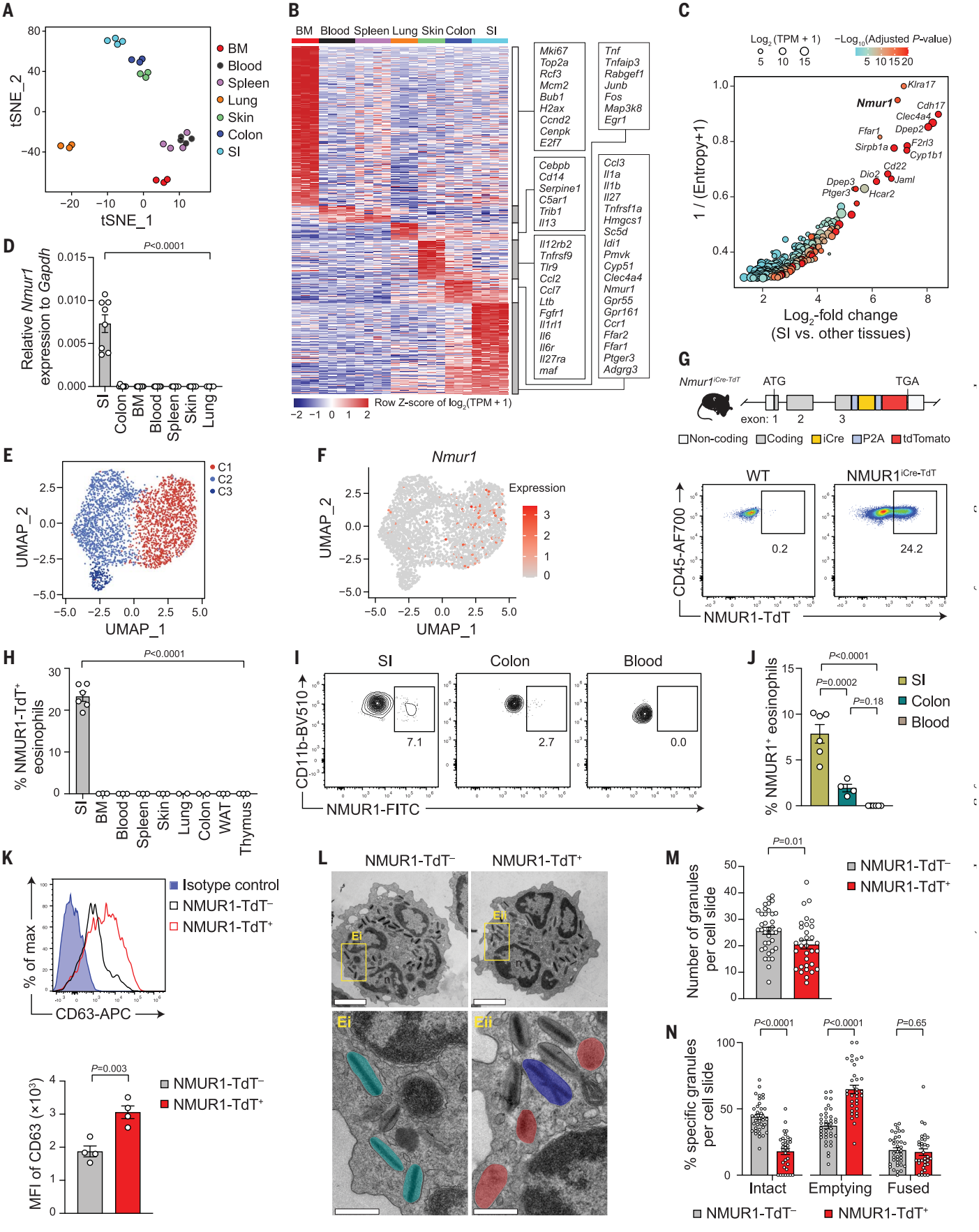
A
tSNE_2
tSNE_1
BM
Blood
Spleen
Lung
Skin
Colon
SI
B
BM Blood Spleen Lung Skin Colon SI
Mki67 Top2a Rcf3 Mcm2 Bub1 H2ax Ccnd2 Cenpk E2f7
Cebpb Cd14 Serpine1 C5ar1 Trib1 Il13
Il12rb2 Tnfrsf9 Tlr9 Ccl2 Ccl7 Ltb Fgfr1 Il1rl1 Il6 Il6r Il27ra maf
Tnf Tnfaip3 Rabgef1 Junb Fos Map3k8 Egr1
Ccl3 Il1a Il1b Il27 Tnfrsf1a Hmgcs1 Sc5d Idi1 Pmvk Cyp51 Clec4a4 Nmur1 Gpr55 Gpr161 Ccr1 Ffar2 Ffar1 Ptger3 Adgrg3
Row Z-score of log2(TPM + 1)
C
Log2 (TPM + 1)
−Log10(Adjusted P-value)
1 / (Entropy+1)
Log2-fold change (SI vs. other tissues)
Klra17
Nmur1
Cdh17
Clec4a4
Dpep2
Ffar1
F2rl3
Sirpb1a
Cyp1b1
Cd22
Dio2
Jaml
Dpep3
Ptger3
Hcar2
D
Relative Nmur1 expression to Gapdh
P<0.0001
SI
Colon
BM
Blood
Spleen
Skin
Lung
E
C1
C2
C3
UMAP_2
UMAP_1
F
Nmur1
Expression
G
Nmur1iCre-TdT
ATG
TGA
exon: 1 2 3
Non-coding Coding iCre P2A tdTomato
WT
NMUR1iCre-TdT
CD45-AF700
NMUR1-TdT
0.2
24.2
H
P<0.0001
% NMUR1-TdT+ eosinophils
SI
BM
Blood
Spleen
Skin
Lung
Colon
WAT
Thymus
I
SI
Colon
Blood
CD11b-BV510
NMUR1-FITC
7.1
2.7
0.0
J
P<0.0001
P=0.0002
P=0.18
% NMUR1+ eosinophils
SI
Colon
Blood
K
Isotype control
NMUR1-TdT−
NMUR1-TdT+
% of max
CD63-APC
P=0.003
MFI of CD63 (×10³)
L
NMUR1-TdT−
NMUR1-TdT+
Ei
M
P=0.01
Number of granules per cell slide
N
P<0.0001
P<0.0001
P=0.65
% specific granules per cell slide
Intact
Emptying
Fused

Fig. 1. Transcriptome analysis identifies a NMUR1$^+$ eosinophil subset in an active degranulation state. (**A**) t-SNE visualization of eosinophil transcriptome profiles in different tissues (n = 3 to 4 mice per group). (**B**) The relative expression [row-wise Z-score of $\log_2$ (TPM + 1)] of genes across different tissues, as indicated (top). TPM, transcripts per million. Representative genes are shown (right). (**C**) Two-dimensional plot showing expression fold change in SI relative to other tissues (x axis) versus entropy score (y axis). Dot size and color represent relative expression and associated significance, respectively. (**D**) Quantification of *Nmur1* transcript abundance by qPCR in eosinophils from indicated tissues (n = 4 to 8 mice per tissue). (**E**) UMAP visualization of SI eosinophil profiles, colored by cluster. (**F**) UMAP plots, as in (E), showing relative expression of *Nmur1*. (**G**) (Top) *Nmur1*$^{iCre\text{-}TdT}$ mouse design. (Bottom) Representative flow plots showing tdTomato$^+$ SI eosinophil percentages in wild-type (WT) and *Nmur1*$^{iCre\text{-}TdT}$ mice. (**H**) Quantification of tdTomato$^+$ eosinophils in indicated tissues of *Nmur1*$^{iCre\text{-}TdT}$ mice (n = 3 to 6 mice per tissue). (**I** and **J**) Representative flow plots (I) and quantification (J) showing NMUR1$^+$ eosinophil percentages in human tissues. n = 4 to 6 donors per tissue were used for quantification. (**K**) (Top) Representative histograms showing CD63 abundance in SI eosinophils measured by flow cytometry. (Bottom) Quantification. MFI, mean fluorescence intensity (n = 4 mice per group). (**L**) Representative electron micrographs of NMUR1$^+$ (n = 43) and NMUR1$^-$ (n = 32) SI eosinophils. The boxed areas (Ei and Eii) are shown at higher magnification below. Red indicates emptying granules, blue indicates granules in the process of fusion, and green indicates intact granules. Scale bars, 2 μm (top) and 0.5 μm (bottom). (**M** and **N**) Quantification of granule numbers (M) or frequencies of granules in each degranulation state (N) in EM imaging (L) of NMUR1$^+$ (n = 43) and NMUR1$^-$ (n = 32) cells. Data are representative of three [(G) and (L)] or four (I) independent experiments or are pooled from three [(D), (H), (K), (M), and (N)] or four (J) independent experiments, shown as means ± SEMs. Statistical significance was tested by one-way analysis of variance (ANOVA) followed by Tukey's multiple comparisons test [(D), (H), and (J)] or two-tailed t test [(K), (M), and (N)].

were predominantly bilobed or ovoid, whereas NMUR1$^-$ eosinophils were enriched for ring-shaped nuclei (fig. S5, B and C). NMUR1$^+$ eosinophils expressed lower levels of CCR3 and were less responsive to CCL11-mediated chemotaxis compared with their NMUR1$^-$ counterparts (fig. S5, D to G). Moreover, NMUR1$^+$ eosinophils expressed higher surface CD11c, CD80, and major histocompatibility complex class II (MHC-II) levels compared with NMUR1$^-$ eosinophils (fig. S5H). CD11c expression is associated with eosinophil redistribution from the crypts into the villi (*9*, *18*). Finally, NMUR1$^+$ eosinophils expressed significantly higher levels of aryl hydrocarbon receptor (*Ahr*) (fig. S5I), which contributes to the adaptation of intestinal eosinophils to their tissue of residency (*10*). Thus, NMUR1 expression appears to be associated with an eosinophil tissue adaptation process in the SI.

NMUR1$^+$ SI eosinophils exhibited a distinct transcriptional state (fig. S6A) characterized by the down-regulation of genes involved in proinflammatory cytokine signaling pathways (e.g., *Il4*) and cell adhesion molecule binding pathways (e.g., *Icam1*) compared with NMUR1$^-$ eosinophils (fig. S6B). NMUR1$^+$ eosinophils highly expressed genes involved in cholesterol biosynthesis and degranulation pathways (fig. S6B), which were enriched in C1 eosinophils in our scRNA-seq dataset (fig. S2D). The overall expression of the NMUR1$^+$ eosinophil signature was consistently highest in C1 cells (fig. S6C). Furthermore, NMUR1$^+$ eosinophils expressed significantly higher levels of SI eosinophil-specific genes (Fig. 1C) compared with NMUR1$^-$ eosinophils (fig. S6D). Thus, the specific transcriptional state of SI eosinophils was predominantly determined by NMUR1$^+$ eosinophils.

NMUR1$^+$ eosinophils up-regulated genes (fig. S2D) involved in degranulation, such as *Cd63* (*19*, *20*), and cholesterol biosynthesis, which is necessary for generating membranes to facilitate efficient intracellular granule formation and for secretory vesicles (*21*). We confirmed the increased expression of CD63 in NMUR1$^+$ eosinophils at the protein level (Fig. 1K). To determine whether degranulation activity differed among the eosinophil populations, we used transmission electron microscopy (TEM), which revealed significantly fewer intracellular granules in NMUR1$^+$ eosinophils compared with their NMUR1$^-$ counterparts (Fig. 1, L and M). We further observed a significant increase in the proportions of emptying granules (a sign of degranulation) and a decrease in the proportions of intact granules (*22*) in NMUR1$^+$ compared with NMUR1$^-$ eosinophils (Fig. 1, L and N). Thus, NMUR1 expression in SI eosinophils is associated with enhanced degranulation activity.

NMUR1 expression in SI eosinophils is programmed by the tissue microenvironment and increased by inflammation

To investigate the ontogeny of NMUR1$^+$ eosinophils, we crossed *Nmur1*$^{iCre\text{-}TdT}$ mice with a strain carrying a *ROSA26-LoxP-STOP-LoxP-GFP* allele (Fig. 2A). TdTomato and green fluorescent protein (GFP) were coexpressed in nearly all eosinophils specifically in the SI (Fig. 2A and fig. S7A), which demonstrates that NMUR1$^+$ eosinophils could not be converted into NMUR1$^-$ cells. Notably, coexpression of GFP and tdTomato in ILC2s was observed in both the lung and the SI (fig. S7B).

We next administered 5-ethynyl-2′-deoxyuridine (EdU), which is only incorporated by eosinophil progenitors (*23*), into *Nmur1*$^{iCre\text{-}TdT}$ mice to assess the replenishment rate of NMUR1-expressing SI eosinophils. The frequency of EdU$^+$ NMUR1-expressing eosinophils in the SI was significantly lower compared with their NMUR1$^-$ counterparts on days 7, 10, and 14 after EdU injection (Fig. 2, B and C), which suggests delayed replenishment of NMUR1$^+$-expressing eosinophils into the SI. To interrogate whether NMUR1 expression was induced over time after homing to the SI, we transferred CD45.2$^+$*Nmur1*$^{iCre\text{-}TdT}$ mouse BM cells into pre-irradiated CD45.1$^+$ recipients (fig. S7C). Newly generated CD45.2$^+$ eosinophils arrived in the SI on day 7 after transfer, whereas NMUR1$^+$ eosinophils did not emerge until day 14 (Fig. 2D and fig. S7D). Thus, NMUR1 expression is programmed by long-term residence and extended exposure to the local microenvironment in the steady-state SI.

To investigate the expression dynamics of NMUR1 in SI eosinophils under inflammatory conditions, we challenged *Nmur1*$^{iCre\text{-}TdT}$ mice with recombinant interleukin-25 (IL-25) or the helminth *Nippostrongylus brasiliensis*. Both stimuli significantly increased the frequencies of NMUR1$^+$ SI eosinophils (Fig. 2, E and F). IL-25 also induced NMUR1 expression in a few villus cells that morphologically resembled cells of a nonhematopoietic lineage (Fig. 2E). Additionally, frequencies of NMUR1$^+$ eosinophils in the SI were augmented by treatment with exogenous 23-residue NMU peptide (NMU-23) or dextran sulfate sodium (DSS) (Fig. 2, G and H). The administration of DSS did not elicit NMUR1 in colonic eosinophils (fig. S7E). Moreover, the intranasal administration of IL-33 or *Alternaria alternata* did not induce NMUR1 in lung eosinophils (fig. S7, F and G). Thus, NMUR1 expression in SI eosinophils is programmed by the tissue-specific microenvironment and is further induced by inflammatory cues.

NMUR1 maintains eosinophil numbers and promotes eosinophil degranulation in the SI

To uncover the function of NMUR1 in regulating eosinophil responses in vivo, we bred *Nmur1*$^{-/-}$ mice with a *Rag2*$^{-/-}$*Il2rg*$^{-/-}$ [referred to hereafter as dKO (double knockout)] strain to exclude the effects of NMUR1 expression in ILC2s and a small population of T cells in the SI (fig. S3, H and I). We confirmed that, in the dKO background, eosinophils were the only hematopoietic compartment cell type that expressed NMUR1 (fig. S8, A and B). Furthermore, NMUR1 expression in SI eosinophils remained unchanged in the dKO backgound, in which lymphocytes and ILCs are absent (fig. S8C). In

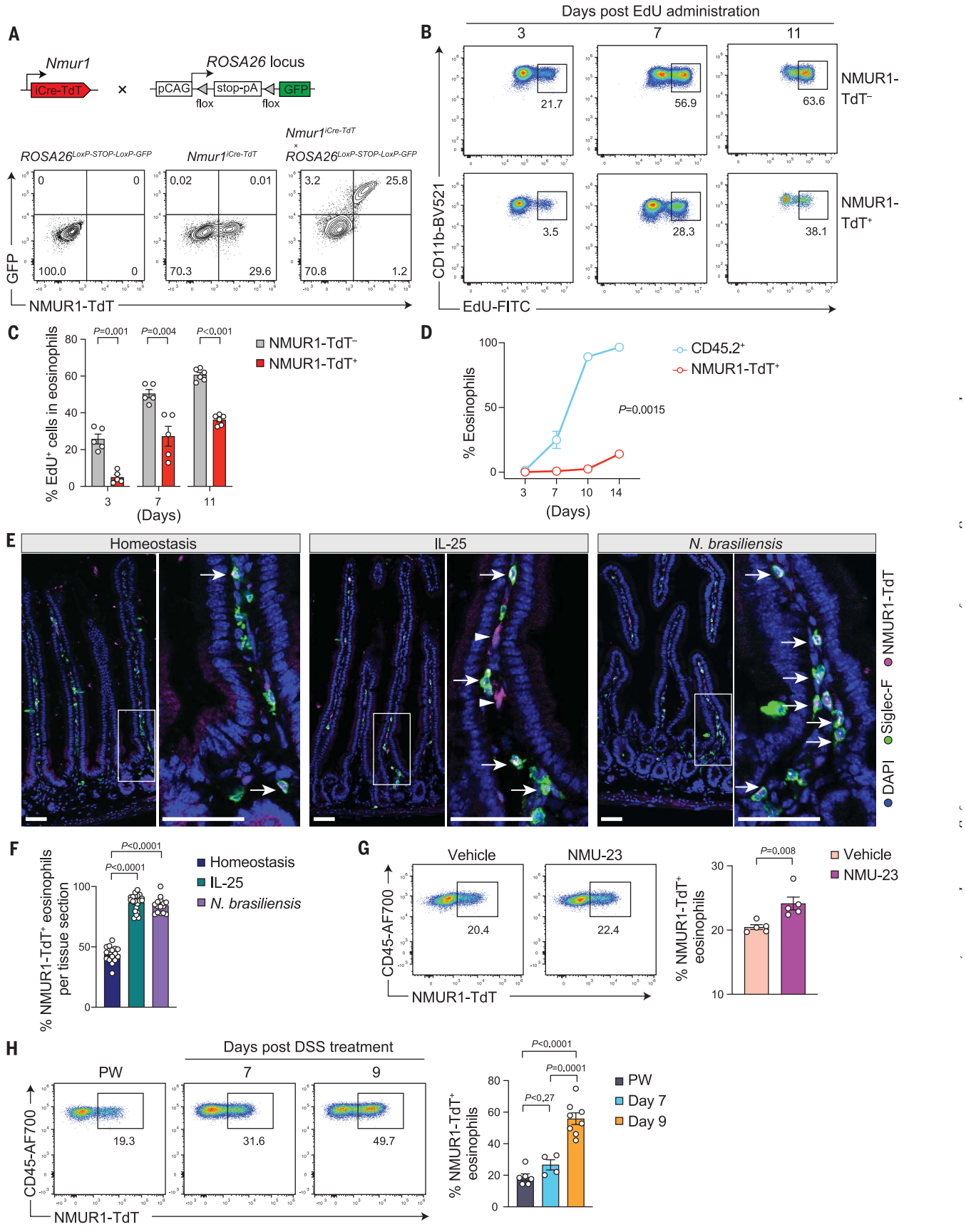

Fig. 2. Tissue-specific microenvironment and inflammatory signals synergistically regulate NMUR1 expression in SI eosinophils. (**A**) (Top) Schematic illustration of fate mapping of NMUR1-expressing SI eosinophils in *Nmur1*$^{iCre\text{-}TdT}$;*R26-GFP* mice. (Bottom) Representative flow plots showing the distribution

of GFP- and/or tdTomato-expressing cells in SI eosinophils in mice with the indicated genotypes (n = 3 mice per group). (**B**) Representative flow plots showing the percentages of EdU^+ cells in $NMUR1^+$ and $NMUR1^-$ SI eosinophils on days 3, 7, and 11 after EdU injection. (**C**) Quantification of EdU^+ cell frequencies from (B) (n = 5 to 6 mice per group). (**D**) Quantification of the frequencies of $CD45.2^+$ cells in total eosinophils (blue line) and the frequencies of $NMUR1^+$ cells in $CD45.2^+$ eosinophils (red line) at different time points after BM transfer (n = 4 mice per group). (**E**) Representative images of Siglec-F staining and NMUR1-TdT in the SI of $Nmur1^{iCre\text{-}TdT}$ mice in homeostasis or treated with IL-25 or *N. brasiliensis*. The individual boxed areas are shown in higher magnification at the right. Arrows indicate $NMUR1^+$ Siglec-F^+ eosinophils, and arrowheads indicate $NMUR1^+$ nonhematopoietic cells. Scale bars, 50 μm. DAPI, 4′,6-diamidino-2-phenylindole. (**F**) Quantification of the densities of $NMUR1^+$ Siglec-F^+ cells (n = 15 to 20 images per condition) from (E). (**G**) (Left) Representative flow plots showing the percentages of $NMUR1^+$ SI eosinophils of $Nmur1^{iCre\text{-}TdT}$ mice treated with NMU-23 or vehicle. (Right) Quantification (n = 5 mice per group). (**H**) (Left) Representative flow plots showing the percentages of $NMUR1^+$ cells in SI eosinophils of $Nmur1^{iCre\text{-}TdT}$ mice treated with DSS or pure water (PW). (Right) Quantification (n = 4 to 8 mice per group). Data are representative of three independent experiments [(A), (B), and (E)] or are pooled from three independent experiments [(C), (D), (F), (G), and (H)], shown as means ± SEMs. Statistical significance was tested by two-way (D) or one-way [(F) and (H)] ANOVA followed by Tukey's multiple comparisons test or two-tailed t test [(C) and (G)].

$Nmur1^{-/-}$ dKO mice, although the total numbers of immune cells in the SI were comparable to those in their $Nmur1^{+/+}$ dKO littermate controls (fig. S9A), the lack of NMUR1 significantly reduced the frequencies and numbers of eosinophils in the SI (Fig. 3A and fig. S9B). This reduction was not the result of the impaired development of BM eosinophils in the $Nmur1^{-/-}$ dKO mice compared with control mice (fig. S9C).

To exclude the potential contribution of $NMUR1^+$ nonhematopoietic cells (Fig. 2E) to phenotypes observed in $Nmur1^{-/-}$ dKO mice (Fig. 3A), we transferred BM cells from $Nmur1^{-/-}$ dKO mice into preirradiated $Nmur1^{+/+}$ dKO mice to generate chimeras (designated $eosinophil^{\Delta nmur1}$) in which the nonhematopoietic cell compartment was NMUR1 competent (fig. S10A). Consistent with our observations in $Nmur1^{-/-}$ dKO mice, the frequencies and numbers of eosinophils were decreased in the SI of $eosinophil^{\Delta nmur1}$ mice compared with control preirradiated $Nmur1^{+/+}$ dKO mice that had received $Nmur1^{+/+}$ BM ($eosinophil^{WT}$) (Fig. 3, B and C). Thus, the regulatory effect of NMUR1 on SI eosinophils is independent of its expression in nonhematopoietic cells.

ILC2s and T cells can regulate eosinophil numbers (*1*, *24*). To determine whether NMUR1 supports SI eosinophils in the presence of ILC2s and T cells, we generated mixed BM chimeras by transferring $Nmur1^{-/-}$ or $Nmur1^{+/+}$ BM cells (20%) together with BM cells (80%) from ΔdblGATA (eosinophil-deficient) mice (*25*) (fig. S10B). We confirmed NMUR1 deficiency in SI eosinophils in ΔdblGATA-$Nmur1^{-/-}$ mixed-BM chimeras (fig. S10C). The frequencies of several major immune cell types, including ILC2s and T cells, were comparable in the SI of ΔdblGATA-$Nmur1^{-/-}$ mixed-BM chimeras and control chimeras (fig. S10, D and E). However, eosinophil frequencies were significantly reduced in the SI—but not the BM—of ΔdblGATA-$Nmur1^{-/-}$ mixed-BM chimeras compared with control chimeras (Fig. 3D and fig. S10F).

We next generated an eosinophil peroxidase (*Epx*)–Cre mouse line (fig. S11A) and confirmed that Cre-mediated gene recombination was specifically present in eosinophils but not other immune cell types in the SI (fig. S11, B to E). We then generated *Nmur1*-conditional knockout ($Epx^{Cre/+}Nmur1^{flox/flox}$) mice (fig. S11, F and G), whose total immune cell numbers in the SI remained comparable between $Epx^{Cre/+}$ $Nmur1^{flox/flox}$ mice and control mice (fig. S11H). However, the frequencies of eosinophils in the SI were significantly reduced in these mice compared with controls (Fig. 3E). Thus, NMUR1 supports the maintenance of eosinophil numbers in the SI in a cell-intrinsic manner.

Because NMUR1 expression is associated with enhanced degranulation (Fig. 1, L to N), we sought to determine whether NMU-NMUR1 signaling supports the constant degranulation of SI eosinophils under homeostasis (*8*). The numbers of intracellular granules were significantly higher in eosinophils from NMUR1-deficient mice compared with those from control mice after NMU stimulation (Fig. 3, F and G). Moreover, NMUR1 deficiency increased the frequencies of intact granules and reduced the frequencies of emptying granules in SI eosinophils (Fig. 3, F and H). Thus, NMUR1-mediated signaling maintains eosinophil number and promotes their degranulation in the SI.

NMUR1-dependent regulation of goblet cell differentiation and mucosal immunity by eosinophils

Given that NMUR1 expression was significantly induced by helminth infection (Fig. 2, E and F) and that eosinophils are important for helminth expulsion (fig. S12A), we challenged NMUR1-deficient animal models with *N. brasiliensis* to investigate NMUR1-dependent eosinophil function in mucosal immunity. Worm burdens were increased in $Nmur1^{-/-}$ dKO mice relative to control mice (fig. S12B), reflecting their compromised antiparasitic immunity. We observed similar increases in $eosinophil^{\Delta nmur1}$ mice (fig. S12C), ΔdblGATA:$Nmur1^{-/-}$ chimeras (Fig. 4A), and $Epx^{Cre/+}Nmur1^{flox/flox}$ mice (Fig. 4B). Thus, NMUR1 has a cell-intrinsic function in eosinophils that mediates antiparasitic mucosal immunity.

In line with defective worm expulsion, goblet cell hyperplasia was significantly reduced in NMUR1-deficient mice (Fig. 4C and fig. S12D). Consistent with findings from previous studies (*4*, *5*), we observed reduced goblet cell numbers and mucus secretion in the SI during homeostasis in eosinophil-deficient ΔdblGATA mice (fig. S13A). To test whether NMU-NMUR1 signaling mediates such an eosinophil-epithelial circuit, we analyzed goblet cells in the SI of NMUR1-deficient mouse models under homeostasis. An NMUR1 defect in eosinophils led to significantly reduced goblet cell numbers (Fig. 4, D and E, and fig. S13, B to D). Furthermore, the adoptive transfer of $Nmur1^{+/+}$ BM-derived eosinophils (BMDEs) (fig. S14, A to D), but not $Nmur1^{-/-}$ BMDEs, significantly restored goblet cell numbers in $Nmur1^{-/-}$ dKO mice (Fig. 4, F and G). Thus, NMUR1 has a crucial cell-intrinsic function in eosinophils that promotes goblet cell differentiation.

NMU is produced by cholinergic neurons in the intestine (*26*, *27*). In electron microscopy (EM) imaging of the SI, we observed eosinophils in close proximity to neurons (fig. S15A). We therefore investigated whether direct inhibition or activation of NMU-expressing cells affects the function of eosinophils in regulating goblet cell differentiation. We adopted a chemogenetic strategy using mice engineered to express designer receptors exclusively activated by designer drugs (DREADDs) (*28*). We confirmed that the administration of the ligand clozapine *N*-oxide (CNO) reduced or increased NMU abundance in mice expressing the inhibitory DREADD hM4Di ($Nmu^{IRES\text{-}Cre}hM4Di^{fl\text{-}stop\text{-}fl/+}$) or the activating DREADD hM3Dq ($Nmu^{IRES\text{-}Cre}hM3Dq^{fl\text{-}stop\text{-}fl/+}$), respectively (fig. S15B). The number of goblet cells were reduced in the SI of mice expressing hM4Di (Fig. 4H). Conversely, mice expressing hM3Dq exhibited increased goblet cell numbers, mucus secretion, and abnormal villi structures after CNO administration (Fig. 4H).

We next established an eosinophil-organoid coculture system to directly analyze NMU-dependent eosinophil-epithelial cross-talk (fig. S16). The

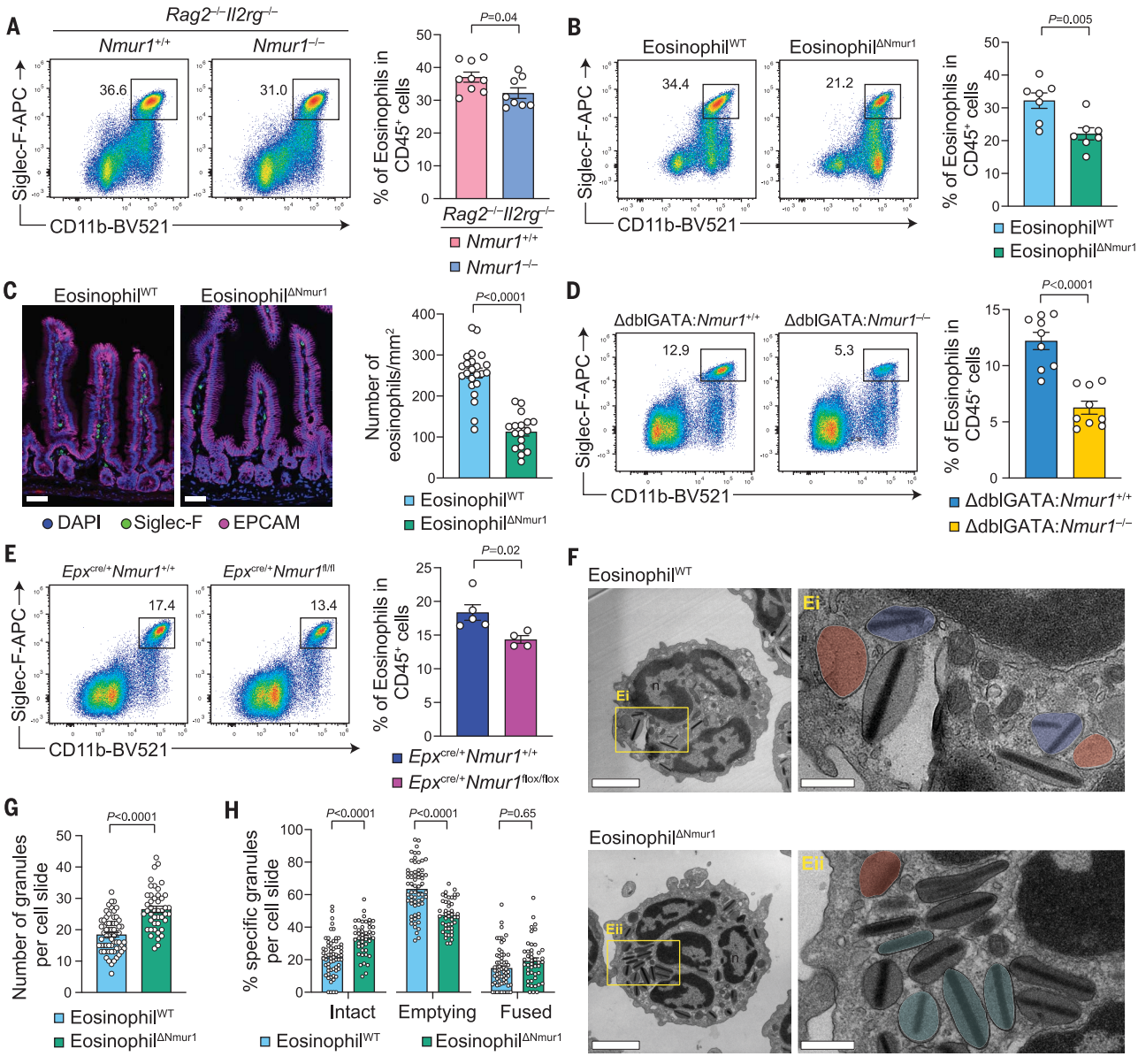

Fig. 3. NMUR1 deficiency reduces eosinophil numbers and degranulation in the SI. (**A**) (Left) Representative flow plots showing the percentages of eosinophils in CD45$^+$ cells in the SI of *Nmur1*$^{+/+}$ dKO and *Nmur1*$^{-/-}$ dKO mice. (Right) Quantification (n = 8 to 9 mice per group). (**B**) (Left) Representative flow plots showing the percentages of eosinophils in CD45$^+$ cells in the SI of eosinophil$^{\Delta Nmur1}$ and eosinophil^{WT} mice. (Right) Quantification (n = 7 mice per group). (**C**) (Left) Representative images of eosinophils (Siglec-F$^+$EPCAM$^-$) in the SI of eosinophil$^{\Delta nmur1}$ and eosinophil^{WT} mice. Scale bars, 50 μm. (Right) Quantification of eosinophil densities (n = 17 to 23 images per group). (**D**) (Left) Representative flow plots showing the percentages of eosinophils in CD45$^+$ cells in the SI of ΔdblGATA:*Nmur1*$^{-/-}$chimeras and control chimeras. (Right) Quantification (n = 9 mice per group). (**E**) (Left) Representative flow plots showing the percentages of eosinophils in CD45$^+$ cells in the SI of *Epx*$^{Cre/+}$ *Nmur1*$^{flox/flox}$ mice and control mice. (Right) Quantification (n = 4 to 5 mice per group). (**F**) Representative electron micrographs of eosinophils isolated from the SI of eosinophil$^{\Delta nmur1}$ (top) and eosinophil^{WT} (bottom) mice at 24 hours after NMU injection. The boxed areas (Ei and Eii) are shown in higher magnification at the right. Red indicates emptying granules, blue indicates granules in the process of fusion, and green indicates intact granules. Scale bars, 2 μm (left) and 0.5 μm (right). (**G** and **H**) Quantification of the numbers of granules (G) or the frequencies of granules in each degranulation state (H) of cells from imaging shown in (F) (n = 64 cells from eosinophil^{WT} mice and n = 45 cells from eosinophil$^{\Delta nmur1}$ mice). Data are representative of two independent experiments (F) or are pooled from two [(B) to (E), (G), and (H)] or three (A) independent experiments, shown as means ± SEMs. Statistical significance was tested by two-tailed t test [(A) to (E), (G), and (H)].

addition of freshly isolated SI eosinophils to intestinal organoid cultures significantly increased organoid growth. Supplementation with additional NMU further increased organoid growth, the formation of budding domains, and complex crypt-villus structures (Fig. 4, I and J). In addition, the highest density of goblet cells was observed in intestinal organoids cocultured with eosinophils plus NMU (Fig. 4K). Thus, SI eosinophils promote goblet cell differentiation that is programmed by NMU-NMUR1 signaling.

Discussion

Nmur1 has been posited to be an ILC2-specific gene (*16*, *17*). By generating a knockin mouse strain that accurately tracks endogenous *Nmur1* gene expression, we demonstrate that NMUR1 expression also occurs in SI eosinophils.

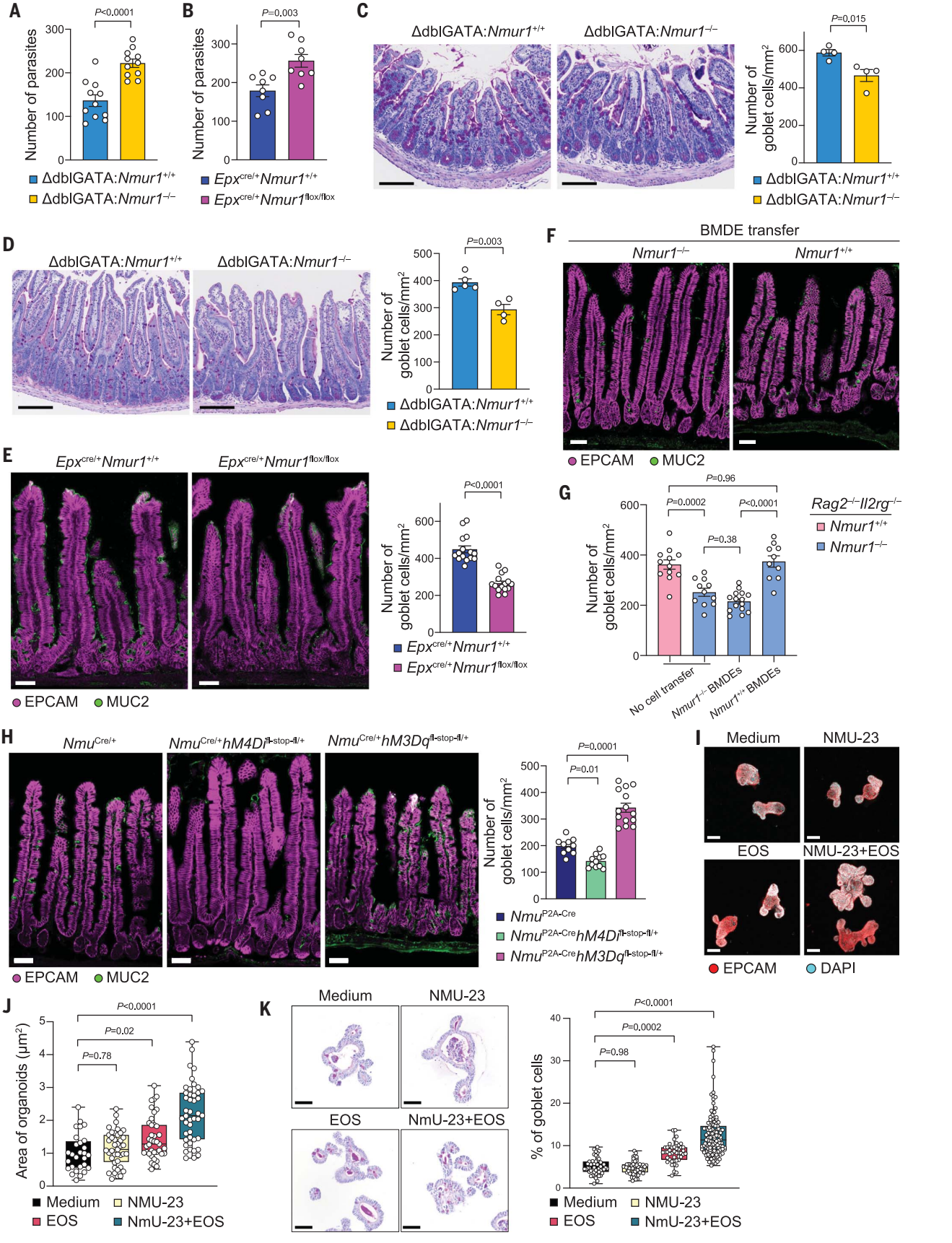

Fig. 4. Eosinophil-mediated goblet cell differentiation and worm expulsion depend on the NMU-NMUR1 pathway. (**A** and **B**) Quantification of parasite numbers in the SI of ΔdblGATA:*Nmur1*$^{-/-}$ chimeras and controls (n = 11 mice per group) (A) and of *Epx*$^{Cre/+}$*Nmur1*$^{flox/flox}$ and control mice (n = 8 mice per group) (B)

on day 7 after *N. brasiliensis* infection. (**C**) (Left) Representative periodic acid–Schiff (PAS) staining images of goblet cells in the SI of ΔdblGATA:*Nmur1*$^{-/-}$ chimeras and controls on day 7 after infection. Scale bars, 200 μm. (Right) Quantification (n = 4 mice per group). (**D**) (Left) Representative PAS staining images of goblet cells in the SI of ΔdblGATA:*Nmur1*$^{-/-}$chimeras and controls under homeostasis. Scale bars, 200 μm. (Right) Quantification (n = 4 to 5 mice per group). (**E**) (Left) Representative images of goblet cells (EPCAM^{+}MUC2^{+}) in the SI of *Epx*$^{Cre/+}$*Nmur1*$^{flox/flox}$ and control mice. Scale bars, 50 μm. (Right) Quantification (n = 15 images per group). (**F**) Representative images of goblet cells (EPCAM^{+}MUC2^{+}) in the SI of *Nmur1*$^{-/-}$ dKO mice transferred with *Nmur1*$^{+/+}$ or *Nmur1*$^{-/-}$ BMDEs (n = 10 to 15 images per group). Scale bars, 50 μm. (**G**) Quantification of goblet cell density in *Nmur1*$^{+/+}$ dKO and *Nmur1*$^{-/-}$ dKO mice under homeostasis or treated as in (F) (n = 10 to 15 images per group). (**H**) (Left) Representative images of goblet cells (EPCAM^{+}MUC2^{+}) in the SI of mice carrying the inhibitory (hM4Di) or activating (hM3Dq) DREADD allele or control mice (*Nmu*^{Cre}) treated with CNO for 7 days. Scale bars, 50 μm. (Right) Quantification (n = 10 to 14 images per group). (**I**) Representative images of SI organoids (EPCAM^{+}DAPI^{+}) cultured with the indicated conditions. Scale bars, 100 μm. EOS, eosinophils. (**J**) Quantification of the surface areas of organoids imaged in (I) (n = 28 to 44 organoids per group). (**K**) (Left) Representative PAS staining images of SI organoids. Scale bars, 50 μm. (Right) Quantification (n = 45 to 126 organoids per group). Data are representative of two (F) or three (I) independent experiments or are pooled from two [(B) to (E), (G), and (H)] or three [(A), (J), and (K)] independent experiments, shown as means ± SEMs. Statistical significance was tested by one-way ANOVA followed by Tukey's multiple comparisons test [(G), (H), (J), and (K)] or two-tailed t test [(A) to (E)].

Furthermore, we detected NMUR1 in a population of SI T cells, consistent with a recent study demonstrating that resident T helper 2 (T_H2) cells express *Nmur1* in the mesenteric adipose tissues during inflammation (*29*). Reduced airway eosinophilia has previously been observed in NMU-deficient mice (*15*). Our finding that NMUR1 is not expressed in lung eosinophils suggests that this reduction in airway inflammation likely occurred as a result of the cell-intrinsic effects of NMU in ILC2s (*12*–*14*) rather than eosinophils.

How signals from the tissue microenvironment promote goblet cell differentiation in the SI under homeostatic conditions remains poorly understood. Our work identifies NMUR1-mediated signaling in eosinophils as a contributor to goblet cell differentiation in the steady-state SI. Cytokines, such as IL-13, have been reported to increase goblet cell number (*30*, *31*). Our finding that the expression of IL-13, along with other proinflammatory cytokines, was downregulated in NMUR1^{+} compared with NMUR1^{-} eosinophils makes it unlikely that these proinflammatory cytokines are involved in goblet cell differentiation through NMU-NMUR1 signaling in eosinophils. Genes that were upregulated in NMUR1^{+} eosinophils are members of degranulation and cholesterol biosynthesis pathways. Future studies will be needed to determine the roles (*21*, *32*, *33*) of these processes in NMUR1^{+} eosinophils in regulating goblet cell differentiation.

We demonstrate that NMUR1 signaling drives a tissue-specific program in SI eosinophils to regulate goblet cell differentiation under homeostasis. This highlights the crucial functions of NMU-NMUR1 signaling that establish distinct neuroimmune cell circuits under both homeostatic and type 2 inflammatory conditions in the SI.

REFERENCES AND NOTES

1. M. E. Rothenberg, S. P. Hogan, *Annu. Rev. Immunol.* **24**, 147–174 (2006).
2. P. F. Weller, L. A. Spencer, *Nat. Rev. Immunol.* **17**, 746–760 (2017).
3. C. W. DeBrosse, J. W. Case, P. E. Putnam, M. H. Collins, M. E. Rothenberg, *Pediatr. Dev. Pathol.* **9**, 210–218 (2006).
4. R. Sugawara *et al*., *J. Exp. Med.* **213**, 555–567 (2016).
5. Y. Jung *et al*., *Mucosal Immunol.* **8**, 930–942 (2015).
6. K. Shah, A. Ignacio, K. D. McCoy, N. L. Harris, *Mucosal Immunol.* **13**, 574–583 (2020).
7. A. Ignacio *et al*., *Immunity* **55**, 1250–1267.e12 (2022).
8. M. Kato *et al*., *Anat. Rec.* **252**, 418–425 (1998).
9. J. J. Xenakis *et al*., *Immunology* **154**, 298–308 (2018).
10. N. L. Diny *et al*., *J. Exp. Med.* **219**, e20210970 (2022).
11. W. L. Wang *et al*., *Proc. Natl. Acad. Sci. U.S.A.* **119**, e2204557119 (2022).
12. V. Cardoso *et al*., *Nature* **549**, 277–281 (2017).
13. C. S. N. Klose *et al*., *Nature* **549**, 282–286 (2017).
14. A. Wallrapp *et al*., *Nature* **549**, 351–356 (2017).
15. M. Moriyama *et al*., *Am. J. Physiol. Lung Cell. Mol. Physiol.* **290**, L971–L977 (2006).
16. A. M. Tsou *et al*., *Nature* **611**, 787–793 (2022).
17. K. J. Jarick *et al*., *Nature* **611**, 794–800 (2022).
18. L. D. Larsen, K. Dockstader, C. L. Olbrich, I. M. Cartwright, L. A. Spencer, *J. Leukoc. Biol.* **111**, 943–952 (2022).
19. N. Verjan Garcia *et al*., *J. Immunol.* **187**, 2268–2277 (2011).
20. L. A. Carmo *et al*., *J. Leukoc. Biol.* **100**, 391–401 (2016).
21. L. A. Spencer, K. Bonjour, R. C. Melo, P. F. Weller, *Front. Immunol.* **5**, 496 (2014).
22. F. F. Dias *et al*., *Front. Immunol.* **9**, 3019 (2018).
23. J. Carlens *et al*., *J. Immunol.* **183**, 5600–5607 (2009).
24. J. C. Nussbaum *et al*., *Nature* **502**, 245–248 (2013).
25. C. Yu *et al*., *J. Exp. Med.* **195**, 1387–1395 (2002).
26. J. Ballesta *et al*., *Neuroscience* **25**, 797–816 (1988).
27. E. Drokhlyansky *et al*., *Cell* **182**, 1606–1622.e23 (2020).
28. B. L. Roth, *Neuron* **89**, 683–694 (2016).
29. A. M. Kabat *et al*., *Sci. Immunol.* **7**, eadd3263 (2022).
30. J. Beumer, H. Clevers, *Nat. Rev. Mol. Cell Biol.* **22**, 39–53 (2021).
31. C. S. De Paiva *et al*., *Mucosal Immunol.* **4**, 397–408 (2011).
32. I. Tabas, *J. Clin. Invest.* **110**, 583–590 (2002).
33. R. Bauer, B. Brüne, T. Schmid, *Front. Pharmacol.* **14**, 1121819 (2023).

ACKNOWLEDGMENTS

We thank J. W. Wang and J. H. Mei for technical support, W. T. Zhu for mouse genotyping, D. Y. Chen for human sample harvest, R. D. Yang for setting up the organoid culture in the laboratory, and C. Huang for initially setting up the parasite infection model and for advice on tissue preparation and flow cytometry. We thank all the members of the Xu and He laboratories for discussion and suggestions. We also thank the Laboratory Animal Resources Center, High-Performance Computing Center, Flow Cytometry Core, Genomic Core, and Microscopy Core at Westlake University. **Funding:** This study was supported by National Natural Science Foundation of China grants U20A20346 and 82325023 (H.X.), National Key R&D Program of China grant 2020YFA0804200 (H.X.), HRHI program of Westlake Laboratory of Life Sciences and Biomedicine 202309001 (H.X.), and the Education Foundation of Westlake University (H.X.). **Author contributions:** Conceptualization: H.X.; Investigation: Y.L., K.Z., Y.C., W.H., and S.Li; Software: S.Liu; Formal analysis: Y.L., S.Liu, and H.X.; Methodology: Y.L.; Resources: Yi.W., Q.W., H.L., and Ya.W.; Writing – original draft: Y.L., S.Liu, and H.X.; Writing – review & editing: D.H. and H.X.; Supervision: H.X.; Visualization: Y.L., S.Liu, and H.X.; Funding acquisition: H.X. **Competing interests:** The authors declare no competing interests. **Data and materials availability:** The transcriptomic sequencing data are available at Gene Expression Omnibus (GEO) under accession no. GSE211112. All other data are available in the manuscript or the supplementary materials. **License information:** Copyright © 2023 the authors, some rights reserved; exclusive licensee American Association for the Advancement of Science. No claim to original US government works. https://www.science.org/about/science-licenses-journal-article-reuse

SUPPLEMENTARY MATERIALS

science.org/doi/10.1126/science.ade4177
Materials and Methods
Figs. S1 to S16
Tables S1 and S2
References (*34*–*49*)
MDAR Reproducibility Checklist

Submitted 10 November 2022; resubmitted 1 May 2023
Accepted 18 August 2023
10.1126/science.ade4177

NEUROSCIENCE

Presynaptic Ube3a E3 ligase promotes synapse elimination through down-regulation of BMP signaling

Kotaro Furusawa[1], Kenichi Ishii[1], Masato Tsuji[1], Nagomi Tokumitsu[1], Eri Hasegawa[1], Kazuo Emoto[1,2]*

Inactivation of the ubiquitin ligase Ube3a causes the developmental disorder Angelman syndrome, whereas increased Ube3a dosage is associated with autism spectrum disorders. Despite the enriched localization of Ube3a in the axon terminals including presynapses, little is known about the presynaptic function of Ube3a and mechanisms underlying its presynaptic localization. We show that developmental synapse elimination requires presynaptic Ube3a activity in *Drosophila* neurons. We further identified the domain of Ube3a that is required for its interaction with the kinesin motor. Angelman syndrome–associated missense mutations in the interaction domain attenuate presynaptic targeting of Ube3a and prevent synapse elimination. Conversely, increased Ube3a activity in presynapses leads to precocious synapse elimination and impairs synaptic transmission. Our findings reveal the physiological role of Ube3a and suggest potential pathogenic mechanisms associated with Ube3a dysregulation.

Angelman syndrome is a developmental disorder characterized by intellectual disability, motor dysfunction, epilepsy, and absence of speech (*1*, *2*). Genetic studies have identified the evolutionarily conserved E3 ubiquitin ligase Ube3a as the causal factor in Angelman syndrome. Loss of functional Ube3a impairs developmental synapse plasticity (*3*–*6*). Conversely, increased Ube3a dosage because of the copy number variations within the *Ube3a* locus leads to autism spectrum disorders (ASDs), which is often associated with impaired synaptic transmission (*7*, *8*). To understand how Ube3a regulates synapse plasticity and function, previous studies have focused primarily on the postsynaptic function of Ube3a (*9*–*11*). However, immunochemical and electron microscopic studies have shown that Ube3a protein in human and mouse cortical neurons is predominantly localized in axon terminals including presynapses, rather than postsynapses and dendrites (*12*–*14*). Compared with the accumulated evidence supporting the role in spine development and postsynaptic plasticity, little is known about presynaptic functions of Ube3a, including whether dysregulation of presynaptic Ube3a contributes to synaptic defects in Angelman syndrome and ASDs.

Drosophila C4da neurons undergo presynapse elimination during metamorphosis

Drosophila class IV dendrite arborization (C4da) sensory neurons innervate dendritic branches over the body wall while projecting axons to the ventral nerve cord (VNC) to form synaptic contacts with second-order neurons (Fig. 1A and fig. S1) (*15*–*17*). C4da neurons have been used to study molecular mechanisms of dendrite remodeling because they undergo dendrite pruning in the first 24 hours after puparium formation (APF) followed by regeneration of adult-specific dendritic arbors in the later pupal stage (*18*–*22*). We show that C4da neurons remodel presynapses as well as dendrites during metamorphosis. To visualize presynapses and axonal-dendritic branches simultaneously in C4da neurons, we expressed the presynaptic marker Bruchpilot (Brp)::mCherry and mCD8GFP in C4da neurons using the GAL4–upstream activator sequence (UAS) system (*23*). Consistent with previous studies (*24*, *25*), Brp::mCherry clearly labeled punctate structures on C4da axon terminals in third instar larvae (Fig. 1B and movie S1), which allowed us to quantify presynapse numbers on C4da axonal terminals. We consistently observed ~400 Brp::mCherry-positive spots in each of the abdominal segment A3 to A5 during wandering larvae and white pupa stages (Fig. 1B). After initiating metamorphosis, however, the number of the Brp::mCherry-positive spots was progressively reduced until 24 hours APF, at which time Brp::mCherry signal was absent from C4da axon terminals, indicating that presynapses in C4da neurons are removed during early metamorphosis (Fig. 1B and movie S2). This presynapse elimination was consistently observed in all segments in 24 hours APF (fig. S2, A and B). Single-cell analyses revealed a progressive loss of presynapses on the contralateral axon branches with concomitant retraction of axon terminals (fig. S3). In adult flies, Brp::mCherry-positive dots were visible on C4da axon terminals, suggesting that C4da neurons regenerate adult-specific synapse connectivity during the late pupal stage (fig. S4). It is thus likely that C4da neurons remodel both presynapses and dendrites in a comparable time window during metamorphosis (Fig. 1C and fig. S4).

Ube3a E3 ligase is required for presynapse elimination

Previous studies identified multiple molecules required for dendrite pruning in C4da neurons, including ecdysone signaling molec… ubiquitin-proteasome system-related m… cules, cytoskeletal regulators, and calcium signaling molecules (*26*–*32*). We thus examined whether dendrite pruning and presynapse elimination are mediated by a common molecular mechanism. We first confirmed that the ecdysone signaling pathway triggers presynapse elimination; a dominant-negative version of the ecdysone receptor EcR or RNA interference (RNAi) suppression of the EcR transcriptional target Sox14 impaired presynapse elimination as well as dendrite pruning in C4da neurons (fig. S5). We next tested the components involved in local degradation of dendritic branches and found that only the E1 ubiquitin-activating enzyme Uba1 was required for both presynapse elimination and dendrite pruning (Fig. 2, A and B, and figs. S6 and S7). Because Uba1 acts with Cullin1 E3 ligase in dendrite pruning (*32*), we next performed RNAi suppression of *Cullin1* in C4da neurons and found that Cullin1 is dispensable for synapse elimination (Fig. 2, A and B, and fig. S7), suggesting that distinct E3 ligases might function in dendrite pruning and synapse elimination. We thus performed an RNAi screen for E3 ligases involved in presynapse elimination, focusing on genes that are expressed in the nervous system according to the FlyBase information (https://flybase.org/reports/FBgg0000069). We found that C4da-specific suppression of *Ube3a* caused severe presynapse elimination defects without affecting dendrite pruning (Fig. 2, A and B; fig. S7; and table S1). Similar presynapse elimination defects were observed with two independent *Ube3a* null alleles (Fig. 2, C and D). Furthermore, C4da neuron–specific expression of wild-type Ube3a, but not a catalytically inactive Ube3a (Ube3a C941A), completely rescued synapse elimination defects in *Ube3a* mutants (Fig. 2, C and D), confirming that Ube3a E3 ligase acts cell-autonomously in C4da neurons to promote presynapse elimination (Fig. 2E).

Ube3a is transported to presynapses in a kinesin motor–dependent manner

How could Ube3a function specifically in presynapse elimination without affecting dendrite pruning? One potential scenario might be localized function of Ube3a in C4da presynapses on the axon terminals. To test this model, we assessed subcellular localization of an epitope-tagged version of Ube3a (Ube3a-Flag) expressed in *Ube3a*-null C4da neurons. Because Ube3a-Flag completely rescued the presynapse elimination defects in *Ube3a* C4da neurons (Fig. 2, C and D), we reasoned that it likely mimics localization of endogenous Ube3a proteins in C4da neurons. We found that Ube3a-Flag was predominantly localized in presynapses on C4da axon terminals, whereas no obvious expression was observed in dendrites (Fig. 3, A

[1]Department of Biological Sciences, Graduate School of Science, The University of Tokyo, 7-3-1 Hongo, Bunkyo-ku, Tokyo 113-0033, Japan. [2]International Research Center for Neurointelligence (WPI-IRCN), The University of Tokyo, 7-3-1 Hongo, Bunkyo-ku, Tokyo 113-0033, Japan.
*Corresponding author. Email: emoto@bs.s.u-tokyo.ac.jp

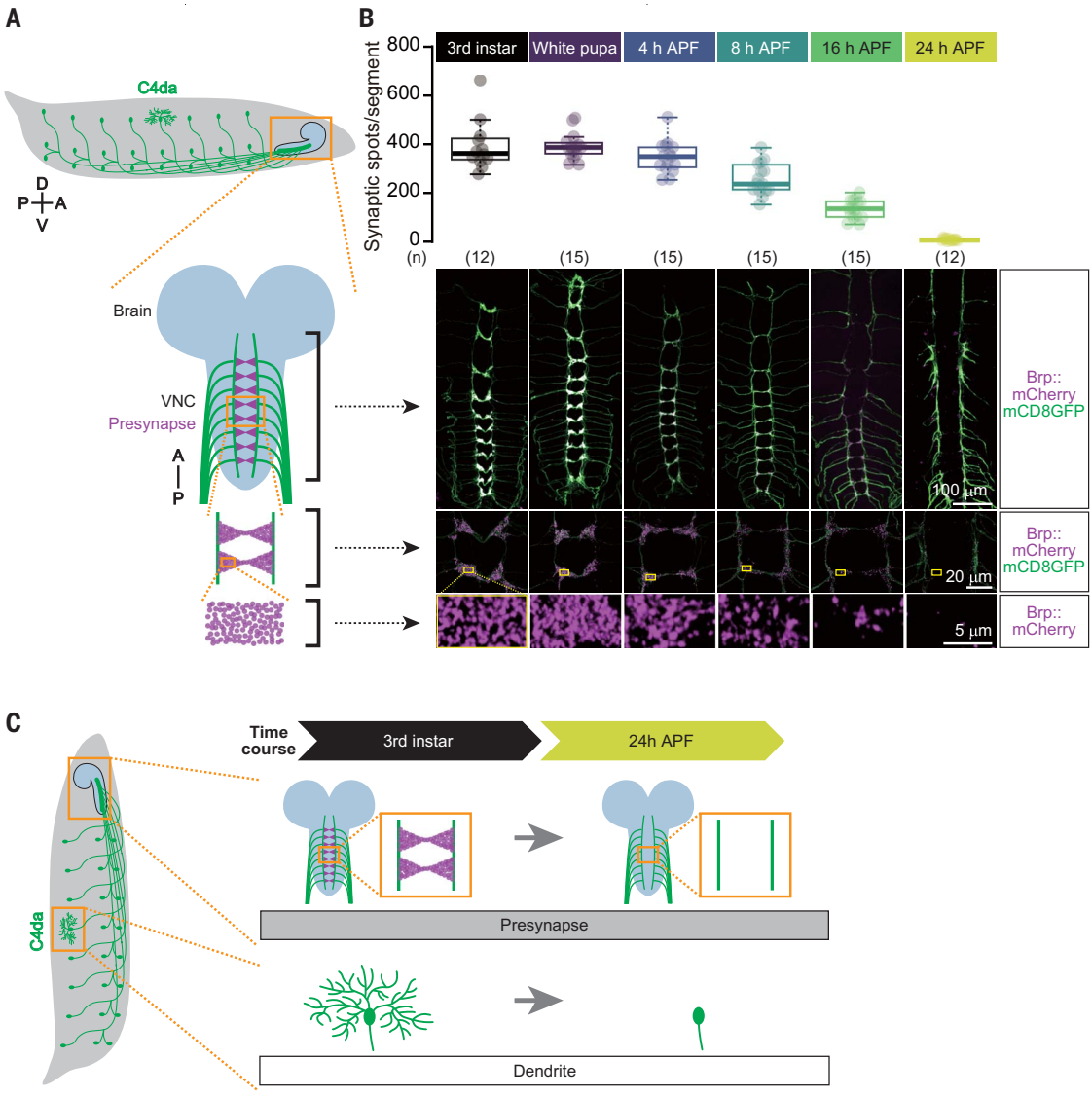

Fig. 1. *Drosophila* C4da neurons undergo presynapse elimination during metamorphosis. (**A**) A schematic view of dendrite arborizations and axonal projections of C4da neurons in third instar larvae. (Bottom) Axon terminal projections (green) and presynapses (magenta) in the ventral nerve cord (VNC). (**B**) The number of presynaptic marker puncta in the abdominal segments of C4da neurons from third instar larval stage to 24 hours APF. Box plots indicate the median, 25th and 75th percentiles, the data range except for outliers, and outliers. (Bottom) Presynapses (magenta) and axon terminals (green) of C4da neurons. (**C**) A schematic view of presynapse elimination and dendrite pruning in C4da neurons during metamorphosis.

and B). Live-imaging of Ube3a::GFP (green fluorescent protein) in C4da axons revealed anterograde transports of Ube3a from the soma to axon terminals with a constant speed (Fig. 3, C to F, and movie S3). This transport speed (483.8 nm/s on average) (Fig. 3F) was within the range of kinesin motor-mediated axon transport (*33*). Indeed, RNAi suppression of *kinesin heavy chain* (*khc*) in C4da neurons impaired presynapse localization of Ube3a (Fig. 3G). Consistently, C4da neurons with *khc* suppression showed severe presynapse elimination defects at 24 hours APF (Fig. 3H). Thus, Ube3a is transported to C4da presynapses through a kinesin motor–dependent mechanism (Fig. 3I).

Angelman syndrome–associated mutations attenuate axonal transport and presynapse localization of Ube3a

Ube3a protein is composed of multiple functional domains including an AZUL (N-terminal zinc-binding) domain at the N terminus and a HECT (homologous to the E6-AP carboxyl terminus) domain at the C terminus (Fig. 4A and fig. S8) (*1*, *2*). To date, the domain responsible for presynaptic targeting has been unknown. To identify such a domain, we constructed multiple mutant Ube3a::GFP that lack different domains and found that deletion of the middle domain containing tandem polar residues (TPRs) completely suppressed Ube3a localization to C4da presynapses, whereas deletion of AZUL or HECT showed less pronounced effects on Ube3a localization in presynapes (Fig. 4B). We found that an Angelman syndrome–linked missense mutation within the middle domain is conserved in *Drosophila* Ube3a (Fig. 4A and fig. S8) and that the same missense mutation D313V significantly interfered with Ube3a::GFP presynapse localizations (Fig. 4B). Because no significant difference was observed in expression levels between wild-type and mutated Ube3a in the soma (Fig. 4C), D313V likely affects presynaptic localization of Ube3a rather than expression levels and/or stability of Ube3a proteins. In addition to D313V, disease-associated mutations in evolutionarily conserved residues adjacent to the middle domain, V216G and I213T, also attenuated Ube3a::GFP localizations in presynapses (fig. S9). Given that Ube3a is transported to presynapses through a kinesin motor–dependent mechanism, we reasoned that these Angelman syndrome–associated mutations in the middle domain might affect interaction of Ube3a with the kinesin motor complex. To test this possibility, we monitored colocalization of Khc::GFP and Ube3a-Flag in C4da axons and found that D313V mutation strongly attenuated colocalization between Khc::GFP and Ube3a-Flag (Fig. 4, D and E). Furthermore, expression of Ube3a::GFP with D313V mutation or Ube3a::GFP lacking the middle region failed to rescue the presynapse elimination defects in *ube3a*-null C4da neurons (Fig. 4F). Similarly, genetic rescue experiments revealed

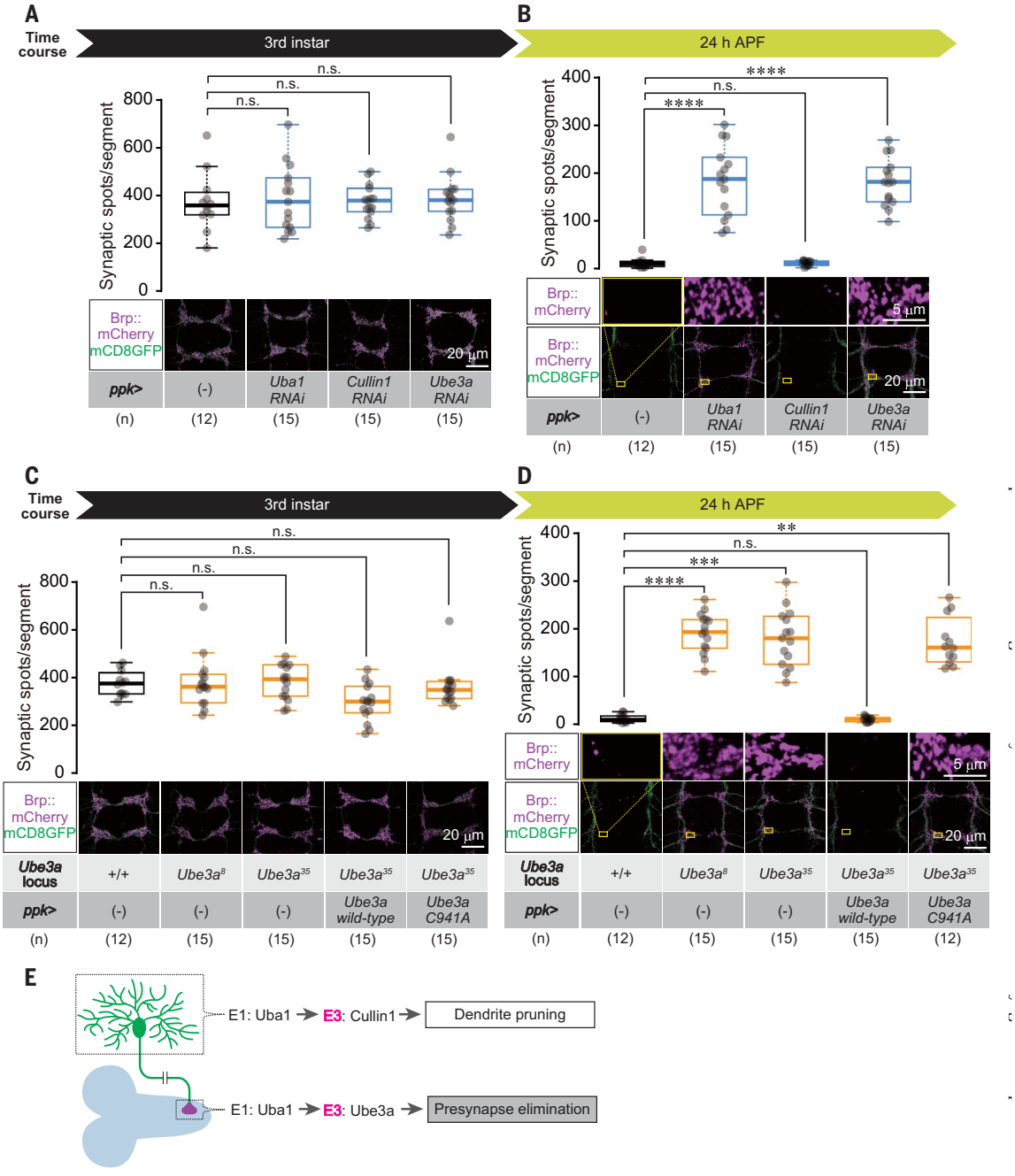

Fig. 2. Ube3a E3 ligase is required for presynapse elimination in C4da neurons. (**A** to **D**) Quantifications of the number of presynaptic marker puncta in an abdominal segment of C4da neurons at [(A) and (C)] third instar larval stage or [(B) and (D)] 24 hours APF. Box plots indicate the median, 25th and 75th percentiles, the data range except for outliers, and outliers. ****$P < 0.0001$, ***$P < 0.001$, **$P < 0.01$, n.s. $P \geq 0.05$, Kruskal-Wallis test with Dunn's multiple comparisons test. (Bottom) Presynapses in the abdominal segments. *ppk*, pickpocket. (**E**) Distinct E3 ligases, Ube3a and Cullin1, act in presynapse elimination and dendrite pruning, respectively.

that I213T and V216G mutations significantly affect Ube3a functions in synapse elimination as well as presynaptic localization of Ube3a in C4da neurons (fig. S9). Taken together, these data indicate that presynaptic localization of Ube3a is essential for its functions in presynapse elimination and suggest that the missense mutations and deletions that affect Ube3a presynaptic localization might impair synapse plasticity and contribute to Angelman syndrome. [Single-letter abbreviations for the amino acid residues are as follows: A, Ala; C, Cys; D, Asp; G, Gly; I, Ile; T, Thr; and V, Val. In the mutants, other amino acids were substituted at certain locations; for example, D313V indicates that aspartate at position 313 was replaced by valine.]

Ube3a down-regulates synaptic BMP signaling for synapse elimination

Because Ube3a-mediated presynapse elimination requires its E3 ligase activity (Fig. 2, C and D), Ube3a likely targets presynaptic proteins for proteosome-dependent degradation. Previous studies reported multiple Ube3a ligase targets, which differed according to cellular contexts as well as organisms (*2*, *34*, *35*). As a first step to determine the functionally relevant targets of Ube3a in presynapse elimination, we used gain-of-function approaches, reasoning that overexpression of bona fide Ube3a targets in a wild-type background should phenocopy the loss of *Ube3a* function. Among the potential Ube3a targets in neurons, overexpression of the bone morphogenetic protein (BMP) receptor Thickvein (Tkv) in C4da neurons caused severe synapse elimination defects comparable with those observed in *Ube3a* mutant neurons (table S2). The synapse elimination defects were further exacerbated by overexpressing a constitutive active version of

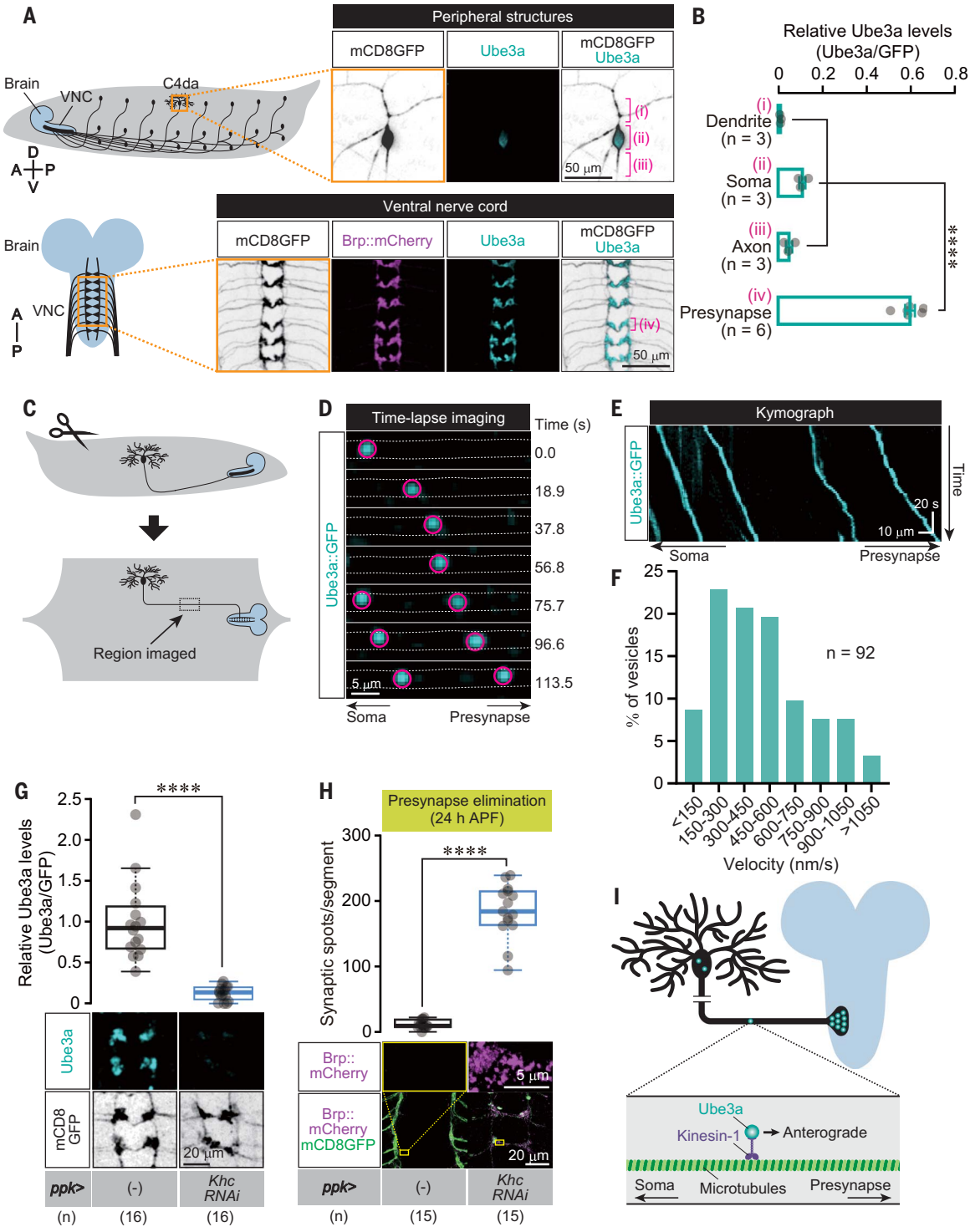

Fig. 3. Ube3a is transported to presynapses in a kinesin motor–dependent manner. (**A**) Subcellular locations of Ube3a-Flag (cyan) in peripheral compartments and the VNC in larval C4da neurons. (i), (ii), (iii), and (iv) indicate the regions of dendrites, soma, axons, and presynapses, respectively. (**B**) Relative expression levels of Ube3a-Flag in each subcellular compartment of C4da neurons. Data are shown as the mean ± SEM. ****$P < 0.0001$, one-way analysis of variance (ANOVA), followed by Tukey's multiple-comparisons test. (**C**) Schematic images of preparations for time-lapse imaging of Ube3a::GFP in C4da axons. (**D**) Time-lapse images showing anterograde transport of Ube3a::GFP vesicles (red circles) in C4da axons. (**E**) Representative kymographs of the anterograde transport of Ube3a::GFP-positive vesicles within C4da axons. (**F**) Velocity of anterograde transport of Ube3a::GFP-positive vesicles. (**G**) Relative expression levels of Ube3a-Flag in axon terminals of *khc*-suppressed neurons. Box plots indicate the median, 25th and 75th percentiles, the data range except for outliers, and outliers. ****$P < 0.0001$, Mann-Whitney test. (**H**) Presynapse numbers in an abdominal segment at 24 hours APF. Box plots indicate the median, 25th and 75th percentiles, and the data range. ****$P < 0.0001$, Mann-Whitney test. (**I**) A schematic image of axonal transport of Ube3a.

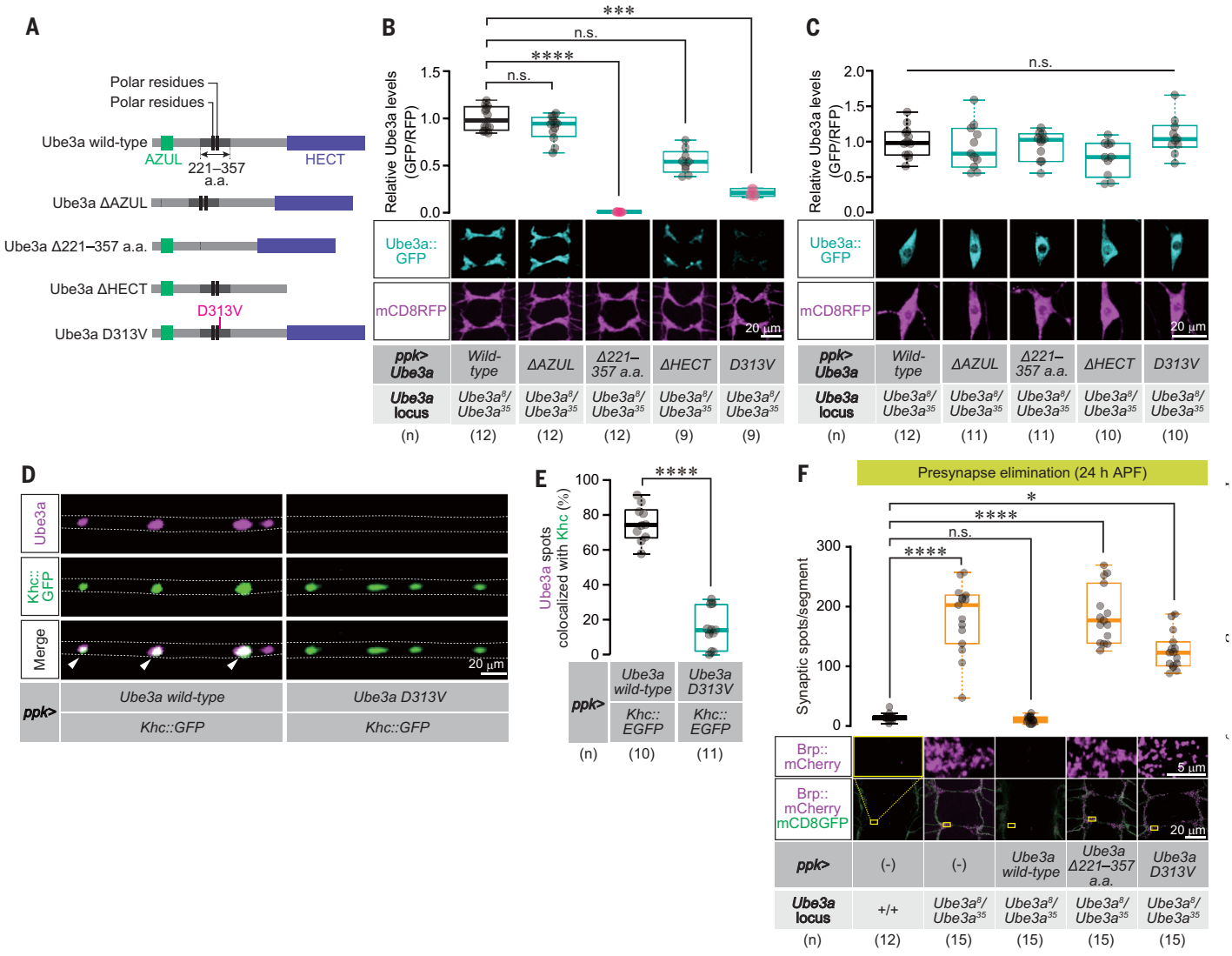

Fig. 4. Angelman syndrome–associated mutations attenuate axonal transport and presynapse localization of Ube3a. (**A**) Schematic views of wild-type and mutant Ube3a::GFP used in this study. (**B** and **C**) Relative expression levels of Ube3a::GFP with a domain deletion or an Angelman syndrome missense mutation in the (B) axon terminals and (C) soma. Box plots indicate the median, 25th and 75th percentiles, and the data range. ****$P < 0.0001$, ***$P < 0.001$, n.s. $P \geq 0.05$, Kruskal-Wallis test with Dunn's multiple comparisons test. (**D**) Colocalization of Ube3a-Flag (wild-type or D313V) and Khc::GFP in C4da axons. Arrowheads indicate Ube3a-Flag (magenta) and Khc::GFP (green)–double-positive vesicles. (**E**) Percentages of Ube3a-Flag (wild-type or D313V) and Khc::GFP–double-positive vesicles. Box plots indicate the median, 25th and 75th percentiles, and the data range. ****$P < 0.0001$, Mann-Whitney test. (**F**) Presynapse numbers in an abdominal segment. Box plots indicate the median, 25th and 75th percentiles, and the data range. ****$P < 0.0001$, *$P < 0.05$, n.s. $P \geq 0.05$, Kruskal-Wallis test with Dunn's multiple comparisons test.

Tkv in C4da neurons (Fig. 5A). No notable defect was observed in dendrite pruning by overexpressing a constitutive active version of Tkv in C4da neurons (fig. S10). We thus checked Tkv expression levels in C4da neurons using a Tkv::GFP reporter and found that presynaptic Tkv levels were significantly reduced by 8 hours APF (Fig. 5B), suggesting that BMP signaling is down-regulated in C4da neurons during early stages of metamorphosis. This Tkv reduction was significantly attenuated in *Ube3a*-null mutants (Fig. 5B), suggesting that Ube3a mediates Tkv down-regulation in C4da neurons. Given that BMP signaling induces Mad phosphorylation (*36*, *37*), we next examined phosphorylated Mad (pMad) levels in C4da neurons. Consistent with the Tkv levels (Fig. 5B), pMad levels in the C4da soma were significantly reduced by 8 hours APF in wild-type control, whereas the pMad reduction was significantly attenuated in *Ube3a*-null mutants (fig. S11). Removal of one copy of *tkv* or *mad*, both of which encode essential components of BMP signaling, largely rescued the presynapse elimination defects of *Ube3a*-null mutants at 24 hours APF (Fig. 5C), providing genetic evidence that enhanced BMP signaling is responsible for the presynapse elimination defects in *Ube3a*-null mutants. Consistent with this notion, synapse elimination defects in *Ube3a*-null mutants were ameliorated by feeding of the selective BMP antagonist LDN-193189 (Fig. 5D) and by expressing Glued-DN or Dad in C4da neurons; both are known to inhibit pMad signaling (fig. S12) (*38*, *39*). These data consistently indicate that Ube3a promotes synapse elimination in C4da neurons at least in part by down-regulating synaptic BMP signaling (Fig. 5E).

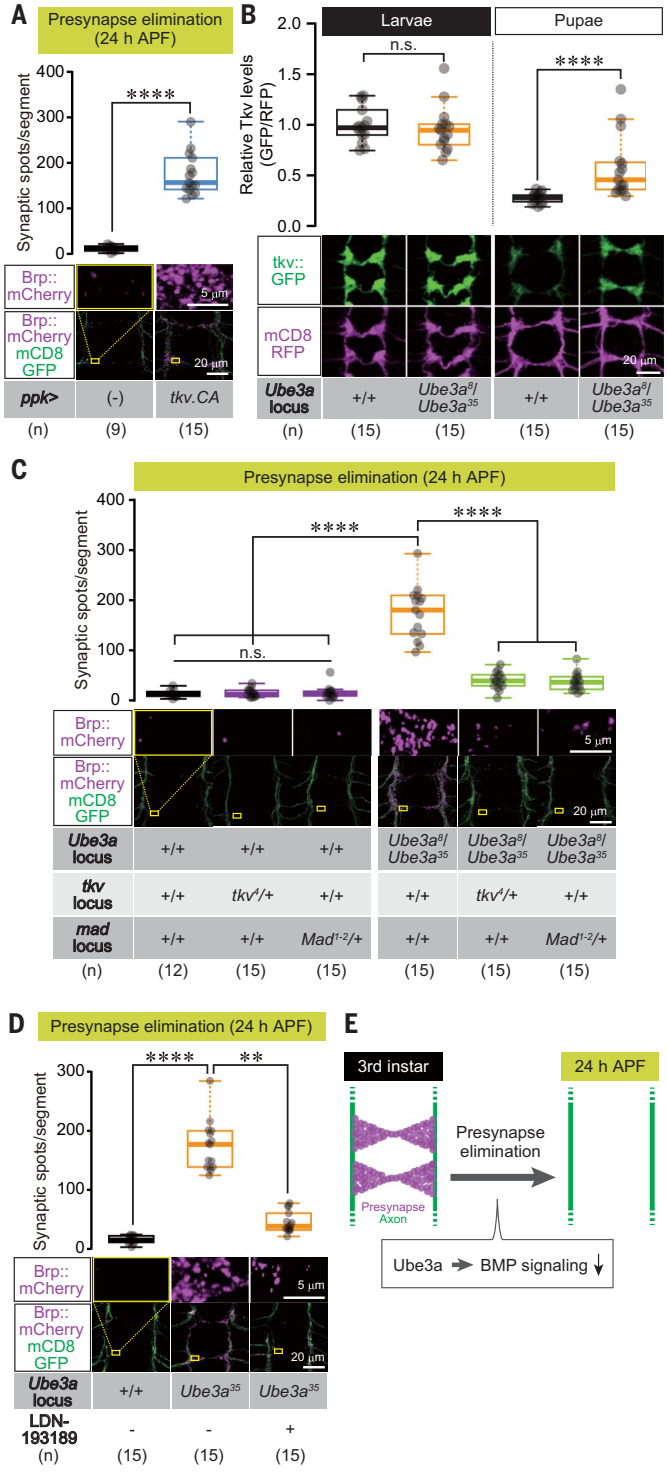

Fig. 5. Ube3a promotes synapse elimination through down-regulation of synaptic BMP signaling. (**A**) Presynaptic numbers in an abdominal segment of C4da neurons at 24 hours APF. Box plots indicate the median, 25th and 75th percentiles, and the data range. ****P < 0.0001, Mann-Whitney test. (**B**) (Top) Relative expression levels of Tkv::GFP at the third instar larval stage (larvae) or 8 hours APF (pupae) in wild-type and *ube3a*-null mutants. Box plots indicate the median, 25th and 75th percentiles, the data range except for outliers, and outliers. ****P < 0.0001, n.s. $P \geq 0.05$, Mann-Whitney test. (**C**) Presynaptic numbers in an abdominal segment of C4da neurons at 24 hours APF. Box plots indicate the median, 25th and 75th percentiles, the data range except for outliers, and outliers. ****P < 0.0001, n.s. $P \geq 0.05$, Kruskal–Wallis test with Dunn's multiple comparisons test. (**D**) Presynaptic numbers in an abdominal segment of C4da neurons at 24 hours APF. Box plots indicate the median, 25th and 75th percentiles, the data range except for outliers, and outliers. ****P < 0.0001, **P < 0.01, Kruskal-Wallis test with Dunn's multiple comparisons test. (**E**) Ube3a down-regulates presynaptic BMP signaling for presynapse elimination in C4da neurons.

Increased Ube3a activity in presynapses causes precocious synapse elimination and impairs synapse transmission

In addition to loss of Ube3a, increased Ube3a dosage is associated with ASDs (*2*, *7*), yet it remains unknown whether increased activity of presynaptic Ube3a might contribute to synapse dysfunction in vivo. To address this issue, we next overexpressed wild-type and mutant Ube3a in C4da neurons and found that overexpression of wild-type Ube3a caused severe presynapse loss in C4da axon terminals in all segments of the third instar larvae (Fig. 6A and figs. S2, C and D). Second instar larvae with Ube3a overexpression showed no obvious changes in the presynapse number compared with that of wild-type control (Fig. 6A), suggesting that increased Ube3a expression in C4da neurons causes precocious elimination of existing presynapses rather than reduction of synapse formation in the earlier larval stages. This precocious synapse elimination was undetectable by overexpressing a catalytically inactivated Ube3a mutant (C941A) or Ube3a harboring an Angelman syndrome mutation (D313V) in C4da neurons (Fig. 6A). In addition, the precocious synapse elimination was partially suppressed by overexpressing a constitutive active Tkv (fig. S13). These data together indicate that increased Ube3a E3 ligase activity in C4da presynapses promotes precocious synapse elimination by down-regulating BMP signaling. We next assessed whether increased Ube3a activity in presynapses might affect synaptic transmission as well as synapse number. To do that, in live larval preparations we optogenetically activated C4da neurons with Channelrhodopsin2 (ChR2) while monitoring intracellular calcium (Ca^{2+}) responses in the downstream A08n neurons expressing jRGEGO1a (Fig. 6B) (*24*, *40*). We found that the C4da-to-A08n synapse transmission upon optogenetic activation of C4da neurons was significantly reduced by overexpressing wild-type Ube3a, but not Ube3a (C941A) and Ube3a (D313V) mutants, in C4da neurons (Fig. 6, C to E). We further checked the impact of Ube3a overexpression on nociceptive behavior in larvae because C4da sensory neurons detect multiple noxious stimuli and evoke robust escape behavior (*24*, *25*, *40*, *41*). To this end, we tested larval rolling latencies using a temperature-controlled probe for local thermonociceptive stimulation (Fig. 6F) (*24*, *25*, *40*, *41*). Consistent with the reduced synapse number and transmission in C4da neurons, third instar larvae overexpressing wild-type Ube3a, but not the catalytically inactive Ube3a (C941A) and the Ube3a with the Angelman syndrome–associated mutation (D313V), showed significantly longer rolling latencies in response to noxious heat stimuli (Fig. 6G), indicating that increased Ube3a activity in presynapses of nociceptive neurons causes hypoalgesia. Hypoalgesia phenotypes are associated with certain types of ASD patients and ASD model mice (*42*–*44*). Taken together, these data all consistently indicate that increased Ube3a activity in presynapses affects synapse numbers and synapse transmission in vivo.

Discussion

In this study, we have established a presynaptic role of Ube3a in synapse elimination and revealed the molecular mechanism underlying presynaptic targeting of Ube3a proteins. We have further shown that Ube3a promotes presynapse elimination by suppressing presynaptic BMP signaling, which presumably causes instability and thus reduction of existing synapses. Last, we have shown that not only reduced activity but also increased activity of

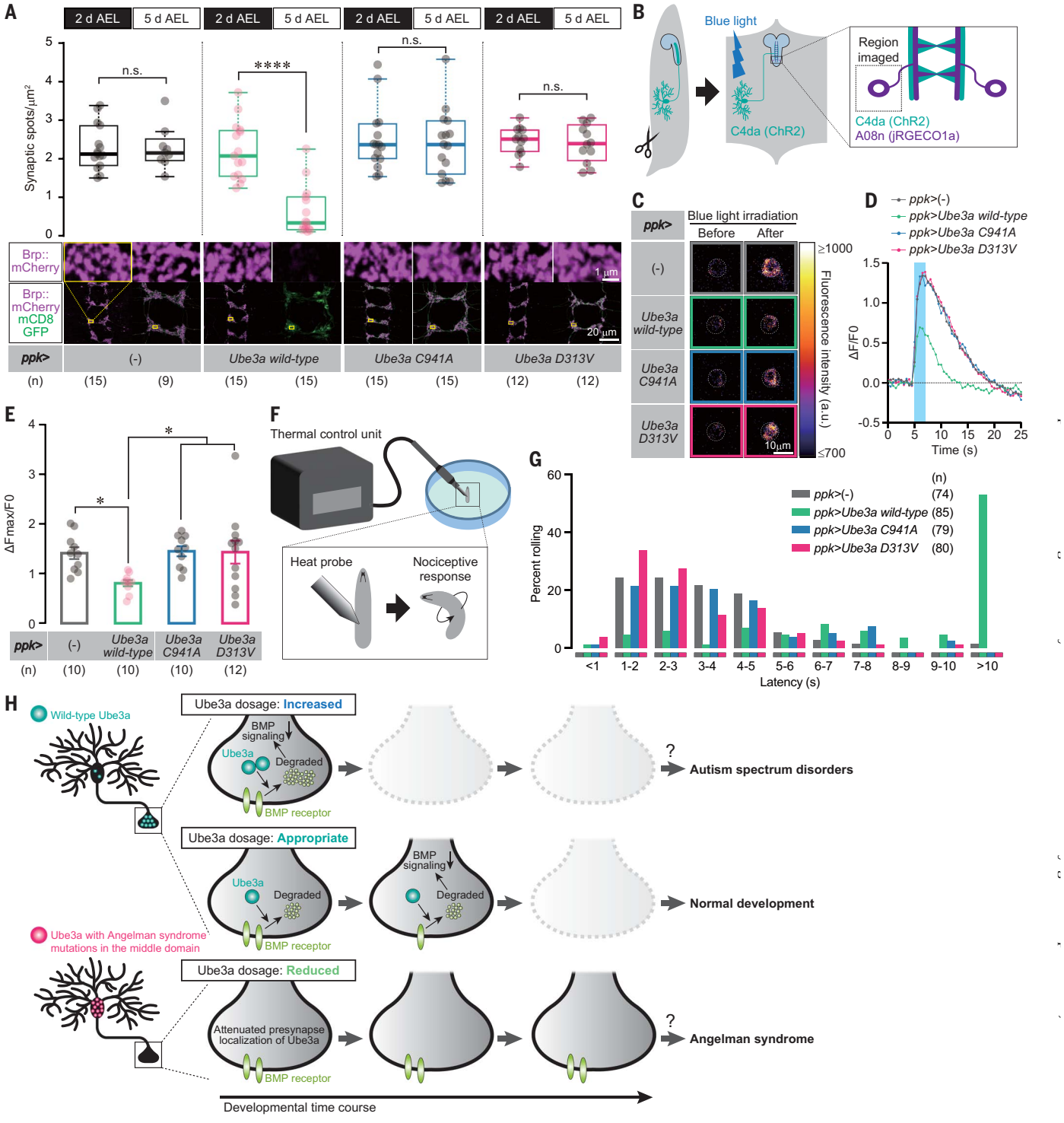

Fig. 6. Increased Ube3a activity in presynapses causes precocious synapse elimination and impairs synapse transmission. (**A**) Presynaptic numbers in an abdominal segment of C4da neurons at 2 days after egg laying (AEL) or 5 days AEL. Box plots indicate the median, 25th and 75th percentiles, the data, range except for outliers, and outliers. ****$P < 0.0001$, n.s. $P \geq 0.05$, Mann-Whitney test. (**B**) Schematic images of preparations for calcium imaging in A08n neurons upon C4da activation. (**C**) Ca^{2+} imaging of A08n neurons upon C4da activation. (**D**) Time series for the average of Ca^{2+} responses in A08n neurons upon optogenetic activation of C4da neurons overexpressing wild-type or mutant Ube3a at the third instar larval stage. (**E**) Average of A08n maximal fluorescence increase ($\Delta F_{max}/F_0$) values upon optogenetic activation of C4da neurons overexpressing wild-type or mutant Ube3a. Data are expressed as the mean ± SEM. *$P < 0.05$, one-way ANOVA, followed by Tukey's multiple-comparisons test. (**F**) Experimental setup for local hot probe assay. (**G**) Latency of nociceptive rolling responses in the third instar larvae overexpressing wild-type or mutant Ube3a. (**H**) Presynaptic Ube3a activity is associated with abnormalities of the synaptic structures and functions.

presynaptic Ube3a E3 ligase affect synaptic structure and function (Fig. 6H). These findings indicate that presynaptic Ube3a E3 ligase is a crucial factor to control synapse number and activity and suggest that mislocalization as well as dysregulation of Ube3a E3 activity might cause aberrant synapse function and neurodevelopmental disorder. In addition to the ecdysone-induced synapse elimination in C4da neurons, we found that presynaptic Ube3a is required for activity-dependent synapse elimination in *Drosophila* photoreceptor neurons (fig. S14, A and B) (*45*). Further genetic evidence suggests that, consistent with the ecdysone-induced synapse elimination in C4da neurons, Ube3a promotes activity-dependent synapse elimination through down-regulation of BMP signaling (fig. S14, C and B). These data support the notion that Ube3a and BMP down-regulation are required for activity-dependent synapse elimination as well as hormone-induced synapse elimination.

Angelman syndrome–associated missense mutations are distributed throughout the human Ube3a protein (figs. S7 and S8), and the pathological impact of each mutation, especially mutations localized between Azul and HECT domains, remains largely unknown. Our findings indicate that the Angelman syndrome–associated mutation D313V in the middle domain disrupts the presynaptic targeting and the function of Ube3a in synapse elimination. It will be intriguing to examine whether other Angelman syndrome–associated mutations might affect synaptic localization of Ube3a in neurons. Our data indicate that the middle domain of Ube3a plays a critical role for association of Ube3a with the kinesin-motor complex and thus presynaptic localization. Because Ube3a is localized in multiple neural compartments (*12*–*14*, *46*), it is of importance to define the compartment-specific role as well as substrates of Ube3a in neural development and function for comprehensive understanding the physiological and pathological role of Ube3a.

We propose that presynaptic Ube3a promotes Tkv down-regulation in C4da neurons. Previous reports suggest that the endocytic pathway controls BMP receptor levels in *Drosophila* neuromuscular junctions (NMJ) (*47*–*49*). We checked whether the endocytic pathway might contribute to Tkv down-regulation in C4da synapses and found that neither overexpression nor RNAi suppression of the components involved in the endocytic control of BMP receptors caused synapse eliminations defects in C4da neurons (fig. S15, A and B). Furthermore, neither overexpression nor RNAi suppression of the components affected reduction of Tkv levels in C4da presynapses during metamorphosis (fig. S16). It is thus likely that the Ube3a-mediated pathway, rather than the endocytic pathway, likely play a dominant role for Tkv down-regulation in C4da neurons during metamorphosis. In *Drosophila* NMJ, multiple molecular pathways, including actin regulation and hormone signaling, function downstream of or in parallel to BMP signaling for synapse development and remodeling (*38*, *39*, *50*, *51*). We checked the potential molecules and found that genetic manipulations of Ftz-f1/Hr39 attenuated both synapse elimination and dendrite pruning in C4da neurons (fig. S17). A previous work on axon pruning in mushroom body (MB) neurons indicated that Ftz-f1/Hr39 promotes axon pruning by up-regulating EcR-B1 levels in parallel to BMP signaling (*52*). Consistently, EcR-B1 levels were significantly reduced by Ftz-f1/Hr39 manipulations in C4da neurons (fig. S17). It is thus likely that Ftz-f1/Hr39 promotes both dendrite pruning and synapse elimination by up-regulating EcR-B1 levels in C4da neurons during metamorphosis. By contrast, presynaptic Ube3a and Tkv down-regulation are specifically required for synapse elimination but not for dendrite pruning, and *Ube3a* mutations and Tkv activation unaffected EcR-B1 levels in C4da neurons during metamorphosis (fig. S18). Therefore, similar to the case in *Drosophila* NMJ and MB neurons, Ftz-f1/Hr39 likely triggers global neural remodeling including dendrite pruning and synapse elimination through up-regulating EcR-B1 levels in C4da neurons, whereas presynaptic Ube3a and Tkv down-regulation locally promotes presynapse elimination at downstream of and/or in parallel to the Ftz-f1/Hr39/EcR signaling. Previous reports suggest that steroid hormones, such as estrogen and glucocorticoid, induce in the mammalian brain (*53*, *54*). It would be of interest to investigate whether presynaptic Ube3a and BMP down-regulation might play a role in steroid hormone–mediated synapse elimination in the mammalian brain.

In ASD model mice with chromosome 15q duplication, the synapse turnover is significantly enhanced because of accelerated synapse elimination and regeneration cycles, leading to synapse instability in cortical neurons (*55*). Given the augmented dosage of Ube3a in the Dup15q model mice, it is feasible that increased Ube3a activity in presynapses of ASD neurons might cause synapse instability and dysfunction. Consistent with this notion, increased dosage of Ube3a attenuates synaptic transmission in *Drosophila* neurons (Fig. 6) as well as mouse cortical neurons (*8*). Furthermore, a recent report indicates that presynaptic BMP signaling regulates synapse turnover in mouse cortical neurons (*56*). It is therefore likely that the role of Ube3a and BMP signaling in presynapses is conserved in flies and mammals. Given that pharmacological as well as genetic manipulations of BMP signaling suppressed synapse elimination defects through aberrant Ube3a functions, neuronal BMP signaling could be a target for interventions of ASD and Angelman syndrome. Further studies deciphering the presynaptic role of Ube3a and subsequent BMP signaling will provide insights into the regulation of local synapse elimination and neurodevelopmental pathology.

REFERENCES AND NOTES

1. K. Buiting, C. Williams, B. Horsthemke, *Nat. Rev. Neurol.* **12**, 584–593 (2016).
2. N. Khatri, H. Y. Man, *Front. Mol. Neurosci.* **12**, 109 (2019).
3. A. M. Mabb, M. C. Judson, M. J. Zylka, B. D. Philpot, *Trends Neurosci.* **34**, 293–303 (2011).
4. H. Kim, P. A. Kunz, R. Mooney, B. D. Philpot, S. L. Smith, *J. Neurosci.* **36**, 4888–4894 (2016).
5. M. Sato, M. P. Stryker, *Proc. Natl. Acad. Sci. U.S.A.* **107**, 5611–5616 (2010).
6. K. Yashiro *et al*., *Nat. Neurosci.* **12**, 777–783 (2009).
7. S. J. Lopez, D. J. Segal, J. M. LaSalle, *Front. Mol. Neurosci.* **11**, 476 (2019).
8. S. E. Smith *et al*., *Sci. Transl. Med.* **3**, 103ra97 (2011).
9. P. L. Greer *et al*., *Cell* **140**, 704–716 (2010).
10. S. S. Margolis *et al*., *Cell* **143**, 442–455 (2010).
11. J. Sun *et al*., *Cell Rep.* **12**, 449–461 (2015).
12. A. C. Burette *et al*., *J. Comp. Neurol.* **525**, 233–251 (2017).
13. A. C. Burette *et al*., *Mol. Autism* **9**, 54 (2018).
14. S. V. Dindot, B. A. Antalffy, M. B. Bhattacharjee, A. L. Beaudet, *Hum. Mol. Genet.* **17**, 111–118 (2008).
15. K. Emoto, *Curr. Opin. Neurobiol.* **22**, 805–811 (2012).
16. R. K. Morikawa, T. Kanamori, K. Yasunaga, K. Emoto, *Proc. Natl. Acad. Sci. U.S.A.* **108**, 19389–19394 (2011).
17. W. B. Grueber *et al*., *Development* **134**, 55–64 (2007).
18. T. Kanamori, K. Togashi, H. Koizumi, K. Emoto, *Int. Rev. Cell Mol. Biol.* **318**, 1–25 (2015b).
19. K. Furusawa, K. Emoto, *Front. Cell. Neurosci.* **14**, 613320 (2021).
20. Y. Kitatani *et al*., *PLOS Genet.* **16**, e1008942 (2020).
21. C. T. Kuo, L. Y. Jan, Y. N. Jan, *Proc. Natl. Acad. Sci. U.S.A.* **102**, 15230–15235 (2005).
22. D. W. Williams, J. W. Truman, *Development* **132**, 3631–3642 (2005).
23. W. Fouquet *et al*., *J. Cell Biol.* **186**, 129–145 (2009).
24. C. Hu *et al*., *Nat. Neurosci.* **20**, 1085–1095 (2017).
25. J. Yoshino, R. K. Morikawa, E. Hasegawa, K. Emoto, *Curr. Biol.* **27**, 2499–2504.e3 (2017).
26. D. Kirilly *et al*., *Neuron* **72**, 86–100 (2011).
27. T. Kanamori *et al*., *Science* **340**, 1475–1478 (2013).
28. T. Kanamori, J. Yoshino, K. Yasunaga, Y. Dairyo, K. Emoto, *Nat. Commun.* **6**, 6515 (2015).
29. C. T. Kuo, S. Zhu, S. Younger, L. Y. Jan, Y. N. Jan, *Neuron* **51**, 283–290 (2006).
30. D. W. Williams, S. Kondo, A. Krzyzanowska, Y. Hiromi, J. W. Truman, *Nat. Neurosci.* **9**, 1234–1236 (2006).
31. J. J. Wong *et al*., *PLOS Biol.* **11**, e1001657 (2013).
32. H. H. Lee, L. Y. Jan, Y. N. Jan, *Proc. Natl. Acad. Sci. U.S.A.* **106**, 6363–6368 (2009).
33. M. T. Kelliher *et al*., *J. Cell Biol.* **217**, 2531–2547 (2018).
34. G. L. Sell, S. S. Margolis, *Front. Neurosci.* **9**, 322 (2015).
35. W. Li *et al*., *PLOS Genet.* **12**, e1006062 (2016).
36. H. Keshishian, Y. S. Kim, *Trends Neurosci.* **27**, 143–147 (2004).
37. E. Eivers, H. Demagny, E. M. De Robertis, *Cytokine Growth Factor Rev.* **20**, 357–365 (2009).
38. H. Aberle *et al*., *Neuron* **33**, 545–558 (2002).
39. B. A. Eaton, G. W. Davis, *Neuron* **47**, 695–708 (2005).
40. T. Kaneko *et al*., *Neuron* **95**, 623–638.e4 (2017).
41. W. D. Tracey Jr., R. I. Wilson, G. Laurent, S. Benzer, *Cell* **113**, 261–273 (2003).
42. S. I. Deutsch, *Am. J. Ment. Defic.* **90**, 631–635 (1986).
43. D. J. Fairburn *et al*., *Behav. Brain Res.* **420**, 113727 (2022).
44. L. Wang *et al*., *Neuropharmacology* **111**, 323–334 (2016).
45. A. Sugie *et al*., *Neuron* **86**, 711–725 (2015).
46. R. Avagliano Trezza *et al*., *Nat. Neurosci.* **22**, 1235–1247 (2019).
47. X. Wang, W. R. Shaw, H. T. Tsang, E. Reid, C. J. O'Kane, *Nat. Neurosci.* **10**, 177–185 (2007).

48. K. M. O'Connor-Giles, L. L. Ho, B. Ganetzky, *Neuron* **58**, 507–518 (2008).
49. R. J. Gleason, A. M. Akintobi, B. D. Grant, R. W. Padgett, *Proc. Natl. Acad. Sci. U.S.A.* **111**, 2578–2583 (2014).
50. A. Boulanger, M. Farge, C. Ramanoudjame, K. Wharton, J. M. Dura, *PLOS ONE* **7**, e40255 (2012).
51. Z. D. Piccioli, J. T. Littleton, *J. Neurosci.* **34**, 4371–4381 (2014).
52. A. Boulanger *et al*., *Nat. Neurosci.* **14**, 37–44 (2011).
53. B. S. McEwen, *Front. Neuroendocrinol.* **49**, 8–30 (2018).
54. B. S. McEwen, *Brain Res.* **1645**, 50–54 (2016).
55. M. Isshiki *et al*., *Nat. Commun.* **5**, 4742 (2014).
56. T. Higashi, S. Tanaka, T. Iida, S. Okabe, *Cell Rep.* **22**, 919–929 (2018).

ACKNOWLEDGMENTS

We thank Y. Q. Zhang, C. Doe, T. Suzuki, and J. Parrish for valuable reagents; Bloomington stock center, Kyoto Stock Center, and Vienna Drosophila Resource Center for fly stocks; J. Parrish for critical reading and comments on the draft; H. Ito and M. Maetani for technical assistance; and the members of Emoto Lab for critical comments and discussion. **Funding:** This work is supported by MEXT Grants-in-Aid for Scientific Research on Innovative Areas "Dynamic regulation of brain function by Scrap and Build system" (KAKENHI 16H06456), JSPS (KAKENHI 16H02504), WPI-IRCN, AMED-CREST (JP21 g310010), JST-CREST (JPMJCR22P6), Toray Foundation, Naito Foundation, Takeda Science Foundation, and Uehara Memorial Foundation to K.E.; JSPS (KAKENHI 18J01378 and 21K15102) to K.F.; and The Leading Initiative for Excellent Young Researchers (LEADER) from MEXT and JSPS (KAKENHI 22K06309) and AMED-PRIME (JP22 g6510011) to K.I. **Author contributions:** Initiation and conceptualization: K.E. Investigation: K.F., K.I., M.T., N.T., and E.H. Writing - original draft: K.E. Writing - editing: K.F. and K.E., with inputs from all authors. Visualization: K.F., K.I., M.T., and K.E. Supervision: E.H. and E.K. Funding acquisition: K.F., K.I., and K.E. **Competing interests:** The authors declare no conflicts of interest. **Data and materials availability:** All data are available in the main text or the supplementary materials. **License information:** Copyright © 2023 the authors, some rights reserved; exclusive licensee American Association for the Advancement of Science. No claim to original US government works. https://www.science.org/about/science-licenses-journal-article-reuse

SUPPLEMENTARY MATERIALS

science.org/doi/10.1126/science.ade8978
Materials and Methods
Figs. S1 to S18
Tables S1 and S2
References (*57*–*62*)
Movies S1 to S4
MDAR Reproducibility Checklist

Submitted 15 September 2022; resubmitted 6 June 2023
Accepted 18 August 2023
10.1126/science.ade8978

NEUROMORPHIC CHIPS

Edge learning using a fully integrated neuro-inspired memristor chip

Wenbin Zhang[1]†, Peng Yao[1]†, Bin Gao[1]*, Qi Liu[1], Dong Wu[1], Qingtian Zhang[1], Yuankun Li[1], Qi Qin[1], Jiaming Li[1], Zhenhua Zhu[2], Yi Cai[2], Dabin Wu[1], Jianshi Tang[1], He Qian[1], Yu Wang[2], Huaqiang Wu[1]*

Learning is highly important for edge intelligence devices to adapt to different application scenes and owners. Current technologies for training neural networks require moving massive amounts of data between computing and memory units, which hinders the implementation of learning on edge devices. We developed a fully integrated memristor chip with the improvement learning ability and low energy cost. The schemes in the STELLAR architecture, including its learning algorithm, hardware realization, and parallel conductance tuning scheme, are general approaches that facilitate on-chip learning by using a memristor crossbar array, regardless of the type of memristor device. Tasks executed in this study included motion control, image classification, and speech recognition.

Humans' ability to learn plays a vital role in the growth of intelligence and fast adaptation to unseen scenes (Fig. 1A) or dynamically changing environments. Edge artificial intelligence (AI) applications also require hardware with such learning abilities to enable the associated devices to adapt to new scenes or user habits (*1*). However, deep neural network (DNN) training (*2*, *3*) is typically implemented with conventional hardware based on the von Neumann computing architecture and high-precision digital computing paradigm (*4*). The extensive data movement between the processor chip and off-chip main memory incurs massive energy consumption and accounts for most of the latency of the whole training process (*5*, *6*). Therefore, although cloud computing platforms can handle such energy-intensive training (*4*, *7*), their high energy consumption hinders the implementation of learning on power-limited edge computing platforms (*1*). By contrast, memristor-based neuro-inspired computing eliminates this extensive data movement through its disruptive computation-in-memory architecture and analog computing paradigm (*6*, *8*–*10*). A memristor crossbar array can store an analog synaptic weight and perform in situ vector-matrix multiplication (VMM) operations in parallel in a single time step by exploiting Ohm's law and Kirchhoff's law. A neuro-inspired computing chip that integrates multiple memristor crossbar arrays and complementary metal-oxide semiconductor (CMOS) circuits can easily implement DNN inference (*11*–*14*) and has great potential to handle fully on-chip learning without any assistance from off-chip memory (*15*–*17*). The substantial energy efficiency enhancement provided by memristor-based neuro-inspired computing makes this paradigm promising for developing future chips that can enable low-power learning devices.

Several studies (*18*–*25*) have experimentally demonstrated learning using memristor crossbar arrays for in situ weight tuning although using software or external digital processors to implement the backpropagation (BP) algorithm (*2*). However, realizing a complete fully integrated memristor chip with strong learning ability and low energy costs remains challenging. The key challenge lies in the inefficiency of mapping the BP algorithm to on-chip hardware. First, an in-memory implementation of the BP algorithm requires costly conductance tuning operations with write verification due to device nonidealities, such as device variability and nonlinear conductance modulation (*15*, *26*–*29*). Second, it is difficult to achieve efficient parallel conductance tuning with write verification (*19*–*21*, *23*), which makes on-chip learning more time- and energy-consuming. Third, the high-precision data processing operations required during weight update calculations require a large circuit area and high energy consumption, leading to unacceptable overhead (*26*, *30*).

In this work, we demonstrated a memristor-based neuro-inspired computing chip that enabled fully on-chip learning, for which a memristor-featured sign- and threshold-based learning (STELLAR) architecture was proposed. In this architecture, the on-chip updating scheme was first proposed to tune the memristor without verification. This scheme saved excessive write-and-read costs in the conductance tuning operations when compared to the write verification scheme, and moreover, it could accommodate device tuning issues of nonlinearity and asymmetry to realize software-comparable accuracies. Second, the on-chip calculation module was designed to determine the weight update direction, and this process solely involved the signs of the inputs, outputs, and errors instead of their high-precision forms. This design reduced the circuit design burden and avoided massive overhead during on-chip learning. Third, a cycle-parallel conductance tuning scheme was proposed, wherein conductance tuning was performed in a row-by-row parallel fashion. This scheme further reduced the induced energy consumption and latency and accommodated the limited endurance of memristors.

The fabricated neuro-inspired computing chip integrated two memristor crossbar arrays (~160,000 cells in total) and all the necessary circuit modules, including controllers for configuration, drivers for computing and programming, low-cost data converters, and memristor-featured learning modules (Fig. 1B). On the basis of the obtained hardware-measured results, the energy consumption of the memristor chip was a factor of 35 lower than that of a digital accelerator-based system. We demonstrated several improvement learning tasks, including motion control for a light-chasing car, image classification, and audio recognition. The scalability of the STELLAR schemes to large neural networks for improvement learning tasks was also verified with the simulation of a residual neural network on the CIFAR-100 dataset (*31*). The memristor-based neuro-inspired computing chip could facilitate the development of edge AI devices that could adapt to new scenes and users (Fig. 1B).

Memristor-featured architecture for on-chip learning

To support on-chip learning with appreciable energy efficiency, area efficiency, and accuracy, we proposed the STELLAR architecture (Fig. 2A). STELLAR architecture exploits the bidirectional analog switching behavior of the memristor device (*32*). During the weight update stage, only the weight update direction must be calculated from the signs of the inputs, outputs, and errors. In addition, the architecture predefines a threshold, which filters out the small errors when calculating the error signs and plays a vital role in the convergence of the learning algorithm by avoiding updates that are exceedingly sensitive and unnecessary. By omitting these small updates, the memristor-based gradient vectors under the STELLAR update scheme could approximate conventional BP gradient vectors more closely to accommodate practical device nonideal factors (such as asymmetric tuning of device conductance). The detailed analysis and simulation can be found in materials and methods section 2 (STELLAR update scheme under device asymmetric switching). This threshold is hardware-reconfigurable to adapt to various learning tasks. The algorithmic details of the STELLAR architecture can be found in materials and methods section 1 (Algorithm for the STELLAR architecture). Depending on

[1]School of Integrated Circuits, Beijing National Research Center for Information Science and Technology (BNRist), Tsinghua University, Beijing, China. [2]Department of Electronic Engineering, Beijing National Research Center for Information Science and Technology (BNRist), Tsinghua University, Beijing, China.
*Corresponding author. Email: gaob1@tsinghua.edu.cn (B.G.); wuhq@tsinghua.edu.cn (H.W.)
†These authors contributed equally to this work.

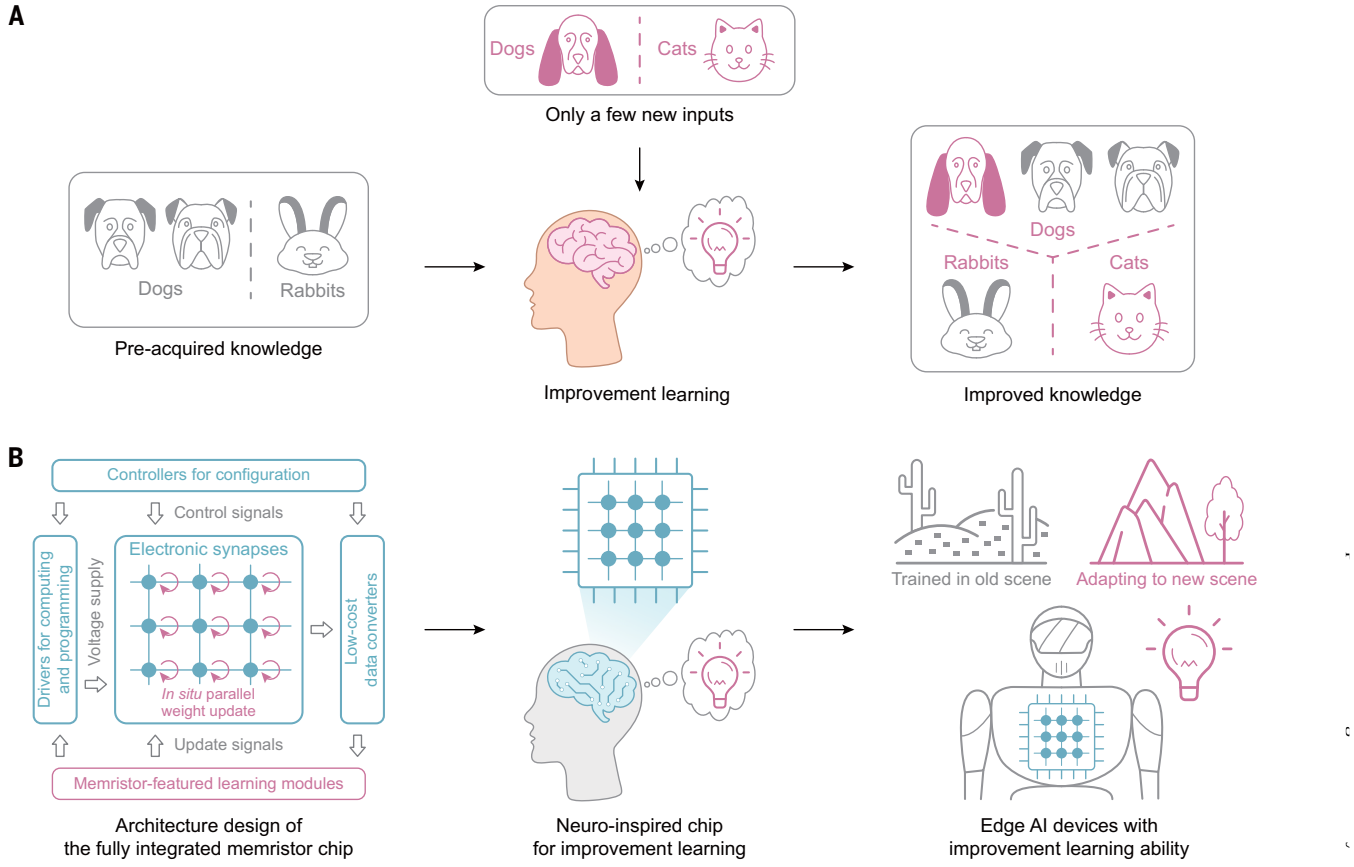

Fig. 1. Edge learning with a neuro-inspired memristor chip. (**A**) Illustration of the improvement learning ability possessed by human brains. With preacquired knowledge about old dogs and rabbits, the learning of new samples (i.e., new dogs) and a new class (i.e., cats) is quickly realized with only a few new inputs. (**B**) Design considerations and future applications of the memristor-based neuro-inspired computing chip. The chip, designed for fully on-chip learning, integrates all the necessary modules with memristor arrays. It equips edge AI devices with the learning ability, enabling them to quickly adapt to new scenes.

the weight update direction, a corresponding identical SET or RESET pulse is applied to the memristor cells. With this scheme, we could realize energy-efficient hardware by avoiding the complex precise weight update calculation and write verification processes as well as the complex peripheral circuit design.

The learning performance of the STELLAR architecture was compared with that of the conventional methods through simulations on the Modified National Institute of Standards and Technology (MNIST) dataset (*33*). Here, all memristors in the second layer were set to random conductance states before the learning process started. Figure 2B shows the learning accuracies of the conventional BP method without and with different write variations (1% and 3%, given as the percentages of the full conductance window of the memristor device) in comparison with those of the proposed method under various thresholds. The simulation details can be found in the materials and methods section 3 (Comparison between STELLAR and the conventional BP algorithm). An appropriately selected threshold yielded improved convergence and learning accuracy (fig. S1A). An extremely small threshold led to weight updates that were too frequent and an oscillating state of the network, and a threshold that was excessively large led to inadequate weight updates. The comparison of the energy consumption among different methods is shown in Fig. 2C. Despite maintaining almost the same accuracy, the energy consumption of the STELLAR architecture was two orders of magnitude lower than that of the conventional BP method owing to the substantial reductions in the precise weight update calculations and the write verification overhead.

The STELLAR architecture realized positive and negative weights with differential pairs of memristor cells (*20*, *23*, *34*, *35*) (Fig. 2D). In conventional crossbar arrays with one-transistor-one-resistor (1T1R) configurations, the two memristor cells in a differential pair are connected to different source lines (SLs), and subtraction is accomplished in a digital fashion. In crossbar arrays with two-transistor-two-resistor (2T2R) configurations, the two memristor cells in a differential pair are connected to the same SL, and subtraction is accomplished directly in the current domain (*11*). The 2T2R design greatly reduces the SL current and thus, the IR drop issues, hence enabling a larger array size. Here, we propose a cycle-parallel conductance tuning scheme for such a differential pair configuration (Fig. 2E). In this scheme, the SET and RESET operations are performed alternately for the learning iterations of arriving input samples (e.g., images). If the SET (RESET) operation is performed in the current learning iteration, then the RESET (SET) operation is performed in the next learning iteration. Only one operation is performed on the whole array in each iteration; this is achieved by selecting which cell of a given differential pair to operate on. Taking the SET update mode as an example, if the weight update direction is positive (i.e., $\Delta W > 0$), the positive cell is updated with the SET operation to increase the weight; if $\Delta W < 0$, the negative cell is updated with the SET operation to decrease the weight; and if $\Delta W = 0$, neither cell is updated. The conductance tuning is performed in a row-by-row parallel fashion, and the detailed schematics of the array operations are shown in fig. S3. The memristor devices in the same row were selected through their word line (WL) signals and tuned depending on the corresponding SL signals, and the bit line (BL) signals remained constant. The cycle-

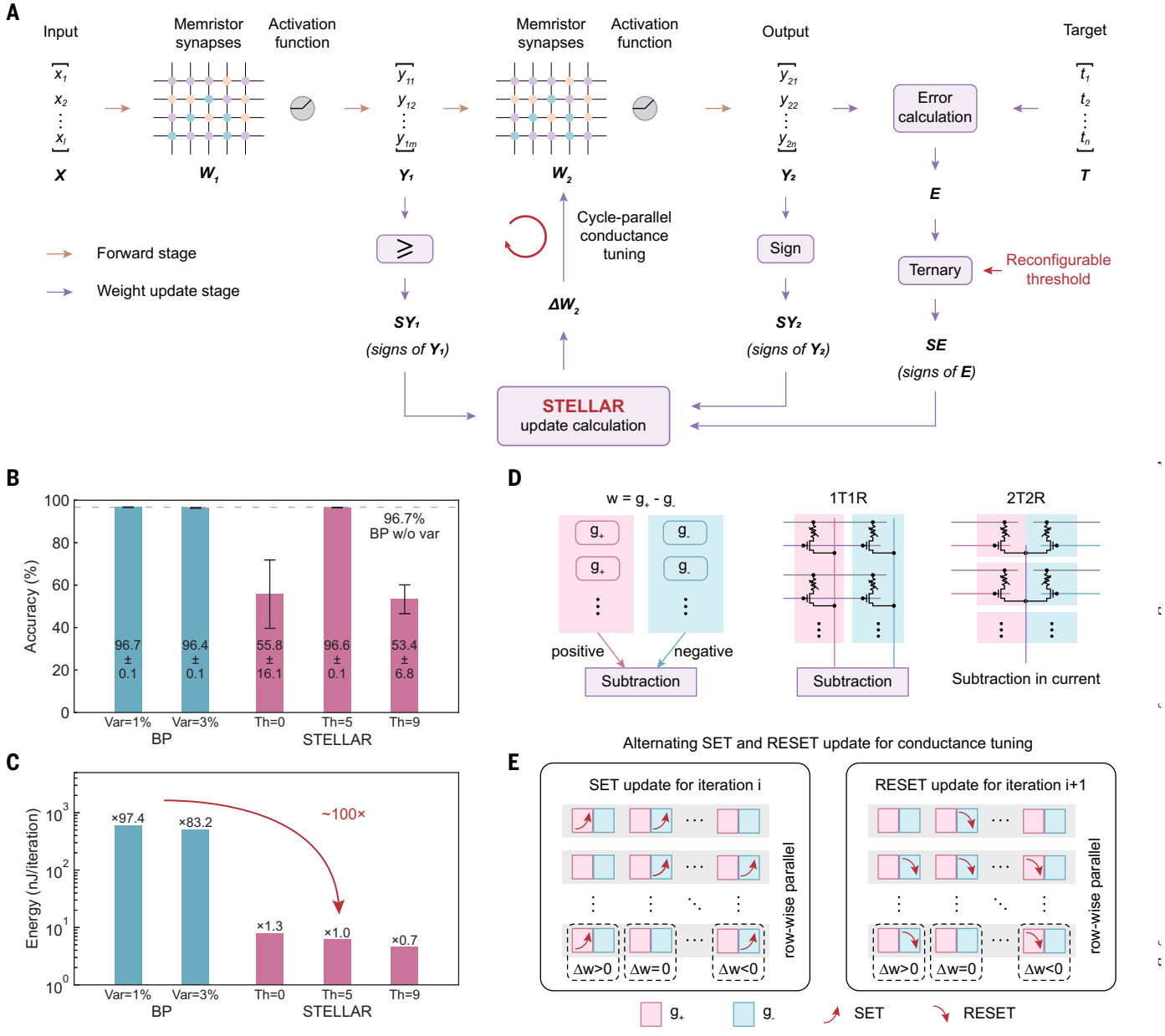

Fig. 2. Design of the memristor-featured architecture for on-chip learning. (**A**) Diagram of the STELLAR architecture used in the memristor chip. The STELLAR algorithm features sign-based weight update calculation and reconfigurable threshold for the error sign calculation during the weight update stage. (**B** and **C**) Comparison of the classification accuracies (B) and the weight update energy consumptions (C) using the STELLAR and the conventional BP algorithm on the MNIST dataset in simulations. (B) and (C) show the results of different write variations when using the BP algorithm and the results of different thresholds in the STELLAR learning approach. The bars and error bars show the averages and standard deviations of the results of 10 repeated experiments, respectively. The dashed line in (B) shows the average accuracy obtained by BP without considering the write variations of the memristors. (**D**) Representations of weights with a differential conductance pair (left) and with 1T1R (center) and 2T2R (right) configurations. (**E**) Illustration of the cycle-parallel conductance tuning scheme. The red and blue rectangles represent the positive and negative memristor cells in each differential pair, respectively. The upward and downward arrows represent the SET and RESET operations on the associated memristor cell, respectively.

parallel conductance tuning scheme could be applied to either 1T1R or 2T2R memristor arrays. Because only one-half of the memristor devices were updated during each on-chip learning iteration, the cycle-parallel conductance tuning scheme reduced the induced energy consumption and alleviated the requirement regarding the memristor endurance. The detailed analysis of endurance requirements can be found in materials and methods section 4 (Endurance requirements for the cycle-parallel conductance tuning scheme).

Chip design, fabrication, and measurements

Figure 3A shows the overall circuit implementation of the proposed STELLAR architecture. This memristor chip consisted of controllers for configuration; a 2T2R memristor array (1568 × 100), a 1T1R memristor array [100 × 20; see materials and methods section 5 (Weight configuration based on the 1T1R memristor array) for details]; BL, WL, and SL drivers for computing and programming; low-cost analog-to-digital converters (ADCs); modules for

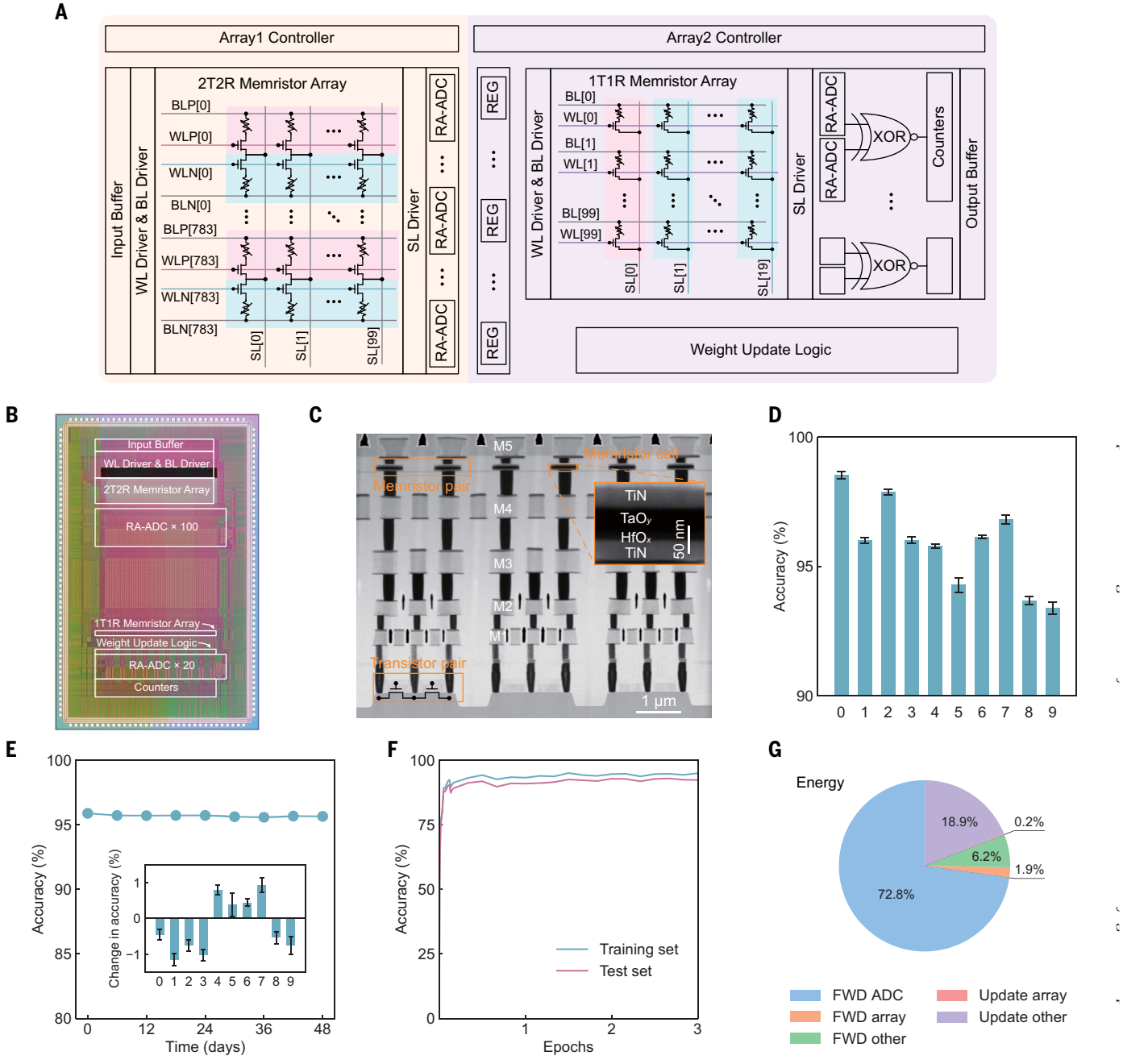

Fig. 3. The memristor chip for on-chip learning. (**A**) Overview of the architecture of the memristor chip. (**B**) Optical microscope image of the chip, where several key components are labeled. (**C**) A cross-section transmission electron microscopy (TEM) image showing 2T2R cells. The transistors in a 2T2R cell share a common source terminal. Inset: Cross-section TEM image of the memristor device. (**D**) On-chip classification accuracy obtained for each class by using the off-chip trained weights for the MNIST dataset, with bars and error bars showing the averages and standard deviations of the accuracies achieved over five inference iterations, respectively. The standard deviations ranged from 0.07 to 0.27. (**E**) Changes in the classification accuracy over 48 days after weight transfer, with each point showing the average accuracy over five inference results. Inset: The average changes in the accuracy of each class after 48 days of weight transfer. The standard deviations in the inset ranged from 0.1 to 0.32. (**F**) Changes in the classification accuracy over three learning epochs in the on-chip learning task for the MNIST dataset, with each epoch including 60,000 iterations. (**G**) Energy breakdown of the memristor chip during the on-chip learning process.

memristor-featured on-chip learning (i.e., error-circulating subtractors and weight update logic); and input and output buffers. The first-layer memristor array adopted a 2T2R configuration to reduce the IR drop issues occurring in such a large array, and the second-layer memristor array adopted a 1T1R configuration to support more flexible in situ weight tuning. The controllers decoded the input stage selection signals and provided the output configuration signals to other circuit modules to switch the chips to different working stages [see materials and methods section 6 (Circuit design of the memristor chip) and fig. S5]. Resolution-adjustable ADCs (RA-ADCs) feature configurable resolutions and support flexible threshold values (*11*). The error calculation was accomplished with subtractors, which were realized with counters. The weight

update logic determined the weight update direction and conductance tuning operations.

A micrograph of the fabricated chip is shown in Fig. 3B. The chip area breakdown is described in fig. S6B. The memristor device used a material stack of TiN/HfO_x/TaO_y/TiN, and the fabrication process was compatible with the standard CMOS process [see materials and methods section 7 (Fabrication of the memristor chip) and fig. S6A]. Consequently, the memristors could be conveniently integrated with complex CMOS circuits to produce an excellent yield (almost 100% of all 160,000 cells). The cross-section transmission electron microscopy (TEM) image in Fig. 3C showed the integration of memristor cells with CMOS circuitry. The fabricated memristors exhibited uniform and repeatable bidirectional analog switching with identical pulse trains (fig. S6D). The ~160,000 total on-chip memristor cells could be uniformly programmed to 32 conductance states, with maximum, minimum, and average success rates of 99.98, 99.69, and 99.90%, respectively [see materials and methods section 8 (Measurements of the memristor devices) and fig. S6C].

The on-chip inference was first demonstrated for MNIST handwritten digit classification. The weights were off-chip trained and then transferred to the chip as memristor conductance [see materials and methods section 9 (Off-chip training and on-chip inference)]. The measured classification accuracy of each class (0 to 9) is presented in Fig. 3D; the average accuracy was 95.8%. The effect of cell conductance fluctuations on the chip accuracy was also evaluated (Fig. 3E). We monitored the accuracy for 48 days, and no obvious accuracy degradation was observed. We also demonstrated real-time handwritten digit recognition with the memristor chip (see movie S3).

An on-chip learning task, MNIST image classification, was further demonstrated to verify the on-chip learning ability based on a 784-100-10 multilayer perceptron (MLP). The weights in the first layer were trained off-chip and then transferred to the chip as memristor conductance. The memristors in the second layer were first programmed to the high-resistance state (HRS) and then updated using the STELLAR scheme. All data processing and signal control processes were executed on the chip. After three epochs of on-chip learning with the training set, the classification accuracies were increased from 8.6 and 8.4% to 94.9 and 92.3% on the training set and test set, respectively (Fig. 3F). We then evaluated the energy consumption of the on-chip learning with hardware-measured results [see materials and methods section 11 (Energy consumption benchmark)]. We also evaluated the energy consumption of a digital accelerator-based system (*36*) for one training iteration with the same MLP network. The energy breakdown of the memristor chip during the on-chip learning process is presented in Fig. 3G. The energy consumption could be further reduced by optimizing the ADC design (*37*–*39*).

On-chip improvement learning

The memristor chip was used to further demonstrate four improvement learning tasks, including the motion control task of learning new samples, audio recognition task of learning new samples, image classification task of learning a new class, and motion control task of learning a new class. The improvement learning featured the fast learning of new knowledge and maintaining preacquired knowledge. As illustrated in Fig. 1A, the learning of new knowledge (e.g., new samples or classes) was quickly realized with only a few new inputs, and this learning was done without losing preacquired knowledge. The implementation of improvement learning mainly included two stages. First, a model was trained off-chip on the base dataset, and then the model was transferred to the chip. Next, under the STELLAR architecture, on-chip improvement learning with new data was performed on the basis of the transferred memristor chip. Improvement learning is a specific learning format to implement lifelong learning. This learning scheme aims to rapidly learn knowledge from the new data without forgetting previous knowledge on the old data, making it different from transfer learning (*40*) that focuses on transferring knowledge from original data to new data, regardless of the accuracy drop on the original data. We demonstrated these improvement learning tasks because we consider that recognizing new classes or samples with a base model is a practical and promising edge learning task.

We first demonstrated the learning of new samples in a motion control task of a light-chasing car (Fig. 4A). The car was designed to pursue the location of a laser light spot; it was equipped with a camera to capture environmental images, steering motor for direction control, and driving motor for throttle control. The memristor chip received the input features of the environmental images from the PC and provided the output control signals for the steering angles and driving throttles [see materials and methods section 12 (Motion control task of learning new samples) for details]. As illustrated in Fig. 4B, a convolutional neural network (CNN) that included six convolution layers and two fully connected (FC) layers with the dimensions of 512 × 100 × 10 was first trained off-chip with old scene data (i.e., dark scene data), and then the weights of these two FC layers were transferred to the two corresponding arrays of the memristor chip. Next, improvement learning of the new scene (i.e., a bright scene) was performed on the chip by tuning the weights of the last FC layer. The details can be found in materials and methods section 16 (The hybrid system for running the motion control task). Before improvement learning, the car could have lost track of the target (i.e., light spot) in the bright scene: It deviated from the target or moved forward even if no target was present. After improvement learning, the car adapted well to the bright scene and still performed well in the dark scene (movie S1). Figure 4C shows the evolution of the scores during improvement learning, where a score of 1.0 denotes the best performance [see materials and methods section 12 (Motion control task of learning new samples)]. The scores became stable after improvement learning with 500 training samples from the new scene. After improvement learning with all the training samples, the average score in the new scene significantly increased from 0.605 to 0.912, and that of the old scene increased from 0.951 to 0.963, showing that no degradation occurred (Fig. 4D). Figure 4E shows the transitions and changes in conductance weights before and after the improvement learning.

Next, we demonstrated the learning of a new class in an image classification task involving the MNIST dataset (Fig. 4F). The base model was trained to recognize images of the digits 0 and 2–9 (old classes) and then transferred to the memristor chip. Next, the improvement learning of the new class (i.e., the digit 1) was performed on the chip. As shown in Fig. 4G, the accuracy achieved for the new class increased substantially during the improvement learning with only a few training samples, and the accuracy for the remaining nine old classes was not significantly reduced. The accuracies yielded for the new class and old classes stabilized after 100 training samples. After improvement learning with 100 training samples, the average accuracy for the new class increased from 7.02 to 93.0%, and that achieved for the old classes slightly decreased from 95.3 to 93.2% (Fig. 4H). The conductance weight distributions before and after improvement learning and their difference are shown in Fig. 4I.

In addition, the memristor chip was also used to implement an audio recognition task of learning new samples and a motion control task of learning a new class. In the audio recognition task, the on-chip improvement learning improved the recognition accuracy for female audio samples based on the weights pretrained with male audio samples (fig. S8A). In the motion control task of learning a new class, the on-chip improvement learning of the "moving backward" action helped the car to accomplish the tough task based on the model only knowing when to move forward or stop (fig. S9A). After improvement learning, the accuracy achieved for the new class (i.e., moving backward) increased from 0 to 95.2%, and that for the old classes (i.e., moving forward or stopping) decreased from 89.5 to 89.4%. The implementation details of these two tasks can be found

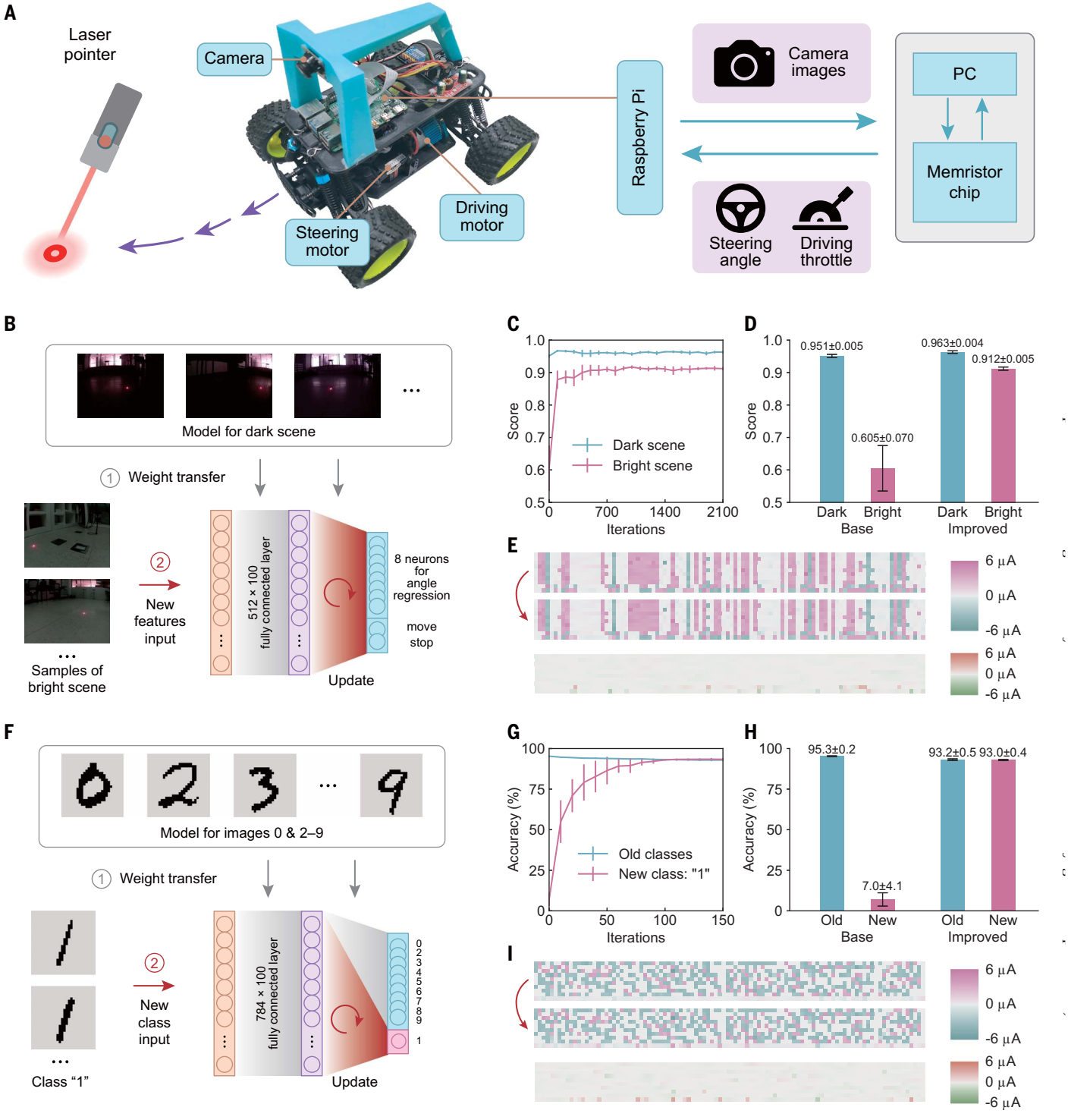

Fig. 4. Improvement learning demonstrations on the memristor chip. (**A**) Illustration of the motion control task (left) and its control system (right). (**B**) Illustration of the learning of new samples in the light-chasing car task. (**C**) Changes in the scores over the course of on-chip improvement learning of bright scene samples. The lines and the error bars show the averages and standard deviations of the scores of 10 repeated experiments with shuffled training sets, respectively. (**D**) The initial and final scores in (C). (**E**) The evolution of the weight distribution (100 × 10) before (top) and after (middle) the on-chip improvement learning. Bottom: distribution of the weight changes. (**F**) Illustration of the learning of a new class in the image classification task. (**G**) Changes in the accuracies over the course of on-chip improvement learning of the new class, showing the results from 10 repeated experiments with 150 randomly selected images from the training set each time. (**H**) The initial accuracies and the accuracies achieved after on-chip improvement learning of 100 iterations in (G). (**I**) The evolution of the weight distribution (100 × 10) before (top) and after (middle) the on-chip improvement learning. Bottom: Distribution of the weight changes.

in materials and methods sections 14 and 15 (Audio recognition task of learning new samples, Motion control task of learning a new class). Moreover, we performed another simulation with a memristor ResNet20 network for CIFAR-100 image recognition, which required 20 unseen classes to be learned after training on the remaining 80 categories. The accuracies on old, new, and whole datasets for this task were similar to software results with the floating-point precision [see materials and methods section 17 (The scalability of the method to larger neural networks) and fig. S10]. These results illustrated that the proposed STELLAR architecture could be scalable to larger neural networks and could realize efficient improvement learning with high-precision software accuracies.

Conclusions

We developed a fully integrated memristor chip with the improvement learning ability and low energy cost. The schemes in the STELLAR architecture, including its learning algorithm, hardware realization, and parallel conductance tuning scheme, are general approaches that facilitate on-chip learning by using a memristor crossbar array, regardless of the type of memristor device. We demonstrated the improvement learning of both new samples and a new class across various tasks, including motion control, image classification, and speech recognition, which showed that the STELLAR architecture accommodated the device nonidealities and equipped the memristor chip with improvement learning ability to adapt to new scenarios. With further circuitry engineering (*41*) based on advanced fabrication technology, the STELLAR architecture could enable on-chip learning memristor chip with an energy efficiency about 75 times higher than that of the digital accelerator (*36*). More details can be seen in materials and methods section 18 (The energy efficiency estimation of the memristor-based learning chip). This study is an important step toward future chips with high energy efficiency and extensive learning capabilities. We hope our findings will accelerate the development of future smart edge devices that can adapt to different application scenarios and owners.

REFERENCES AND NOTES

1. W. Shi, J. Cao, Q. Zhang, Y. Li, L. Xu, *IEEE Internet Things J.* **3**, 637–646 (2016).
2. D. E. Rumelhart, G. Hinton, R. J. Williams, *Nature* **323**, 533–536 (1986).
3. Y. LeCun, Y. Bengio, G. Hinton, *Nature* **521**, 436–444 (2015).
4. A. Coates *et al*., in *Proceedings of the 30th International Conference on Machine Learning* (PMLR, 2013), pp. 1337–1345.
5. M. Horowitz, "1.1 Computing's energy problem (and what we can do about it)" in *2014 IEEE International Solid-State Circuits Conference Digest of Technical Papers (ISSCC)* (IEEE, 2014), pp. 10–14.
6. H.-S. P. Wong, S. Salahuddin, *Nat. Nanotechnol.* **10**, 191–194 (2015).
7. E. Strubell, A. Ganesh, A. McCallum, in *Proceedings of the AAAI Conference on Artificial Intelligence* (AAAI, 2020), pp. 13693–13696.
8. D. Ielmini, H.-S. P. Wong, *Nat. Electron.* **1**, 333–343 (2018).
9. M. A. Zidan, J. P. Strachan, W. D. Lu, *Nat. Electron.* **1**, 22–29 (2018).
10. M. Lanza *et al*., *Science* **376**, eabj9979 (2022).
11. Q. Liu *et al*., in *2020 IEEE International Solid- State Circuits Conference - (ISSCC)* (IEEE, 2020), pp. 500–502.
12. W. Wan *et al*., in *2020 IEEE International Solid- State Circuits Conference - (ISSCC)* (IEEE, 2020), pp. 498–500.
13. C.-X. Xue *et al*., *Nat. Electron.* **4**, 81–90 (2021).
14. W.-H. Chen *et al*., *Nat. Electron.* **2**, 420–428 (2019).
15. S. Ambrogio *et al*., *Nature* **558**, 60–67 (2018).
16. A. Sebastian, M. Le Gallo, R. Khaddam-Aljameh, E. Eleftheriou, *Nat. Nanotechnol.* **15**, 529–544 (2020).
17. W. Zhang *et al*., *Nat. Electron.* **3**, 371–382 (2020).
18. M. Prezioso *et al*., *Nature* **521**, 61–64 (2015).
19. P. Yao *et al*., *Nat. Commun.* **8**, 15199 (2017).
20. C. Li *et al*., *Nat. Commun.* **9**, 2385 (2018).
21. Z. Wang *et al*., *Nat. Electron.* **2**, 115–124 (2019).
22. C. Li *et al*., *Nat. Mach. Intell.* **1**, 49–57 (2019).
23. P. Yao *et al*., *Nature* **577**, 641–646 (2020).
24. F. Cai *et al*., *Nat. Electron.* **2**, 290–299 (2019).
25. E. J. Fuller *et al*., *Science* **364**, 570–574 (2019).
26. G. W. Burr *et al*., *IEEE Trans. Electron Dev.* **62**, 3498–3507 (2015).
27. H. Wu *et al*., in *2017 IEEE International Electron Devices Meeting (IEDM)* (IEEE, 2017), pp. 11.5.1–11.5.4.
28. P. Y. Chen, X. Peng, S. Yu, *IEEE Trans. Comput. Aided Des. Integrated Circ. Syst.* **37**, 3067–3080 (2018).
29. Y. Xi *et al*., *Proc. IEEE* **109**, 14–42 (2021).
30. Q. Zhang *et al*., *Neural Netw.* **108**, 217–223 (2018).
31. A. Krizhevsky, G. Hinton, "Learning multiple layers of features from tiny images"; (Univ. of Toronto, 2009) https://www.cs.toronto.edu/~kriz/learning-features-2009-TR.pdf.
32. W. Wu *et al*., in *2018 IEEE Symposium on VLSI Technology* (IEEE, 2018), pp. 103–104.
33. Y. Lecun, L. Bottou, Y. Bengio, P. Haffner, *Proc. IEEE* **86**, 2278–2324 (1998).
34. P. Chi *et al*., in *Proceedings of the 43rd International Symposium on Computer Architecture* (ACM/IEEE, 2016), pp. 27-39.
35. L. Song, X. Qian, H. Li, Y. Chen, in *2017 IEEE International Symposium on High Performance Computer Architecture (HPCA)* (IEEE, 2017), pp. 541–552.
36. D. Han *et al*., *IEEE J. Solid-State Circuits* **56**, 2858–2869 (2021).
37. R. Khaddam-Aljameh *et al*., in *2021 Symposium on VLSI Circuits* (IEEE, 2021), pp. 1–2.
38. W. Wan *et al*., in *2020 IEEE Symposium on VLSI Technology* (IEEE, 2020), pp. 1–2.
39. J.-M. Hung *et al*., *Nat. Electron.* **4**, 921–930 (2021).
40. K. Weiss, T. M. Khoshgoftaar, D. Wang, *J. Big Data* **3**, 9 (2016).
41. W.-H. Huang *et al*., in *2023 IEEE International Solid- State Circuits Conference (ISSCC)* (IEEE, 2023), pp. 15–17.
42. W. Zhang, P. Yao, B. Gao, H. Wu, Data for Edge Learning Using a Fully Integrated Neuro-Inspired Memristor Chip, Zenodo, (2023); https://doi.org/10.5281/zenodo.8145521.
43. W. Zhang, P. Yao, B. Gao, H. Wu, *Zenodo* (2023); https://doi.org/10.5281/zenodo.8151757.

ACKNOWLEDGMENTS

Funding: This work was supported in part by the STI 2030-Major Projects (2021ZD0201200), the National Natural Science Foundation of China (92064001, 62025111), the XPLORER Prize, the Shanghai Municipal Science and Technology Major Project, and the Beijing Advanced Innovation Center for Integrated Circuits.
Author contributions: B.G. and H.W. supervised this project and proposed the overall architecture. W.Z., P.Y., and B.G. contributed to the whole experiment design and the writing of the manuscript. P.Y., Q.L., Do.W., and Da.W. designed the circuits. B.G., J.T., H.Q., and H.W. contributed to the memristor device fabrication and integration with CMOS. W.Z., P.Y., and Q.L. contributed to the implementation of the test system. Q.Z. worked on the development of AI models. W.Z. implemented the AI models on the chip and conducted the chip and system measurements. W.Z., P.Y., Y.L., Q.Q., J.L., Z.Z., Y.C., and Y.W. performed the simulation and benchmark. All authors discussed the results and reviewed the manuscript. **Competing interests:** The authors declare that they have no competing interests. **Data and materials availability:** All data are available in the manuscript or the supplementary material and can be found in Zenodo (*42*). All other software and data for running the simulations and experiments is available through Zenodo (*43*) and Github, including our hardware platform code, neural networks for improvement learning tasks, and simulation code to verify the advantages and scalability of the STELLAR schemes. **License information:** Copyright © 2023 the authors, some rights reserved; exclusive licensee American Association for the Advancement of Science. No claim to original US government works. https://www.sciencemag.org/about/science-licenses-journal-article-reuse

SUPPLEMENTARY MATERIALS

science.org/doi/10.1126/science.ade3483
Materials and Methods
Figs. S1 to S11
Tables S1 to S3
References (*44*–*53*)
Movies S1 to S3

Submitted 11 August 2022; resubmitted 30 May 2023
Accepted 8 August 2023
10.1126/science.ade3483

MICROROBOTICS

Powerful, soft combustion actuators for insect-scale robots

Cameron A. Aubin[1], Ronald H. Heisser[1], Ofek Peretz[1,2], Julia Timko[1], Jacqueline Lo[1], E. Farrell Helbling[3], Sadaf Sobhani[1], Amir D. Gat[2], Robert F. Shepherd[1]*

Insects perform feats of strength and endurance that belie their small stature. Insect-scale robots—although subject to the same scaling laws—demonstrate reduced performance because existing microactuator technologies are driven by low–energy density power sources and produce small forces and/or displacements. The use of high–energy density chemical fuels to power small, soft actuators represents a possible solution. We demonstrate a 325-milligram soft combustion microactuator that can achieve displacements of 140%, operate at frequencies >100 hertz, and generate forces >9.5 newtons. With these actuators, we powered an insect-scale quadrupedal robot, which demonstrated a variety of gait patterns, directional control, and a payload capacity 22 times its body weight. These features enabled locomotion through uneven terrain and over obstacles.

Swarms of centimeter-scale robots that can crawl (*1*–*3*), jump (*4*–*7*), and fly (*8*, *9*) like insects have the potential to survey and report on phenomena of interest and even influence their local environment. Applications span an array of fields, including healthcare, exploration, communication, and agriculture (*10*). For example, broad area surveillance of local soil conditions could ensure exact application of nitrogen, reducing the impact of excessive fertilizer use. Other robots could be deployed in hazardous or inaccessible environments to scan for signs of life in a search-and-rescue mission. To achieve the transportation distances (hundreds of meters) and speeds (tens of centimeters per second) required to realize their potential at costs that are affordable for large quantities (hundreds) of robots, substantial improvements to the size, weight, power, and fabrication limitations of microactuators are needed.

Because of the payload constraints, scaling laws, and manufacturing restrictions relevant to insect-scale robots, the state of the art in microactuator technologies is dominated by bespoke devices (*11*–*13*). Popular electromechanical options for actuation at this scale include piezoelectric bimorphs and dielectric elastomer actuators (DEAs). These microactuators operate at high frequencies (f = 10 to 1000 Hz) and demonstrate respectable power densities (Π_{max} ~ 600 W kg^{-1}) (*2*, *14*). However, DEAs and piezoelectric bimorphs lag behind their biological counterparts in some key areas. Individual actuations are low-force ($F \ll 1$N) and low-amplitude ($\delta_{\mu piezo} \ll 10\%$, $\delta_{\mu DEA} < 25\%$), and they must be operated near resonance (f ~ 100 to 1000 Hz) to achieve suitable performance (*2*, *9*, *15*–*17*). These limitations result in a lower average work (energy) density. Still, other microactuators used in robotics—including electrostatic (e.g., comb drives and parallel plates), thermal (e.g., phase change, shape-memory alloys and polymers), and magnetic actuators (e.g., magnetostrictive, external field)—lack either the cycling speeds, force, and/or displacement to perform meaningful work (*15*, *18*, *19*).

Chemical fuels represent a possible solution to these problems. The energy density of combustibles such as methanol (Γ = 22.7 MJ kg^{-1}) or butane (Γ = 49.5 MJ kg^{-1}) greatly exceeds that of electrical sources [e.g., Li-ion microbatteries, Γ < 1.0 MJ kg^{-1} (*20*)]. Centimeter-scale internal combustion engines (ICEs) have previously been explored for use in microaerial vehicles, portable devices, and small spacecraft. They suffer, however, from several issues, including leakage versus stiction, thermal management, efficiency, material restrictions, weight, and fabrication complexity, that make them incompatible with insect-scale robots (*21*). Soft robots, often actuated through volumetric expansion, have also been successfully driven by using combustible chemical fuels (*22*–*24*), as have soft pumps (*25*, *26*) and even soft haptic displays (*27*).

Despite clear utility, the combustion of chemical fuels has seldom been explored in robots at or below the centimeter scale. Some recent examples use only a single, noncyclic combustion event for a one-time actuation (*28*, *29*). Other robots such as the Octobot (*30*) and RoBeetle (*3*) are untethered, housing onboard fuel reserves, but contain low-frequency and low-force actuators. The large energetic potential of chemical fuels has yet to be fully exploited within this domain.

We present a lightweight (m = 325 mg), power-dense (Π_{stroke} = 277.2 kW kg^{-1}), high-frequency microactuator (Fig. 1) driven by the combustion of chemical fuels and describe its integration into an insect-scale robot. The actuator can produce forces greater than 9 N—an order of magnitude larger than existing microactuators of similar size, weight, and/or material composition—in submillisecond impulses. It operates at a range of desirable frequencies and can exceed 100 Hz.

[1]Sibley School of Mechanical and Aerospace Engineering, Cornell University, Ithaca, NY 14853, USA. [2]Faculty of Mechanical Engineering, Technion-Israel Institute of Technology, Haifa 3200003, Israel. [3]Department of Electrical and Computer Engineering, Cornell University, Ithaca, NY 14853, USA.
*Corresponding author. Email: rfs247@cornell.edu

Actuator fabrication and operation

We used a CLIP (continuous liquid interface production) 3D printer and a V-0 flame-resistant resin (EPX-86 FR; Carbon, Inc.) to fabricate the microactuators (Fig. 1A). This combination of material and manufacturing strategy gave us the ability to rapidly and cost-effectively produce small, lightweight, high-resolution combustion chamber bodies with favorable thermal properties. We determined the precise geometry of the roughly cylindrical combustion chambers (volume V = 0.09 mL) with early qualitative tests [supplementary materials (SM) section S7] (*27*) through which we evaluated flame propagation and venting behavior, as well as actuator integrity. We fitted these chambers with sparking electrodes, a flame arrestor module, and a thin elastomer (Dragon Skin 10, Smooth-On) membrane that served as the actuating surface. The complete manufacturing process for these devices can be found in SM section M1.

Much like a conventional ICE, the operation of the microactuator starts with the transfer of fuel—a mixture of gaseous methane and oxygen—into the combustion chamber (Fig. 1B). This process is facilitated by off-board mass flow controllers (MFCs) that continuously deliver prescribed amounts of fuel into the actuators through a thin length of tubing (fig. S1). This fuel is ignited with a small spark generated by offboard high-voltage (U_{spark} ~ 800 to 1200 V, depending on manufacturing variations) electronics connected to the electrode wires (fig. S2). The ensuing exothermic reaction causes product gases to expand and the elastomer membrane to inflate simultaneously (Fig. 1C and movie S1). This rapid (inflation time, $t_{inflate} \leq 0.55$ ms), piston-like actuation of the membrane can be used to powerfully drive end effectors, launch objects, or otherwise perform work. The actuation process ends when the product gases passively vent (deflation time, $t_{deflate} \sim t_{inflate}$) from the combustion chamber, and the cycle is then repeated. Passive flame quenching—defined here as the dissipation of flame fronts without the use of valves or active mechanisms—allows this process to occur continuously and repeatedly at high frequencies. We achieved passive quenching in our system through a combination of factors: (i) limiting flame propagation with a sub-milliliter combustion chamber volume, (ii) constructing the actuator from a material with flame-quenching properties, (iii) application of a dedicated onboard flame arrestor,

and (iv) usage of fuel-lean reactant chemistries. We further discuss the design decisions that contributed to passive quenching in SM section S1.

Actuator characterization

The performance of the actuator can be dynamically modulated by driving it at different frequencies or at different fuel-oxidizer concentrations, denoted by ϕ:

$$\phi = \frac{\left(\frac{n_{fuel}}{n_{oxid}}\right)_{actual}}{\left(\frac{n_{fuel}}{n_{oxid}}\right)_{stoich}} \quad (1)$$

$$CH_4 + 2O_2 \rightarrow CO_2 + 2H_2O + heat \quad (2)$$

where ϕ is the historically defined fuel-air equivalence ratio (*31*), and n_{fuel} and n_{oxid} represent moles of methane and oxygen, respectively. When $\phi = 1$, the system will react stoichiometrically (Eq. 2). Ratios corresponding to $\phi < 1$ are termed "fuel lean" because the reaction concludes with a surplus of oxygen. We operate our actuator at fuel-lean equivalence ratios, typically between $0.2 < \phi < 0.6$, because this limits the production of unwanted byproducts (e.g., soot, NO_x compounds); reduces the risk of flashback, in which flames reverse propagate up feed lines toward the fuel source; and decreases the probability of damaging the actuator. Figure 1D shows how increasing the equivalence ratio toward stoichiometric levels while maintaining actuation frequency and gas flow rate corresponds with an increase in membrane deformation. A greater fuel volume leads to an increase in the heat of combustion, which results in a greater expansion of product gases and an increase in membrane inflation.

We characterized the performance of the actuator by conducting membrane displacement (Fig. 1E) and blocked-force testing (Fig. 1F) across a range of equivalence ratios and frequencies (figs. S3 to S5). We captured displacement data using a high-speed camera and processed the video in ImageJ. The actuation frequency was dynamically adjusted with an Arduino microcontroller interfacing with the high-voltage–generating electronics. Custom LabVIEW code allowed for control of the fuel's equivalence ratio and flow rate by way of the MFCs. The reported reduction in membrane displacement with increasing frequency was a consequence of the experiments being conducted at a constant fuel flow rate ($Q = 2 \pm 0.1$ ml s^{-1}, composition dictated by ϕ); for a set volumetric flow rate, a higher rate of combustion corresponds to a smaller volume of fuel being consumed in each combustion event. Adjusting the flow rate allowed us to achieve any combination of frequencies and displacements within the ranges of $0 < f < 100$ Hz and ~$0.75 < \delta < 7$ mm. These ranges are not fundamental limitations to our technique but represent practical limitations of our initial experimental setup. The peak membrane displacement that we report, $\delta = 7$ mm, corresponds to a linear strain of the hyperelastic membrane of y =180% and a total actuator elongation of z = 140%, which is greater than contemporary microactuators employing soft materials (*16*) but far less than the ultimate strain (y_{ult} ~ 1000%) of the silicone copolymer we used in our membrane.

We measured the blocked force of these actuators using a high-precision load cell (fig. S4;

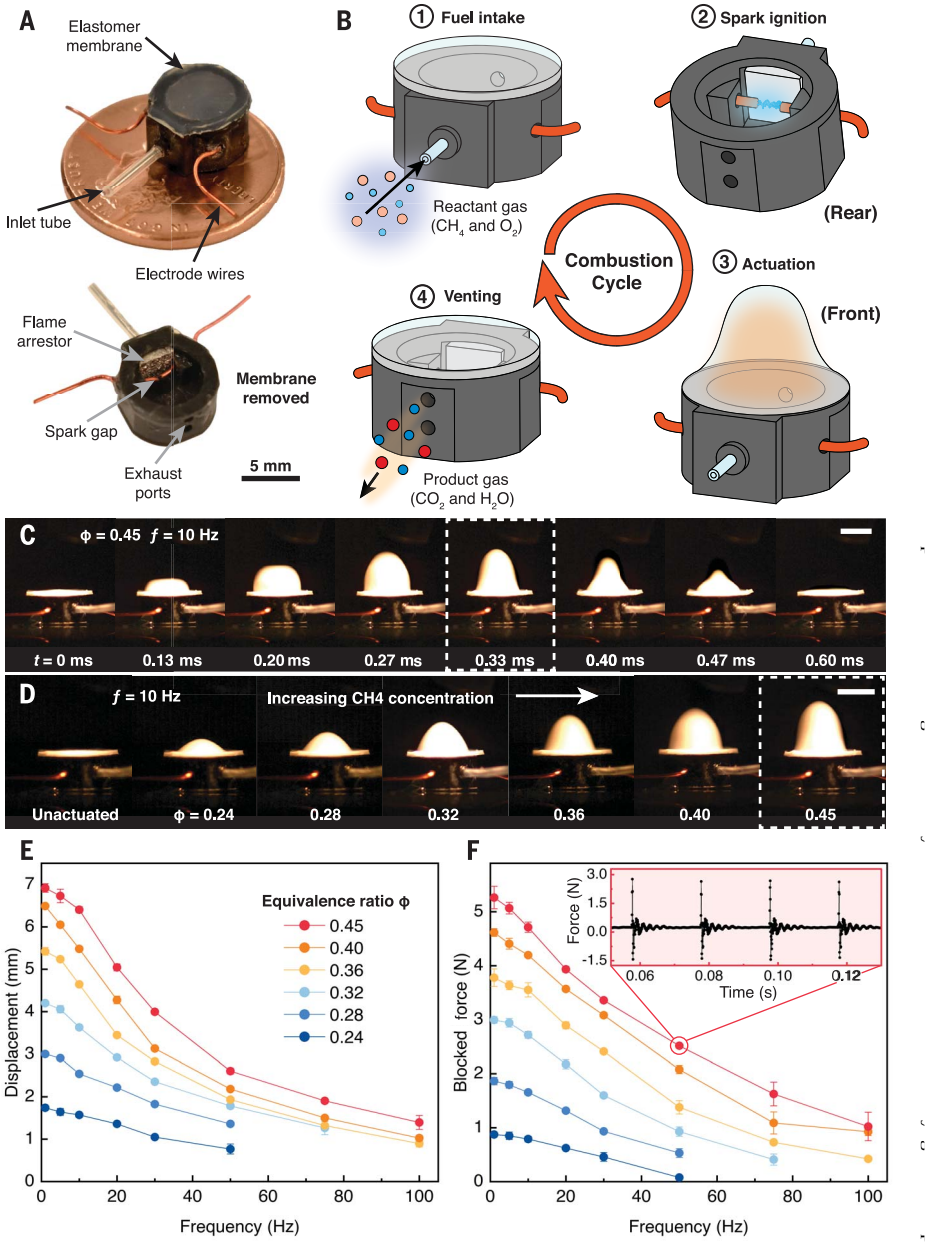

Fig. 1. Operation and characterization of the combustion-driven microactuator. (**A**) Front (top) and rear (bottom) view of the actuator and its component materials. (**B**) Diagram of the combustion actuation process. (**C**) Time-lapse image of a single actuation cycle. *t*, time. (**D**) Images of the actuator at different maximum displacements for a range of fuel-oxidizer (equivalence) ratios (ϕ). Photos were taken at the same actuation frequency $f = 10$ Hz. The dotted boxes indicate matching images in (C) and (D), which both occurred at $\phi = 0.45$ and $f = 10$ Hz. Scale bars [(C) and (D)], 5 mm. (**E**) Actuator displacement and (**F**) blocked force as a function of different frequencies for a series of equivalence ratios ($n = 5$ actuator tests, error bars = 1 SD). The inset plot shows the force profile achieved when tested at $\phi = 0.45$ and $f = 50$ Hz. Data are not available above $f = 50$ Hz for $\phi = 0.24$ and 0.28 or above $f = 75$ Hz for $\phi = 0.32$ because the volume of fuel in the actuator under these conditions is too small to sustain combustion.

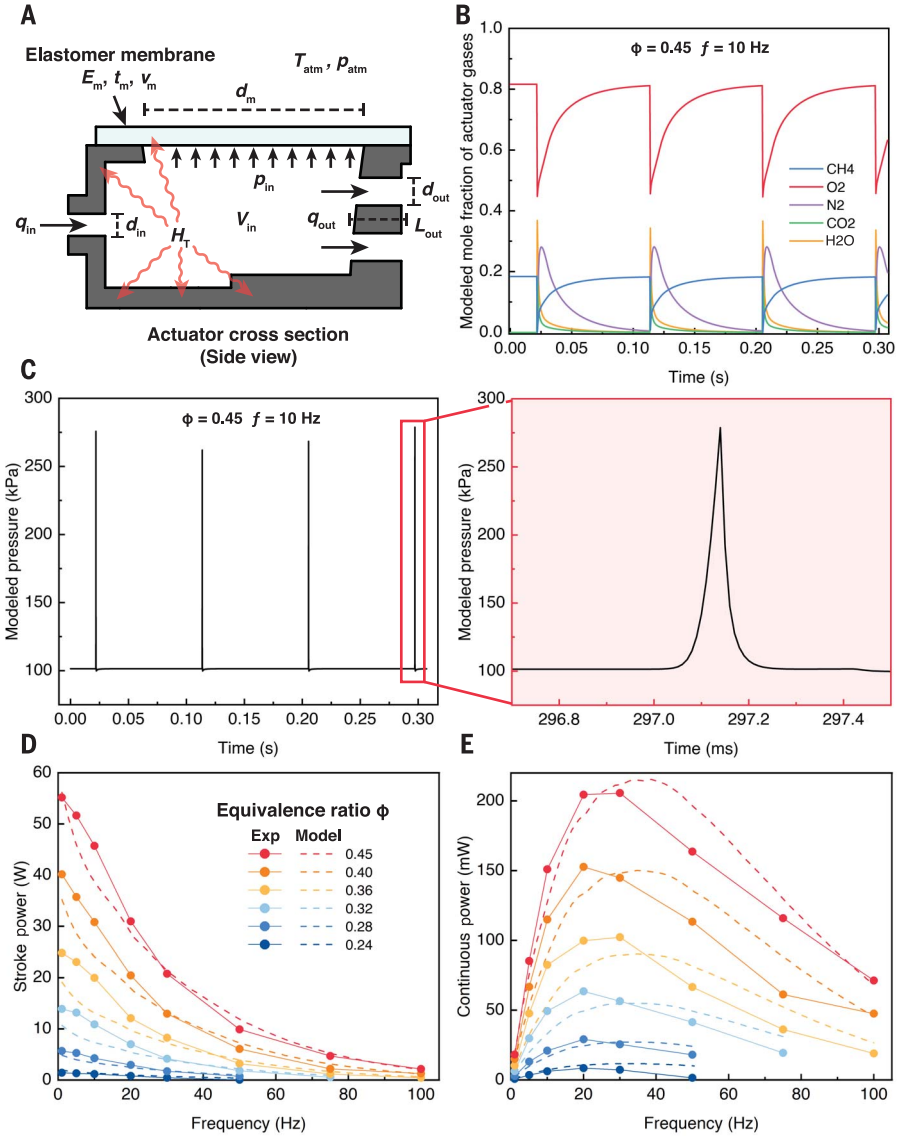

Fig. 2. Model of microactuator performance. (**A**) A schematic diagram of the model actuator used in our analysis. E_m, Young's modulus of the elastomer membrane; t_m, membrane thickness; ν_m, Poisson's ratio of membrane material; d_m, membrane diameter; T_{atm}, atmospheric temperature; p_{atm}, atmospheric pressure; q_{in}, gas flow rate into actuator; q_{out}, flux out of actuator; p_{in}, internal actuator pressure; V_{in}, internal volume of actuator; d_{in} and d_{out}, diameters of the inlet and outlet ports, respectively; L, the length of the exhaust port; H_T, heat-transfer coefficient. (**B**) The change in the concentration of reactant and product gases during actuation at f = 10 Hz as predicted by our model. (**C**) The internal pressure of our actuator during operation, modeled as a function of time. A magnified inset is provided for clarity. (**D**) The experimentally derived stroke-power and (**E**) continuous-power output of our actuator compared with our model predictions. A magnified image of the lowest equivalence ratios in (D) is shown in fig. S12.

SM section M4) at constant Q for different f and ϕ values. Exemplary force profiles can be seen as an inset in Fig. 1F and fig. S5. The peak force that we detected during blocked-force testing, F_{max} = 9.5 N at ϕ = 0.6 (fig. S5), is an order of magnitude greater than that of previously reported high-frequency microactuators (SM section S2). Some of our testing at ϕ = 0.6 resulted in tearing and delamination of the membrane; we consequently denote the actuator's performance at this equivalence ratio as being an upper bound limited by our present system's durability. As shown in Fig. 1F, the actuator can continually produce forces in excess of F = 5 N at a lower equivalence ratio of ϕ = 0.45 without accruing membrane damage. Durability tests and subsequent SEM analysis of the membranes confirmed that the actuator can continuously operate for more than 750,000 cycles (ϕ = 0.30 and f = 25 Hz) without any perceived drop in performance (figs. S6 and S7 and SM section M5).

We calculated the microactuator's work and power output (figs. S8 and S9 and SM section S4) using the equations:

$$W = \frac{1}{2} F_b \delta \tag{3}$$

$$P_{stroke} = \frac{1}{2(t_{inflate})} F_b \delta \tag{4}$$

$$P_{cont} = \frac{1}{2} F_b \delta f \tag{5}$$

where δ, F_b, $t_{inflate}$, and f are the actuator's displacement, blocked force, inflation time, and operating frequency, respectively. We calculated a maximum work output of ~30 mJ when the actuator is driven at ϕ = 0.6 (18.2 mJ at ϕ = 0.45), which corresponds to a peak energy density of 91.4 J kg^{-1}. We further characterized actuator power using two metrics: stroke power, P_{stroke}, calculated only over the time frame during which actuation is occurring; and continuous power, P_{cont}, calculated over the entire operational period. Because of our rapid, submillisecond actuation times, the traditional P_{cont} metric inadvertently includes large amounts of idle time in its calculation (e.g., an actuator operating at f = 10 Hz would spend less than 1% of its operating time actuating). Conversely, the P_{stroke} metric narrows our focus to relevant, but brief, windows of time in the actuation cycle. Used together, both metrics give a more complete picture of actuator performance.

From our experiments, we measured a maximum power of P_{cont} = 288.7 mW (ϕ = 0.6, f = 20 Hz) and P_{stroke} = 90.1 W (ϕ = 0.6; fig. S9). The corresponding power densities are Π_{cont} = 888.3 W kg^{-1} and Π_{stroke} = 277.2 kW kg^{-1}, respectively. The peak theoretical continuous power is $P_{cont\text{-}max}$ = 2.97 W ($\Pi_{cont\text{-}max}$ = 9.1 kW kg^{-1}) (SM section S4). We also estimated the maximum efficiency of our actuator at ~4% (figs. S8 and S9 and SM section S4); the magnitude of this value is a normal consequence of combustion in submilliliter volumes (*32*), but is also affected by our open-venting configuration, the lack of compression in our system, and our fuel-lean equivalence ratios.

Modeling the actuator

To gain insight into the dominant physical phenomena that govern combustion actuation, we derived a simplified system model that takes into account the elasticity of the membrane, the fuel flow within the cell, the energy released by ignition of the fuel, and the effects of the internal pressure and temperature within the microactuator. Using this model, we were able to predict values for the displacement of the actuator membrane, the blocked force of the actuator, the jumping height of the robot, and the exhaust flow rate as functions of the actuation

frequency and fuel equivalence ratio. The model consists of three coupled segments: (i) chamber elasticity and deformation in response to an increase in internal pressure, (ii) fluidic flow balance, and (iii) energy balance of the heat of combustion and its conversion into thermal energy and pressure. The governing equations for these segments are derived and summarized in SM section S5. Relevant code for our models can be found in our online repository (*33*).

Figure 2A shows a schematic diagram of our model microactuator, complete with relevant variables. Using our model, we were able to predict the concentrations of major reactant and product species (Fig. 2B; $\phi = 0.45, f = 10$ Hz) (a magnified image of this data during the combustion window can be seen in fig. S10), as well as the rapidly increasing internal pressure of the actuator (Fig. 2C) when undergoing combustion. The duration of these pressure spikes (t_{model} ~ 0.15 ms versus $t_{reaction}$ ~ 0.12 ms and $t_{inflation}$ ~ 0.33 ms) shows that our modeled data agree with our observed reaction kinetics. Using this pressure data, we were able to predict the blocked force of our actuators and compare it with our experimentally acquired force data (fig. S11). Our model also takes into account the elastic properties of the rapidly deforming membrane and can predict the free displacement of the membrane during combustion (fig. S11). Performing calculations with this modeled data, as described above for our experimental data, allowed us to generate predictions for the work and power output of our modeled actuator (Fig. 2, D and E, and fig. S12). The trends and magnitude of our modeled data accurately approximate our experimental results.

We also characterized the thermal activity of our actuator using a combination of experimental measurements and modeled data to calculate the external and internal wall temperatures, as well as the gas temperatures during combustion (fig. S13, SM section S6). The chamber temperature is an important consideration for device durability; at frequencies exceeding 50 Hz (for all equivalence ratios), the steady-state temperature of the actuator rises to a level that can result in ignition and burning of the chamber. We therefore recommend intermittent operation at these frequencies, allowing several seconds of cooling for every 1 to 2 min of actuation. Notably, the actuators can be operated with impunity at frequencies below 50 Hz (as evidenced by our 8.5-hour, 750,000-cycle durability test), and the frequency limitations of the robot do not put it in danger of thermal damage.

Powering an insect-scale robot

To demonstrate the effectiveness of our microactuators in powering insect-scale devices, we designed and fabricated a combustion-driven quadrupedal robot (Fig. 3A). The assembly

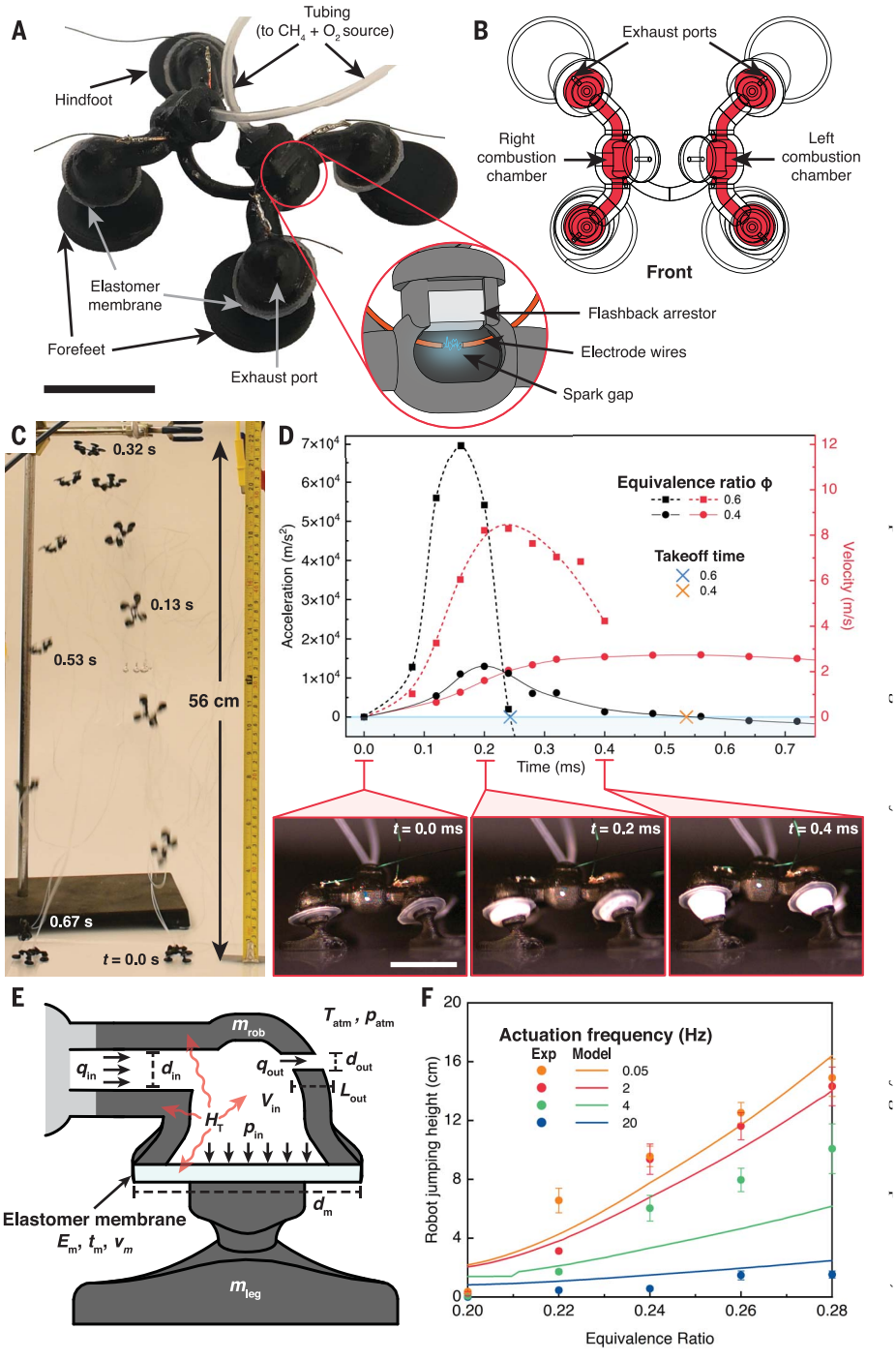

Fig. 3. Jumping performance of the quadrupedal, insect-scale robot. (**A**) Photograph of the robot with component parts labeled. A schematic of the interior of the combustion chamber is also provided. Scale bar, 1 cm. (**B**) A transparent diagram of the robot, with the two independent combustion chambers highlighted in red. (**C**) Time-lapse image of our robot performing a 56-cm vertical leap. (**D**) Acceleration (black) and velocity (red) data of the robot body during takeoff at $\phi = 0.6$ (square data points) and 0.4 (circular data points). The associated images outlined in red depict a takeoff experiment at $\phi = 0.60$. Scale bar, 1 cm. (**E**) A schematic diagram of our idealized model robot leg. The variable definitions are the same as those in Fig. 2A, with the addition of m_{rob}, mass of the robot body, and m_{leg}, mass of the robot leg. (**F**) Modeled robot jumping height as a function of equivalence ratio for a series of actuation frequencies. Experimental data are depicted as solid circles ($n = 5$ robot tests; error bars, 1 SD), whereas a solid line denotes the height predicted by our model.

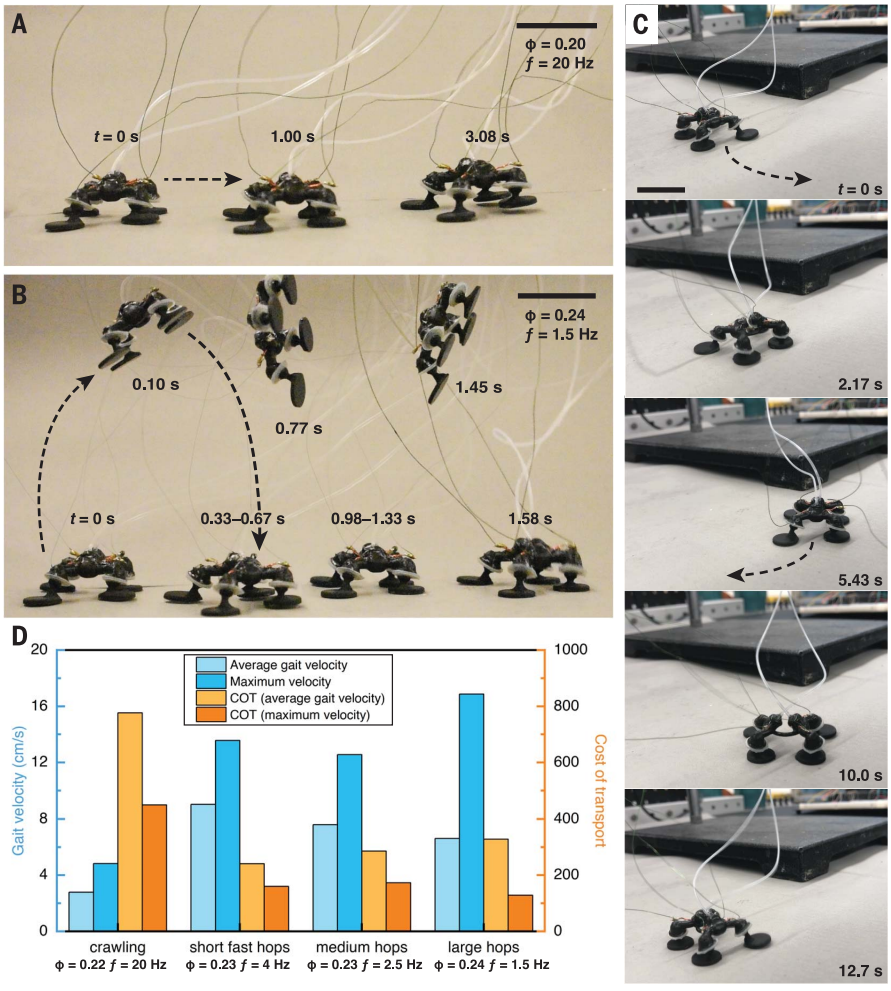

Fig. 4. Characterization of the robot's multigait functionality. (**A**) Timelapse image of the robot performing a crawling gait and (**B**) a hopping gait. In (B), the tethers have been dimmed in all but the rightmost image so as not to obscure the robot's trajectory. (**C**) Timelapse image of the robot performing a counterclockwise rotation, followed by a clockwise rotation. Scale bars [(A), (B), and (C)], 2 cm. (**D**) A graphical representation of the velocities and cost of transport of different gait patterns performed by the robot.

process and bill of materials was similar to that of the individual microactuators and is outlined in SM section M6 and fig. S14. The robot (L = 29 mm, m = 1.6 g) is composed of two symmetric halves connected by a curved, rigid linkage. The hollow interiors of these halves are distinct, functioning as separate combustion chambers that drive one front and one rear foot each (Fig. 3B). A methane and oxygen mixture is delivered through thin tubing into the two ellipsoidal drums at the center of the robot (the same two-MFC testing configuration is used to operate both the robot and the actuators; fig S1). Ignition is achieved by using the same sparking configuration as in the microactuator tests and results in the expansion of the elastomer membranes at either end of the chamber (Fig. 3, C and D). The robot geometry draws on several of the microactuators' design features, displaying similar internal volumes, vent hole configurations, actuation and combustion chamber dimensions, and membrane dimensions (SM section S7). The four actuating feet of the robot are functionally similar to the micro actuators, but they are paired together and fed from a central chamber.

Varying the different input parameters (sparking frequency f, equivalence ratio ϕ, fuel flow rate Q, and combustion chamber selection) creates different locomotion modes. For example, actuating both chambers simultaneously at large equivalence ratios ($\phi > 0.35$) resulted in a large vertical leap (Fig. 3C and movie S2), which allowed the robot to clear obstacles or land on top of elevated terrain (movie S3). While performing jumping experiments, the robot was able to achieve a maximum vertical height of 59 cm (n = 4, SD = 0.96 cm) and a horizontal distance of 16 cm, which are 20 and 5.5 times the robot's body length (BL), respectively (SM section M8). We used a high-speed camera to study the dynamics of the robot at the moment of takeoff (movie S4). Figure 3D shows the acceleration and velocity of the robot's body when driven at two different equivalence ratios. The takeoff time—when the feet begin to leave the ground—corresponds to the moment when the instantaneous acceleration transitions from a positive to a negative value.

We estimated the jumping height of our robot by modifying our blocked-force actuator model (changing the dimensions of relevant parameters) and applying it to our quadruped architecture. Figure 3E shows an idealized schematic diagram of our robot's leg and foot, which we used in modeling the jumping dynamics. Conservation of momentum and conservation of energy were used to derive the maximum jumping height of the robot from its internal pressure at different actuation frequencies and equivalence ratios (SM section S5). The results are shown in Fig. 3F. Deviation of the experimental data from the model can largely be explained by the model's tendency to underestimate blocked-force values at lower equivalence ratios (ϕ = 0.26 to 0.28) (fig. S11B).

When operated at lower equivalence ratios ($\phi < 0.35$) and higher frequencies (1 Hz < f < 30 Hz), the robot is capable of performing several distinct movement patterns, including a crawling, vibration-like gait and forward hopping sequences of different heights (Fig. 4, A and B, and movie S5). The robot can dynamically switch between these movement styles by modifying the fuel equivalence ratio and/or the sparking frequency. We were able to preprogram these movement patterns by hard-coding the sparking sequence.

By inducing combustion in only one of the robot's two chambers at a time, we demonstrated limited directional control. Figure 4C shows counterclockwise and clockwise turns that were generated by repeatedly actuating just the right or left side of the robot, respectively. This behavior is a consequence of the foot orientation, with the front (fore) feet angled inward toward the body's centerline and the rear (hind) feet angled away, resulting in an approximately trapezoidal footprint. Actuating one side of the robot causes the corresponding hindfoot and both forefeet (which jump together owing to their proximity) to leave the ground. The opposite hindfoot remains mostly stationary and serves as the pivot point around which the robot rotates. We were able to demonstrate several rotation-based movements, including a snake-like forward walk, a rapid 360° rotation, and a reversal of direction when the robot encountered an impassable route (movie S6).

We characterized the performance of four representative gaits that manifest through the inputs shown in Fig. 4D. The highest equivalence ratio used in our gait analysis testing was ϕ = 0.24; larger ϕ values were reserved for vertical leaping. When performing a hopping

gait at this ϕ, our robot demonstrated a maximum velocity of 16.9 cm s^{-1}, or 5.8 BL s^{-1}. For this gait, the cost of transport—a standard metric for the energy efficiency of moving bodies [defined as (input power)/(mass × gravity × velocity)]—was 128.8 (SM sections S8 and S9 and table S3). While executing a crawling gait, the robot demonstrated a maximum carrying capacity of 36 g, which is more than 22 time the robot's body weight (movie S7). Additionally, we tested our robot on a variety of surfaces, including acrylic, high-friction sandpaper, rubber, and sand (movie S8 and table S4).

We compared our robot's maximum horizontal velocity during crawling and hopping, along with its vertical leaping capabilities, with that of other robots in the literature (figs. S15 and S16). The robots that we used in these comparisons are summarized in tables S5 and S6. Notably, our robot can both crawl at high speeds and perform large vertical leaps. The crawling robots in our literature comparison lack the capacity to leap in any meaningful way. Similarly, most of the jumping robots shown in our comparison do not possess alternative locomotion capabilities. Our robot's multigait functionality is a direct result of the high-force and high-frequency capabilities of the embedded actuators.

Our actuators possess several advantages over existing systems that are used to power insect-scale devices: (i) the use of 3D printing as the dominant fabrication strategy allows for ease of scalability and integration with other systems; (ii) a soft actuation surface allows for device durability and a nondestructive means of interfacing with the environment; and (iii) the combination of high actuation speeds, forces, displacements, and frequencies leads to high power densities. When incorporated into a quadrupedal robot, the actuators enable multimodal locomotion and obstacle avoidance.

REFERENCES AND NOTES

1. B. Goldberg *et al*., *IEEE Robot. Autom. Lett.* **3**, 987–993 (2018).
2. X. Ji *et al*., *Sci. Robot.* **4**, eaaz6451 (2019).
3. X. Yang, L. Chang, N. O. Pérez-Arancibia, *Sci. Robot.* **5**, eaba0015 (2020).
4. R. Kurniawan *et al*., "An Untethered 216-mg Insect-Sized Jumping Robot with Wireless Power Transmission" in *2020 IEEE/RSJ International Conference on Intelligent Robots and Systems (IROS)*, Las Vegas, NV, 24 October 2020 to 24 January 2021, pp. 7881–7886; https://doi.org/10.1109/IROS45743.2020.9341238.
5. M. Noh, S.-W. Kim, S. An, J.-S. Koh, K.-J. Cho, *IEEE Trans. Robot.* **28**, 1007–1018 (2012).
6. J.-S. Koh *et al*., *Science* **349**, 517–521 (2015).
7. M. Kovac, M. Fuchs, A. Guignard, J.-C. Zufferey, D. Floreano, "A miniature 7g jumping robot," *2008 IEEE International Conference on Robotics and Automation*, Pasadena, CA, 19 to 23 May 2008, pp. 373–378; https://doi.org/10.1109/ROBOT.2008.4543236.
8. N. T. Jafferis, E. F. Helbling, M. Karpelson, R. J. Wood, *Nature* **570**, 491–495 (2019).
9. Z. Ren *et al*., *Adv. Mater.* **34**, e2106757 (2022).
10. M. Dorigo, G. Theraulaz, V. Trianni, *Sci. Robot.* **5**, eabe4385 (2020).
11. A. Ghosh, B. Corves, *Introduction to Micromechanisms and Microactuators* (Springer, 2015), vol. 28 of *Mechanisms and Machine Science*.
12. W. S. N. Trimmer, *Sens. Actuators* **19**, 267–287 (1989).
13. R. J. Wood, S. Avadhanula, R. Sahai, E. Steltz, R. S. Fearing, *J. Mech. Des.* **130**, 052304 (2008).
14. Y. Chen *et al*., *Nature* **575**, 324–329 (2019).
15. D. J. Bell, T. J. Lu, N. A. Fleck, S. M. Spearing, *J. Micromech. Microeng.* **15**, S153–S164 (2005).
16. Z. Ma, D. Sameoto, *Micromachines* **13**, 1881 (2022).
17. N. T. Jafferis, K. Jayaram, P. A. York, R. J. Wood, *Sens. Actuators A Phys.* **332**, 113155 (2021).
18. M. Karpelson, G.-Y. Wei, R. J. Wood, "A review of actuation and power electronics options for flapping-wing robotic insects," *2008 IEEE International Conference on Robotics and Automation*, Pasadena, CA, 19 to 23 May 2008, pp. 779–786; https://doi.org/10.1109/ROBOT.2008.4543300.
19. I. Morkvenaite-Vilkonciene *et al*., *Micromachines* **13**, 1256 (2022).
20. X. Yue *et al*., *Adv. Mater.* **33**, e2101760 (2021).
21. A. C. Fernandez-Pello, *Proc. Combust. Inst.* **29**, 883–899 (2002).
22. H. Wang, Y. Yang, G. Lin, P. Jiao, Z. He, *Smart Mater. Struct.* **30**, 015035 (2021).
23. M. T. Tolley *et al*., "An untethered jumping soft robot," *2014 IEEE/RSJ International Conference on Intelligent Robots and Systems*, Chicago, IL, 14 to 18 September 2014 (IEEE), pp. 561–566; https://doi.org/10.1109/IROS.2014.6942615.
24. R. F. Shepherd *et al*., *Angew. Chem. Int. Ed.* **52**, 2892–2896 (2013).
25. C. Stergiopulos *et al*., "A Soft Combustion-Driven Pump for Soft Robots," *Proceedings of theASME 2014 Conference on Smart Materials, Adaptive Structures and Intelligent Systems, vol. 2*, Newport, RI, 8 to 10 September 2014 (American Society of Mechanical Engineers), p. V002T04A011; https://doi.org/10.1115/SMASIS2014-7536.
26. M. Loepfe, C. M. Schumacher, W. J. Stark, *Ind. Eng. Chem. Res.* **53**, 12519–12526 (2014).
27. R. H. Heisser *et al*., *Proc. Natl. Acad. Sci. U.S.A.* **118**, e2106553118 (2021).
28. W. A. Churaman, L. J. Currano, C. J. Morris, J. E. Rajkowski, S. Bergbreiter, *J. Microelectromech. Syst.* **21**, 198–205 (2012).
29. Y. Chen *et al*., *Sci. Robot.* **2**, eaao5619 (2017).
30. M. Wehner *et al*., *Nature* **536**, 451–455 (2016).
31. S. R. Turns, *Introduction to combustion* (McGraw-Hill Companies, 1996), vol. 287.
32. W. Wang, Z. Zuo, J. Liu, *Energy Convers. Manage.* **112**, 101–114 (2016).
33. caa243, caa243/Combustion-driven-microactuators: Main release, version 1.0, Zenodo (2023); https://doi.org/10.5281/zenodo.7888443.

ACKNOWLEDGMENTS

We thank M. Ulinski for his assistance in assembling experimental apparatuses and D. Woodie for coordinating safety efforts. **Funding:** Air Force Office of Scientific Research contract FA9550-20-1-0254 (R.F.S.); National Science Foundation contract EFMA-1830924 (R.F.S.); Office of Naval Research contract N00014-22-1-2595 (R.F.S.). **Author contributions:** Conceptualization: C.A.A. and R.F.S.; Methodology: C.A.A., R.H.H., O.P., and A.G.; Investigation: C.A.A., R.H.H., O.P., J.T., and J.L.; Visualization: C.A.A., R.H.H., O.P., J.T., and J.L.; Funding acquisition: A.D.G. and R.F.S.; Project administration: E.F.H., S.S., A.D.G., and R.F.S.; Supervision: E.F.H., S.S., A.D.G., and R.F.S.; Writing – original draft: C.A.A. and R.F.S.; Writing – review and editing: C.A.A., R.H., O.P., E.F.H., S.S., A.D.G., and R.F.S. **Competing interests:** The authors declare that they have no competing interests. **Data and materials availability:** All data are available in the main text or the supplementary materials. Code used in modeling our actuators, for controlling our experimental setup, and for controlling our high voltage electronics can be found online (*33*). **Licensing information:** Copyright © 2023 the authors, some rights reserved; exclusive licensee American Association for the Advancement of Science. No claim to original US government works. https://www.science.org/about/science-licenses-journal-article-reuse

SUPPLEMENTARY MATERIALS

science.org/doi/10.1126/science.adg5067
Materials and Methods
Supplementary Text
Figs. S1 to S17
Tables S1 to S6
References (*34*–*103*)
Movies S1 to S8

Submitted 1 January 2023; accepted 4 August 2023
10.1126/science.adg5067

RESEARCH ARTICLE SUMMARY

SIGNALING COMPLEXES

Architecture of the MKK6-p38α complex defines the basis of MAPK specificity and activation

Pauline Juyoux, Ioannis Galdadas†, Dorothea Gobbo†, Jill von Velsen, Martin Pelosse, Mark Tully, Oscar Vadas, Francesco Luigi Gervasio*, Erika Pellegrini*, Matthew W. Bowler*

INTRODUCTION: Mitogen-activated protein kinases (MAPKs) are important signaling proteins found in eukaryotes. They respond to external signals and regulate various cellular processes. One such MAPK is p38α, which plays a crucial role in cell stress, inflammation, and response to infection, including the cytokine storm associated with severe COVID-19 and influenza. Dysregulation of p38α signaling is linked to several diseases, making p38α an important drug target. Understanding the interactions between p38α and its upstream activating MAP2K, MKK6, is essential to devise drug development strategies targeting allosteric sites. The MAP2Ks have a kinase interaction motif (KIM, or D motif) at the beginning of their intrinsically disordered N termini, which interacts with an allosteric docking site on their target MAPK, ensuring some level of specificity. Once engaged, the MAP2K phosphorylates a TxY motif (where T is threonine, Y is tyrosine, and x is any residue) on the MAPK activation loop (A loop), allowing it to adopt an active conformation. Whereas the individual kinases and their interactions through KIM motifs have been extensively studied, the overall interactions between components of the MAP kinase cascades are not yet fully understood. In particular, how specificity is maintained between different MAPK pathways and how MAP2Ks can phosphorylate both tyrosine and threonine residues—which is highly unusual in protein kinases—is unknown.

RATIONALE: The interaction between the kinases needs to be transient in order to maintain signal transmission. However, this fast interaction time hinders structural studies. We used a multidisciplinary approach—including cryo–electron microscopy (cryo-EM), small-angle x-ray scattering (SAXS), enhanced sampling molecular dynamics (MD) simulations, Bayesian modeling, hydrogen-deuterium exchange mass spectrometry, and cellular assays—to characterize the complex between p38α (MAPK14) and its activating MAP2K, MKK6 (MAP2K6).

RESULTS: The study provides a detailed molecular model of the dynamic MKK6-p38α complex, shedding light on specificity and multistep catalysis within the MAP kinase pathway. The cryo-EM structure shows that the kinases adopt a face-to-face conformation, with all con between the kinases distal to the MKK6 a site. The structure reveals two major contacts occurring during complex formation: The MKK6 KIM binds at the expected p38α common docking site, and the MKK6 αG helix engages the p38α C lobe at the so-called lipid-binding site that is specific to MAPKs and has been implicated in regulation of the pathway. MD simulations reveal that the observed conformation facilitates the approach of the A loop of p38α to the active site of MKK6 without compromising the dual specificity of MKK6. The simulations show that both the A-loop threonine and tyrosine can access the active site without specific recognition or binding of the A loop. Adaptive-sampling MD simulations combined with solution SAXS data in a Bayesian/maximum-entropy approach were then used to reconstruct the heterogeneous conformational ensemble and understand how the two kinases assemble and initiate phosphorylation. The populations of the main states captured in this ensemble, as well as the reaction paths connecting them, show the importance of the N terminus of MKK6 and the C lobes of the two kinases in correctly positioning them for phosphorylation. Cellular assays performed with variants of MKK6 N termini revealed that the length and structure of the N-terminal linker are important in determining specificity between MAP2K and MAPK pairs.

CONCLUSION: Resolving the architecture of a MAP2K activating its target MAPK has identified the interaction sites between the two kinases and allowed us to model the mechanism of activation and discover components that are important in specificity. The N termini of MAP2Ks guide the engagement of specific kinases by being tuned to the correct distance for MAP2K/MAPK pairs. Once bound, rather than acting like a classical enzyme and positioning substrates precisely for catalysis, MKK6 creates a zone of proximity enabling either the tyrosine or threonine to approach the active site, regardless of their state, allowing dual specificity. Through a comprehensive multidisciplinary approach, the study elucidated the architecture and dynamics of the formation of the MKK6-p38α complex. The findings pave the way for targeted drug development and enhance our understanding of essential steps in kinase signaling cascades. ■

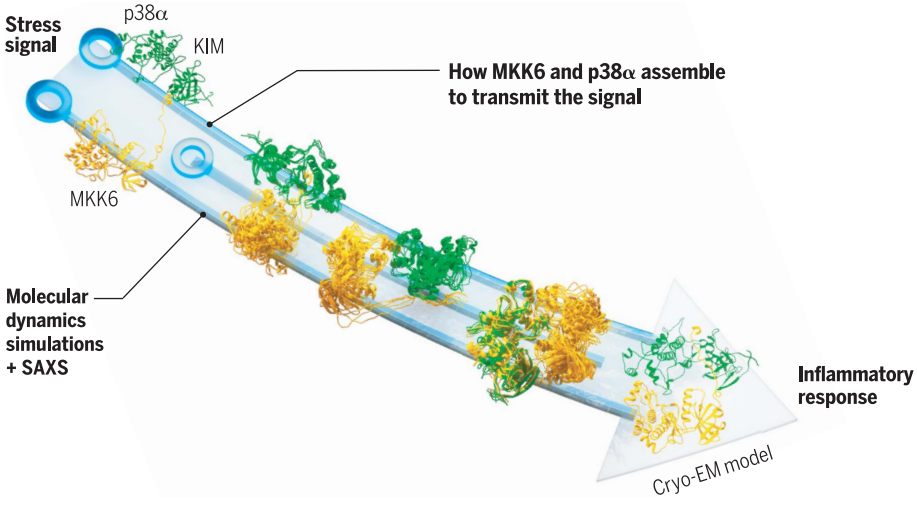

Structure and dynamics of MAP kinase activation. The MAP2K MKK6 binds its substrate MAPK p38α through a KIM motif and then samples many conformations before engaging at the C-terminal lobes (right). Once bound in the catalytically active conformation, the activation loop of p38α approaches the active site of MKK6, leading to phosphorylation and activation of the MAPK.

The list of author affiliations is available in the full article.
*Corresponding author. Email: francesco.gervasio@unige.ch (F.L.G.); epellegr@embl.fr (E.P.); mbowler@embl.fr (M.W.B.)
†These authors contributed equally to this work.

READ THE FULL ARTICLE AT
https://doi.org/10.1126/science.add7859

SIGNALING COMPLEXES

Architecture of the MKK6-p38α complex defines the basis of MAPK specificity and activation

Pauline Juyoux[1]†, Ioannis Galdadas[2,3]‡, Dorothea Gobbo[2,3]‡, Jill von Velsen[1], Martin Pelosse[1], Mark Tully[4], Oscar Vadas[5], Francesco Luigi Gervasio[2,3,6,7,8]*, Erika Pellegrini[1]*, Matthew W. Bowler[1]*

The mitogen-activated protein kinase (MAPK) p38α is a central component of signaling in inflammation and the immune response and is, therefore, an important drug target. Little is known about the molecular mechanism of its activation by double phosphorylation from MAPK kinases (MAP2Ks), because of the challenge of trapping a transient and dynamic heterokinase complex. We applied a multidisciplinary approach to generate a structural model of p38α in complex with its MAP2K, MKK6, and to understand the activation mechanism. Integrating cryo–electron microscopy with molecular dynamics simulations, hydrogen-deuterium exchange mass spectrometry, and experiments in cells, we demonstrate a dynamic, multistep phosphorylation mechanism, identify catalytically relevant interactions, and show that MAP2K-disordered amino termini determine pathway specificity. Our work captures a fundamental step of cell signaling: a kinase phosphorylating its downstream target kinase.

Mitogen-activated protein kinases (MAPKs) are conserved in all eukaryotes, where they form signaling cascades responding to extracellular stimuli and leading to diverse responses from differentiation to apoptosis. In higher organisms, the MAPK p38α acts in response to stresses such as irradiation, hypoxia, and osmotic shock, and also to signaling from inflammatory cytokines (*1*). Pathogens, including severe acute respiratory syndrome coronavirus 2 (SARS-CoV-2), often elicit up-regulation of p38α, which can lead to the cytokine storm associated with severe COVID-19 (*2*, *3*). Signals propagate through phosphorylation of successive protein kinases (MAP4K, MAP3K to MAP2K), which eventually phosphorylate and activate a MAPK through double phosphorylation at the TxY motif in the activation loop (A loop), leading to a conformational change (*4*, *5*). When the A loop is phosphorylated, key residues surrounding the adenosine triphosphate (ATP) and Mg^{2+} ions reorient, stabilizing the activated MAPK. The activated MAPK is then transported to the nucleus, where it modulates gene expression (*6*–*8*).

The key role of p38α in inflammation and the implication that aberrant p38α signaling is involved in numerous diseases, such as arthritis and cancer, but also in the response to infection, make it a highly studied drug target (*1*). Despite initial successes in developing potent compounds that target the kinase nucleotide-binding pocket, many potential therapies have failed in clinical trials because of off-target effects (*9*). Therefore, a molecular understanding of p38α's interaction with upstream activators is essential to develop strategies to target allosteric sites, either in p38α or its activators. The structures of individual MAPKs (*10*–*12*) and MAP2Ks (*13*–*16*) have been extensively studied, and subsequent work has defined the interacting regions between these partners (*17*–*20*). The MAP2Ks contain a kinase interaction motif (KIM, or D motif) at the start of their intrinsically disordered N termini, which interacts with an allosteric common docking (CD) site on their target MAPK. The KIM partially ensures specificity between members of the pathway (*17*); acts allosterically to expose the A loop, preparing the MAPK for activation (*21*, *22*); and enhances the local concentration of kinase and substrate (*23*). However, there is little structural data on the global interactions between MAPK-cascade components. Beyond the KIM interaction, molecular details of selectivity and activation of a MAPK by its upstream MAP2K remain unknown. Moreover, our knowledge of kinase-kinase interactions, in general, is restricted to homodimers and inactive conformations (*24*–*29*).

To further our understanding of how signals are transmitted through the MAPK pathway, we applied a multidisciplinary approach—combining cryo–electron microscopy (cryo-EM) with hydrogen-deuterium exchange mass spectrometry (HDX-MS), small angle x-ray scattering (SAXS), enhanced sampling molecular dynamics (MD) simulations, and cellular assays—to characterize a complex between the MAP kinase p38α (MAPK14) and its activating MAP2K, MKK6 (MAP2K6). We present a detailed molecular model of this highly dynamic and transient interaction between signaling components, providing insights into specificity and multistep catalysis. Our findings open routes to drug development for the MAPK signaling pathway and lead to a better understanding of a crucial step in kinase signaling cascades.

[1]European Molecular Biology Laboratory (EMBL), Grenoble, France. [2]Institute of Pharmaceutical Sciences of Western Switzerland, University of Geneva, Geneva, Switzerland. [3]School of Pharmaceutical Sciences, University of Geneva, Geneva, Switzerland. [4]European Synchrotron Radiation Facility, Grenoble, France. [5]Protein and peptide purification platform, Faculty of Medicine, University of Geneva, Geneva, Switzerland. [6]Department of Chemistry, University College London, London, UK. [7]Institute of Structural and Molecular Biology, University College London, London, UK. [8]Swiss Institute of Bioinformatics, Geneva, Switzerland.
*Corresponding author. Email: francesco.gervasio@unige.ch (F.L.G.); epellegr@embl.fr (E.P.); mbowler@embl.fr (M.W.B.)
†Present address: Université Grenoble Alpes, CNRS, Commissariat à l'Energie Atomique et aux Energies Alternatives, Institute of Structural Biology, Grenoble F-38000, France.
‡These authors contributed equally to this work.

Engineering an active and stable MKK6-p38α complex for structural studies

The MAP kinases are malleable proteins that must adapt to multiple upstream and downstream effectors, as well as phosphorylate a large range of substrates. The proteins therefore adopt multiple conformations, and interactions with effectors and substrates must be transient to maintain signal transmission. To stabilize the MKK6-p38α complex for structural studies, we created a chimera of MKK6, named $MKK6^{DD}$GRA, in which we replaced the native KIM with that from the *Toxoplasma gondii* effector protein GRA24 (*30*), which has a 100-fold higher affinity for p38α but induces the same conformation on p38α as the MKK6 KIM (fig. S1A) (*31*). We also inserted phosphomimetic mutations in the MKK6 A loop (S207D and T211D) to transform the kinase into a constitutively active form that is ready to phosphorylate p38α (Fig. 1A and fig. S1, B and C). SAXS analysis revealed heterogeneity in the size of the complex formed with p38α (fig. S2A). By screening $MKK6^{DD}$GRA with a combination of different nucleotide analogs and p38α A-loop mutants, we identified the mutant $p38\alpha^{T180V}$ (one of the phosphosites of the A loop) in combination with the transition-state analog $ADP.AlF_4^-$ as the complex with the smallest radius of gyration (Rg) (table S1). Because a smaller Rg for a given sample indicates a more compact structure, we reasoned that in this sample, the transition-state analog complex is stably assembled with the single residue available in the A loop (Y182) and should be suitable for structural studies. Subsequent analysis, including HDX-MS, MD, and Bayesian modeling, confirmed that the engineering increases the population of the transphosphorylation-competent state of the complex and that its nature is consistent with that of the wild type (WT).

Architecture of the MKK6-p38α complex

We imaged the 80-kDa $MKK6^{DD}$GRA-$p38\alpha^{T180V}$ complex with cryo-EM (Fig. 1). The purified complex was well dispersed and yielded two-dimensional (2D) class averages that showed clear secondary-structure features (Fig. 1B). The selected particles allowed the 3D reconstruction to a nominal resolution of 4 Å (map range 2.7 to 6.5 Å) (Fig. 1C, fig. S3, and movie S1). The final resolution was limited not only by the small size of the complex but also by the highly dynamic nature of the interaction between the kinases, leading to particle heterogeneity. Therefore, very strict selection of

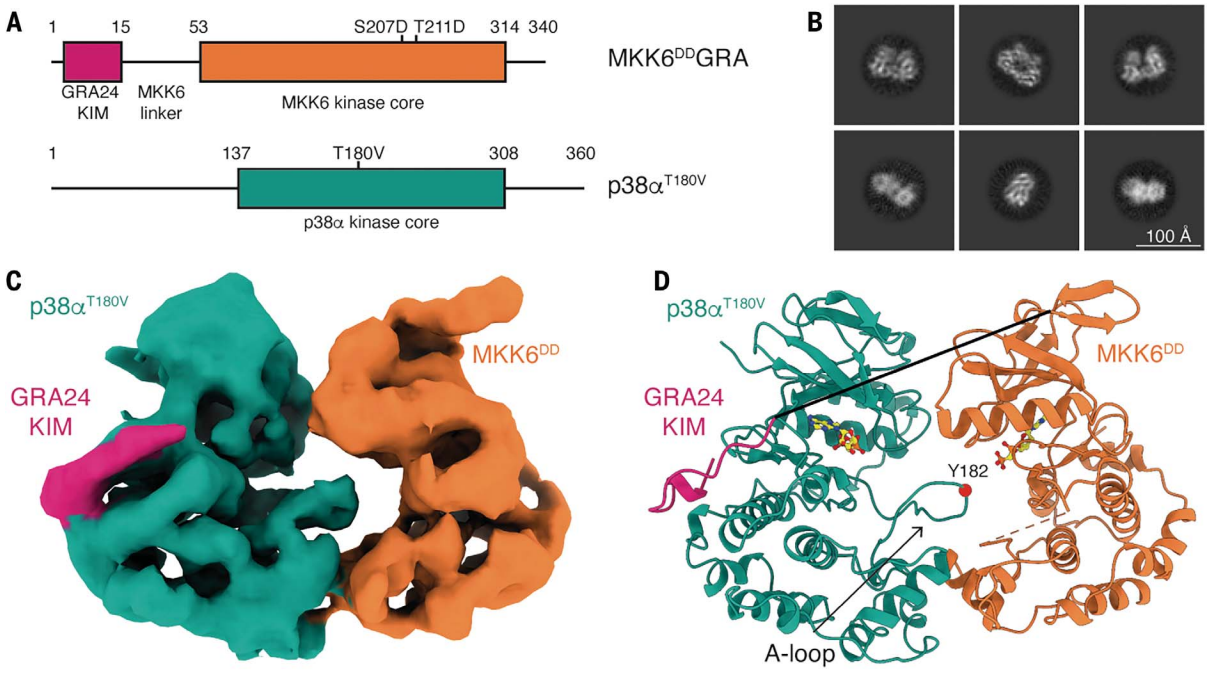

Fig. 1. Structure of the MKK6^{DD}GRA-p38α^{T180V} complex. (**A**) Schematic of the two protein constructs. Key domains and mutations are indicated. Single-letter abbreviations for the amino acid residues are as follows: A, Ala; C, Cys; D, Asp; E, Glu; F, Phe; G, Gly; H, His; I, Ile; K, Lys; L, Leu; M, Met; N, Asn; P, Pro; Q, Gln; R, Arg; S, Ser; T, Thr; V, Val; W, Trp; and Y, Tyr. In the mutants, other amino acids were substituted at certain locations; for example, S207D indicates that serine at position 207 was replaced with aspartic acid. (**B**) Representative 2D class averages from single-particle cryo-EM analysis of the MKK6^{DD}GRA-p38α^{T180V} complex. Scale bar, 100 Å. (**C**) Segmented single-particle reconstruction cryo-EM map of the MKK6^{DD}GRA-p38α^{T180V} complex, resolved to 4-Å resolution and colored according to (A). (**D**) Model of the MKK6^{DD}GRA-p38α^{T180V} complex, showing the overall structure of the complex. MKK6^{DD}GRA-p38α^{T180V} is represented as a cartoon and colored according to (A). AMP-CP nucleotides are represented as balls and sticks (carbon atoms are yellow). The MKK6 linker and A loop are disordered and respectively shown as a full black line and an orange dashed line. The position of the Y182 residue in the p38α A loop is indicated by a red sphere.

particles was necessary to capture this conformation. Multiple rounds of picking—with a combination of Topaz (*32*), template picking, and 2D classification to eliminate the noisy 2D class averages—led to a good-quality set of particles that could then be further selected to remove particles clearly showing only a single kinase or two loosely connected kinases (these classes were always low resolution). Classification in 3D was then used to select particles corresponding to the heterokinase complex, and further 2D classification was then used to select class averages showing strong features and low background. Subsequent rounds of heterogeneous refinement and quality assessment with 2D classification were then used to differentiate between face-to-face conformations where the A loop was stabilized or disordered.

To build the model of the complex, we docked structures of p38α and MKK6 into the map. Because all available structures of inactive p38α have an unstructured or mobile A loop, we determined the crystal structures of human p38α and of an inactive mutant (p38α^{K53R}), in which the A loops are well ordered in the occluded conformation in order to have a starting point for refinement of the extended conformation (table S2). The available MKK6 structures are not in the active conformation (fig. S4). We therefore modeled the structure from the active conformation of MKK7 (*16*). Docking of these structures was followed by one round of morphing and real-space refinement. To select the model that best recapitulates the available data, we then computed the cross-correlation between experimental and predicted maps for relevant structures obtained from the ensemble that we derived by combining Bayesian inference with MD simulations and SAXS data (Fig. 1D, fig. S3C, and tables S3 and S4). The reconstruction shows the kinases adopting a face-to-face conformation, with most contact between the C lobes. MKK6 is in the active kinase conformation according to its αC-helix rotated position and in the DFG-in BLAminus conformation according to kinase nomenclature (*33*) (fig. S4), and density can be observed for nucleotide in its active site (fig. S5). The p38α A loop is ordered and extends toward the MKK6 active site; however, it remains dynamic, limiting the resolution of this region (fig. S5). The p38α active site also binds nucleotide (fig. S5), implying that it is already in an active conformation. MKK6 interacts with the p38α CD site through the GRA24 KIM at the start of its N-terminal extension, which can be traced in the density (Fig. 1C and fig. S5). Most of the linker between the KIM and the MKK6 kinase core, as well as the MKK6 A loop, remains disordered and, therefore, unresolved. AlphaFold2 multimer (*34*) predicts a similar face-to-face conformation for the MKK6-p38α^{WT} complex, as well as for MKK6^{DD}-p38α^{WT} and MKK6^{DD}GRA-p38α^{T180V} (fig. S6). Superimposing the predicted models to our experimental model shows a high consensus of the interaction. However, relative domain rotation in the prediction leads to differences in the interface of the two kinases (fig. S6A). High confidence in intermolecular contact placement seen in the predicted aligned error (PAE) plots (fig. S6, D to F) supports the overall face-to-face conformation of the complex.

The main kinase core–fold interaction is between the αG helix (residues 262 to 273) of MKK6 and a hydrophobic pocket in p38α, partly formed by the MAPK-specific insert in the C lobe (Fig. 2, A, C, and D, and movie S2), which clamps the MKK6 αG helix upon binding (movie S3). This insert has been described as a lipid-binding site important in regulation (*35*, *36*), and several studies have identified small molecules that target this pocket (*37*–*41*) (fig. S7). This site has also been shown to be important in MAPK substrate binding (*42*, *43*) (fig. S7). The exposed residues of this helix, as

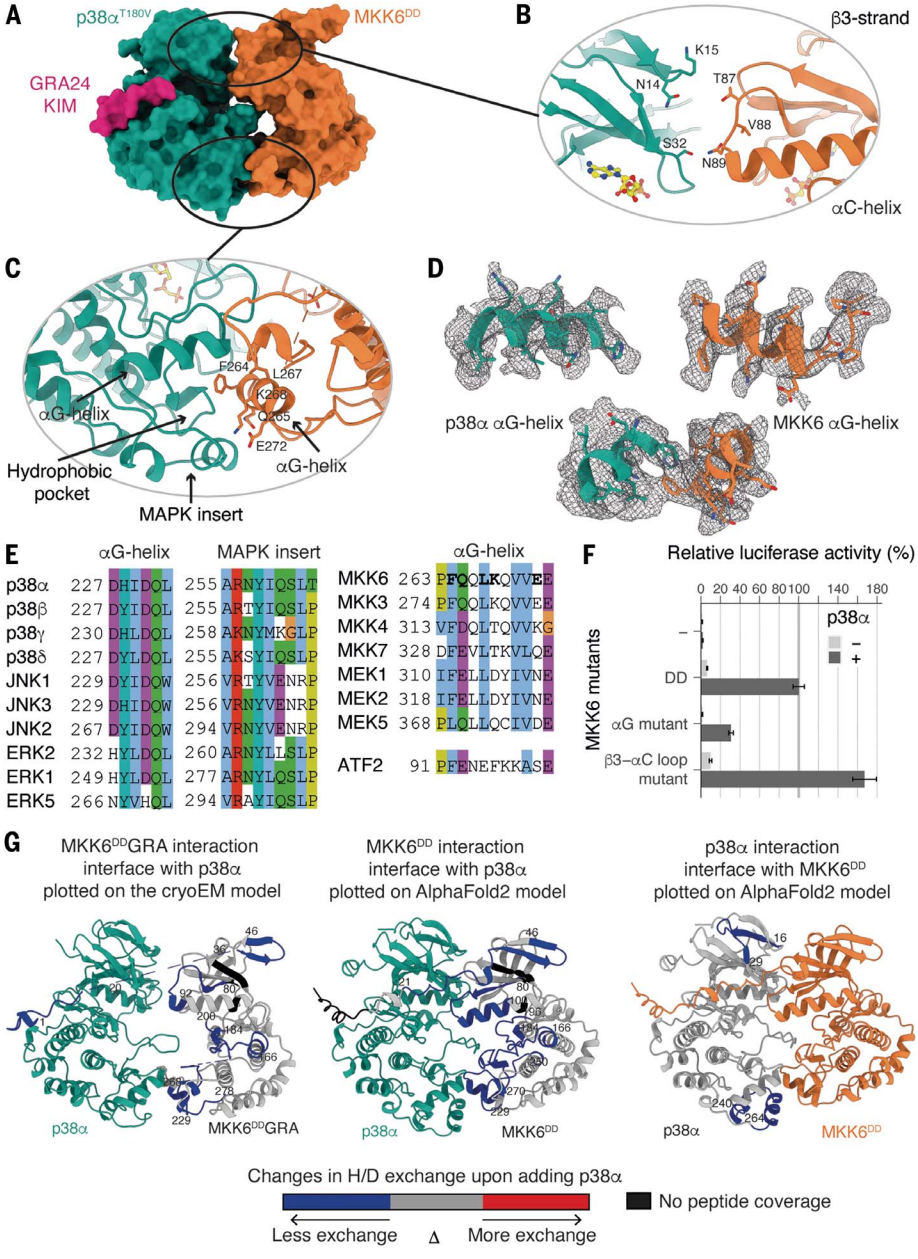

Fig. 2. Interaction interfaces between MKK6 and p38α, distal from the active site. (**A**) Surface representation of the MKK6^{DD}GRA-p38α^{T180V} complex. (**B**) Potential interaction between the N lobes. (**C**) Interaction between the αG helix of MKK6 and the hydrophobic pocket of p38α. (**D**) αG helices of p38α and MKK6 in the sharpened Coulomb potential map (black mesh). (**E**) Sequence alignment of MAPK hydrophobic pockets, MAP2K αG helices, and the p38α substrate ATF2 peptide (Clustal coloring scheme). (**F**) Luciferase reporter assay to monitor the activity of the p38α signaling pathway in HEK293T cells, showing the ability of MKK6^{DD} mutants to activate p38α (statistical analysis in table S6 and protein expression levels in fig. S10). (**G**) (Left) MKK6^{DD}GRA and (middle) MKK6^{DD} interaction sites with p38α and (right) p38α interaction sites with MKK6^{DD}, identified with HDX-MS. Regions showing protection upon the addition of p38α or MKK6^{DD}, indicative of interaction, are highlighted in blue.

well as residues lining the MAPK hydrophobic pocket, are highly conserved in the MAP2Ks and MAPKs, respectively, suggesting a common interaction site for the pathways (Fig. 2E). Additionally, there is a potential interaction between the N lobes through the loop between the β3 sheet and αC helix of MKK6 (residues 87 to 89) and β strands 1, 2, and 3 of the N lobe of p38α (Fig. 2B). We validated the observed interactions using HDX-MS (*44*). In both the MKK6^{DD} (with the wild-type KIM) and chimera MKK6^{DD}GRA, several regions were protected from hydrogen-deuterium exchange in the presence of an excess of p38α: the N terminus, the β3 strand, the A loop, and the αG helix (Fig. 2G, fig. S8, and table S5). The interaction sites identified in solution highly correlate with the cryo-EM model for both the wild-type and chimeric complexes. Although no peptide was detected for MKK6 KIM, the GRA24 KIM was strongly protected upon binding with p38α. In an excess of MKK6^{DD}, only the p38α MAPK insert and a small region of the N lobe are protected from exchange (Fig. 2G and fig. S8). We also evaluated the protection on p38α when we mutated the MKK6 αG-helix residues facing the p38α hydrophobic pocket to alanine (F264A, Q265A, L267A, K268A, and E272A—referred to as the MKK6^{DD} αG-helix mutant). Whereas its interaction with MKK6^{DD} is stable, the p38α MAPK insert is not protected in the presence of the MKK6^{DD} αG-helix mutant, which implies that this mutant cannot interact with p38α in that region (fig. S9). Free-energy calculations of p38α-MKK6 and p38α-MKK6 αG-helix mutant further support the lower stability of the C-lobe interface in the latter (supplementary text and fig. S9). These experiments define the αG-helix–MAPK-insert interaction as the primary site of interaction between the two kinases during phosphorylation of the p38α A loop.

To further study the importance of these interactions on p38α activation, we used the MKK6^{DD} αG-helix mutant and also mutated the β3-αC loop of the MKK6 N-terminal interaction to alanine residues (T87A, V88A, and N89A, referred to as the MKK6^{DD} β3-αC loop mutant) and read out the effect on p38α signaling in cells using a luciferase reporter assay (Fig. 2F). We transiently transfected human embryonic kidney (HEK)293T cells with p38α and MKK6^{DD} mutants, together with a plasmid encoding firefly luciferase under the control of the activator protein 1 (AP-1) promoter, in which AP-1 activity is stimulated by p38α through several substrates [e.g., activating transcription factor 2 (ATF2); materials and methods]. The MKK6^{DD} αG-helix mutant reduced p38α signaling by 70% when compared with MKK6^{DD}, demonstrating the substantial role that this interaction plays in p38α activation. The MKK6^{DD} β3-αC loop mutant increased signaling to ~170% over MKK6^{DD}. This loop is the site of numerous activating mutations, particularly in cancer, that stabilize the "αC-in" conformation (*45*, *46*). This could explain the observed increase in signaling but does not rule out a role for the p38α N lobe in the stabilization of the active conformation of MKK6 in the face-to-face complex.

Molecular dynamics confirm that the complex is metastable and show how catalytically competent states can be formed

To better understand the details of the heterogeneous structural ensemble of the complex

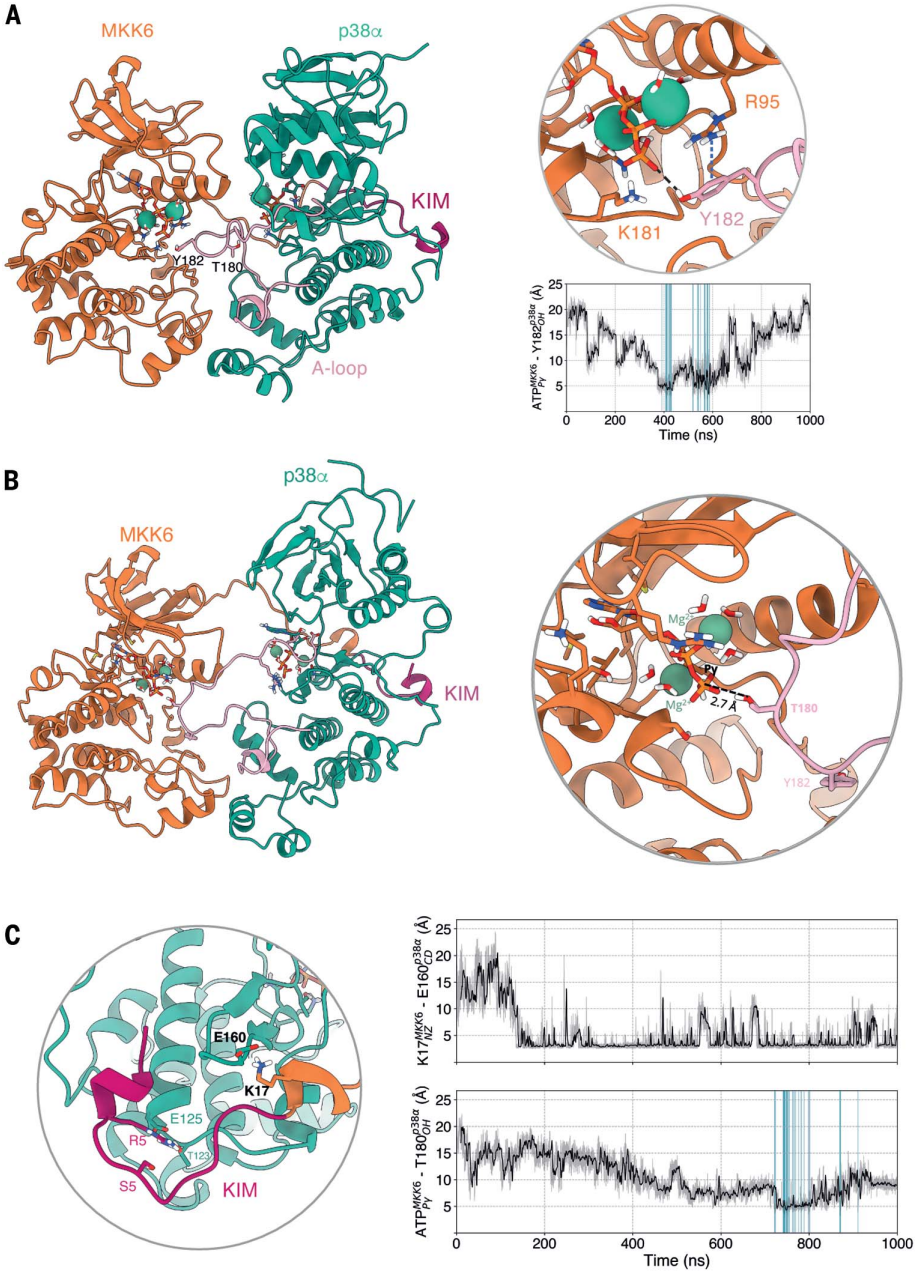

Fig. 3. MD simulations show that both p38α Y182 and T180 can approach MKK6 ATP and that a rotated conformation of p38α favors T180 phosphorylation. (**A**) Frame extracted from one of the unrestrained MD simulations in which Y182 approaches the γ-phosphate of MKK6 ATP at a catalytically compatible distance (3.8 Å). The π-cation interaction of R95 with Y182 that further stabilizes Y182 close to ATP is shown in a blue dashed line. The frames where p38α Y182 reaches MKK6 ATP at a catalytically compatible distance in this set of simulations are highlighted in the plot of distances over time (blue). (**B**) Simulation frame in which p38α has rotated around its axis with respect to the cryo-EM structure. (**C**) Detailed view around the KIM. The frames where T180 reaches MKK6 ATP at a catalytically compatible distance in this set of simulations are highlighted in the plot of distances over time (blue).

and the mechanism of transphosphorylation of p38α on T180 and Y182 by MKK6, we ran a series of MD simulations, starting with a set of 18 simulations, each 1 μs long (table S7). The simulations started from models derived from the cryo-EM structure: MKK6GRA-p38α (with wild-type A loop) and MKK6-p38α, in which we reverted the GRA24 KIM back to the wild-type sequence.

The simulations explored several conformations. In most cases, the contact between the KIM and p38α was retained, and catalytically competent states, in which p38α T180 or Y182 approached the γ-phosphate of MKK6 ATP at a catalytically compatible distance, were observed. Partial detachment of p38α from MKK6 was also observed in some instances. Additionally, the C-lobe interface proved to be important for the stability of the dimer, which is in agreement with our other observations. In all simulations in which the two kinases break apart, this tight hydrogen-bonding network at the C-lobe level is the last point of contact to be lost. In particular, the interaction between MKK6 αG-helix residues K268 and E272 and p38α S261 seems to be one of the main interactions keeping the two kinases in close proximity (fig. S9E). The observed conformational variety is consistent with the SAXS and cryo-EM data, which are indicative of the transient nature of the interaction of the two kinases. With respect to the phosphorylation mechanism, in a number of trajectories, either p38α T180 or Y182 approach the ATP γ-phosphate located in the MKK6 active site (*47*) (Fig. 3, table S8, and movies S4 and S5). In particular, in the simulations of MKK6-p38α, both T180 and Y182 come close to the catalytic site. The tendency of monomeric, unphosphorylated p38α to adopt inactive, sequestered A-loop conformations has been shown in previous studies (*48*). Thus, the observation that the unphosphorylated A loop of p38α adopts an exposed conformation in multiple instances is indicative of an active role of MKK6 in stabilizing such conformations. The active role of MKK6 is confirmed by the fact that in the simulations in which the MKK6 KIM detaches, leading to the separation of the two kinases, the p38α A loop transitions from an exposed to a sequestered conformation (fig. S11).

A rotated complex might facilitate the phosphorylation of p38α T180

In this initial set of MKK6GRA-p38α simulations, we observe some complexes in which T180 approaches the γ-phosphate of ATP in the catalytic site of MKK6 from an unexpected angle, where the p38α N lobe underwent a 50° to 80° rotation around its axis (Fig. 3B and movie S4). In this conformation, p38α was kept close to MKK6 through the KIM, despite the rotation. Before T180 gets close to the ATP, K17, a key lysine located just after the KIM, forms a salt bridge with p38α E160 that seems to initiate the rotation of p38α (Fig. 3C).

Integration of simulations with SAXS data through Bayesian/maximum-entropy reweighting shows how the kinases associate

To better characterize intermediate states involved in the formation of the catalytically competent dimer, we extended the conformational sampling of the MD simulations using adaptive Markov state model (MSM) simulations (*49*, *50*) (supplementary material sp. S8 and fig. S13) and used a kinetic-based clustering of the total accumulated MD trajectories to

determine the main metastable states. By extending the sampling to more than 18 μs and performing the kinetic clustering, we obtained five macrostates for p38α with MKK6GRA (Fig. 4 and movies S6 to S10). In the case of MKK6GRA-p38α, one of the clusters corresponds to an ensemble that contains conformations where the two kinases are face-to-face, equivalent to the cryo-EM structure (state A, movie S6). In this macrostate, we also see conformations corresponding to the rotated N lobe of p38α, in which T180 is ideally positioned for phosphorylation. The clustering of the face-to-face and rotated conformations within the same metastable state reflects the rapid interconversion from one to the other (few μs). In the second macrostate, the KIM is tightly bound, whereas MKK6 adopts different orientations (state E, movie S7). The third macrostate represents conformations resulting from the detachment and nonspecific binding of the two kinases, in which MKK6 binds to different surfaces of p38α (state C, movie S8). Lastly, we observed two macrostates in which the two kinases are held together through the C-lobe interface and in which the KIM is either bound (state B, movie S9) or explores the N lobe of p38α (state D, movie S10). The connections between the macrostates (Fig. 4) indicate one or more reactive trajectories connecting one state to another. The resulting network shows that the binding of the KIM to its recognition site plays a fundamental role in establishing the specific contacts needed for the formation of the face-to-face dimer.

Despite a total sampling time of more than 18 μs, we could not fully converge the kinetics and the population of all the macrostates directly from the simulations, probably thanks to the slow nature of some of the transitions seen in protein-protein associations (*50*). An exhaustive sampling of complex formation from the detached states would require a prohibitive number of long MD simulations and might still be affected by the quality of the force field. We therefore refined the structural ensemble and validated the clustering results by using the SAXS data and a Bayesian/maximum-entropy approach (*51*–*53*). The SAXS profile of each conformer within the clustered MD ensemble was calculated, and the weights associated with each conformer in the ensemble that maximize the agreement with experiments were iteratively determined (fig. S12A). For the refinement of the MKK6GRA-p38α ensemble, we used the SAXS curves of the complex with ADP.AlF_4^- and with the nonhydrolyzable ATP analog β,γ-methyleneadenosine 5′-triphosphate (AMP-PCP). The reweighted ensemble fits extremely well with the SAXS curve of $MKK6^{DD}$GRA-$p38\alpha^{T180V}$ with ADP.AlF_4^- (χ^2 = 0.89; movie S15), which showed the most compact conformation (table S1). Reassuringly, all the macrostates from kinetic modeling contribute to the SAXS curve (Fig. 4). State A, which contains conformations equivalent to the cryo-EM structure, is the most populated (62.5%), followed by state C (27.8%), which reflects the transient nature of the complex and the nonspecific binding associated with such transient complexes, and then ensemble E (2.5%). From the weights (and the other experiments), we deduce that the latter is the main intermediate for the formation of the face-to-face complex. After the KIM domain is bound, the MD simulations indicate an important role for the hydrophobic patch and a network of hydrogen bonds located at the interface of the C lobes of the two kinases in the formation of the complex. These conclusions are in accordance with the 70% decrease in activity seen in the $MKK6^{DD}$ αG-helix mutant (Fig. 2F), as well as the metadynamics free-energy calculations and the HDX-MS data (fig. S9).

The ensemble reweighted to match the SAXS data obtained from the $MKK6^{DD}$GRA-$p38\alpha^{WT}$ with the ATP analog AMP-PCP also resulted in a good fit (χ^2 = 2.1). The population of the face-to-face cluster A decreases to 1%, whereas that of the detached cluster C and intermediate D increases considerably, to 71.5 and 21.7%, respectively (fig. S12, B and C). Although the populations of the macrostates shift, which is expected because the transition state is not stabilized, the general description of the macrostates remains similar. Within cluster A, the weights of the "rotated" face-to-face dimer increase (fig. S12B). We also sampled the conformational space of the MKK6-p38α with the same adaptive MSM approach. The four macrostates found in the MKK6-p38α complex are equivalent to four of the macrostates found in MKK6GRA-p38α (fig. S13), reflecting the similarity of the dynamics of the two complexes (supplementary text).

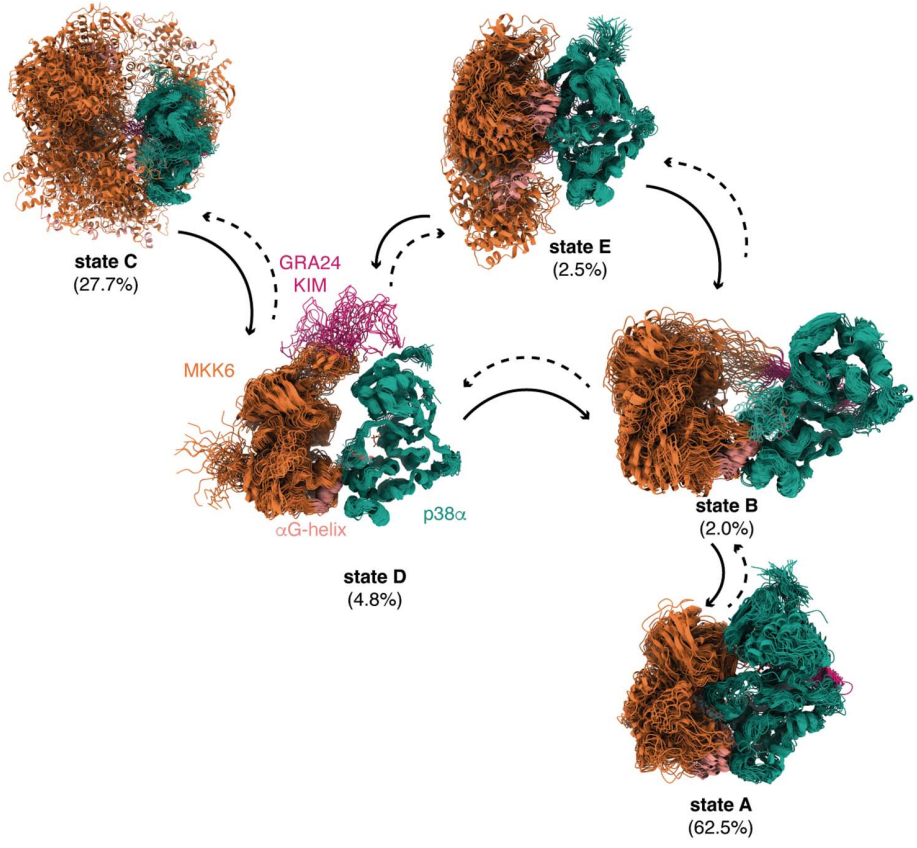

Fig. 4. Kinetic-based clustering of the accumulated simulations of MKK6GRA-p38α. Each macrostate shows an overlay of 50 representative conformations sampled proportionally to the equilibrium probability of each microstate in the corresponding macrostate that correlates to different kinetically distinct states. The population of each state as derived from the fitting to the $MKK6^{DD}$GRA + $p38\alpha^{WT}$ + ADP + AlF_4^- SAXS curve (fig. S2) is given in parenthesis. The solid arrows indicate the main directions of the observed reactive trajectories connecting the macrostates.

The N-terminal extension of MKK6 remains mainly disordered, and its length and secondary-structure elements contribute to pathway specificity

Our structure and macrostate modeling imply that once the KIM is bound, the N-terminal linker plays an important role in conformational sampling, allowing the catalytically competent state to form, a phenomenon that has been observed in other tethering proteins (*54*). There is

a wealth of data on interactions between KIMs and MAPKs, but the role of the remainder of the N terminus is poorly understood (*55*, *56*). In our cryo-EM map, the engineered KIM is clearly visible (Fig. 1C and fig. S5), but it does not appear to interact further with p38α. To investigate whether the N-terminal extension has a role beyond simply associating the kinase to the KIM, we again used the luciferase reporter assay. We produced constructs that scan the region between the KIM and the first consensus β sheet of the kinase core with alanine blocks to determine if there is sequence specificity or direct interaction with p38α (Fig. 5). Our results show that the sequence of the middle region ($MKK6^{DD}$ Ala scan 28 to 39) of the N-terminal linker has no effect on p38α signaling in cellulo. However, the sequence of the linker close to the KIM ($MKK6^{DD}$ Ala scan 18 to 29) and the region close to the kinase core, which comprises the predicted β strands ($MKK6^{DD}$ Ala scan 38 to 49) (Fig. 5) seem to have some importance because their mutation to alanine reduced p38α signaling by 27 and 58%, respectively.

Although KIM sequences are important, they do not sufficiently explain specificity. When the N-terminal linkers of the MAP2Ks are compared, it is found that they differ in their length and secondary-structure elements (*16*, *57*, *58*) (Fig. 5, B and C). Could this contribute to specificity between the pathways? When we substituted the MKK6 linker with those from the MAP2Ks of the other pathways, activity was reduced (Fig. 5D). This is most observable with the linkers from MEK1 and 2. The linkers from MAP2Ks that activate p38α also see reduced activity and are not sufficient to rescue the activation, even though the KIM, MAP2K, and MAPK are in the correct combination. Our structure and macrostate models imply that the length of the linker is just sufficient to allow

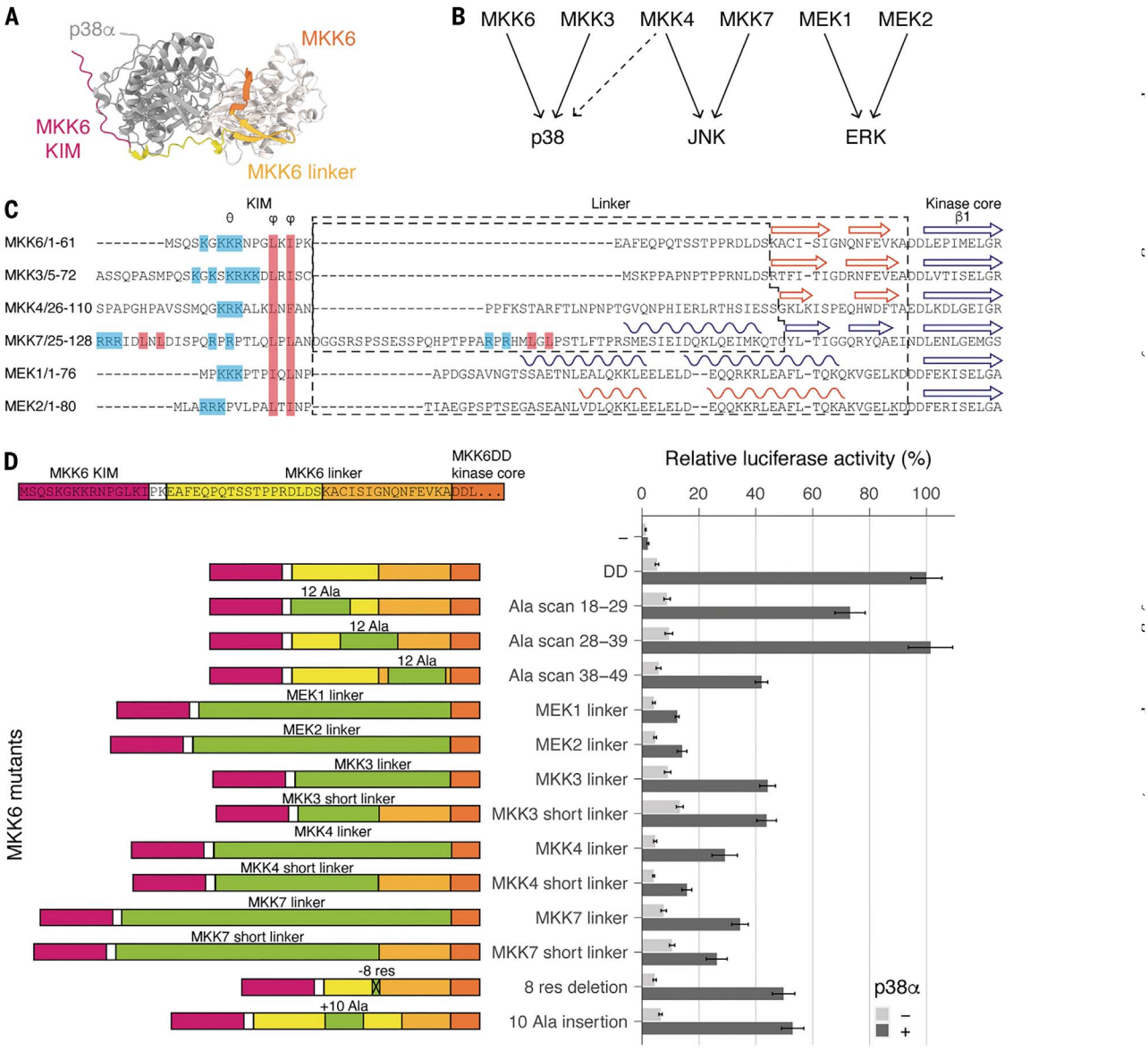

Fig. 5. MKK6 N-terminal extension length and secondary structure define the specificity of p38α activation. (**A**) Top view of an MKK6-p38α AlphaFold2 multimer model, for illustrative purposes. (**B**) Specificity of the MAP2K/MAPK signaling pathways. (**C**) Sequence alignment of MAP2K N termini. Secondary structure elements are indicated, from experimental structures in blue and AlphaFold2 predictions [predicted local difference distance test (pLDDT) score > 65] in orange. (**D**) Luciferase reporter assay to monitor the activity of the p38α signaling pathway in HEK293T cells, showing the ability of $MKK6^{DD}$ mutants and chimeras to activate p38α (statistical analysis in table S9 and protein expression levels in fig. S10).

the observed interactions between the kinases, in particular, the MAP2K αG-helix position relative to the MAPK hydrophobic pocket formed by the MAPK insert. By removing or adding 10 residues to the linker region, activity is reduced by ~50%. This implies that the length of the linker, controlled by the number of amino acids and/or by secondary-structure elements, is important in the positioning of the MAP2K for engagement with the MAPK and is finely tuned for MAP kinase pairs. The specificity of a MAP2K is therefore defined by cooperation between the KIM, the linker, and the kinase core folds themselves.

Discussion

Initial docking

The N termini of the MAP2Ks contain a conserved KIM motif that is required for binding to their substrate MAPKs. The first step in activation is KIM binding, after which a wide variety of conformations are observed, showing the fast timescale of association and dissociation (Fig. 4). During the MD simulations, KIM binding induced allosteric changes in p38α, which adopts a prone-to-be-phosphorylated conformation with its A loop extended, exposing the tyrosine and threonine residues, which is in agreement with crystal structures. Our data indicate that the interaction between the MKK6 N terminus and p38α extends beyond the hydrophobic residues of the KIM and is important in the activation process. Although most of the MKK6 N-terminal linker remains disordered, its length seems to be tightly linked to the substrate MAPK, and the presence of some secondary structural elements differs between MAP2Ks, contributing to specificity (Fig. 5C). Our reweighted ensemble, obtained by combining Bayesian inference with adaptive MSM simulations and SAXS data, shows that once the KIM is bound, many conformations are sampled before the engagement of the αG helix (Fig. 4). This sampling is fully consistent with the experiments that show that if the linker is not the correct length, the engagement of the αG helix will be impeded. Once p38α is recruited, some parts of the MKK6 N-terminal linker could participate in the conformational shift toward the MKK6 active conformation, but its main function appears to be to prepare the MAPK A loop and to guide the engagement with the αG helix.

Engagement with substrate

We show that the predominant interaction during activation is mediated by the αG helix of the MAP2K MKK6 and the p38α hydrophobic pocket formed by the αG helix of p38α and the specific MAPK insert. This region is also important in MAPKs for substrate recognition (*42*) and interaction with scaffold proteins and downstream regulators such as phosphatases (*27*, *43*, *59*). The engagement of αG helices seems to be an emerging theme in kinase heterodimers: Only a few structures have been determined, such as the KSR2-MEK1 heterodimer (*27*) and more recently, the BRAF-MEK1 complex (*25*), both upstream components of the related extracellular signal–regulated kinase (ERK) MAPK pathway. In both these structures, the αG-helices interaction is very similar, as well as the relative orientation of the kinases. Several studies have shown that small molecules can target this region in p38 isoforms (*37*–*41*) and modulate the position of the MAPK-insert helices (fig. S7). However, as the pocket is very deep, the molecules may not extend far enough to disrupt the interactions identified here. There has been intense interest, and some success (*60*), in developing drugs that target p38α, mostly binding to the nucleotide pocket, but they have been mired by off-target and toxicity effects (*9*). The molecules that have been identified as binding to the MAPK-insert pocket could be further developed to better disrupt both the MAP2K interaction and that of substrates, which could lead to highly specific p38 inhibitors.

The MKK6 KIM–p38α docking site, the MKK6 N-terminal linker, and the MKK6 αG-helix–p38α hydrophobic pocket interactions are essential for defining the specificity of the kinase-substrate interaction, for positioning the two kinases, and for triggering the necessary changes toward the MKK6 active kinase conformation and positioning the A loop of p38α to be accessible for phosphorylation. Our data demonstrate that altering any of these three components perturbs the activation of downstream signaling.

Freedom of interaction at the catalytic center

All contacts observed between the kinases are distal to the active site, which explains the lack of sequence specificity or conservation in MAPK A loops in the region preceding the TxY motif (*58*), and our HDX-MS data show no tight interaction between the A loop of p38α and MKK6 (Fig. 2 and fig. S8). Rather than the active site of a classical enzyme, where substrates are perfectly positioned for catalysis, the MAP2K-MAPK complex appears to provide a zone of proximity, allowing the flexible activation loop to move but increasing the probability, or local concentration, of the p38α T180 and Y182 residues to be positioned for nucleophilic attack of the γ-phosphate of ATP by relative positioning of the two kinases. Dual-specificity MAP2Ks are unusual because the two amino acids targeted are considerably different from each other when compared with serine/threonine kinases. In addition, the two substrate-phosphorylation sites are only one residue apart, and the MAP2Ks need to have an active site that can accommodate, effectively, four substrates [(A-loop **T**-x-Y; T-x-**Y**; **T**-x-Y^P; and T^P-x-**Y** (targeted residue in bold)], all with markedly different sizes and charges. This implies that flexibility in the active site is essential to accommodate such a wide variety of substrates. By not binding any residues of the A loop specifically, various residues and phosphorylation states could be accommodated by sacrificing catalytic efficiency for flexibility.

The MD simulations revealed that the face-to-face architecture of the heterokinase dimer of our model is compatible with the phosphorylation of either T180 or Y182 of the p38α A loop (Fig. 3 and fig. S14). Another conformation, where p38α rotated, emerged and seems to favor the phosphorylation of T180. Kinetic data have shown that the dual phosphorylation of p38α by MKK6 involves a partially processive mechanism in vitro, in which the monophosphorylated intermediates can either dissociate from the enzyme or proceed to the next catalytic step. Wang *et al.* (*61*) and others (*62*) propose that both p38α monophosphorylated forms can be produced by MKK6 catalysis with a preference for Y182, whose phosphorylation is four times as fast as that of T180. With respect to the second catalytic step, the experimentally measured kinetic rates indicate that phosphorylation at Y182 in the first step enhances the catalytic efficiency of MKK6 phosphorylation at T180 in the second step. According to our simulations (Fig. 3 and fig. S14), when the N lobe of p38α undergoes a large conformational change toward the rotated dimer, T180 is in the right position to be phosphorylated, but Y182 is more distant from the catalytic site, which might explain the lower catalytic efficiency of MKK6 observed with kinetic measurements when the second phosphorylation is on Y182. Conversely, Y182 seems to be able to easily approach MKK6 ATP in the face-to-face catalytically competent conformations and then be phosphorylated. Thus, the difference in the experimental kinetic rates measured for the first phosphorylation step may reflect the rotation of the p38α N lobe around its axis, which seems to be involved in the T180 phosphorylation only. The partial processivity of the dual phosphorylation in a cellular context remains an open question (*63*, *64*), but the architecture of the interaction that we observed between MKK6 and p38α, as well as the microstates seen in modeling, seem to be compatible with either a distributive, partially processive or fully processive mechanism.

By combining cryo-EM and MD simulations, together with HDX-MS and structure-driven mutagenesis in cellulo, we describe the range of attributes that lead to MKK6 selectivity and p38α activation. Moreover, we identify critical interfaces for dimer stabilization. In this regard, small molecules that prevent MKK6-p38α complex dimerization could be therapeutically effective in treating diseases resulting from abnormal MKK6-p38α–mediated signaling. What is more, our data describe molecular details of

the activation of one protein kinase by another—one of the most fundamental mechanisms in cell signaling.

Materials and methods summary

The details of the methodology are described in the supplementary materials and are summarized here as follows:

Purification of MKK6-p38α

To increase the affinity of the constitutively active $MKK6^{DD}$ mutant (S207D and T211D) for p38α for structural studies, the natural KIM sequence was replaced with the *T. gondii* effector protein GRA24 KIM sequence ($MKK6^{DD}$GRA), and a C-terminal Twin-Strep tag (IBA Lifesciences) was added. $MKK6^{DD}$ and $MKK6^{DD}$GRA were expressed in *Sf*21 insect cells and purified through streptavidin affinity and size-exclusion chromatography (SEC). Human MAPK p38α constructs were expressed in *Escherichia coli* with an N-terminal His6 tag and purified through nickel affinity and SEC. The heterokinase complex was prepared by mixing $MKK6^{DD}$GRA and p38α in a 1:1 molar ratio followed by SEC. The transphosphorylation conformation was then assembled by using the transition-state analog $ADP.AlF_4^-$ through incubation with 10 mM ADP, 10 mM NH_4F, and 1 mM $AlCl_3$ for 30 min before proceeding with biophysical studies.

Cryo-EM grid preparation, imaging, data processing, and modeling

Purified $MKK6^{DD}$GRA-$p38\alpha^{T180V}$ with $ADP.AlF_4^-$ was applied to UltraAufoil 1.2/1.3 grids (Quantifoil) and plunge-cooled with a Vitrobot Mark IV (FEI), screened on a FEI Talos Glacios (EMBL Grenoble), and imaged on a FEI Titan Krios (EMBL Heidelberg). Data processing in CryoSPARC (*65*) yielded a final map with an average resolution of 4.0 Å [Fourier shell correlation (FSC) 0.143], showing the two kinases in a face-to-face conformation with the A loop of p38α extended toward the active site of MKK6.

MD simulations and modeling

The cryo-EM structure was used as the starting conformation of the MD simulations, and bound nucleotides were replaced with ATP. The simulations were set up by using GROMACS v.2021.3 with the DES-Amber force field and TIP4PD water molecules. The PLUMED plugin was used for free-energy calculations. Adaptive MD simulations were performed to further explore the prebound and bound states of the complex. The conformational ensembles were clustered kinetically and refined using an iterative Bayesian/maximum-entropy (iBME) protocol to obtain a structural ensemble that reflects the states captured in the solution SAXS data.

REFERENCES AND NOTES

1. B. Canovas, A. R. Nebreda, *Nat. Rev. Mol. Cell Biol.* **22**, 346–366 (2021).
2. M. Bouhaddou *et al*., *Cell* **182**, 685–712.e19 (2020).
3. D. S. Battagello *et al*., *Clin. Sci.* **134**, 2137–2160 (2020).
4. S. Bellon, M. J. Fitzgibbon, T. Fox, H.-M. Hsiao, K. P. Wilson, *Structure* **7**, 1057–1065 (1999).
5. S. S. Taylor, A. P. Kornev, *Trends Biochem. Sci.* **36**, 65–77 (2011).
6. N. Blüthgen *et al*., *FEBS J.* **273**, 895–906 (2006).
7. F. Ortega, L. Acerenza, H. V. Westerhoff, F. Mas, M. Cascante, *Proc. Natl. Acad. Sci. U.S.A.* **99**, 1170–1175 (2002).
8. M. Thattai, A. van Oudenaarden, *Biophys. J.* **82**, 2943–2950 (2002).
9. D. Hammaker, G. S. Firestein, *Ann. Rheum. Dis.* **69**, i77–i82 (2010).
10. K. P. Wilson *et al*., *J. Biol. Chem.* **271**, 27696–27700 (1996).
11. X. Xie *et al*., *Structure* **6**, 983–991 (1998).
12. F. Zhang, A. Strand, D. Robbins, M. H. Cobb, E. J. Goldsmith, *Nature* **367**, 704–711 (1994).
13. X. Min *et al*., *Structure* **17**, 96–104 (2009).
14. T. Matsumoto *et al*., *J. Biochem.* **151**, 541–549 (2012).
15. J. F. Ohren *et al*., *Nat. Struct. Mol. Biol.* **11**, 1192–1197 (2004).
16. M. Schröder *et al*., *Cell Chem. Biol.* **27**, 1285–1295.e4 (2020).
17. Á. Garai *et al*., *Sci. Signal.* **5**, ra74 (2012).
18. T. Tanoue, M. Adachi, T. Moriguchi, E. Nishida, *Nat. Cell Biol.* **2**, 110–116 (2000).
19. W. Peti, R. Page, *Protein Sci.* **22**, 1698–1710 (2013).
20. A. Zeke *et al*., *Mol. Syst. Biol.* **11**, 837 (2015).
21. T. Zhou, L. Sun, J. Humphreys, E. J. Goldsmith, *Structure* **14**, 1011–1019 (2006).
22. C. I. Chang, B. E. Xu, R. Akella, M. H. Cobb, E. J. Goldsmith, *Mol. Cell* **9**, 1241–1249 (2002).
23. M. Dyla, M. Kjaergaard, *Proc. Natl. Acad. Sci. U.S.A.* **117**, 21413–21419 (2020).
24. J. Beenstock, N. Mooshayef, D. Engelberg, *Trends Biochem. Sci.* **41**, 938–953 (2016).
25. E. Park *et al*., *Nature* **575**, 545–550 (2019).
26. Y. Kondo *et al*., *Science* **366**, 109–115 (2019).
27. D. F. Brennan *et al*., *Nature* **472**, 366–369 (2011).
28. P. Sok *et al*., *Structure* **28**, 1101–1113.e5 (2020).
29. E. T. Haar, P. Prabakhar, X. Liu, C. Lepre, *J. Biol. Chem.* **282**, 9733–9739 (2007).
30. L. Braun *et al*., *J. Exp. Med.* **210**, 2071–2086 (2013).
31. E. Pellegrini *et al*., *Structure* **25**, 16–26 (2017).
32. T. Bepler *et al*., *Nat. Methods* **16**, 1153–1160 (2019).
33. V. Modi, R. L. Dunbrack Jr., *Proc. Natl. Acad. Sci. U.S.A.* **116**, 6818–6827 (2019).
34. R. Evans, *et al*., *bioRxiv*2021.10.04.463034 [Preprint] (2022).
35. R. Diskin, D. Engelberg, O. Livnah, *J. Mol. Biol.* **375**, 70–79 (2008).
36. N. Tzarum, Y. Eisenberg-Domovich, J. J. Gills, P. A. Dennis, O. Livnah, *J. Mol. Biol.* **424**, 339–353 (2012).
37. M. Bührmann, J. Hardick, J. Weisner, L. Quambusch, D. Rauh, *Angew. Chem. Int. Ed.* **56**, 13232–13236 (2017).
38. M. Bührmann *et al*., *PLOS ONE* **12**, e0184627 (2017).
39. K. M. Comess *et al*., *ACS Chem. Biol.* **6**, 234–244 (2011).
40. O. Laufkötter, H. Hu, F. Miljković, J. Bajorath, *J. Med. Chem.* **65**, 922–934 (2022).
41. X. H. Zhang *et al*., *FEBS Lett.* **595**, 2570–2592 (2021).
42. K. Kirsch *et al*., *Nat. Commun.* **11**, 5769 (2020).
43. X. Liu *et al*., *Nat. Commun.* **7**, 10879 (2016).
44. E. I. James, T. A. Murphree, C. Vorauer, J. R. Engen, M. Guttman, *Chem. Rev.* **122**, 7562–7623 (2022).
45. S. A. Foster *et al*., *Cancer Cell* **29**, 477–493 (2016).
46. B. Zhang *et al*., *Mol. Genet. Genomic Med.* **8**, e1395 (2020).
47. A. Pérez-Gallegos, M. Garcia-Viloca, À. González-Lafont, J. M. Lluch, *Phys. Chem. Chem. Phys.* **17**, 3497–3511 (2015).
48. A. Kuzmanic *et al*., *eLife* **6**, e22175 (2017).
49. S. Doerr, G. De Fabritiis, *J. Chem. Theory Comput.* **10**, 2064–2069 (2014).
50. N. Plattner, S. Doerr, G. De Fabritiis, F. Noé, *Nat. Chem.* **9**, 1005–1011 (2017).
51. F. Pesce, K. Lindorff-Larsen, *Biophys. J.* **120**, 5124–5135 (2021).
52. A. H. Larsen *et al*., *PLOS Comput. Biol.* **16**, e1007870 (2020).
53. S. Orioli, A. H. Larsen, S. Bottaro, K. Lindorff-Larsen, *Prog. Mol. Biol. Transl. Sci.* **170**, 123–176 (2020).
54. N. S. González-Foutel *et al*., *Nat. Struct. Mol. Biol.* **29**, 781–790 (2022).
55. Y. Fleming *et al*., *Biochem. J.* **352**, 145–154 (2000).
56. C. Tournier, A. J. Whitmarsh, J. Cavanagh, T. Barrett, R. J. Davis, *Mol. Cell. Biol.* **19**, 1569–1581 (1999).
57. T. O. Fischmann *et al*., *Biochemistry* **48**, 2661–2674 (2009).
58. V. Modi, R. L. Dunbrack Jr., *Sci. Rep.* **9**, 19790 (2019).
59. Y. Y. Zhang, J. W. Wu, Z. X. Wang, *Sci. Signal.* **4**, ra88 (2011).
60. C. Dominguez, D. A. Powers, N. Tamayo, *Curr. Opin. Drug Discov. Devel.* **8**, 421–430 (2005).
61. Y. L. Wang *et al*., *FEBS J.* **286**, 1030–1052 (2019).
62. J. M. Humphreys, A. T. Piala, R. Akella, H. He, E. J. Goldsmith, *J. Biol. Chem.* **288**, 23322–23330 (2013).
63. K. Aoki, K. Takahashi, K. Kaizu, M. Matsuda, *Sci. Rep.* **3**, 1541 (2013).
64. C. Salazar, T. Höfer, *FEBS J.* **276**, 3177–3198 (2009).
65. A. Punjani, J. L. Rubinstein, D. J. Fleet, M. A. Brubaker, *Nat. Methods* **14**, 290–296 (2017).
66. F. L. Gervasio, I. Galdadas, D. Gobbo, Architecture of the MKK6-p38α complex defines the basis of MAPK specificity and activation, Yareta (2023); https://doi.org/10.26037/yareta:jmnbt6lzkrfrpdcf3m3343smxq.

ACKNOWLEDGMENTS

We thank S. Cusack and A. McCarthy (EMBL Grenoble) for encouragement, W. Galej (EMBL Grenoble) for critical reading of the manuscript, and M.-A. Hakimi (IAB, Grenoble) for introducing us to the *T. gondii* protein GRA24. We acknowledge S. Schneider for her support in using the EM Facility at EMBL Grenoble and thank F. Weiss, W. Hagen, and S. Fromm for excellent data collection at the EMBL Imaging Centre. We thank A. Aubert (EMBL Grenoble) for support in eukaryotic protein expression, the proteomic core facility at EMBL Heidelberg for mass spectrometry, and U. Kapp (ESRF) for assistance in the crystallization of p38α. We acknowledge M. Bonomi (Institut Pasteur, CNRS, France) for discussions and technical support in cross-correlation analysis. K. Lindorff-Larsen, S. Bottaro, and F. Pesce are acknowledged for support in running the BME procedure. This work used the platforms of the Grenoble Instruct-ERIC center (ISBG; UAR 3518 CNRS-CEA-UGA-EMBL) within the Grenoble Partnership for Structural Biology (PSB), supported by FRISBI (ANR-10-INBS-0005-02) and GRAL, and financed within the Université Grenoble Alpes graduate school (Écoles Universitaires de Recherche) CBH-EUR-GS (ANR-17-EURE-0003). We acknowledge the European Synchrotron Radiation Facility for the provision of synchrotron radiation facilities, and we would like to thank the staff of the ESRF and EMBL Grenoble for assistance and support in using beamlines ID23-1 and ID23-2. SAXS data were collected at beamline B21 at Diamond Light Source, UK. Molecular graphics and analyses were performed with UCSF ChimeraX, developed by the Resource for Biocomputing, Visualization, and Informatics at the University of California, San Francisco, with support from NIH R01-GM129325 and the Office of Cyber Infrastructure and Computational Biology, National Institute of Allergy and Infectious Diseases. We acknowledge PRACE and the Swiss National Supercomputing Centre (CSCS) for large supercomputer time allocations on Piz Daint (project IDs: pr126, s1107). **Funding:** This project was funded by EMBL (M.W.B.), the Swiss National Science Foundation [project no. 200021_204795] (F.L.G.), and Bridge [project no. 40B2-0_203628] (F.L.G.). P.J. was supported by a EMBL predoctoral fellowship. **Author contributions:** Conceptualization: P.J., E.P., F.L.G., and M.W.B. Methodology: P.J., I.G., D.G., J.v.V., M.P., and O.V. Investigation: P.J., I.G., D.G., J.v.V., O.V., M.T., F.L.G., E.P., and M.W.B. Visualization: P.J., I.G., D.G., J.v.V., and O.V. Funding acquisition: F.L.G. and M.W.B. Supervision: F.L.G., E.P., and M.W.B. Writing – original draft: – P.J. and M.W.B. Writing – review and editing: P.J., I.G., D.G., J.v.V., M.P., O.V., M.T., F.L.G., E.P., and M.W.B. **Competing interests:** The authors declare that they have no competing interests. **Data and materials availability:** Structure of the $MKK6^{DD}$GRA-$p38\alpha^{T180V}$ complex: EMPIAR-11203 (raw micrographs; Electron Microscopy Public Image Archive), EMD-15233 (map; Electron Microscopy Data Bank), and PDB-8A8M [coordinates; Protein Data Bank (PDB)]. Crystal structures of apo p38α and $p38\alpha^{K53R}$: PDB-5ETC and PDB-5ETI (coordinates and structure factors; PDB). The SAXS curves and pair distribution functions are deposited in the Small Angle Scattering Biological Data Bank (access codes: SASBDB-SASDRC6 and SASBDB-SASDRD6). The mass spectrometry proteomics data have been deposited to the ProteomeXchange Consortium through the PRIDE partner repository with the dataset identifier PXD040499 and 10.6019/PXD040499. The MD simulations data (trajectories, topology files, and structures of the SAXS-refined ensembles) are deposited in the Yareta repository (*66*).

License information: Copyright © 2023 the authors, some rights reserved; exclusive licensee American Association for the Advancement of Science. No claim to original US government works. https://www.science.org/about/science-licenses-journal-article-reuse

SUPPLEMENTARY MATERIALS

science.org/doi/10.1126/science.add7859
Materials and Methods
Supplementary Text
Figs. S1 to S16
Tables S1 to S10
References (*67*–*112*)
MDAR Reproducibility Checklist
Movies S1 to S16

Submitted 5 July 2022; resubmitted 7 April 2023
Accepted 9 August 2023
10.1126/science.add7859

WORKING LIFE

By **Kwabena Boahen Asare**

Finding my community

The lab doors swung open, and as I stepped inside my ambitions of becoming a Black scientist stood tall. Fueled by lifelong dreams of breaking barriers and shattering ceilings, I was set to embark on my first stint as an undergraduate researcher. But reality soon hit hard. The stark absence of Black scientists left me questioning my place in science. Would other researchers doubt my abilities? See me as an outsider? Or worse, feel hatred? For nearly a year, these fears brought me to tears and dimmed the flame of my aspirations. But when I joined an immersive program, living alongside aspiring scientists who looked like me, my trajectory took a much-needed turn.

Growing up, science shaped my world. I found solace peering through a magnifying glass at the intricate bodies of dead insects alongside my neighborhood friends, and I knew from that time that I wanted to spend my life unraveling the mysteries of science.

When I got to college, I decided to apply for research positions after learning about opportunities available to undergraduate students. Eventually, I joined a lab that studies skin cancers. There, I felt like a newly sprouted seed, surrounded by faculty and colleagues who nurtured my growth. My mentor believed in me, patiently explained concepts, and encouraged my initiative.

But within a month I was thinking about quitting. I battled imposter syndrome, feeling that my slow grasp of some lab concepts rendered me unfit for research. The absence of Black scientists in my lab and the wider community compounded my feelings of isolation and fueled my self-doubt. I began to wonder whether my ambitions were unconventional for a Black person and out of reach.

"I began to wonder whether my ambitions were unconventional for a Black person."

I spoke with mentors at a center on campus that helps students from underrepresented groups. They reassured me that my feelings were common among students like me. However, they also encouraged me to continue to pursue research. To support my sense of belonging, they recommended a program on campus that was developed to create community and safe spaces for students from underrepresented groups who are interested in research. I submitted my application and was accepted to start the summer after my first year.

The program offered summer housing so we could all live together while doing research in various labs across campus. Early on, I spoke with a student who was studying artificial intelligence. As I listened to him talk with confidence about his work, I felt a rush of anxiety, knowing that I, too, would have to share the progress of my work. At the time, I was struggling to amplify DNA in the lab and my imposter syndrome was hitting the roof. But then he began to share how often his computer codes fail and how he sometimes feels like an imposter while working with experienced Ph.D. researchers and postdocs. I felt relieved that I could share my failures, too.

I continued to hear more stories like that at our program's weekly meetings and other social events, which strengthened my self-esteem and reinforced my belief that I, too, can become a successful scientist. I realized that the journey of science is similar for everyone—there are always going to be ups and downs, and everyone encounters failure at one point or another. The mere fact that there were other students like me pursuing research also gave me a new sense of hope and enthusiasm.

As the summer unfolded, I became more confident in the lab. I could openly discuss failures with my colleagues without fear that they'd judge me as being unfit for research. I succeeded in amplifying the DNA and carefully mapped out my next steps for the project. And when I hit roadblocks, I took a step back and troubleshooted the issues without internalizing them as personal shortcomings.

A year has now passed and I can say that the program's impact on me has been profound. Interacting with people who share both my skin color and my passion for science has reinvigorated my drive to be a scientist. Representation matters, and support from my own community was essential for creating a world where I can not only exist, but thrive. ■

Kwabena Boahen Asare is an undergraduate student at Dartmouth College. Send your career story to SciCareerEditor@aaas.org.

Browse the 2024 Portfolio of Gordon Research Conferences

Conferences are scheduled in the United States and Europe from January–March and May–August 2024.

Applications are being accepted today for all conferences at www.grc.org!

January–March 2024

Advanced Materials for Sustainable Infrastructure Development +GFS

FEB 25 - MAR 1, 2024
VENTURA BEACH MARRIOTT, VENTURA, CA
CHAIRS: William Weiss and Ravindra Gettu
VICE CHAIRS: Liberato Ferrara and Rupert Myers

Alcohol and the Nervous System +GFS

FEB 11-16, 2024
GRAND GALVEZ, GALVESTON, TX
CHAIRS: Rajita Sinha and Joyce Besheer
VICE CHAIRS: Patrick Mulholland and Christina Gremel

Angiotensin +GFS

FEB 25 - MAR 1, 2024
RENAISSANCE TUSCANY IL CIOCCO, LUCCA (BARGA), ITALY
CHAIR: Rhian Touyz
VICE CHAIR: Ulrike (Muscha) Steckelings

Antibody Biology and Engineering +GFS

MAR 17-22, 2024
RENAISSANCE TUSCANY IL CIOCCO, LUCCA (BARGA), ITALY
CHAIRS: Pierre Bruhns and Lynn Macdonald
VICE CHAIR: Jenna Guthmiller

Atomically Precise Nanochemistry +GFS

FEB 4-9, 2024
GRAND GALVEZ, GALVESTON, TX
CHAIRS: Thalappil Pradeep and Stefanie Dehnen
VICE CHAIRS: Stacy Copp and Hannu Häkkinen

Autophagy in Stress, Development and Disease +GFS

MAR 10-15, 2024
RENAISSANCE TUSCANY IL CIOCCO, LUCCA (BARGA), ITALY
CHAIRS: James Hurley and Patricia Boya
VICE CHAIR: Rushika Perera

Basal Ganglia +GFS

MAR 24-29, 2024
FOUR POINTS SHERATON / HOLIDAY INN EXPRESS, VENTURA, CA
CHAIRS: Zayd Khaliq and Ilana Witten
VICE CHAIRS: Talia Lerner and Jun Ding

Batteries +GFS

FEB 25 - MAR 1, 2024
FOUR POINTS SHERATON / HOLIDAY INN EXPRESS, VENTURA, CA
CHAIRS: Neil Dasgupta and Kelsey Hatzell
VICE CHAIRS: Partha Mukherjee and Rachel Carter

Biology of Acute Respiratory Infection +GFS

FEB 25 - MAR 1, 2024
GRAND GALVEZ, GALVESTON, TX
CHAIRS: Bethany Moore and Charles Dela Cruz
VICE CHAIRS: Janet Lee and Scott Evans

Biology of Spirochetes +GFS

JAN 14-19, 2024
VENTURA BEACH MARRIOTT, VENTURA, CA
CHAIR: Mathieu Picardeau
VICE CHAIR: Melissa Caimano

"GRC continues to play an essential role in the dissemination of the most important cutting-edge results and approaches in all of science."

DR. RANDY SCHEKMAN, University of California, Berkeley

Biotherapeutics and Vaccines Development +GRS

MAR 17-22, 2024
GRAND GALVEZ, GALVESTON, TX
CHAIRS: Peter Tessier and Jessica Molek
VICE CHAIRS: Jennitte Stevens and Alexander Kabanov

Bones and Teeth +GRS

JAN 28 - FEB 2, 2024
GRAND GALVEZ, GALVESTON, TX
CHAIR: Charles O'Brien
VICE CHAIR: Joy Wu

Chemical Separations +GRS

JAN 21-26, 2024
GRAND GALVEZ, GALVESTON, TX
CHAIRS: Vassiliki-Alexandra Glezakou and Mark Shiflett
VICE CHAIRS: Burcu Gurkan and Jared Anderson

Chemistry and Biology of Peptides +GRS

FEB 11-16, 2024
VENTURA BEACH MARRIOTT, VENTURA, CA
CHAIRS: Yftah Tal-Gan and Elizabeth Denton
VICE CHAIRS: Florence Brunel and Juan Del Valle

Climate Engineering +GRS

FEB 18-23, 2024
RENAISSANCE TUSCANY IL CIOCCO, LUCCA (BARGA), ITALY
CHAIRS: Simone Tilmes and Sarah Doherty
VICE CHAIRS: Michael Diamond and Lili Xia

Colloidal, Macromolecular and Polyelectrolyte Solutions +GRS

FEB 11-16, 2024
FOUR POINTS SHERATON / HOLIDAY INN EXPRESS, VENTURA, CA
CHAIRS: Kelly Schultz and Daeyeon Lee
VICE CHAIRS: Michael Bevan and Jacinta Conrad

DNA Damage, Mutation and Cancer +GRS

MAR 10-15, 2024
VENTURA BEACH MARRIOTT, VENTURA, CA
CHAIR: Jeremy Stark
VICE CHAIR: Shan Zha

Electrochemistry +GRS

JAN 7-12, 2024
FOUR POINTS SHERATON / HOLIDAY INN EXPRESS, VENTURA, CA
CHAIR: Francis Zamborini
VICE CHAIR: Shannon Boettcher

Fibroblast Growth Factors in Development and Disease +GRS

MAR 24-29, 2024
GRAND GALVEZ, GALVESTON, TX
CHAIRS: Amy Merrill and Jarrad Scarlett
VICE CHAIR: Chiara Francavilla

Food Allergy +GRS

JAN 7-12, 2024
VENTURA BEACH MARRIOTT, VENTURA, CA
CHAIRS: Stephanie Eisenbarth and Simon Hogan
VICE CHAIRS: Caroline Sokol and Sarita Patil

THE GRC POWER HOUR™

The GRC Power Hour is designed to address ways to improve diversity and inclusion in science by providing a safe environment for informal and meaningful conversations amongst colleagues of all career stages.

Geobiology +GRS

JAN 14-19, 2024
GRAND GALVEZ, GALVESTON, TX
CHAIRS: Karen Lloyd and Clara Chan
VICE CHAIRS: Victoria Petryshyn and Alex Sessions

Glycolipid and Sphingolipid Biology +GRS

FEB 18-23, 2024
GRAND GALVEZ, GALVESTON, TX
CHAIR: Maurizio Del Poeta
VICE CHAIRS: Giovanni D'Angelo and Gerhild Van Echten-Deckert

Immunoengineering +GRS

FEB 11-16, 2024
RENAISSANCE TUSCANY IL CIOCCO, LUCCA (BARGA), ITALY
CHAIRS: Susan Thomas and Madhav Dhodapkar
VICE CHAIRS: Yvonne Chen and Marco Colonna

Ligand Recognition and Molecular Gating +GRS

MAR 24-29, 2024
VENTURA BEACH MARRIOTT, VENTURA, CA
CHAIR: Kaspar Locher
VICE CHAIRS: Simon Scheuring and Inga Hänelt

Liquid Phase Electron Microscopy +GRS

JAN 28 - FEB 2, 2024
RENAISSANCE TUSCANY IL CIOCCO, LUCCA (BARGA), ITALY
CHAIRS: Frances Ross and Nathan Gianneschi
VICE CHAIRS: Haimei Zheng and Taylor Woehl

Lymphatics +GRS

MAR 3-8, 2024
FOUR POINTS SHERATON / HOLIDAY INN EXPRESS, VENTURA, CA
CHAIRS: Hong Chen and Ben Hogan
VICE CHAIRS: Tatiana Petrova and Brant Weinstein

Marine Natural Products +GRS

MAR 10-15, 2024
FOUR POINTS SHERATON / HOLIDAY INN EXPRESS, VENTURA, CA
CHAIR: Hendrik Luesch
VICE CHAIR: Marcy Balunas

Mechanical Systems in the Quantum Regime +GRS

MAR 3-8, 2024
VENTURA BEACH MARRIOTT, VENTURA, CA
CHAIRS: Thomas Purdy and Amir Safavi-Naeini
VICE CHAIRS: Yiwen Chu and Albert Schliesser

Metals in Biology +GRS

JAN 21-26, 2024
FOUR POINTS SHERATON / HOLIDAY INN EXPRESS, VENTURA, CA
CHAIR: Stephen Ragsdale
VICE CHAIR: Sarah Michel

Molecular and Ionic Clusters +GRS

FEB 4-9, 2024
FOUR POINTS SHERATON / HOLIDAY INN EXPRESS, VENTURA, CA
CHAIRS: Martin Beyer and Caroline Jarrold
VICE CHAIRS: Stuart Mackenzie and Laura McCaslin

Multifunctional Materials and Structures +GRS

JAN 28 - FEB 2, 2024
VENTURA BEACH MARRIOTT, VENTURA, CA
CHAIRS: Chiara Daraio and Ioannis Chasiotis
VICE CHAIRS: Gregory Reich and H. Jerry Qi

Myelin +GRS

MAR 17-22, 2024
FOUR POINTS SHERATON / HOLIDAY INN EXPRESS, VENTURA, CA
CHAIRS: Terri Wood and Jonah Chan
VICE CHAIRS: Laura Feltri and David Lyons

Neuroelectronic Interfaces +GRS

MAR 10-15, 2024
GRAND GALVEZ, GALVESTON, TX
CHAIRS: Jack Judy and Stéphanie Lacour
VICE CHAIRS: Cristin Welle and Maria Asplund

New Antibacterial Discovery and Development +GRS

MAR 17-22, 2024
VENTURA BEACH MARRIOTT, VENTURA, CA
CHAIRS: Peter Smith and Silvia Cardona
VICE CHAIR: Georgina Cox

Photosensory Receptors and Signal Transduction +GRS

MAR 3-8, 2024
RENAISSANCE TUSCANY IL CIOCCO, LUCCA (BARGA), ITALY
CHAIR: Brian Crane
VICE CHAIR: Eirini Kaiserli

Plasminogen Activation and Extracellular Proteolysis +GRS

FEB 18-23, 2024
FOUR POINTS SHERATON / HOLIDAY INN EXPRESS, VENTURA, CA
CHAIRS: Li Zhang and Ruby Law
VICE CHAIRS: Ze Zheng and Paul Kim

Predator-Prey Interactions +GRS

JAN 28 - FEB 2, 2024
FOUR POINTS SHERATON / HOLIDAY INN EXPRESS, VENTURA, CA
CHAIRS: Bridie Allan and Michael Sheriff
VICE CHAIRS: Barney Luttbeg and Kaitlyn Gaynor

Protein Folding Dynamics +GRS

JAN 7-12, 2024
GRAND GALVEZ, GALVESTON, TX
CHAIRS: Robert Best and Martin Gruebele
VICE CHAIRS: Caitlin Davis and Eugene Shakhnovich

Renewable Energy: Solar Fuels +GRS

FEB 4-9, 2024
VENTURA BEACH MARRIOTT, VENTURA, CA
CHAIRS: Can Li and Jillian Dempsey
VICE CHAIRS: Vincent Artero and Francesca Maria Toma

Robotics +GRS

JAN 14-19, 2024
FOUR POINTS SHERATON / HOLIDAY INN EXPRESS, VENTURA, CA
CHAIRS: Cecilia Laschi and Metin Sitti
VICE CHAIRS: Auke Ijspeert and Vijay Kumar

Sensory Transduction in Microorganisms +GRS

JAN 21-26, 2024
VENTURA BEACH MARRIOTT, VENTURA, CA
CHAIR: Birgit Scharf
VICE CHAIR: Ariane Briegel

Sleep Regulation and Function +GRS

MAR 3-8, 2024
GRAND GALVEZ, GALVESTON, TX
CHAIR: Derk-Jan Dijk
VICE CHAIRS: Ying-Hui Fu and Janet Mullington

Thalamocortical Interactions +GRS

FEB 18-23, 2024
VENTURA BEACH MARRIOTT, VENTURA, CA
CHAIRS: Jeanne Paz and Adam Hantman
VICE CHAIRS: Solange Brown and Farran Briggs

Ultrafast Phenomena in Cooperative Systems +GRS

FEB 4-9, 2024
RENAISSANCE TUSCANY IL CIOCCO, LUCCA (BARGA), ITALY
CHAIR: Daniele Fausti
VICE CHAIR: Prineha Narang

May–August 2024

Additive Manufacturing of Soft Materials +GRS

AUG 11-16, 2024
BRYANT UNIVERSITY, SMITHFIELD, RI
CHAIRS: Timothy Long and AJ Boydston
VICE CHAIRS: Callie Higgins and Alshakim Nelson

Aqueous Corrosion +GRS

JUL 7-12, 2024
COLBY-SAWYER COLLEGE, NEW LONDON, NH
CHAIR: Mary Ryan
VICE CHAIRS: Jenifer Locke and Arjan Mol

Auditory System +GRS

JUL 14-19, 2024
BRYANT UNIVERSITY, SMITHFIELD, RI
CHAIR: Allison Coffin
VICE CHAIR: Michael Roberts

Bacterial Cell Surfaces +GRS

JUN 23-28, 2024
MOUNT SNOW, WEST DOVER, VT
CHAIRS: Natividad Ruiz and Jean-Francois Collet
VICE CHAIRS: Rut Carballido-Lopez and Thomas Bernhardt

Barriers of the CNS +GRS

JUN 9-14, 2024
COLBY-SAWYER COLLEGE, NEW LONDON, NH
CHAIR: Matthew Campbell
VICE CHAIR: Dionna Williams

Bioanalytical Sensors +GRS

JUN 23-28, 2024
SALVE REGINA UNIVERSITY, NEWPORT, RI
CHAIRS: Charles Mace and Chenzhong Li
VICE CHAIRS: Rebecca Whelan and Matthew Lockett

Biocatalysis +GRS

JUL 7-12, 2024
SOUTHERN NEW HAMPSHIRE UNIVERSITY, MANCHESTER, NH
CHAIRS: Sabine Flitsch and Carlos Martinez
VICE CHAIRS: Radka Snajdrova and Mélanie Hall

Biogenic Hydrocarbons and the Atmosphere +GRS

JUN 9-14, 2024
REY DON JAIME GRAND HOTEL, CASTELLDEFELS, SPAIN
CHAIRS: Kirsti Ashworth and Zhaozhong Feng
VICE CHAIRS: Karena McKinney and Armin Hansel

Bioinspired Materials +GRS

JUN 16-21, 2024
LES DIABLERETS CONFERENCE CENTER, LES DIABLERETS, SWITZERLAND
CHAIRS: Christoph Weder and Molly Stevens
VICE CHAIRS: Cole DeForest and Ullrich Steiner

Biointerface Science +GRS

JUN 16-21, 2024
RENAISSANCE TUSCANY IL CIOCCO, LUCCA (BARGA), ITALY
CHAIR: Katharina Maniura
VICE CHAIR: Khalid Salaita

"At the core of any GRC is exceptional technical programming and a vibrant scientific community."

DR. KRISTI ANSETH, University of Colorado Boulder

Biology of Host-Parasite Interactions +GRS

JUN 9-14, 2024
SALVE REGINA UNIVERSITY, NEWPORT, RI
CHAIRS: Gary Ward and F. Nina Papavasiliou
VICE CHAIRS: Laura Knoll and Gerald Spaeth

Biomineralization +GRS

AUG 4-9, 2024
COLBY-SAWYER COLLEGE, NEW LONDON, NH
CHAIR: Nils Kröger
VICE CHAIR: Lara Estroff

Bioorganic Chemistry +GRS

JUN 9-14, 2024
PROCTOR ACADEMY, ANDOVER, NH
CHAIRS: Amanda Hargrove and Jeremy Baryza

Calcium Signaling +GRS

JUN 30 - JUL 5, 2024
RENAISSANCE TUSCANY IL CIOCCO, LUCCA (BARGA), ITALY
CHAIRS: Ivan Bogeski and Cristina Mammucari
VICE CHAIRS: Ivana Kuo and Jeremy Smyth

Cardiac Regulatory Mechanisms +GRS

JUN 23-28, 2024
COLBY-SAWYER COLLEGE, NEW LONDON, NH
CHAIRS: Rong Tian and Benjamin Prosser
VICE CHAIRS: Lucie Carrier and Timothy McKinsey

Catalysis +GRS

JUN 16-21, 2024
COLBY-SAWYER COLLEGE, NEW LONDON, NH
CHAIR: Javier Guzman
VICE CHAIR: Eranda Nikolla

Cell Biology of the Neuron +GRS

JUN 23-28, 2024
WATERVILLE VALLEY, WATERVILLE VALLEY, NH
CHAIRS: Monica Driscoll and Patrik Verstreken
VICE CHAIRS: Rejji Kuruvilla and Giampietro Schiavo

Cell Death +GRS

JUL 28 - AUG 2, 2024
JORDAN HOTEL AT SUNDAY RIVER, NEWRY, ME
CHAIR: Pascal Meier
VICE CHAIR: Ana Garcia-Saez

Cell Polarity Signaling +GRS

JUN 2-7, 2024
SOUTHERN NEW HAMPSHIRE UNIVERSITY, MANCHESTER, NH
CHAIR: Yukiko Yamashita
VICE CHAIRS: Danelle Devenport and Jessica Feldman

Cellular and Molecular Fungal Biology +GRS

JUN 16-21, 2024
HOLDERNESS SCHOOL, HOLDERNESS, NH
CHAIRS: Nick Talbot and Anna Selmecki
VICE CHAIRS: Bridget Barker and Elaine Bignell

Centromere Biology +GRS

JUL 28 - AUG 2, 2024
MOUNT SNOW, WEST DOVER, VT
CHAIRS: Iain Cheeseman and Barbara Mellone
VICE CHAIRS: Daniel Foltz and Elaine Dunleavy

Chemistry and Biology of Tetrapyrroles +GRS

JUL 14-19, 2024
SALVE REGINA UNIVERSITY, NEWPORT, RI
CHAIR: Amy Medlock
VICE CHAIR: Celia Goulding

Chemotactic Cytokines +GRS

JUN 2-7, 2024
MOUNT SNOW, WEST DOVER, VT
CHAIR: Ronen Alon
VICE CHAIR: Daniel Legler

Chromatin Structure and Function +GRS

JUL 7-12, 2024
BRYANT UNIVERSITY, SMITHFIELD, RI
CHAIR: Geeta Narlikar
VICE CHAIR: Andreas Ladurner

Colloidal Semiconductor Nanocrystals +GRS

JUN 30 - JUL 5, 2024
LES DIABLERETS CONFERENCE CENTER, LES DIABLERETS, SWITZERLAND
CHAIRS: Gordana Dukovic and Efrat Lifshitz
VICE CHAIRS: Brandi Cossairt and Raffaella Buonsanti

Computational Chemistry +GRS

JUL 21-26, 2024
MOUNT SNOW, WEST DOVER, VT
CHAIRS: Natalie Fey and Robert Paton
VICE CHAIRS: Marco De Vivo and Rommie Amaro

Computational Materials Science and Engineering +GRS

JUL 21-26, 2024
JORDAN HOTEL AT SUNDAY RIVER, NEWRY, ME
CHAIRS: Katsuyo Thornton and Heather Kulik
VICE CHAIRS: Yaroslava Yingling and André Schleife

Correlated Electron Systems +GRS

JUN 23-28, 2024
MOUNT HOLYOKE COLLEGE, SOUTH HADLEY, MA
CHAIRS: Senthil Todadri and Suchitra Sebastian
VICE CHAIRS: Jie Shan and Ashvin Vishwanath

Craniofacial Morphogenesis and Tissue Regeneration +GRS

MAY 26-31, 2024
REY DON JAIME GRAND HOTEL, CASTELLDEFELS, SPAIN
CHAIR: Gage Crump
VICE CHAIRS: Samantha Brugmann and Karen Liu

Crystal Engineering +GRS

JUN 23-28, 2024
GRAND SUMMIT HOTEL AT SUNDAY RIVER, NEWRY, ME
CHAIR: Andy Cooper
VICE CHAIR: Susan Reutzel-Edens

Cyclic Nucleotide Phosphodiesterases +GRS

JUN 16-21, 2024
BATES COLLEGE, LEWISTON, ME
CHAIRS: Viacheslav Nikolaev and Michy Kelly
VICE CHAIRS: Leila Gobejishvili and Finn Olav Levy

Cytoskeletal Motors +GRS

JUL 7-12, 2024
MOUNT SNOW, WEST DOVER, VT
CHAIR: Margaret Titus
VICE CHAIR: Richard McKenney

Defects in Semiconductors +GRS

AUG 4-9, 2024
JORDAN HOTEL AT SUNDAY RIVER, NEWRY, ME
CHAIR: Kai-Mei Fu
VICE CHAIR: Joel Varley

Drug Carriers in Medicine and Biology +GRS

AUG 4-9, 2024
MOUNT SNOW, WEST DOVER, VT
CHAIRS: Kathryn Whitehead and Vadim Dudkin
VICE CHAIRS: Theresa Reineke and Natalie Artzi

Drug Metabolism +GRS

JUL 7-12, 2024
HOLDERNESS SCHOOL, HOLDERNESS, NH
CHAIR: John Harrelson
VICE CHAIR: Mitchell Taub

Drug Resistance +GRS

JUN 23-28, 2024
BRYANT UNIVERSITY, SMITHFIELD, RI
CHAIRS: Alexis Kaushansky and Amir Mitchell
VICE CHAIRS: Priscilla Yang and Zemer Gitai

Electron Donor-Acceptor Interactions +GRS

JUL 28 - AUG 2, 2024
SALVE REGINA UNIVERSITY, NEWPORT, RI
CHAIRS: Lin Chen and Ferdinand Grozema
VICE CHAIRS: Jeffrey Rack and Gemma Solomon

Electronic Processes in Organic Materials +GRS

JUL 7-12, 2024
RENAISSANCE TUSCANY IL CIOCCO, LUCCA (BARGA), ITALY
CHAIRS: Garry Rumbles and Gitti Frey
VICE CHAIRS: Yana Vaynzof and Thuc-Quyen Nguyen

Endothelial Cell Phenotypes in Health and Disease +GRS

JUN 30 - JUL 5, 2024
REY DON JAIME GRAND HOTEL, CASTELLDEFELS, SPAIN
CHAIR: Christiana Ruhrberg
VICE CHAIR: Timothy Hla

Energetic Materials +GRS

JUN 2-7, 2024
GRAND SUMMIT HOTEL AT SUNDAY RIVER, NEWRY, ME
CHAIR: Lori Groven
VICE CHAIRS: Jennifer Gottfried and Carole Morrison

Environmental Endocrine Disruptors

JUN 23-28, 2024
RENAISSANCE TUSCANY IL CIOCCO, LUCCA (BARGA), ITALY
CHAIRS: Juliette Legler and Angel Nadal
VICE CHAIRS: Laura Vandenberg and Chris Kassotis

Environmental Sciences: Water

JUN 23-28, 2024
HOLDERNESS SCHOOL, HOLDERNESS, NH
CHAIRS: Thomas Hofstetter and Christy Remucal
VICE CHAIR: Rainer Lohmann

Enzymes, Coenzymes and Metabolic Pathways

JUL 28 - AUG 2, 2024
WATERVILLE VALLEY, WATERVILLE VALLEY, NH
CHAIRS: Pablo Sobrado and Erika Taylor
VICE CHAIRS: Randy Kipp and Y. Jessie Zhang

Epithelial Stem Cells and Niches

AUG 11-16, 2024
REY DON JAIME GRAND HOTEL, CASTELLDEFELS, SPAIN
CHAIRS: Ophir Klein and Kim Jensen
VICE CHAIRS: Sarah Knox and Kara McKinley

Extracellular Vesicles

JUL 28 - AUG 2, 2024
GRAND SUMMIT HOTEL AT SUNDAY RIVER, NEWRY, ME
CHAIRS: Esther Nolte-'t Hoen and Edit Buzas
VICE CHAIRS: Lucia Languino and Eva Rohde

Flow and Transport in Permeable Media

JUL 14-19, 2024
GRAND SUMMIT HOTEL AT SUNDAY RIVER, NEWRY, ME
CHAIR: Marc Hesse
VICE CHAIRS: Masa Prodanovic and Joaquin Jimenez-Martinez

Fragile X and Autism-Related Disorders

MAY 12-17, 2024
RENAISSANCE TUSCANY IL CIOCCO, LUCCA (BARGA), ITALY
CHAIR: Kimberly Huber
VICE CHAIRS: Sebastian Jacquemont and David Nelson

Frontal Cortex

AUG 4-9, 2024
HOLDERNESS SCHOOL, HOLDERNESS, NH
CHAIRS: Rebecca Shansky and David Moorman
VICE CHAIRS: Shannon Gourley and Maria Diehl

Fuel Cells

JUL 28 - AUG 2, 2024
BRYANT UNIVERSITY, SMITHFIELD, RI
CHAIRS: Iryna Zenyuk and Vojislav Stamenkovic
VICE CHAIRS: Shawn Litster and Jasna Jankovic

Genetic Biocontrol

MAY 19-24, 2024
REY DON JAIME GRAND HOTEL, CASTELLDEFELS, SPAIN
CHAIRS: Omar Akbari and Yoosook Lee
VICE CHAIRS: Molly Duman Scheel and Bruce Hay

Geochemistry of Mineral Deposits

JUN 23-28, 2024
JORDAN HOTEL AT SUNDAY RIVER, NEWRY, ME
CHAIR: Isabelle Chambefort
VICE CHAIRS: Natalie Caciagli and Marco Fiorentini

Granular Matter

JUN 23-28, 2024
STONEHILL COLLEGE, EASTON, MA
CHAIRS: Kimberly Hill and Joshua Dijksman
VICE CHAIRS: Kerstin Nordstrom and Christopher Ness

Green Chemistry

JUL 28 - AUG 2, 2024
REY DON JAIME GRAND HOTEL, CASTELLDEFELS, SPAIN
CHAIRS: Audrey Moores and Jinlong Gong
VICE CHAIRS: Mahdi Abu-Omar and Martina Peters

"GRCs are among the most venerable and outstanding conferences with an ideal format to encourage interactions among scientists."

DR. DAVID WEITZ, Harvard University

Hemostasis +GRS

AUG 4-9, 2024
WATERVILLE VALLEY, WATERVILLE VALLEY, NH
CHAIR: Gow Arepally
VICE CHAIRS: A. Valance Washington and Marvin Nieman

Heterocyclic Compounds +GRS

JUN 16-21, 2024
SALVE REGINA UNIVERSITY, NEWPORT, RI
CHAIR: Eric Voight
VICE CHAIR: Anita Mattson

Hypothalamus +GRS

JUL 28 - AUG 2, 2024
BATES COLLEGE, LEWISTON, ME
CHAIRS: Matt Carter and Alexander Jackson
VICE CHAIRS: Stephanie Correa and Annegret Falkner

Image Science +GRS

JUN 9-14, 2024
GRAND SUMMIT HOTEL AT SUNDAY RIVER, NEWRY, ME
CHAIR: Jannick Rolland
VICE CHAIR: Sylvain Gigan

Immunochemistry and Immunobiology +GRS

JUN 16-21, 2024
GRAND SUMMIT HOTEL AT SUNDAY RIVER, NEWRY, ME
CHAIR: Alexander Rudensky
VICE CHAIRS: Carla Rothlin and Matteo Iannacone

Immunometabolism in Health and Disease +GRS

JUN 16-21, 2024
BRYANT UNIVERSITY, SMITHFIELD, RI
CHAIRS: Jeff Rathmell and Catherine 'Lynn' Hedrick
VICE CHAIRS: Ping-Chih Ho and Nancie MacIver

In Vivo Magnetic Resonance +GRS

JUL 14-19, 2024
PROCTOR ACADEMY, ANDOVER, NH
CHAIR: Kim Butts Pauly
VICE CHAIR: Karin Shmueli

In Vivo Ultrasound Imaging +GRS

AUG 25-30, 2024
MOUNT SNOW, WEST DOVER, VT
CHAIRS: Michael Kolios and Oliver Kripfgans
VICE CHAIRS: Hong Chen and Agata Exner

Industrial Ecology +GRS

MAY 26-31, 2024
LES DIABLERETS CONFERENCE CENTER, LES DIABLERETS, SWITZERLAND
CHAIR: Ming Xu
VICE CHAIR: Matthew Eckelman

Inorganic Chemistry +GRS

JUN 2-7, 2024
SALVE REGINA UNIVERSITY, NEWPORT, RI
CHAIR: Jacqueline Veauthier
VICE CHAIR: Ellen Matson

Intermediate Filaments +GRS

JUN 16-21, 2024
REY DON JAIME GRAND HOTEL, CASTELLDEFELS, SPAIN
CHAIRS: Elly Hol and Howard Worman
VICE CHAIRS: Gisele Bonne and Giulio Agnetti

Intrinsically Disordered Proteins +GRS

JUN 23-28, 2024
LES DIABLERETS CONFERENCE CENTER, LES DIABLERETS, SWITZERLAND
CHAIRS: Birthe B. Kragelund and Tanja Mittag
VICE CHAIRS: Xavier Salvatella and Shahar Sukenik

Ion Channels +GRS

JUL 7-12, 2024
MOUNT HOLYOKE COLLEGE, SOUTH HADLEY, MA
CHAIRS: Teresa Giraldez and Baron Chanda
VICE CHAIRS: Sudha Chakrapani and Julio Cordero-Morales

Ionic Liquids +GRS

AUG 4-9, 2024
GRAND SUMMIT HOTEL AT SUNDAY RIVER, NEWRY, ME
CHAIR: Jared Anderson
VICE CHAIR: Claudio Margulis

Lignin +GRS

JUL 14-19, 2024
STONEHILL COLLEGE, EASTON, MA
CHAIRS: Laura Bartley and Jeremy Luterbacher
VICE CHAIRS: Mojgan Nejad and Yuki Tobimatsu

Lipidomics

MAY 5-10, 2024
RENAISSANCE TUSCANY IL CIOCCO, LUCCA (BARGA), ITALY
CHAIRS: Gerhard Liebisch and Xianlin Han
VICE CHAIRS: Erin Baker and Jeffrey McDonald

Lipoprotein Metabolism

JUN 2-7, 2024
WATERVILLE VALLEY, WATERVILLE VALLEY, NH
CHAIRS: Marlys Koschinsky and Daisy Sahoo
VICE CHAIRS: J. Mark Brown and Thomas Vallim

Lysosomes and Endocytosis

JUN 16-21, 2024
PROCTOR ACADEMY, ANDOVER, NH
CHAIR: Phyllis Hanson
VICE CHAIR: Graca Raposo

Mammalian Reproduction

Jul 21-26, 2024
Rey Don Jaime Grand Hotel, Castelldefels, Spain
CHAIRS: Richard Freiman and Joan Jorgensen
VICE CHAIRS: James Turner and Julie Kim

Mammary Gland Biology

JUN 2-7, 2024
RENAISSANCE TUSCANY IL CIOCCO, LUCCA (BARGA), ITALY
CHAIRS: Walid Khaled and Leonie Young
VICE CHAIRS: Traci Lyons and Eran Andrechek

Marine Microbes

JUN 9-14, 2024
LES DIABLERETS CONFERENCE CENTER, LES DIABLERETS, SWITZERLAND
CHAIR: Lasse Riemann
VICE CHAIR: Naomi Levine

Mechanisms of Epilepsy and Neuronal Synchronization

Aug 18-23, 2024
Mount Snow, West Dover, VT
CHAIRS: Helen Scharfman and Viji Santhakumar
VICE CHAIRS: Esther Krook-Magnuson and Ethan Goldberg

Medicinal Chemistry

AUG 11-16, 2024
COLBY-SAWYER COLLEGE, NEW LONDON, NH
CHAIR: Erin DiMauro

Meiosis

JUN 2-7, 2024
COLBY-SAWYER COLLEGE, NEW LONDON, NH
CHAIR: Jeff Sekelsky
VICE CHAIR: Needhi Bhalla

Membrane Transport Proteins

JUL 21-26, 2024
GRAND SUMMIT HOTEL AT SUNDAY RIVER, NEWRY, ME
CHAIRS: Renae Ryan and Susan Ingram
VICE CHAIRS: Habibeh Khoshbouei and Hanne Poulsen

Membranes: Materials and Processes

JUL 28 - AUG 2, 2024
COLBY-SAWYER COLLEGE, NEW LONDON, NH
CHAIRS: J.R. Johnson and Lucy Mar Camacho
VICE CHAIRS: Haiqing Lin and Hee Jeung Oh

Metallocofactors

JUN 9-14, 2024
STONEHILL COLLEGE, EASTON, MA
CHAIR: Kyle Lancaster
VICE CHAIR: Kelly Chacon

Metals in Medicine

JUN 23-28, 2024
PROCTOR ACADEMY, ANDOVER, NH
CHAIRS: Carolyn Anderson and Anne-Kathrin Duhme-Klair
VICE CHAIRS: Maria Contel and Gilles Gasser

Microbial Stress Response

JUL 14-19, 2024
MOUNT HOLYOKE COLLEGE, SOUTH HADLEY, MA
CHAIRS: Amy Schmid and Peter Chien
VICE CHAIRS: Christina Stallings and Frederic Barras

"GRCs are an excellent mechanism for building communities that support career advancement for junior and senior scientists alike. GRCs in recent years have helped promote diversity and inclusion among their participants."

DR. CYNTHIA BURROWS, University of Utah

Microbial Toxins and Pathogenicity +GRS

JUL 14-19, 2024
WATERVILLE VALLEY, WATERVILLE VALLEY, NH
CHAIR: Mary O'Riordan
VICE CHAIR: Victor Torres

Mitochondria and Chloroplasts +GRS

JUL 7-12, 2024
REY DON JAIME GRAND HOTEL, CASTELLDEFELS, SPAIN
CHAIR: Antoni Barrientos
VICE CHAIR: Andreas Weber

Molecular and Cellular Neurobiology +GRS

MAY 26-31, 2024
RENAISSANCE TUSCANY IL CIOCCO, LUCCA (BARGA), ITALY
CHAIR: Mingjie Zhang
VICE CHAIRS: Tianyi Mao and Matthew Dalva

Molecular Basis of Microbial One-Carbon Metabolism +GRS

AUG 11-16, 2024
WATERVILLE VALLEY, WATERVILLE VALLEY, NH
CHAIR: Christopher Marx
VICE CHAIRS: Marina Kalyuzhnaya and Tobias Erb

Molecular Interactions and Dynamics +GRS

JUL 7-12, 2024
STONEHILL COLLEGE, EASTON, MA
CHAIR: Ricardo Metz
VICE CHAIR: Joseph Subotnik

Multiphoton Processes +GRS

JUN 9-14, 2024
BRYANT UNIVERSITY, SMITHFIELD, RI
CHAIRS: Nirit Dudovich and Daniel Rolles
VICE CHAIRS: Marc Vrakking and Albert Stolow

Multiscale Mechanochemistry and Mechanobiology +GRS

JUL 21-26, 2024
BATES COLLEGE, LEWISTON, ME
CHAIR: Kerstin Blank
VICE CHAIRS: Anna Tarakanova and Stephen Schrettl

Multiscale Plant Vascular Biology +GRS

JUN 9-14, 2024
MOUNT SNOW, WEST DOVER, VT
CHAIRS: Rachel Spicer and Walid Sadok
VICE CHAIRS: Jessica Guo and Daniel Johnson

Musculoskeletal Biology and Bioengineering +GRS

AUG 4-9, 2024
PROCTOR ACADEMY, ANDOVER, NH
CHAIR: Louis DeFrate
VICE CHAIRS: Alayna Loiselle and Constance Chu

Mutagenesis +GRS

JUN 16-21, 2024
WATERVILLE VALLEY, WATERVILLE VALLEY, NH
CHAIR: Houra Merrikh
VICE CHAIR: Marcel Tijsterman

Nanoscale Science and Engineering for Agriculture and Food Systems +GRS

JUN 23-28, 2024
SOUTHERN NEW HAMPSHIRE UNIVERSITY, MANCHESTER, NH
CHAIRS: Carmen Gomes and Melanie Kah
VICE CHAIRS: Timothy Duncan and Jason White

Nasopharyngeal Carcinoma +GRS

JUN 2-7, 2024
LES DIABLERETS CONFERENCE CENTER, LES DIABLERETS, SWITZERLAND
CHAIRS: Mu Sheng Zeng and Alan Chiang
VICE CHAIRS: Brigette Ma and Shannon Kenney

Natural Products and Bioactive Compounds +GRS

JUL 28 - AUG 2, 2024
PROCTOR ACADEMY, ANDOVER, NH
CHAIR: Dirk Trauner
VICE CHAIRS: Cheryl Hayward and David Sarlah

Neural Development +GRS

JUL 28 - AUG 2, 2024
RENAISSANCE TUSCANY IL CIOCCO, LUCCA (BARGA), ITALY
CHAIR: Debby Silver
VICE CHAIR: Bassem Hassan

Neural Mechanisms of Acoustic Communication +GRS

JUL 28 - AUG 2, 2024
MOUNT HOLYOKE COLLEGE, SOUTH HADLEY, MA
CHAIRS: Mala Murthy and Marc Schmidt
VICE CHAIRS: Alison Barker and Vikram Gadagkar

Neurobiology of Brain Disorders +GRS

AUG 4-9, 2024
REY DON JAIME GRAND HOTEL, CASTELLDEFELS, SPAIN
CHAIRS: Karen Duff and Chris Shaw
VICE CHAIRS: Michael Ward and Hemali Phatnani

Neurobiology of Cognition +GS

JUL 21-26, 2024
WATERVILLE VALLEY, WATERVILLE VALLEY, NH
CHAIRS: Joni Wallis and Aaron Batista
VICE CHAIRS: Erin Rich and Theresa Desrochers

Neurobiology of Drug Addiction +GS

AUG 18-23, 2024
GRAND SUMMIT HOTEL AT SUNDAY RIVER, NEWRY, ME
CHAIRS: Marina Picciotto and Serge Ahmed
VICE CHAIRS: Diana Martinez and Nii Addy

Noble Metal Nanoparticles +GS

JUN 16-21, 2024
MOUNT HOLYOKE COLLEGE, SOUTH HADLEY, MA
CHAIR: Gregory Hartland
VICE CHAIR: David Masiello

Notch Signaling in Development, Regeneration and Disease +GS

JUL 14-19, 2024
BATES COLLEGE, LEWISTON, ME
CHAIRS: Anna Bigas and Robert Haltiwanger
VICE CHAIRS: Wendy Gordon and Emma Andersson

Ocean Mixing +GS

JUN 9-14, 2024
MOUNT HOLYOKE COLLEGE, SOUTH HADLEY, MA
CHAIRS: Sonya Legg and Alberto Naveira Garabato
VICE CHAIRS: Yueng Lenn and Leif Thomas

Optics and Photonics in Medicine and Biology +GS

JUL 7-12, 2024
BATES COLLEGE, LEWISTON, ME
CHAIRS: E. Duco Jansen and Snow Tseng
VICE CHAIRS: Alex Vitkin and Euiheon Chung

Optogenetic Approaches to Understanding Neural Circuits and Behavior +GS

JUL 21-26, 2024
RENAISSANCE TUSCANY IL CIOCCO, LUCCA (BARGA), ITALY
CHAIR: Ofer Yizhar
VICE CHAIRS: Steve Ramirez and Bianca Jones Marlin

Organic Geochemistry +GS

JUL 28 - AUG 2, 2024
HOLDERNESS SCHOOL, HOLDERNESS, NH
CHAIR: Anna Martini
VICE CHAIR: Julio Sepúlveda

Organic Reactions and Processes +GS

JUL 21-26, 2024
BRYANT UNIVERSITY, SMITHFIELD, RI
CHAIRS: Philip Wheeler and Alexander Grenning
VICE CHAIR: Andrew Harned

Organometallic Chemistry +GS

JUL 7-12, 2024
SALVE REGINA UNIVERSITY, NEWPORT, RI
CHAIR: Paula Diaconescu

Oscillations and Dynamic Instabilities in Chemical Systems +GS

JUL 14-19, 2024
LES DIABLERETS CONFERENCE CENTER, LES DIABLERETS, SWITZERLAND
CHAIR: Carsten Beta
VICE CHAIR: Sumana Dutta

Phosphorylation and G-Protein Mediated Signaling Networks +GS

JUN 9-14, 2024
WATERVILLE VALLEY, WATERVILLE VALLEY, NH
CHAIR: Alan Smrcka
VICE CHAIR: Angeline Lyon

Plant and Microbial Cytoskeleton +GS

AUG 11-16, 2024
PROCTOR ACADEMY, ANDOVER, NH
CHAIRS: Sophie Martin and Alexander Paredez
VICE CHAIRS: Alex Bisson and Sabine Mueller

Plant Molecular Biology +GS

JUN 9-14, 2024
HOLDERNESS SCHOOL, HOLDERNESS, NH
CHAIR: Rebecca Mosher
VICE CHAIR: Maria Harrison

Plasma Processing Science +GS

JUL 21-26, 2024
PROCTOR ACADEMY, ANDOVER, NH
CHAIR: Lorenzo Mangolini
VICE CHAIR: Sylvain Coulombe

Plasmonics and Nanophotonics +GS

JUL 7-12, 2024
GRAND SUMMIT HOTEL AT SUNDAY RIVER, NEWRY, ME
CHAIR: Javier Aizpurua
VICE CHAIR: Jason Valentine

Polymer Physics +GS

JUL 21-26, 2024
MOUNT HOLYOKE COLLEGE, SOUTH HADLEY, MA
CHAIR: Rachel Segalman
VICE CHAIR: Arthi Jayaraman

Post-Transcriptional Gene Regulation +GS

JUL 14-19, 2024
MOUNT SNOW, WEST DOVER, VT
CHAIRS: Karla Neugebauer and Nicholas Conrad
VICE CHAIRS: Wendy Gilbert and Auinash Kalsotra

Protein Processing, Trafficking and Secretion +GS

JUL 14-19, 2024
COLBY-SAWYER COLLEGE, NEW LONDON, NH
CHAIRS: Julia von Blume and Mondira Kundu
VICE CHAIR: Jason Gestwicki

Proteoglycans +GS

JUL 7-12, 2024
PROCTOR ACADEMY, ANDOVER, NH
CHAIRS: Catherine Merry and Alyssa Panitch
VICE CHAIRS: Jian Liu and Rashmin Savani

Proteolytic Enzymes and Their Inhibitors +GS

JUN 9-14, 2024
RENAISSANCE TUSCANY IL CIOCCO, LUCCA (BARGA), ITALY
CHAIR: Jeanne Hardy
VICE CHAIR: Galia Blum

Quantum Science +GS

JUL 28 - AUG 2, 2024
STONEHILL COLLEGE, EASTON, MA
CHAIRS: Susanne Yelin and Jonathan Simon
VICE CHAIRS: Eun-Ah Kim and Ania Bleszynski-Jayich

Radionuclide Theranostics for the Management of Cancer +GS

JUL 7-12, 2024
JORDAN HOTEL AT SUNDAY RIVER, NEWRY, ME
CHAIRS: Elcin Zan and Michael Schultz
VICE CHAIRS: Ken Herrmann and Oluwatayo Ikotun

Research at High Pressure +GS

JUL 14-19, 2024
HOLDERNESS SCHOOL, HOLDERNESS, NH
CHAIR: Chris Pickard
VICE CHAIR: Timothy Strobel

Rock Deformation +GS

AUG 4-9, 2024
BATES COLLEGE, LEWISTON, ME
CHAIR: Heather Savage
VICE CHAIRS: Christine McCarthy and Lars Hansen

Salt and Water Stress in Plants +GS

AUG 25-30, 2024
GRAND SUMMIT HOTEL AT SUNDAY RIVER, NEWRY, ME
CHAIRS: Thomas Juenger and Amelia Henry
VICE CHAIRS: Siobhan Brady and Paul Verslues

Scientific Methods in Cultural Heritage Research +GS

JUL 7-12, 2024
LES DIABLERETS CONFERENCE CENTER, LES DIABLERETS, SWITZERLAND
CHAIRS: Admir Masic and Costanza Miliani
VICE CHAIRS: Samuel Webb and Ilaria Bonaduce

Signal Transduction by Engineered Extracellular Matrices +GS

JUL 21-26, 2024
SOUTHERN NEW HAMPSHIRE UNIVERSITY, MANCHESTER, NH
CHAIRS: Shelly Peyton and Sanjay Kumar
VICE CHAIRS: Beth Pruitt and Kelly Stevens

Signaling by Adhesion Receptors +GS

JUL 14-19, 2024
SOUTHERN NEW HAMPSHIRE UNIVERSITY, MANCHESTER, NH
CHAIR: Patrick Derksen
VICE CHAIRS: Maddy Parsons and Alex Dunn

Single Molecule Approaches to Biology +GS

JUL 14-19, 2024
JORDAN HOTEL AT SUNDAY RIVER, NEWRY, ME
CHAIRS: Samuel Hess and Suliana Manley
VICE CHAIRS: Sonja Schmid and Kevin Welsher

Single-Cell Cancer Biology +GS

JUN 9-14, 2024
SOUTHERN NEW HAMPSHIRE UNIVERSITY, MANCHESTER, NH
CHAIRS: Mario Suva and Sohrab Shah
VICE CHAIRS: Devon Lawson and Ken Chen

Single-Cell Genomics +GS

MAY 19-24, 2024
LES DIABLERETS CONFERENCE CENTER, LES DIABLERETS, SWITZERLAND
CHAIRS: Xiaowei Zhuang and Rong Fan
VICE CHAIRS: Xiaoliang Sunney Xie and Angela Oliveira Pisco

Solid State Chemistry +GS

JUL 21-26, 2024
COLBY-SAWYER COLLEGE, NEW LONDON, NH
CHAIR: Arthur Mar
VICE CHAIR: Catherine Oertel

Solid State Studies in Ceramics +GS

AUG 4-9, 2024
MOUNT HOLYOKE COLLEGE, SOUTH HADLEY, MA
CHAIRS: Wayne Kaplan and Edwin Garcia
VICE CHAIRS: Elizabeth Dickey and Sossina Haile

Stereochemistry +GS

Jul 21-26, 2024
SALVE REGINA UNIVERSITY, NEWPORT, RI
CHAIRS: Eric Jacobsen and Tamas Benkovics
VICE CHAIRS: Sarah Reisman and Oliver Thiel

Streptococcal Biology +GS

AUG 11-16, 2024
GRAND SUMMIT HOTEL AT SUNDAY RIVER, NEWRY, ME
CHAIRS: Michael Federle and Jan-Willem Veening
VICE CHAIRS: Kimberly Kline and Jose Lemos

Structural Nanomaterials +GS

MAY 12-17, 2024
LES DIABLERETS CONFERENCE CENTER, LES DIABLERETS, SWITZERLAND
CHAIRS: Lei Lu and Xun-Li Wang
VICE CHAIRS: Ruth Schwaiger and Wendy Gu

Synaptic Transmission +GS

JUL 14-19, 2024
RENAISSANCE TUSCANY IL CIOCCO, LUCCA (BARGA), ITALY
CHAIRS: Daniel Choquet and Graeme Davis
VICE CHAIRS: Inna Slutsky and Samuel Young

Systems Aging +GS

Jun 2-7, 2024
Rey Don Jaime Grand Hotel, Castelldefels, Spain
CHAIR: Steve Horvath
VICE CHAIR: Sara Hagg

Systems Chemistry +GS

JUN 16-21, 2024
MOUNT SNOW, WEST DOVER, VT
CHAIRS: Rebecca Schulman and Rafal Klajn
VICE CHAIRS: Akif Tezcan and Rienk Eelkema

Thiol-Based Redox Regulation and Signaling +GS

JUL 14-19, 2024
REY DON JAIME GRAND HOTEL, CASTELLDEFELS, SPAIN
CHAIR: Carolyn Sevier
VICE CHAIR: Elizabeth Veal

Three Dimensional Electron Microscopy +GS

JUN 23-28, 2024
REY DON JAIME GRAND HOTEL, CASTELLDEFELS, SPAIN
CHAIR: Sriram Subramaniam
VICE CHAIR: Julia Mahamid

Tribology +GS

JUN 23-28, 2024
BATES COLLEGE, LEWISTON, ME
CHAIR: Seong Kim
VICE CHAIR: Rosa M. Espinosa-Marzal

Two Dimensional Electronics Beyond Graphene +GRS

JUN 16-21, 2024
SOUTHERN NEW HAMPSHIRE UNIVERSITY, MANCHESTER, NH
CHAIRS: Jie Shan and Frank Koppens
VICE CHAIRS: Cory Dean and Deep Jariwala

Unconventional Semiconductors and Their Applications +GRS

JUN 16-21, 2024
STONEHILL COLLEGE, EASTON, MA
CHAIRS: Hanwei Gao and Iván Mora-Seró
VICE CHAIRS: Joseph Berry and Laura Herz

Unifying Ecology Across Scales +GRS

JUL 28 - AUG 2, 2024
SOUTHERN NEW HAMPSHIRE UNIVERSITY, MANCHESTER, NH
CHAIR: John DeLong
VICE CHAIR: Jennifer Sunday

Venom Evolution, Function and Biomedical Applications +GRS

AUG 11-16, 2024
MOUNT SNOW, WEST DOVER, VT
CHAIRS: Stephen Mackessy and Irina Vetter
VICE CHAIRS: Maria Vittoria Modica and Darin Rokyta

Vibrational Spectroscopy +GRS

AUG 4-9, 2024
BRYANT UNIVERSITY, SMITHFIELD, RI
CHAIRS: Judy Kim and Poul Petersen
VICE CHAIRS: Jahan Dawlaty and Julianne Gibbs

Visual System Development +GRS

MAY 19-24, 2024
RENAISSANCE TUSCANY IL CIOCCO, LUCCA (BARGA), ITALY
CHAIR: Valerie Wallace
VICE CHAIRS: Jeremy Kay and Justin Kumar

Water and Aqueous Solutions +GRS

JUL 21-26, 2024
HOLDERNESS SCHOOL, HOLDERNESS, NH
CHAIR: Susan Rempe
VICE CHAIR: Mischa Bonn

"GRCs plays such an important role in introducing young people to their scientific communities, maintaining vibrant discussions in established fields, and in the scientific development of new fields."

DR. FRANCES H. ARNOLD, California Institute of Technology